Microstructure of vanadium micro-alloyed steels for automotive applications

Interaction of precipitation with austenite-to-ferrite phase transformation studied by SANS and neutron diffraction

Ioannidou, C.

DOI
10.4233/uuid:2dda1059-5567-40d4-b95d-94e66ed7a108

Publication date
2022

Document Version
Final published version

Citation (APA)
Ioannidou, C. (2022). *Microstructure of vanadium micro-alloyed steels for automotive applications: Interaction of precipitation with austenite-to-ferrite phase transformation studied by SANS and neutron diffraction*. [Dissertation (TU Delft), Delft University of Technology]. https://doi.org/10.4233/uuid:2dda1059-5567-40d4-b95d-94e66ed7a108

Microstructure of vanadium micro-alloyed steels for automotive applications

Interaction of precipitation with austenite-to-ferrite phase transformation studied by SANS and neutron diffraction

Microstructure of vanadium micro-alloyed steels for automotive applications

Interaction of precipitation with austenite-to-ferrite phase transformation studied by SANS and neutron diffraction

Dissertation

for the purpose of obtaining the degree of doctor
at Delft University of Technology
by the authority of the Rector Magnificus, Prof.dr.ir. T.H.J.J. van der Hagen
chair of the Board for Doctorates
to be defended publicly on
Wednesday, 30 March 2022 at 12:30 o'clock

by

Chrysoula IOANNIDOU

Master of Science in Nanosciences and Nanotechnologies, Aristotle University of Thessaloniki, Greece
Master in Electrical and Computer Engineering, Aristotle University of Thessaloniki, Greece

born in Didymoteicho, Greece

This dissertation has been approved by the promotors.

Composition of the doctoral committee:

Rector Magnificus	chairperson
Dr.ir. S.Erik Offerman	Delft University of Technology, promotor
Dr.ir. Ad.A. van Well	Delft University of Technology, copromotor

Independent members:

Prof.dr.ir. L.A.I. Kestens	Ghent University, Belgium
Prof.dr.ir. B.J. Kooi	University of Groningen
Prof.dr. M.J. Santofimia Navarro	Delft University of Technology
Dr.ir. N.H. van Dijk	Delft University of Technology
Dr.ir. C. Bos	Delft University of Technology, reserve member

Other member:

Dr. R.A. Rijkenberg	Tata Steel

Keywords: vanadium micro-alloyed steel, in-situ measurements, Small-Angle Neutron Scattering, Neutron Diffraction, phase-transformation kinetics, precipitation kinetics.

The research described in this thesis was carried out in the Department of Materials Science and Engineering, Faculty of Mechanical, Maritime and Materials Engineering, and in the Department of Radiation Science and Technology, Faculty of Applied Sciences.
The research was supported by the Materials Innovation Institute (M2i) and the Technology Foundation TTW, which is part of the Netherlands Organization for Scientific Research (NWO). Peter Smaal Foundation provided 3-month support to this research.

An electronic copy of this dissertation is available at: https://repository.tudelft.nl/ .

Printed by ProefschriftMaken || www.proefschriftmaken.nl

Author email: c.ioannidou@tudelft.nl

Summary

The focus of the present work is on the micro-alloying element vanadium, which is well known for providing precipitation strengthening to steels and which has, therefore, attracted a lot of interest the last decades. Vanadium carbide precipitation can take place in the migrating austenite/ferrite interface during the austenite-to-ferrite phase transformation, i.e. interphase precipitation, and in ferrite. Due to the beneficial contribution of the vanadium carbides to the mechanical properties of the steel and the necessity to make optimum use of vanadium, it is critical to understand and quantify the vanadium carbide precipitation and its interaction with the austenite-to-ferrite phase transformation.

We study the precipitation kinetics of vanadium carbides and its interaction with the phase transformation kinetics in vanadium micro-alloyed steels that differ in vanadium and carbon concentrations and that have undergone different isothermal annealing treatments. In Chapter 1, the introduction to the research topic and the scope of this thesis are described. The novelty of our research is the use of advanced neutron scattering techniques i.e. Neutron Diffraction and Small-angle Neutron Scattering (SANS), coupled to Atom Probe Tomography (APT) and Transmission Electron Microscopy (TEM), to study model vanadium micro-alloyed steels during heat-treatments. The combination of neutron diffraction and SANS to study, simultaneously and in-situ, the interaction between the phase-transformation and precipitation kinetics is unique, as is the furnace that is designed and developed for these in-situ measurements. The results provide fundamental insight into the role of vanadium on the phase-transformation and precipitation kinetics, which is deemed essential for the development of micro-alloyed steels with reduced amounts of alloying elements without compromising properties.

In Chapter 2, the vanadium carbide precipitation kinetics and its interaction with the phase transformation kinetics is investigated. Two micro-alloyed steels that differ in vanadium and carbon concentrations by a factor of two, but have the same vanadium-to-carbon atomic ratio of 1:1 are studied. Dilatometry is used for heat-treating the specimens and studying the phase-transformation kinetics during isothermal annealing at 900 °C, 750 °C and 650 °C for up to 10 h. Samples annealed for different holding times are used for ex-situ SANS, TEM and APT to study the precipitation kinetics. Vanadium carbide precipitation is only observed during or after the austenite-to-ferrite phase transformation at 650 °C and not during annealing at 900 °C and 750 °C. The precipitate volume fraction and mean radius continuously increase as the holding time increases, while the precipitate number density starts to decrease after 20 min, which corresponds to the time at which the phase transformation has finished. This indicates that nucleation and growth are dominant during the first 20 min, while later precipitate growth and coarsening take place. TEM indicates the presence of spherical/slightly ellipsoidal precipitates in all steels after annealing at 650 °C and APT shows gradual changes in the precipitate chemical composition during annealing at 650 °C, which finally reaches a 1:1 atomic ratio of vanadium-to-carbon in the core of the precipitates after 10 h.

Chapter 3 introduces a custom-made furnace designed and built by our group at TU Delft. It is able to facilitate in-situ and simultaneous neutron diffraction and SANS measurements during heat-treatments of metals. In-situ and simultaneous studies on phase-transformation and precipitation kinetics are necessary in order to gain an in-depth understanding of the nucleation and growth of precipitates in relation to the evolution of austenite decomposition at high temperatures. Precipitation, occurring during solid-state phase transformations in micro-alloyed steels, is generally studied through TEM, APT and ex-situ SANS measurements. The advantage of SANS over the other two characterization techniques is that it allows for the quantitative determination of size distribution, volume fraction, and number density of a statistically significant number of precipitates within the resulting iron matrix at room

temperature. However, individual ex-situ SANS measurements do not provide information regarding the correlation between interphase precipitation and phase transformations. The presented furnace is, thus, developed for in-situ studies in which SANS measurements can be performed simultaneously to neutron diffraction measurements during typical high-temperature thermal treatments for steels. The furnace is capable of carrying out thermal treatments involving fast heating and cooling as well as high operation temperatures (up to 1200 °C) for a long period of time with accurate temperature control in a protective atmosphere and in a magnetic field of up to 1.5 T. The characteristics of this furnace give the possibility of developing new research studies for better insight of the relationship between phase-transformation and precipitation kinetics in steels and also in other types of materials containing nano-scale microstructural features.

In Chapter 4, in-situ SANS is used to determine the time evolution of the chemical composition of precipitates at 650 °C and 700 °C in three micro-alloyed steels with different vanadium and carbon concentrations. The evolution of the ratio of the nuclear to magnetic SANS component is used for this analysis. The samples are heat-treated in the furnace presented in Chapter 3. Precipitates with a distribution of sub-stoichiometric carbon-to-metal ratios in all steels are detected. The precipitates have a high iron content at the early stages of annealing, which is gradually being substituted by vanadium during isothermal holding. Eventually a plateau in the composition of the precipitate phase is reached. Faster changes in the precipitate chemical composition are observed at the higher temperature in all steels. We found that the addition of vanadium and carbon to the steel has an accelerating effect on the evolution of the precipitate composition. Addition of vanadium to the nominal composition of the steel increases the concentration of vanadium in the precipitates, reduces the iron concentration and leads to a smaller carbon-to-metal ratio. APT measurements prove the presence of precipitates with a distribution of carbon-to-metal ratios, ranging from 0.75 to 1, after 10 h of annealing at 650 °C or 700 °C in all studied steels.

In Chapter 5, in-situ neutron diffraction and SANS are employed for the first time simultaneously in order to reveal the interaction between the austenite-to-ferrite phase-transformation and the precipitation kinetics in-situ in vanadium micro-alloyed steels. The neutron scattering measurements are performed in three steels with different vanadium and carbon concentrations during isothermal annealing treatments at 650 °C and 700 °C for 10 h. The furnace introduced in Chapter 3 is used for the heat treatments. The austenite-to-ferrite phase-transformation and precipitation kinetics are quantified and the interaction between these two phenomena is explained. We show that the phase transformation is completed during the 10 h annealing treatment in all cases and that it is faster at 650 °C than at 700 °C for all alloys. Our analysis shows that additions of vanadium and carbon to the steel composition cause a retardation of the phase transformation and the effect of each element is explained through its contribution to the Gibbs free energy dissipation. The phase transformation is found to initiate the vanadium carbide precipitation. The presence of ellipsoidal precipitates is confirmed by TEM, contributing to the SANS data analysis. Larger and fewer precipitates are detected at the higher temperature in all three steels, and a larger number density of precipitates is detected in the steel with higher concentrations of vanadium and carbon. The effect of the precipitation kinetics to the phase-transformation kinetics is also discussed. An important outcome is that the external magnetic field applied during the experiments, necessary for the SANS measurements, causes a delay in the onset and time evolution of the phase transformation and consequently on the precipitation kinetics.

Sammenvatting

De focus van het huidige werk ligt op het micro-legeringselement vanadium, dat bekend staat om zijn precipitatieversterking van staal en dat daarom de laatste decennia veel belangstelling heeft gewekt. Vanadiumcarbideprecipitatie kan plaatsvinden in het migrerende austeniet/ferriet-grensvlak tijdens de fasetransformatie van austeniet naar ferriet, dat wil zeggen grensvlakprecipitatie, en in ferriet. Vanwege de gunstige bijdrage van vanadiumcarbide aan de mechanische eigenschappen van het staal en de noodzaak om optimaal gebruik te maken van vanadium, is het van cruciaal belang om de precipitatie van vanadiumcarbide en de interactie ervan met de fasetransformatie te begrijpen en te kwantificeren.
We bestuderen de precipitatiekinetiek van vanadiumcarbide en de interactie ervan met de austeniet-naar-ferriet fasetransformatie in vanadium micro-gelegeerde staalsoorten die verschillen in vanadium- en koolstofconcentraties en die verschillende isotherme gloeibehandelingen hebben ondergaan. In Hoofdstuk 1 worden de inleiding tot het onderzoeksonderwerp en de reikwijdte van dit proefschrift beschreven. Een van de vernieuwende aspecten van ons onderzoek is het gebruik van geavanceerde neutronenverstrooiingstechnieken, d.w.z. neutronendiffractie en kleine-hoek-neutronenverstrooiing (SANS), gekoppeld aan Atom Probe Tomography (APT) en transmissie-elektronenmicroscopie (TEM), om modellegeringen van vanadium micro-gelegeerd staal te bestuderen tijdens warmtebehandelingen. De combinatie van neutronendiffractie en SANS om gelijktijdig en in-situ de interactie tussen de fasetransformatie en precipitatiekinetiek te bestuderen is uniek, net als de oven die ontworpen en ontwikkeld is voor deze in-situ metingen. De resultaten geven fundamenteel inzicht in de rol van vanadium in de fasetransformatie en precipitatiekinetiek, hetgeen essentieel wordt geacht voor de ontwikkeling van micro-gelegeerde staalsoorten met verminderde hoeveelheden legeringselementen zonder afbreuk te doen aan de eigenschappen.
In Hoofdstuk 2 wordt de precipitatiekinetiek van vanadiumcarbide en de interactie met de fasetransformatie onderzocht. Er worden twee micro-gelegeerde staalsoorten bestudeerd die een factor twee verschillen in vanadium- en koolstofconcentraties, maar dezelfde atomaire verhouding vanadium tot koolstof van 1:1 hebben. Dilatometrie wordt gebruikt voor de warmtebehandelingen van de proefstukken en voor het bestuderen van de fasetransformatiekinetiek tijdens gloeien bij 900 °C, 750 °C en 650 °C gedurende maximaal 10 uur. Voor het bestuderen van de precipitatiekinetiek worden ex-situ SANS-, TEM- en APT-metingen worden uitgevoerd . Vanadiumcarbideprecipitatie wordt alleen waargenomen tijdens of na de fasetransformatie van austeniet naar ferriet bij 650 °C en niet tijdens gloeien bij 900 °C en 750 °C. De volumefractie en de gemiddelde straal van de precipitaten nemen continu toe naarmate de gloeitijd toeneemt, terwijl het aantal precipitaten per volume eenheid na 20 minuten begint af te nemen, hetgeen overeenkomt met het tijdstip waarop de fasetransformatie is voltooid. Dit geeft aan dat kiemvorming/nucleatie en groei dominant zijn tijdens de eerste 20 minuten, terwijl later groei en vergroving van de precipitaten plaatsvindt. TEM toont de aanwezigheid aan van bolvormige of licht ellipsvormige precipitaten in alle bestudeerde staalsoorten na gloeien bij 650 °C. APT toont geleidelijke veranderingen in de chemische samenstelling aan van het precipitaat tijdens gloeien bij 650 °C. De kern van de precipitaten bereikt uiteindelijk een samenstelling met een atomaire verhouding van vanadium-tot-koolstof van 1:1 na 10 uur gloeien op 650 °C.
in hoofdstuk 3 wordt een oven geïntroduceerd, die speciaal voor dit onderzoek is ontworpen en gebouwd door onze groep aan de TU Delft waarmee in-situ en gelijktijdige neutronendiffractie en SANS-metingen tijdens warmtebehandelingen van metalen uitgevoerd kunnen worden. In-situ en simultaan onderzoek naar fasetransformatie- en precipitatiekinetiek is nodig om een fundamenteel inzicht te krijgen in de nucleatie en groei van precipitaten in

relatie tot de fasetransformatiekinetiek van austeniet naar ferriet bij hoge temperaturen. De vorming van precipitaten, die optreedt tijdens vaste-stof-fasetransformaties in micro-gelegeerde staalsoorten, wordt over het algemeen bestudeerd door middel van TEM-, APT- en ex-situ SANS-metingen. Het voordeel van SANS ten opzichte van de andere twee karakteriseringstechnieken is dat het de kwantitatieve bepaling mogelijk maakt van de grootteverdeling, volumefractie en kiemdichtheid van een statistisch significant aantal precipitaten in de ijzer matrix. Individuele ex-situ SANS-metingen geven echter geen informatie over de correlatie tussen de kinetiek van grensvlakprecipitatie en de kinetiek van de fasetransformatie. De oven die wij hebben ontwikkeld is geschikt voor in-situ studies waarin SANS-metingen gelijktijdig kunnen worden uitgevoerd met neutronendiffractiemetingen tijdens typische thermische behandelingen van staal bij hoge temperaturen. De oven is in staat om thermische behandelingen uit te voeren met snelle opwarming en koeling, bij hoge bedrijfstemperaturen (tot 1200 °C) gedurende een lange periode met een nauwkeurige temperatuurregeling in een beschermende atmosfeer en in een magnetisch veld tot 1,5 T. Dit maakt deze oven geschikt voor onderzoek dat erop is gericht om een beter inzicht te krijgen in de relatie tussen fasetransformatie- en precipitatiekinetiek in staal. De oven kan ook gebruikt worden om structuren op de schaal van nanometers in andere materialen te bestuderen.
In hoofdstuk 4 wordt beschreven hoe de chemische samenstelling van de precipitaten, zoals gemeten met in-situ SANS, verandert met de tijd tijdens het gloeien op 650 °C en 700 °C van drie micro-gelegeerde staalsoorten met verschillende vanadium- en koolstofconcentraties. De verhouding tussen het aantal ijzer en vanadium atomen en de verhouding tussen het aantal koolstof en metaal atomen in de precipitaten wordt afgeleid uit de verhouding tussen de nucleaire en magnetische SANS-componenten. De warmtebehandeling van de stalen wordt uitgevoerd met de oven die wordt beschreven in hoofdstuk 3. De precipitaten blijken een sub-stoichiometrische verhouding van koolstof-tot-metaalatomen te hebben in alle onderzochte staalsoorten. De precipitaten hebben een hoog ijzergehalte in de eerste stadia van gloeien, maar geleidelijk worden de ijzer atomen vervangen door vanadium atomen. Na lang gloeien verandert de samenstelling van de precipitaten niet meer. Snellere veranderingen in de chemische samenstelling van de precipitaten worden waargenomen bij de hogere temperatuur in alle onderzochte staalsoorten. Verder nemen we waar dat de toevoeging van vanadium en koolstof aan het staal eveneens een versnellend effect heeft op de ontwikkeling van de precipitaatsamenstelling. Toevoeging van vanadium aan de nominale samenstelling van het staal verhoogt de concentratie vanadium in de precipitaten, verlaagt de ijzerconcentratie en leidt tot een kleinere koolstof/metaalverhouding. Uit APT-metingen blijkt dat de koolstof-tot-metaalverhouding in de precipitaten variëert van 0,75 tot 1, na 10 uur gloeien bij 650 °C of 700 °C in alle onderzochte staalsoorten.
In hoofdstuk 5 worden in-situ neutronendiffractie en SANS voor het eerst gelijktijdig gebruikt om de interactie tussen de fasetransformatiekinetiek van austeniet naar ferriet en de precipitatiekinetiek in-situ in vanadium micro-gelegeerd staal te bestuderen. De neutronenverstrooiingsmetingen worden uitgevoerd in drie staalsoorten met verschillende vanadium- en koolstofconcentraties tijdens isotherme gloeibehandelingen bij 650 ° C en 700 ° C gedurende 10 uur. Voor de warmtebehandelingen wordt de in hoofdstuk 3 geïntroduceerde oven gebruikt. De fase-transformatie- en precipitatiekinetiek worden gekwantificeerd in alle staalsoorten bij beide temperaturen en de interactie tussen deze twee fenomenen wordt uitgelegd. We laten zien dat de fasetransformatie in alle gevallen voltooid is tijdens de 10 uur durende gloeibehandeling en dat de transformatie sneller is bij 650 ° C dan bij 700 ° C voor alle onderzochte legeringen. Onze analyse toont aan dat toevoegingen van vanadium en koolstof aan de staalsamenstelling een vertraging van de fasetransformatie veroorzaken en het effect van elk element wordt verklaard door zijn bijdrage aan de Gibbs vrije-energiedissipatie. De fasetransformatie blijkt de vanadiumcarbide-precipitatie te initiëren. De aanwezigheid van

precipitaten met de vorm van een ellipsoïde wordt bevestigd door TEM. Deze informatie gebruiken we voor de analyse van de SANS-metingen. Bij alle drie de staalsoorten worden grotere maar minder precipitaten gedetecteerd bij de hogere temperatuur. Een grotere dichtheid in het aantal precipitaten wordt gedetecteerd in het staal met hogere concentraties vanadium en koolstof. Het effect van de precipitatiekinetiek op de fasetransformatiekinetiek wordt ook besproken. Een interessante uitkomst is dat het externe magnetische veld dat tijdens de experimenten wordt aangelegd en dat nodig is voor de SANS-metingen, een vertraging veroorzaakt van de fasetransformatie van austeniet naar ferriet en bijgevolg van de precipitatiekinetiek.

Contents

Chapter 1 - Introduction

1.1. Introduction

Nowadays, the key drivers for reducing the weight of vehicles are resource efficiency, improvement of fuel economy and reduction of CO_2 emissions of cars with an internal combustion engine. These can be achieved simultaneously by making efficient use of steel. Partial global switching to higher strength steel could save 105 million tons of steel per year and 20% of the costs of the global use of steel [1]. Vehicle weight reduction includes weight reduction in the chassis and suspension system as well, implying that the steel developed for these applications should offer advanced properties. In particular, high strength, ductility and stretch flange-ability are required for chassis and suspension parts that are made of steel.
In order to meet the high demands for the steels used in automotive applications, the steel industry has developed Advanced High Strength Steels (AHSS). However, the conventional AHSS cannot provide the enhanced combination of properties required for the chassis and suspension system, i.e. the high strength combined with ductility and stretch flange-ability, as AHSS consist of a multiphase microstructure, which is sensitive to the formation of voids and cracks during e.g. stretch-flanging. The mechanism behind the formation of voids and cracks is the stress localization at the interfaces between the hard phases, e.g. martensite, and the soft ductile ferrite.
A new generation of AHSS, referred to as NANOHITEN or nano-steels, were recently developed and are promising candidates to meet the above unique combination of properties (Fig. 1.1a). Nano-steels are micro-alloyed steels whose microstructure consists of a ferritic matrix that provides ductility, and of nanometer-sized precipitates that provide strength. The microstructures of the nano-steel and the conventional multiphase AHSS are schematically illustrated in Figs. 1.1b and c [2].

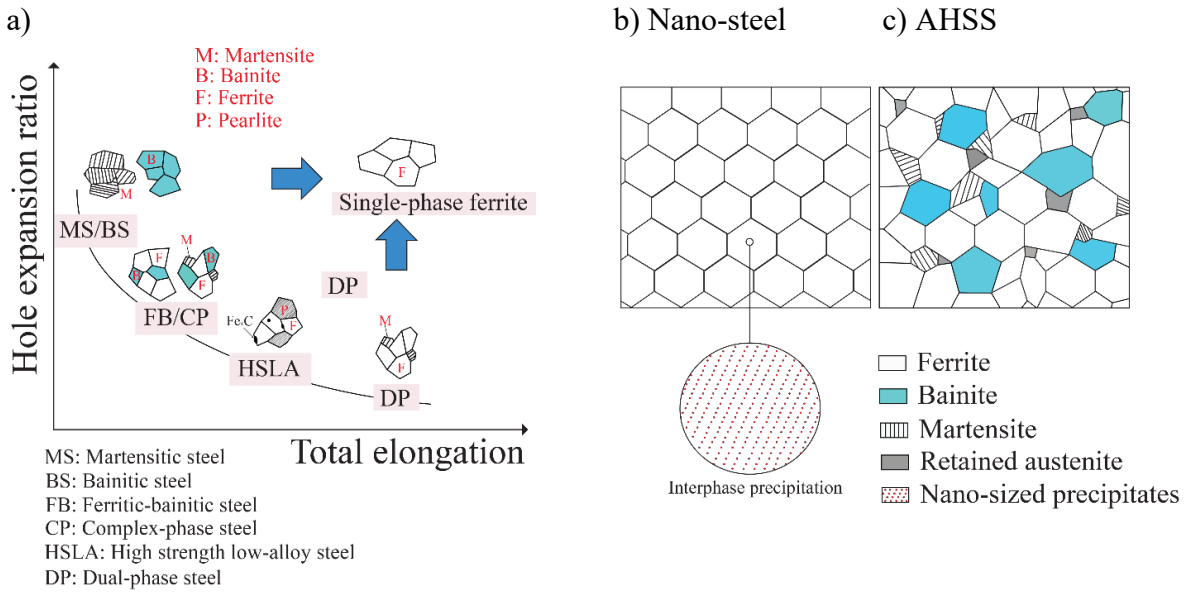

Fig. 1.1. a) Hole expansion ratio as a function of total elongation in steels with difference microstructures. Microstructure of b) nano-steel and c) conventional AHSS. The Figures are reproduced from Ref. [2].

Since they offer advantageous characteristics, nano-steels are being used in chassis and suspension parts. However, the downside of nano-steels is that they include a considerable

amount of micro-alloying elements, i.e. typically summing up to 0.1 wt.%, but in some cases up to 0.4 wt.%, such as niobium, titanium, and/or vanadium and possibly in combination with molybdenum. These elements are necessary for the formation of the nano-scale precipitates [3]-[6]. Along with the consumption of large amounts of these elements when considering the worldwide steel production, their high cost makes the efficient use of these elements of high importance. Moreover, niobium has a high supply risk for the EU thus it is considered as a very critical raw material [7]. Vanadium and titanium are also considered to be critical raw materials by the EU, albeit less critical than niobium. Consequently, developing resource-efficient nano-steels, which contain smaller amounts of micro-alloying elements and fewer critical raw materials while maintaining their good mechanical properties, is of great interest for the automotive community.

The focus of the present work is on vanadium, well-known for providing strong precipitation strengthening to steels [8],[9]. Vanadium carbide (VC) precipitation takes place in the migrating austenite/ferrite interface during the austenite-to-ferrite phase transformation as well as in ferrite, since both phenomena occur within the same range of temperatures during thermal processing of nano-steels. The first type of precipitation is called interphase precipitation. The solubility of vanadium in austenite is high, higher than that of titanium and niobium, and therefore vanadium carbides do not tend to form in austenite. However, due to the solubility drop of vanadium when austenite transforms to ferrite, interphase precipitation as well as precipitation in ferrite are favored [10]. This leads to a high precipitate nucleation rate and a fine precipitate distribution, which is essential for the strengthening of the steel [10].

Due to the beneficial contribution of the vanadium carbides to the overall mechanical properties of steel and the necessity to make optimum use of vanadium, more research is required to understand the vanadium carbide precipitation and its interaction with the austenite-to-ferrite phase transformation. However, disentangling the kinetics between these two phenomena has been proven challenging, highlighting the necessity of performing in-situ and simultaneous measurements.

The novelty of this thesis lies in the combination of model alloys, heat-treatments, advanced neutron scattering characterization techniques, i.e. Neutron Diffraction and Small-angle Neutron Scattering (SANS), Atom Probe Tomography (APT) and Transmission Electron Microscopy (TEM). Coupling neutron diffraction and SANS, aiming to monitor the interaction between the phase-transformation and precipitation kinetics in-situ and simultaneously, is unique. The furnace developed by our group in order to facilitate these in-situ measurements, together with the advanced neutron characterization techniques, can open new horizons in acquiring valuable quantitative data during the processing of steels with different compositions and under different heat-treatments.

1.2. Scope and outline of the thesis

The aim of this thesis is to provide insight into the kinetics of vanadium carbides in steels and its interaction with the austenite-to-ferrite phase-transformation kinetics. The quantitative results can contribute to modelling and eventually predicting the precipitation and phase-transformation kinetics in steels, which can lead to the optimization of steel designs for automotive applications with reduced energy consumption.

In Chapter 2, dilatometry is used for heat-treating the steel specimens and for studying the phase transformation kinetics during isothermal annealing treatments. Ex-situ SANS, TEM and APT measurements are performed in the heat-treated samples to study the precipitation kinetics. The precipitate nucleation, growth and coarsening kinetics are, in this way, quantitatively related to the phase-transformation kinetics.

In Chapter 3, a custom-made furnace developed by our group at TU Delft is presented. The furnace facilitates in-situ and simultaneous neutron diffraction and SANS measurements during heat-treatments of metals. It is capable of carrying out heat treatments involving fast heating and cooling as well as high operating temperatures for several hours with accurate temperature control in a protective atmosphere and under a magnetic field of up to 1.5 T. The furnace can be easily installed at the Larmor Instrument at ISIS Neutron and Muon Source, where the whole experimental setup gives the opportunity to develop new research studies in metals that contain nano-scale structural features, aiming to provide a better understanding of the relationship between phase transformation and precipitation kinetics.
In Chapter 4, we perform in-situ SANS in order to follow the time evolution of the chemical composition of the precipitates in different vanadium micro-alloyed steels during isothermal annealing treatments. The evolution of the ratio of the nuclear to magnetic SANS component is monitored and used for this analysis. The sub-stoichiometric precipitate composition and the concentration of iron in the precipitates are quantified, and the effects of the steel composition, annealing temperature and time on the precipitate composition are explained. APT is also used to study the precipitate composition, supporting the SANS data analysis.
In Chapter 5, in-situ neutron diffraction and SANS are performed simultaneously and the interaction between the austenite-to-ferrite phase transformation and the precipitation kinetics is revealed. The phase transformation is found to initiate the vanadium carbide precipitation. We find that additions of vanadium and carbon to the steel cause a retardation of the phase transformation. The effect of each element is explained through its contribution to the Gibbs free energy dissipation. We finally show that the external magnetic field applied during the experiments, affects the onset and time evolution of the phase transformation and consequently the precipitation kinetics.

References

[1] Allwood, J. and Cullen, J. “Sustainable Materials - With Both Eyes Open”, Cambridge: UIT Cambridge Ltd, 2012.
[2] Z. Arechabaleta Guenechea and S. E. Offerman, World Scientific Series in Current Energy Issues, Critical Materials, pp. 193-221 (2019), Chapter 10: Substitution Case Study: Replacing Niobium by Vanadium in Nano-Steels.
[3] Y. Funakawa, T. Shiozaki, K. Tomita, T. Yamamoto, and E. Maeda, “Development of high strength hot-rolled sheet steel consisting of ferrite and nanometer-sized carbides,” ISIJ Int., vol. 44, no. 11, pp. 1945–1951, 2004.
[4] T. N. Baker, “Microalloyed steels,” Ironmak. Steelmak., vol. 43, no. 4, 264–307, 2016.
[5] T. N. Baker, “Processes, microstructure and properties of vanadium microalloyed steels,” Mater. Sci. Technol., vol. 25, no. 9, pp. 1083–1107, 2009.
[6] S. Shanmugam, M. Tanniru, R. D. K. Misra, D. Panda, and S. Jansto, “Microalloyed V-Nb-Ti and V steels Part 2 - Precipitation behaviour during processing of structural beams,” Mater. Sci. Technol., vol. 21, no. 2, pp. 165–177, 2005.
[7] European Commision, “Report on critical raw materials for the EU”, Report of the Ad hoc Working Group on defining critical raw materials, May 2014 and up-dates in 2020.
[8] T. N. Baker, “Processes, microstructure and properties of vanadium microalloyed steels,” Mater. Sci. Technol., vol. 25, no. 9, pp. 1083–1107, 2009.
[9] S. Z. and B. H. Rune Lagneborg, Tadeusz Siwecki, “Role of vanadium in microalloyed steels,” Stal’, no. 12, pp. 58–59, 2001.
[10] Lagneborg, R., Hutchinson, B., Siwecki, T., and Zajac, S., “The role of Vanadium in microalloyed steels”, Scandinavian Journal of Metellurgy, Vol. 28, page 186-242, 1999.

Chapter 2 - Interaction of precipitation with austenite-to-ferrite phase transformation in vanadium micro-alloyed steels – An ex-situ neutron scattering study

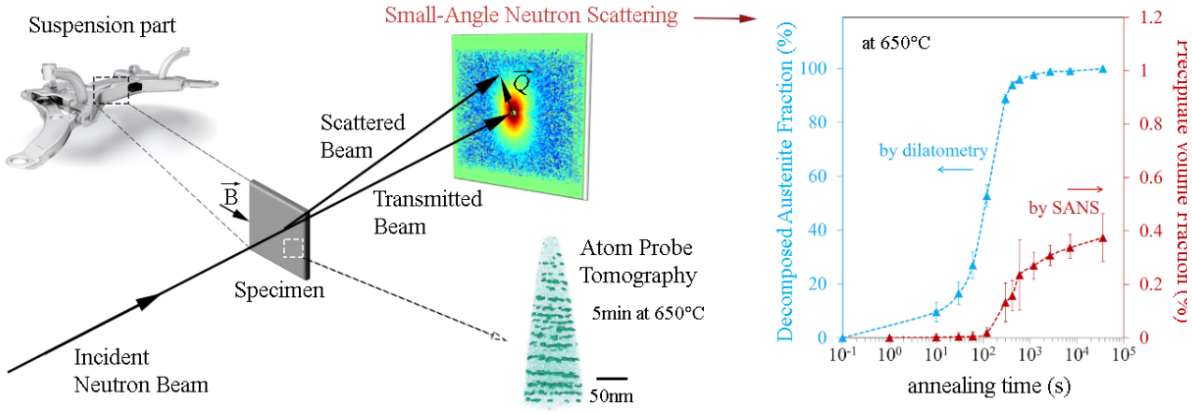

Abstract

The precipitation kinetics of vanadium carbides and its interaction with the austenite-to-ferrite phase transformation is studied in two micro-alloyed steels that differ in vanadium and carbon concentrations by a factor of two, but have the same vanadium-to-carbon atomic ratio of 1:1. Dilatometry is used for heat-treating the specimens and studying the phase transformation kinetics during annealing at isothermal holding temperatures of 900 °C, 750 °C and 650 °C for up to 10 h. Small-Angle Neutron Scattering (SANS) and Atom Probe Tomography (APT) measurements are performed to study the vanadium carbide precipitation kinetics. Vanadium carbide precipitation is not observed after annealing for 10 h at 900 °C and 750 °C, which is contrary to predictions from thermodynamic equilibrium calculations. Vanadium carbide precipitation is only observed during or after the austenite-to-ferrite phase transformation at 650 °C. The precipitate volume fraction and mean radius continuously increase as holding time increases, while the precipitate number density starts to decrease after 20 min, which corresponds to the time at which the austenite-to-ferrite phase transformation is finished. This indicates that nucleation and growth are dominant during the first 20 min, while later precipitate growth with soft impingement (overlapping diffusion fields) and coarsening take place. APT shows gradual changes in the precipitate chemical composition during annealing at 650 °C, which finally reaches a 1:1 atomic ratio of vanadium-to-carbon in the core of the precipitates after 10 h.

Reproduced from: "C. Ioannidou, Z. Arechabaleta, A. Navarro-López, A. Rijkenberg, R. M. Dalgliesh, S. Kölling, V. Bliznuk, C. Pappas, J. Sietsma, A. A. van Well, S. E. Offerman, "Interaction of precipitation with austenite-to-ferrite phase transformation in vanadium micro-alloyed steels', Acta Materialia 181 (2019) 10–24."

2.1. Introduction

The improvement of fuel economy, the reduction of CO_2 emissions and the fulfilment of European Union initiatives [1] and legislations [2] are key drivers for the automotive industry nowadays to reduce the vehicle weight. This includes weight reduction in the chassis and suspension system, which requires that steel offers high strength, ductility and stretch flange-ability for the manufacturing of intricate and complex light-weight components. Micro-alloyed steels containing nano-sized precipitates in a ferrite matrix are promising candidates to meet these requirements simultaneously [3]-[6] and are already used in chassis and suspension parts [3],[4],[7]-[9]. However, these alloys contain a considerable amount of micro-alloying additions [6]. Based on the above demands, resource-efficient steels, which contain smaller amounts of micro-alloying elements and critical raw materials [10] while maintaining their good mechanical properties, are of great interest.

Titanium (Ti), niobium (Nb), molybdenum (Mo) and vanadium (V) are widely used as micro-alloying elements to improve the performance of steel through their effect on the microstructure and consequently on the mechanical properties [3]-[6],[11]-[22]. These elements may cause grain size refinement, recrystallization retardation and precipitate formation. The focus of the present work is on vanadium, which is well-known for providing precipitation strengthening to steels and which has, therefore, attracted a lot of interest in the last decades [4],[6],[13],[15]-[20],[23],[24]. Vanadium carbide (VC) precipitation can take place in the migrating austenite/ferrite interface during the austenite-to-ferrite phase transformation, i.e. interphase precipitation, and in ferrite. The solubility of vanadium in austenite is high, higher than the solubility of Ti and Nb, and therefore vanadium carbides do not tend to form in austenite. However, due to the solubility drop of vanadium when austenite transforms to ferrite, interphase precipitation as well as precipitation in ferrite are favored [15]. This reduces the rate of precipitate coarsening and leads to a fine precipitate distribution, which is critical for the hardening of the steel [15]. Due to the beneficial contribution of the vanadium carbides to the overall mechanical properties of steel and the necessity to make optimum use of vanadium, more research is required to understand the vanadium carbide precipitation and its interaction with the austenite-to-ferrite phase transformation.

Extensive research has been carried out on vanadium carbides and it is found that the precipitates' characteristics and kinetics are strongly dependent on the steel composition and treatment conditions. The transformation temperature and time are critical factors for the precipitation, determining the type of precipitation (interphase or random) and the precipitate size, shape, composition, number density and volume fraction [15]-[29]. The vanadium carbide crystal structure is observed to be of the NaCl-type of stoichiometric VC [16],[24], $VC_{0.9}$ [20], V_4C_3 [13],[27], or V_6C_5 [28], in a range of transformation temperatures from 600 to 700 °C. The precipitates have a Baker Nutting orientation relationship with the BCC ferrite matrix [16],[30], while their nucleation is favorable at non-Kurdjumov-Sachs ferrite/austenite interfaces [31],[32]. Their shape can be spherical [13],[17]-[19],[23],[24], disk-like [13],[20],[24], ellipsoidal [19],[20], rod-like [13], needle-like or cuboid [27], depending on the conditions described above. Furthermore, different levels of alloying elements (like Mo, Ti, Nb and N) are found to affect the vanadium carbide precipitates composition [13],[15],[16], shape [13],[27] and preferable growth direction [13],[15],[16],[27]. For instance, in Ref. [13], in low-carbon steels containing vanadium and molybdenum, the latter is present in the precipitates, forming disk-shaped (V,Mo)C growing along the (001) ferrite plane, and rod-shaped $(V,Mo)_4C_3$ growing along the (011) ferrite plane.

Transmission Electron Microscopy (TEM) and Atom Probe Tomography (APT) are mainly used for the precipitates characterization [12]-[14],[17]-[21],[23]-[28],[31]-[34]. Detailed research on vanadium carbide precipitation in low-carbon steels has been done by Kamikawa

et al. [19] and Zhang et al. [26],[29], who have extensively measured the precipitate size distribution and number density and their effect on the mechanical properties of the steel as a function of temperature and for various steel compositions. However, scarce literature on the kinetics of the precipitation is reported. Moreover, APT and TEM are limited in providing accurate statistical information on precipitate size distribution, number density and volume fraction, as the measured sample volume is usually relatively small (in the order of 10^6 nm^3).
Small-Angle Neutron Scattering (SANS) delivers statistical information regarding the average size, volume fraction, number density and size distribution of precipitates over larger specimen volumes [35] (e.g. 10x10x1 mm^3). Previous SANS studies have been performed on Ti-Mo micro-alloyed steel [14], NbC precipitates in austenite [22] and in ferrite [36], Fe-Cu alloys [37], Fe-Au alloys [38], maraging steels [39] and low-carbon steels [40]. SANS measurements on low-carbon V-micro-alloyed steels have only recently been reported [20],[23],[24]. The precipitation kinetics of disk-shaped and oblate vanadium carbides at 700 °C in a low-carbon steel [20], and of spherical and disk-shaped vanadium carbides in a temperature range from 600 to 700 °C in a medium-carbon steel, has been characterized by SANS at room temperature [24].
The present study aims to provide quantitative information on the vanadium carbide precipitation kinetics in low-carbon steels differing in vanadium and carbon content and heat treated at different temperatures (900, 750 and 650 °C) than previously reported in the literature. Emphasis is given on the kinetics of precipitation for up to 10 hours of annealing, on the interaction of the precipitation kinetics with the austenite-to-ferrite phase transformation kinetics and on the time evolution of the precipitate chemical composition during annealing. Small-Angle Neutron Scattering is combined with dilatometry, Atom Probe Tomography and Transmission Electron Microscopy for a comprehensive study of the precipitation and phase transformation kinetics.

2.2. Experimental

Two Fe-C-Mn-V steels produced by Tata Steel as 3 mm thick hot-rolled plates are studied. The chemical composition of the alloys is listed in Table 2.1. The two steels have different carbon and vanadium contents, therefore, they are referred to as LCLV (low carbon - low vanadium alloy) and HCHV (high carbon - high vanadium alloy) in this study, whereas the content of other alloying elements is kept as low as possible. The HCHV steel contains twice the fraction of vanadium and carbon with respect to the LCLV steel and the atomic ratio of V:C is 1:1 in both steels.

Table 2.1. Chemical composition of the steel samples in weight percent (wt%) and atomic percent (at%) with balance Fe.

Steel		C	Mn	V	Si	P	Cr	Al
LCLV	wt %	0.07	1.84	0.29	.010	.0010	.010	.004
	at %	0.33	1.86	0.32	.026	.0018	.011	.008
HCHV	wt %	0.14	1.83	0.57	.013	.0010	.007	.008
	at %	0.62	1.85	0.62	.026	.0018	.007	.002

Rectangular dilatometry specimens with dimensions 14 x 10 x 1 mm^3 are machined from the center of the as-received plates. These specimens are heat treated in a DIL-805 A/D dilatometer in which inductive heating under a low pressure of 10^{-4} mbar is used, while cooling is achieved by a flow of helium gas. An S-type thermocouple is spot-welded in the center of the specimen

surface in order to control and monitor the temperature during the thermal cycle. The change in length of the specimen is recorded as a function of temperature and the obtained dilatometry data are used to study the phase transformation kinetics in each treatment. Micro-segregation of alloying elements like manganese and vanadium is considered not significant based on Electron Probe Micro-Analysis (EPMA), therefore no prior homogenization treatment of the steels is performed.

The heat treatments performed in the dilatometer are schematically shown in Fig. 2.1. The specimens are heated to a high temperature (1050 °C for the LCLV and 1100 ºC for the HCHV steel) in the austenitic region for 15 minutes. These temperatures are chosen to be 50 °C above the precipitates' dissolution temperature in each steel as predicted by the ThermoCalc software [41]. The precipitates' dissolution temperatures are 994 °C and 1050 °C for the LCLV and HCHV steels, respectively (see Fig. 2.2). One specimen of each alloy is quenched to room temperature after soaking. These specimens are used to measure the prior austenite grain size (PAGS) in the ImageJ software [42], in optical micrographs taken in a KEYENCE VHX-5000 Digital Optical Microscope. The specimens have been prepared by following the standard metallographic preparation procedure, which includes grinding, polishing to 1 μm and etching with picric acid. The other specimens are cooled at a rate of 15 °C/s from the soaking temperature to a lower temperature (900, 750 or 650 ºC), where an isothermal annealing is applied for different holding times (10 s, 30 s, 1 min, 2 min, 5 min, 7 min, 10 min, 20 min, 45 min, 2 h and 10 h). The isothermal holding temperatures have been chosen based on the ThermoCalc predictions presented in Fig. 2.2, aiming to study the precipitation kinetics in austenite, during the austenite-to-ferrite phase transformation and in ferrite. Analysis of the dilatometry data indicates that the phase transformation takes place only during the isothermal holdings and not during cooling from the soaking temperature to the isothermal holding temperature. The thermal cycle is completed by a rapid quench to room temperature.

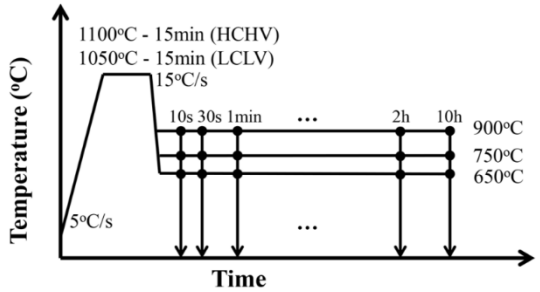

Fig. 2.1. Schematic representation of the thermal cycles applied in the dilatometer.

The microstructural evolution of the LCLV and HCHV steels during annealing at the three isothermal holding temperatures is revealed by means of Scanning-Electron Microscopy (SEM). The SEM measurements are performed at room temperature using a JEOL JSM 6500F microscope on the specimens previously treated in the dilatometer. The specimens are prepared for SEM following the metallographic preparation procedure described above and finally etched with 2% Nital.

Rectangular specimens with dimensions 10 x 10 x 1 mm^3 are machined from the dilatometry treated specimens and measured at room temperature by SANS. The aim is to study the precipitation kinetics of the LCLV and HCHV steels at the three isothermal temperatures mentioned above. The SANS measurements are performed on the Larmor Instrument at the ISIS Neutron and Muon Source (STFC Rutherford Appleton Laboratory). A 5 x 5 mm^2 neutron beam and a wavelength range of 0.42 - 1.33 nm are used. Wavelengths smaller than 0.42 nm are not considered to avoid effects from multiple Bragg scattering. A 3473-70 GMW

electromagnet is used to generate a transversal magnetic field of 1.65 T, perpendicular to the neutron beam. This strong magnetic field is necessary to magnetically saturate the specimens, avoid any contribution to the scattering signal from magnetic domains, and separate the nuclear and magnetic scattering contribution from the SANS pattern. The SANS detector is a 600 x 600 mm^2 ^3He tube array with an 8 x 8 mm^2 pixel size at a distance of 4.3 meters from the sample. Each specimen is exposed to the neutron beam for 35 minutes. The SANS data analysis is performed using the Mantid software [43].
The type of precipitation (interphase/random) as well as the precipitate shape and size are identified by TEM. The TEM analysis is performed on the LCLV and HCHV samples that are isothermally annealed at the temperature of 650 °C. A JEOL JEM-2200FS Transmission Electron Microscope with an accelerating voltage of 200 kV and a resolution of 1.3 Å is used. Thin foils are prepared by grinding the specimens to 100 μm and disks of a diameter of 3 mm are punched out from these thin foils. The extracted disks are electro-polished in a twin-jet Struers Tenupol-3, electro-polishing setup at 19 V and a pump flow rate of 12 l/min at 20 ºC. The electrolyte solution consisted of 5% perchloric acid ($HClO_4$) and 95% acetic acid (CH_3COOH). The imaging is carried out in the scanning mode (STEM) of the instrument during the measurements.
Atom Probe Tomography is used for the dilatometry heat-treated samples of LCLV and HCHV steels annealed at 650 °C to study the evolution of chemical composition, shape and morphology of precipitates during annealing. The specimens annealed for 5 min, 45 min and 10 h at 650 °C for both compositions are analyzed by APT to capture the precipitates' growth and coarsening kinetics. More than 5 tips are extracted from each specimen to optimize the statistics of the APT cluster analysis.
The specimens are prepared by the lift-out method using Focused Ion Beam milling (FIB) [44]. A last sputtering with 5 kV and 44 pA is applied to reduce the effect that the Gallium beam causes on the tips. After the FIB procedure, the tips are coated using an electron-beam induced Cobalt deposition [45] in order to limit Carbon diffusion along the shank [46]. The APT specimens are measured in a LEAP 4000X-HR system from CAMECA Instruments. Laser-assisted excitation is used with a pulse energy of 35 - 50 pJ, a pulse rate of 65-125 kHz, and a specimen base temperature of ~20 K.
The IVAS 3.8.0 software package from CAMECA Instruments is used for the APT data reconstruction and analysis. The entire analysis is based on isotope distribution (Mass-to-Charge-State Ratio - Da) [47]. The vanadium peaks are detected in 17, 25 and 25.5 Da in the Mass-to-Charge-State Ratio Spectrum, while carbon peaks are detected at 6, 6.5, 12 and 13 Da. Frequency distribution analysis for the elements proves that vanadium and carbon are clustered.

2.3. Results and Discussion

2.3.1. Phase transformation kinetics

2.3.1.1. Phase transformation kinetics at 900 and 750 °C

The PAGS is measured in the specimens directly quenched from the austenitization temperature to room temperature and the average values are 63 ± 3 μm for the LCLV and 62 ± 2 μm for the HCHV steel. Consequently, differences in the microstructural evolution of the two steels during annealing cannot be attributed to PAGS effects.
Analysis of the dilatometry data reveals no phase transformation in the LCLV and HCHV steels during annealing at 900 °C. This temperature is above the theoretical A_3 equilibrium temperatures, predicted by ThermoCalc [41] to be 830 °C and 834 °C in the LCLV and HCHV steels, respectively (Fig. 2.2). At 750 °C, only a very small fraction of ferrite is formed in the

LCLV steel after 10 h of annealing, while almost no transformation is taking place in the HCHV steel. Fig. 2.3a and b show the SEM micrographs of the LCLV and HCHV specimens annealed at 750 °C for 10 h, respectively. As seen in Fig. 2.3a, a small fraction of allotriomorphic ferrite is formed in the LCLV steel after 10 h, while the microstructure is almost fully martensitic for the same conditions in HCHV steel in Fig. 2.3b, confirming the dilatometry data interpretation.

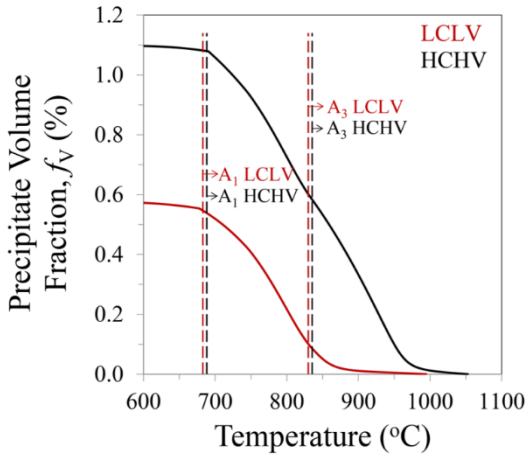

Fig. 2.2. Precipitate volume fraction versus temperature and the A_1 and A_3 transition temperatures for the LCLV and HCHV steels as predicted by ThermoCalc [41].

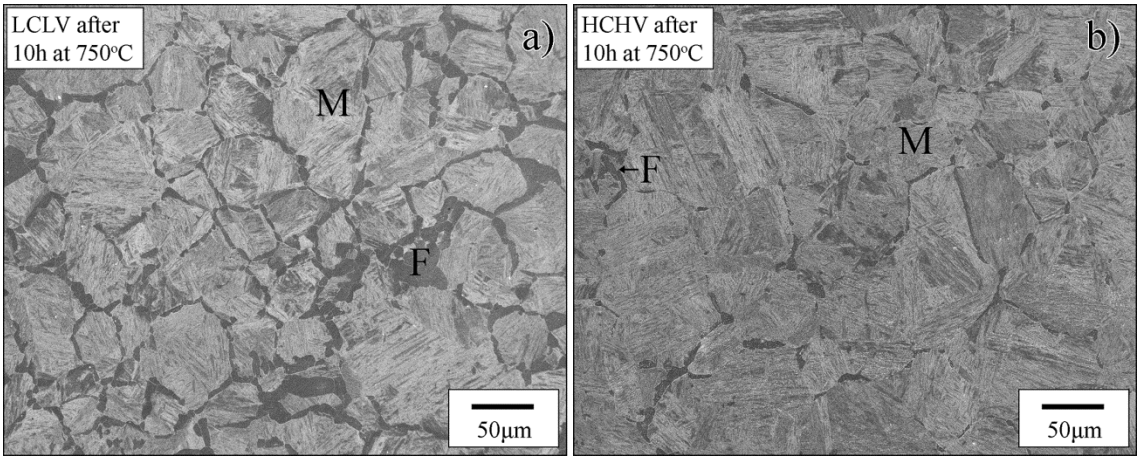

Fig. 2.3. SEM micrographs of the a) LCLV and b) HCHV samples isothermally annealed at 750 °C for 10 h. The existent ferritic (F) and martensitic (M) areas are indicated.

2.3.1.2. Phase transformation kinetics at 650 °C

At 650 °C, austenite transforms into ferrite in both steels according to the dilatometry curves. Fig. 2.4 shows the fraction of transformed phase during annealing at 650 °C for LCLV and HCHV steels as a function of annealing time. In both steels, more than 97% of the initial austenite is transformed after 20 min isothermal holding at 650 °C, so the final microstructure of the samples annealed for longer times mainly consists of ferrite. For shorter times, the microstructure consists of a mixture of ferrite and martensite. The martensite forms from the untransformed austenite during the final quenching to room temperature. According to Fig. 2.4, the onset of the austenite-to-ferrite phase transformation is delayed in the HCHV steel compared to the LCLV steel. This can be attributed to the higher carbon content of the HCHV steel, which stabilizes the austenite and delays the onset of phase transformation. In addition, vanadium can retard ferrite nucleation due to the formation of precipitates/clusters at the possible nucleation sites of ferrite [48]. However, the effect of vanadium on the phase-transformation kinetics requires further investigation (see Chapter 5 of this thesis). Based on theoretical TTT (time-temperature-transformation) diagram calculations using the program MUCG83 [49], the effect of carbon on the delay of the onset of phase transformation is stronger than the effect of vanadium in these steels.

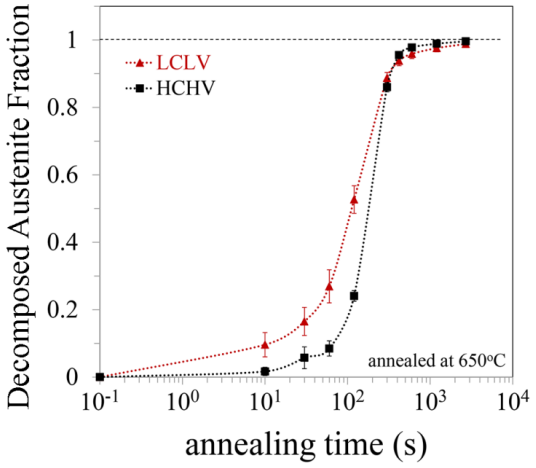

Fig. 2.4. Austenite to ferrite and pearlite phase transformation kinetics of LCLV(▲) and HCHV(■) steels during isothermal annealing at 650°C (from dilatometry). According to SEM, the fraction of pearlite formed can be neglected.

Representative SEM images showing the microstructural evolution during annealing at 650 °C for both steels are presented in Fig. 2.5. Figs. 2.5a, c and e are related to the LCLV steel specimens annealed for 2 min, 10 min and 10 h, respectively, while the micrographs in Figs. 2.5b, d and f correspond to HCHV specimens annealed for 1 min, 7 min and 10 h, respectively. The existent ferritic (F), martensitic (M) and pearlitic (P) areas are indicated in each condition. The SEM analysis shows the local formation of a small fraction of pearlite in both steels. The cementite precipitation is observed after 2 min of annealing in the LCLV steel and after 1min in the HCHV steel, as shown in Fig. 2.5a and b.

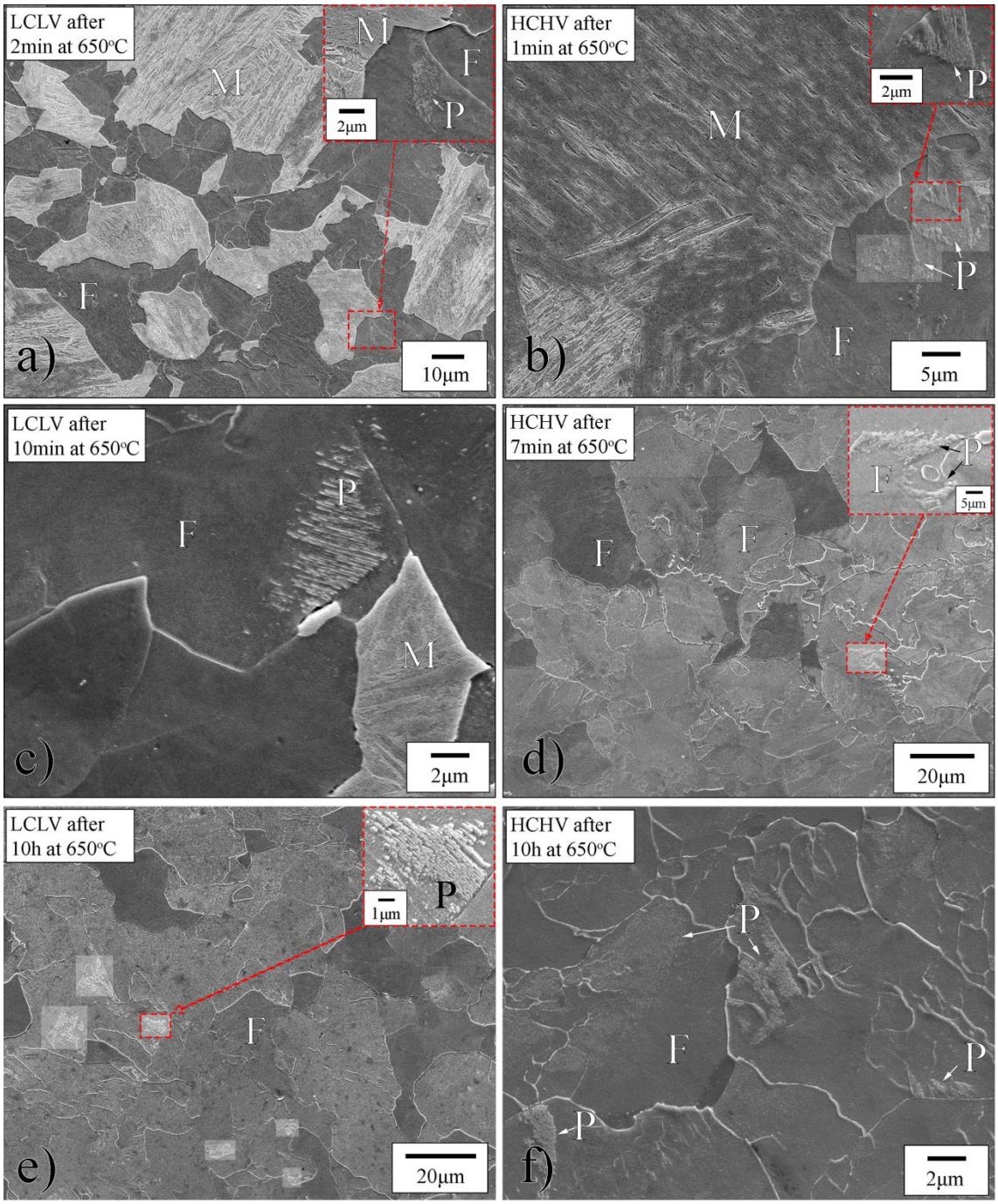

Fig. 2.5. SEM micrographs of the LCLV and HCHV steels isothermally annealed at 650°C for different times and subsequently quenched to room temperature. Microstructure of LCLV specimens annealed for a) 2min, c) 10min and e) 10h and of HCHV specimens annealed for b) 1min, d) 7min and f) 10h. The existent ferritic (F), martensitic (M) and pearlitic (P) areas in each condition are indicated.

2.3.2. Precipitation kinetics

2.3.2.1. Method for the Small-Angle Neutron Scattering data analysis

The Small-Angle Neutron Scattering intensity is a 2D pattern that reflects the macroscopic differential scattering cross-section, $(d\Sigma/d\Omega)(\mathbf{Q})$. This is a function of the scattering vector, **Q**, and is obtained from the SANS intensity after background correction and calibration of the neutron flux considering the detector efficiency and sample transmission [50]. The $(d\Sigma/d\Omega)(\mathbf{Q})$ may have two components because of the two different interactions of neutrons with matter. Neutrons interact with the nuclei of the atoms via nuclear forces, leading to the nuclear cross-section, $(d\Sigma/d\Omega)_{NUC}(Q)$, and with the magnetic moments of the unpaired electrons through the dipole-dipole interaction [35], leading to the magnetic cross-section, $(d\Sigma/d\Omega)_{MAG}(Q)$. The selection rules for the magnetic scattering are such that neutrons "see" only the magnetization components that are perpendicular to the scattering vector, **Q**. Thus, if an external magnetic field is high enough to saturate the magnetization and is applied along a direction contained in the detector plane, the macroscopic differential scattering cross-section can be written as [35]:

$$\left(\frac{d\Sigma}{d\Omega}\right)(\mathbf{Q}) = \left(\frac{d\Sigma}{d\Omega}\right)_{NUC}(Q) + \left(\frac{d\Sigma}{d\Omega}\right)_{MAG}(Q)\cdot\sin^2\alpha \ , \qquad \text{(Eq. 2.1)}$$

where α is the angle between the magnetic field direction and **Q**. In this way, it is possible to distinguish the nuclear and magnetic contribution to the scattering. For this purpose, we consider sectors of 30°, parallel and perpendicular to the magnetic field, leading to $(d\Sigma/d\Omega)_{NUC}$ and $(d\Sigma/d\Omega)_{NUC}+(d\Sigma/d\Omega)_{MAG}$, respectively, and the $(d\Sigma/d\Omega)_{MAG}$ is calculated as the difference between these results. We then obtain quantitative information on the precipitation kinetics in the steel matrix by a detailed analysis of the nuclear differential scattering cross-section, which for a dilute system of precipitates within a homogeneous matrix is given by [50]:

$$\left(\frac{d\Sigma}{d\Omega}\right)_{NUC}(Q) = (\Delta\rho_{NUC})^2 \int D_N(R)\cdot V^2(R)\cdot P^2(Q,R)\,dR \ , \qquad \text{(Eq. 2.2)}$$

with R and V the precipitate radius and volume (for spherical precipitates it is $V=(4/3)\pi R^3$) respectively. The log-normal number distribution, $D_N(R)$, is assumed to be given by:

$$D_N(R) = \frac{N_p}{R\sigma\sqrt{2\pi}}\exp\left\{-\frac{\left[\ln(R)-\ln(R_m)\right]^2}{2\sigma^2}\right\} \ , \qquad \text{(Eq. 2.3)}$$

where N_p is the precipitate number density, R_m is the mean precipitate radius and σ is the standard deviation of the size distribution. The precipitate volume distribution is the product $D_V(R) = D_N(R)\cdot V$.

$P(Q,R)$ is the form factor describing the precipitate shape, which for spherical precipitates is $P(Q,R)=3[\sin(QR)-(QR)\cos(QR)]/(QR)^3$ [50],[51].

Finally, $\Delta\rho_{NUC}$ is the difference in nuclear scattering length density between the matrix and the precipitates (nuclear contrast) and is given by $\Delta\rho_{NUC} = \rho^{Fe} - \rho^{VC} \approx N_o^{Fe}\, b_c^{Fe} - N_o^{VC}\, b_c^{VC}$. The term N_o is the number density calculated for Fe and VC considering their bulk density, ρ_m, and their molecular weight, M, using $N_o = N_A\,\rho_m/M$, yielding the number density of Fe atoms $N_o^{Fe} = 84.9$ nm^{-3} and of VC, with the stoichiometric ratio of V/C = 1, $N_o^{VC} = 55.1$ nm^{-3}. N_A is the Avogadro's number and b_c is the coherent scattering length. The scattering length of the matrix and the precipitates is $b_c^{Fe} = 9.45 \times 10^{-15}$ m and $b_c^{VC} = 6.26 \times 10^{-15}$ m, respectively, resulting in

ρ^{Fe}= 8.02 x 10^{-4} nm^{-2} for iron and ρ^{VC} = 3.46 x 10^{-4} nm^{-2} for the vanadium carbides, and eventually in $\Delta\rho_{NUC}^2$ = 20.8 x 10^{-8} nm^{-4}.
The precipitate volume fraction, f_V, is calculated by integrating the area under the $[Q,Q^2(d\Sigma/d\Omega)_{NUC}]$ curve, which is commonly known as Kratky Plot. For a dual-phase system, the area $Q_{o,NUC}$ below the Kratky Plot is [35]:

$$Q_{o,NUC} = \int_0^{\infty} \left(\frac{d\Sigma}{d\Omega}\right)_{NUC} Q^2 dQ = 2\pi^2 \left(\Delta\rho_{NUC}\right)^2 f_V \left(1 - f_V\right) . \quad \text{(Eq. 2.4)}$$

When the precipitate volume fraction is low, the above equation is simplified to:

$$f_V \cong \frac{Q_{o,NUC}}{2\pi^2 \left(\Delta\rho_{NUC}\right)^2} . \quad \text{(Eq. 2.5)}$$

The precipitation kinetics of both steels during annealing at 900, 750 and 650 °C is discussed below based on the SANS measurements.
Similar to the nuclear scattering length density, the difference in magnetic scattering length density between the matrix and the precipitates (magnetic contrast), $\Delta\rho_{MAG}$, is given by $\Delta\rho_{MAG} = \rho_{MAG}^{Fe} - \rho_{MAG}^{VC}$**.** The matrix magnetic scattering length, ρ_{MAG}^{Fe}, is $\rho_{MAG}^{Fe} = p / V_{bcc}$. The p is the magnetic scattering length of Fe given by p = 2.699 x 10^{-15} m $* \mu$, where μ is the saturation per iron atom in μ_B units. The magnetic scattering from the precipitates can be neglected here as the precipitates are considered to be non-magnetic, resulting in $\Delta\rho_{MAG} = \rho_{MAG}^{Fe}$ = 5.09 x 10^{-4} nm^{-2} at room temperature. The magnetic differential scattering cross section can be used in the same way as the nuclear differential scattering cross section for quantifying the precipitation kinetics providing the same results, however, these calculations are not included in the current work.

2.3.2.2. Precipitation kinetics at 900 and 750 °C

The SANS intensity of the LCLV and HCHV steels that have undergone an isothermal annealing treatment at 900 and 750 °C for 10 h is compared to the corresponding intensity of the specimen of each steel that is directly quenched from the soaking temperature to room temperature and does not contain any precipitates. No significant differences are observed, leading to the conclusion that precipitates are not detected in any in these conditions. The SANS intensity curves of the samples annealed at 900 and 750 °C can be found in the supplementary material of this manuscript (Appendix A).
The absence of precipitates at 900 and 750 °C in both steels is closely related to the (near) non-occurrence of the austenite-to-ferrite phase transformation as discussed during the interpretation of the dilatometry and SEM data. Since the austenite-to-ferrite phase transformation does neither take place at 900 °C in any of the steels nor at 750 °C in the HCHV steel, and due to the high solubility of the vanadium in austenite, precipitates are not formed in these conditions, which is in agreement with Ref. [15]. Precipitates are also not detected in the LCLV steel at 750 °C after 10 h of isothermal holding despite the transformation of a small fraction of austenite into ferrite in this steel. Nucleation of precipitates might have started in this condition, however, the precipitates size and volume fraction are expected to be extremely small, i.e. radius below 1 nm and volume fraction below 0.1 %, respectively, and, therefore, not detectable by the SANS technique.

Moreover, it is worth mentioning here that ThermoCalc equilibrium calculations are not in agreement with our studies, since ThermoCalc predicts precipitation and phase transformation at 750 °C in both steels and precipitation at 900 °C for the HCHV alloy (Fig. 2.2). The difference between our experimental results and ThermoCalc could be attributed either to the Gibbs-Thomson effect, which could be significant for small nano-sized precipitates, or to the fact that the system has not reached equilibrium after 10 h of annealing.
The equilibrium concentration of vanadium in the matrix taking into account the Gibbs-Thomson effect, $X_{eq,r}$, is given by [52]:

$$X_{eq,r} = X_{eq,\infty} \exp\left(\frac{2\gamma v_{at}^{VC}}{X_p r k_B T} \right). \quad \text{(Eq. 2.6)}$$

In the equation above, $X_{eq,\infty}$ is the solubility limit of vanadium in ferrite according to ThermoCalc, γ the interface energy between the precipitates and the ferritic matrix, v_{at}^{VC} the average atomic volume of the vanadium carbides, X_p the equilibrium mole fraction of vanadium in the VC-precipitates calculated by ThermoCalc, r the precipitate radius, k_B the Boltzmann constant and T the temperature. For precipitates with an average radius in the range 1.1 - 2 nm and for typical precipitate-ferritic matrix interface energy values in the range 0.2 - 0.8 J/m^2 [53], the resulted $X_{eq,r}$ at 750 and at 900 °C is very close to the $X_{eq,\infty}$ and always smaller than the total amount of vanadium in both steels. This means that the increase in the solubility limit of vanadium in the matrix due to the increase in Gibbs free energy of the precipitates (attributed to the Gibbs Thomson effect) is very small and not sufficient to prevent precipitation in the steels. Based on the above calculations, we conclude that the Gibbs Thomson effect cannot – on its own – explain the difference between the experimental results and equilibrium ThermoCalc calculations, and other kinetics factors may play a role.
The most possible explanation is that the system is far from equilibrium after 10 h at 750 and 900 ºC for both alloys. According to ThermoCalc, the maximum ferrite fraction that can form at 750 ºC is 86 % and 87 % for the LCLV and the HCHV alloy, respectively. As a result, a maximum precipitate volume fraction that could form would be 0.42 and 0.95 % in the LCLV and the HCHV steels, respectively. At 900 ºC, ferrite formation is not predicted by ThermoCalc in either of the steels, however, precipitation of a maximum of 0.3 % would be possible in the HCHV steel. The equilibrium conditions predicted by ThermoCalc could be reached by applying longer annealing times at 750 and 900 ºC.

2.3.2.3. Precipitation kinetics at 650 °C

The SANS nuclear differential scattering cross sections of the LCLV and HCHV steels annealed at 650 °C are shown in Fig. 2.6a and b, respectively. The corresponding magnetic components are presented in Fig. 2.6c and d. For the sake of simplicity we only show the scattering curves obtained at the most informative annealing times (30 s, 2 min, 5 min, 20 min, 45 min, 2 h and for 10 h at 650 °C). The nuclear and magnetic scattering cross sections of the direct-quenched specimens are also provided.
SANS is used to study the precipitation kinetics in the LCLV and HCHV steels, in which it should be kept in mind that the dislocations from the martensite phase also contribute to the SANS pattern. The analysis of the precipitation kinetics that is explained below refers to both LCLV and HCHV steels as their nuclear scattering cross sections follow the same trend during annealing.

For the specimens of both steels annealed for less than 2 min at 650 °C, the SANS intensity follows a Q^{-4} power law (Porod's Law), indicating that scattering originates from large-scale objects like grain boundaries and interfaces [37],[49],[54]. In the absence of deviations from the Q^{-4} power law, we conclude that neither precipitation nor phase transformation have started. Between 2 and 20 min of annealing, a decrease in the nuclear intensity is observed in the low-Q area ($Q < 0.2$ nm-1). The $(d\Sigma/d\Omega)_{NUC}$ at low-Q values originates from large objects like grain boundaries, dislocations and large precipitates [37],[49],[54]. Therefore, the decrease in the $(d\Sigma/d\Omega)_{NUC}$ in the low-Q area of the 2 - 20 min curves is attributed to the phase transformation through the decrease of the fraction of martensite (which forms directly after the quench from 650 °C to room temperature and contains high dislocation and grain boundary densities) in agreement to the phase transformation kinetics curve in Fig. 2.2. For higher Q values, in the 2-20 min curves, an increase in $(d\Sigma/d\Omega)_{NUC}$ is observed, originating from the scattering of small precipitates. For annealing times longer than 20 min, when the phase transformation is almost complete, additional scattering is observed over the whole Q range. In the low-Q range, the major contribution to the signal comes from cementite as well as from the large VC precipitates. The small increase in $(d\Sigma/d\Omega)_{NUC}$ in the high-Q area is caused by smaller precipitates.
The magnetic scattering cross sections of the LCLV and HCHV steels, depicted in Fig. 2.6c and d, do not show the same Q dependence and time evolution as the corresponding nuclear scattering cross sections, indicating different nuclear and magnetic structures in our steels. A decrease in $(d\Sigma/d\Omega)_{MAG}$ curves is observed over the entire Q range in both steels up to 2 h of annealing while an increase is observed for longer annealing times. The martensitic phase having a high dislocation density, large number of Low-Angle Grain Boundaries (LAGB) and iron carbides may pin the walls between the magnetic domains and hinder their alignment along the magnetic field. The precipitation of cementite and the formation of pearlite also affect the magnetic SANS intensity, but this feature is not further analyzed in this paper.

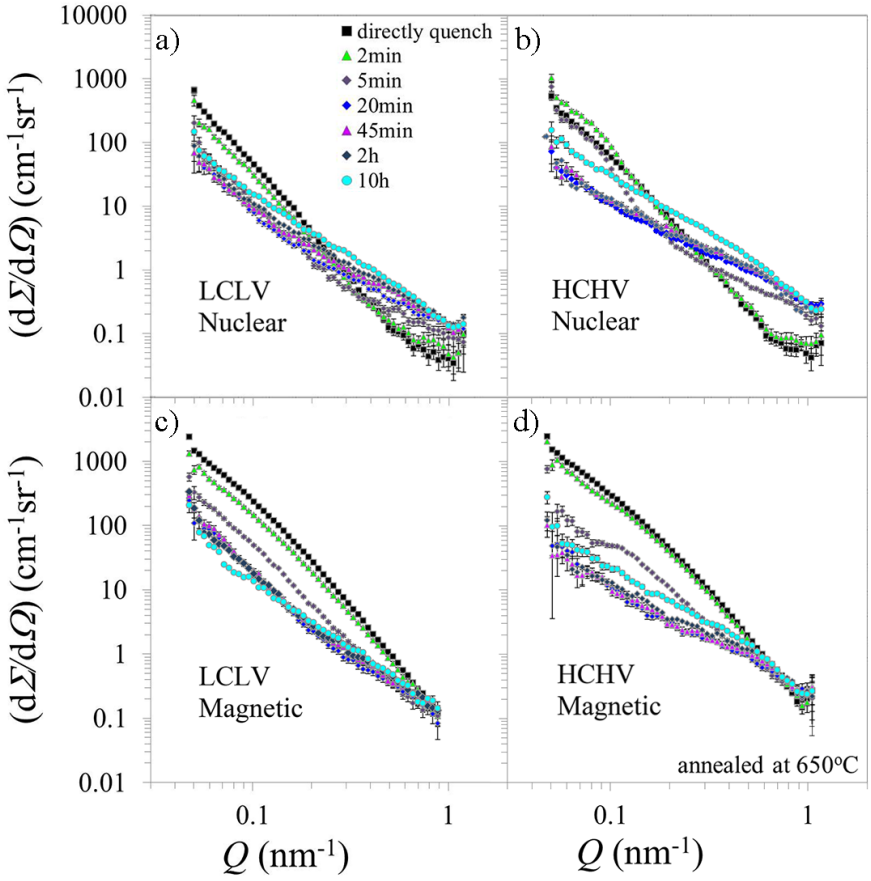

Fig. 2.6. Nuclear differential scattering cross section of a) LCLV and b) HCHV steel as a function of Q measured at room temperature after annealing at 650 ºC for up to 10h. The corresponding magnetic differential scattering cross sections are plotted in c) and d) for LCLV and HCHV steel, respectively. The scattering curves of the samples heat-treated at the most representative conditions are shown.

Quantitative information on the precipitation kinetics is obtained from Kratky plots, in which $Q^2(d\Sigma/d\Omega)_{NUC}$ is plotted as a function of Q. Fig. 2.7a and b show such plots for different annealing times at 650 °C of LCLV and HCHV for some representative conditions. For an accurate analysis of the VC precipitation kinetics by SANS, only the scattering from the precipitates is considered whereas all other contributions are subtracted.

During isothermal annealing, a progressive increase in the $Q^2(d\Sigma/d\Omega)_{NUC}$ intensity in both LCLV and HCHV steels is observed. As the holding time increases, the peak position of the curves gradually moves towards the lower Q area, reflecting the increasing precipitate size (growth or coarsening).

The experimentally derived Kratky plots are fitted to the theoretical Kratky-plot equation (Eq. 2.2 multiplied by Q^2) leading to the calculation of the fitting parameters R_m, N_p and σ for each curve. The fitting is performed for the specimens of LCLV and HCHV steels annealed for times longer than 5 min at 650 °C. For shorter annealing times, the experimental $Q^2(d\Sigma/d\Omega)_{NUC}$ curves cannot be fitted as they have a completely flat profile (precipitates are not detected before 2 min as explained before).

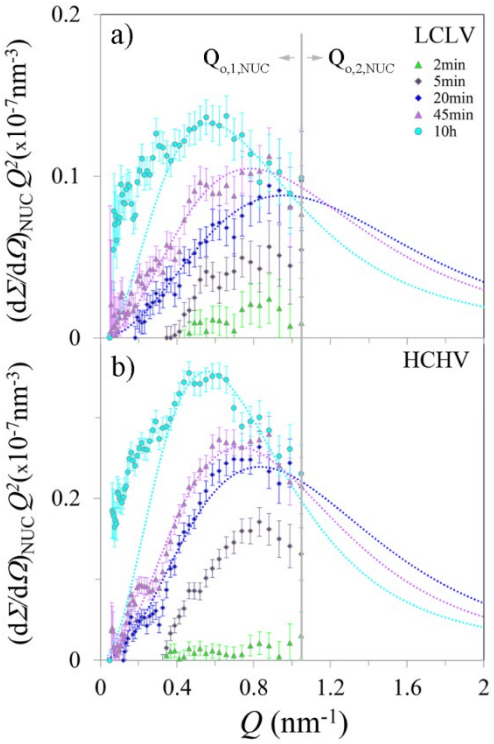

Fig. 2.7. Time evolution of $Q^2(d\Sigma/d\Omega)_{NUC}$ vs Q for the a) LCLV and the b) HCHV steel during holding at 650°C for up to 10h (data points), after background subtraction. The thinner dotted lines represent the theoretical $Q^2(d\Sigma/d\Omega)_{NUC}$ curves originating from the fitting.

The evolution of the precipitate mean radius, R_m, and number density, N_p, during annealing from 5 min to 10 h is shown in Fig. 2.8a and b, respectively. The precipitates' growth during annealing in both steels is reflected in the increase of the precipitate mean radius (Fig. 2.8a). A maximum precipitate radius of 1.5 and 1.8 nm is reached after 10 h of annealing for LCLV and HCHV steels, respectively.

Like the mean precipitate radius, the precipitate number density follows the same trend for both steels. The gradual increase in the precipitate number density (Fig. 2.8b) from the beginning of annealing and for the first 10 min at 650 °C suggests intense precipitate nucleation. Between 10 and 20 min of annealing, the precipitate number density remains constant while their radius is increasing, indicating that precipitate growth is the dominant phenomenon. We define as time period 1 the first 20 min of annealing and period 2 from 20 min to the end of annealing. During period 2, the precipitate number density continuously decreases due to precipitate coarsening.

At the beginning of annealing the precipitates are small and their size is comparable to the resolution of the SANS instrument, leading to larger error bars in the precipitate mean radius (Fig. 2.8a) and number density (Fig. 2.8b). Additionally, the background contribution from dislocations decreases with time and fitting the Kratky-plot curves results in lower error values for longer annealing times.

As shown in the $(d\Sigma/d\Omega)_{NUC}(Q)$ curves of Fig. 2.6a and c, the Q range of the nuclear differential scattering cross sections is restricted to $0.04 \leq Q \leq 1.05$ nm^{-1}, limiting the Q range of the Kratky-plot curves (Fig. 2.7a and b) and, consequently, leading to an underestimation of the precipitate volume fraction, f_V, if only this Q-range is used for the integration. For an accurate volume fraction determination, first the area below the $Q^2(d\Sigma/d\Omega)_{NUC}$ curves, $Q_{o,NUC}$, is calculated as the sum of $Q_{o,1,NUC}+Q_{o,2,NUC}$, and then the precipitate volume fraction is derived from Eq. 2.5. $Q_{o,1,NUC}$ is the area below the curve determined by the data in the Q range 0.04 - 1.05 nm^{-1}. These data are calculated by multiplying $(d\Sigma/d\Omega)_{NUC}(Q)$ (corrected after background subtraction) with Q^2, as described above. $Q_{o,2,NUC}$ is the area below each dotted Kratky plot for Q values between 1.05 and 2 nm^{-1} (Fig. 2.7a and b). The dotted curve is the theoretical calculated Kratky plot curve in the Q range 1.05 - 2 nm^{-1}. It is calculated for each annealed

specimen using the R_m, N_p and σ values obtained from the fitting of the experimental Kratky plot in the Q range 0.04 - 1.05 nm^{-1}. Deviations between experiments and theory in the low Q range are most probably related to difficulties in the background subtraction.

The time evolution of the precipitate volume fraction during annealing at 650 °C is illustrated in Fig. 2.8c for both LCLV and HCHV steels. Before 2 min, no precipitates are detected and the measured precipitate volume fraction curve is practically zero. After 2 min, the volume fraction increases continuously, reaching a maximum 0.37 ± 0.09 % for the LCLV steel and 0.93 ± 0.16 % for the HCHV steel after 10 h of annealing. Precipitation takes place during and after the phase transformation and precipitates are measured in both steels when a certain volume fraction of ferrite is formed after 5 min. This is illustrated in Fig. 2.9a and b, in which the precipitation and phase transformation kinetics are plotted for the LCLV and HCHV steels, respectively. The enhanced precipitation during phase transformation is a result of solubility drop of the vanadium when austenite transforms to ferrite, giving rise to a high driving force for precipitation. The precipitates formed during the transformation are aligned in rows (interphase precipitation, see TEM image, Fig. 2.11, and APT maps, Fig. 2.12a and d), while those nucleating after the completion of the phase transformation are randomly dispersed and have a smaller diameter. The small increase in the nuclear scattering intensity in the large-Q area after 20 min of annealing at 650 °C, as shown in Fig. 2.6a and c, originates from these small precipitates.

The continuous increase in volume fraction after 20 min (Fig. 2.8c), combined to the increase in precipitate size (Fig. 2.8a) and the decrease in precipitate number density (Fig. 2.8b), indicates combined precipitate growth and coarsening. Fig. 2.8d shows the evolution of the amount of vanadium in solid solution, $f_{vanadium,ss}$, in both alloys. It decreases rapidly during precipitate nucleation and growth (during time period 1) and continues decreasing till the end of the annealing treatment due to the combined growth and coarsening (period 2).

The measured volume fraction, average precipitate size and number density of the precipitates are compared to the SANS results of previous studies of a steel with a similar that is annealed at 700 °C (instead of 650 °C) [20]. We observe similarities and important differences between annealing at 700 and 650 °C. We observe an increase in precipitate volume fraction in the LCLV steel from 0.13 to 0.37 % from 5 min to 10 h of annealing at 650 °C, which is similar to the findings reported in Ref. [20], which reports an increase from 0.09 to 0.28% during annealing in the same time range at 700 °C in a steel with similar vanadium content. However, we measure small (<2 nm) spherical / slightly ellipsoidal precipitates with number density of ~10^{23} m^{-3}, while in ref. [20], ~10 times larger disk-shape and oblate precipitates are detected with number density ~10^{21} m^{-3}, suggesting that small changes, like a 50 °C change in the annealing temperature, lead to very different precipitation kinetics. The precipitate number density values deduced from our SANS data are comparable to previous studies on vanadium carbides at the same temperatures for medium [18],[24] and low-carbon steels [19].

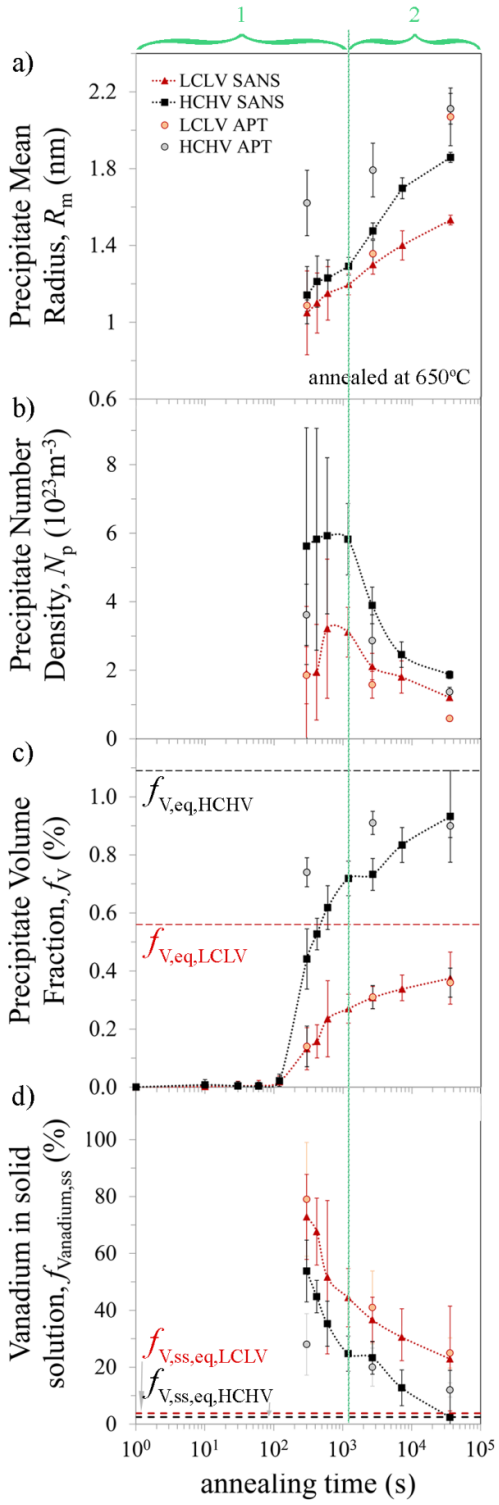

Fig. 2.8. Precipitate a) mean radius, R_m, b) number density, N_p, c) volume fraction, f_V, and, d) amount of vanadium in solid solution, $f_{vanadium,ss}$, evolution during annealing at 650 °C for the LCLV(▲) and HCHV(■) steels. During time period 1, phase transformation takes place and precipitate nucleation and growth are dominant. In period 2, phase transformation is almost complete (>97% of austenite transformed) and precipitate growth (with overlapping diffusion fields) and coarsening take place. The dashed lines indicate the equilibrium values calculated by ThermoCalc [41].

Thermodynamic calculations performed with the ThermoCalc software [41] give an equilibrium volume fraction for VC of 0.56% in the LCLV steel and 1.09% in the HCHV steel at 650 °C (Fig. 2.2), which is slightly higher than the values deduced by SANS. From these results, it is concluded that after 10 h of isothermal holding most of the vanadium is in the precipitates, but the volume fraction has not reached its maximum value.

The precipitation kinetics are found to have the same behavior in the LCLV and HCHV steels during annealing from 5 min to 10 h at 650 °C due to the same phase transformation kinetics

in this time range. Due to the delay in the onset of austenite-to-ferrite phase transformation in HCHV steel compared to LCLV steel at 650 °C (Fig. 2.2), and considering the fact that precipitation of vanadium carbides is more favored after the beginning of the phase transformation, a delay in precipitation kinetics in the HCHV steel is expected in order to follow the trend of the phase transformation curve. According to the phase transformation kinetics curves of Fig. 2.2, the delay should be observed during the first 5 min of annealing. However, because of the limitations of the SANS technique, precipitates are only detected after 5 min of annealing in both steels. Therefore possible differences in the start of the precipitation kinetics between both steels in the first 5 min of annealing cannot be observed.
Moreover, according to the dilatometry results in Fig. 2.2, after 5 min, the phase transformation kinetics for the LCLV and HCHV steels show similar behavior. This is reflected in the precipitation kinetics which follows the same trend in both steels after 5min as shown in Fig. 2.8a, b and c.

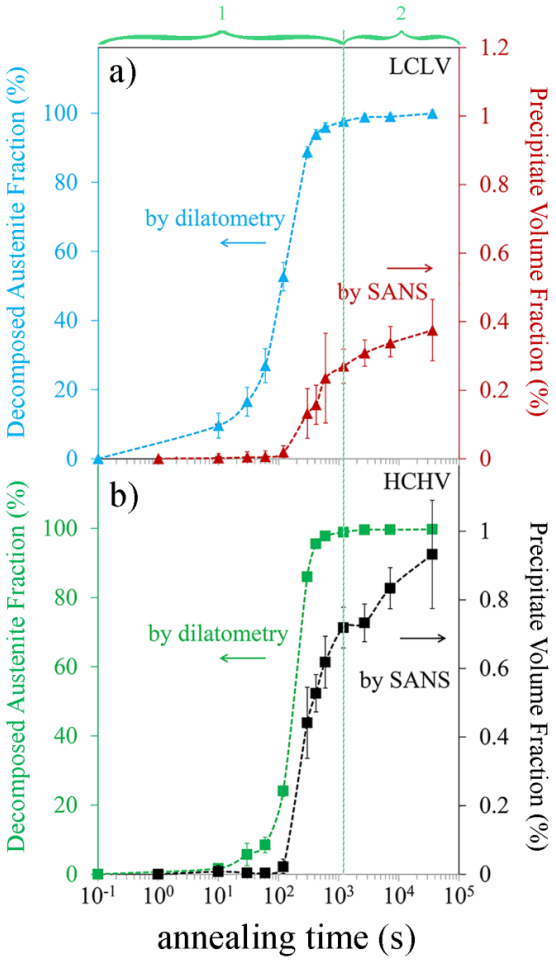

Fig. 2.9. Vanadium carbide precipitation and austenite-to-ferrite phase transformation kinetics (see Fig. 2.4) during isothermal annealing at 650 °C in the a) LCLV and b) HCHV steels. In both steels, precipitation takes place during and after the phase transformation. During time period 1, phase transformation takes place and precipitate nucleation and growth are dominant. In 2, phase transformation is almost complete (>97% of austenite transformed) and precipitate growth and coarsening take place.

As a last step in the precipitation kinetics analysis, Fig. 2.10a and b show the time evolution of the log-normal precipitate volume distribution of the VC precipitates in the LCLV and HCHV steels, respectively. The average precipitate size determines the peak position of the volume distribution curve while the area below each curve is the precipitate volume fraction at that time of annealing. For both steels, the peak area of the distribution increases with time until 20 min of annealing, without any shift in the peak position, indicating pronounced nucleation of small sized nuclei. After 20 min, the volume distribution curves broaden with increasing holding time, coupled with a decrease in peak height and a shift in the peak position to larger

R values. We thus conclude that the growth and coarsening effect is dominant in this time range and is becoming stronger with holding time.

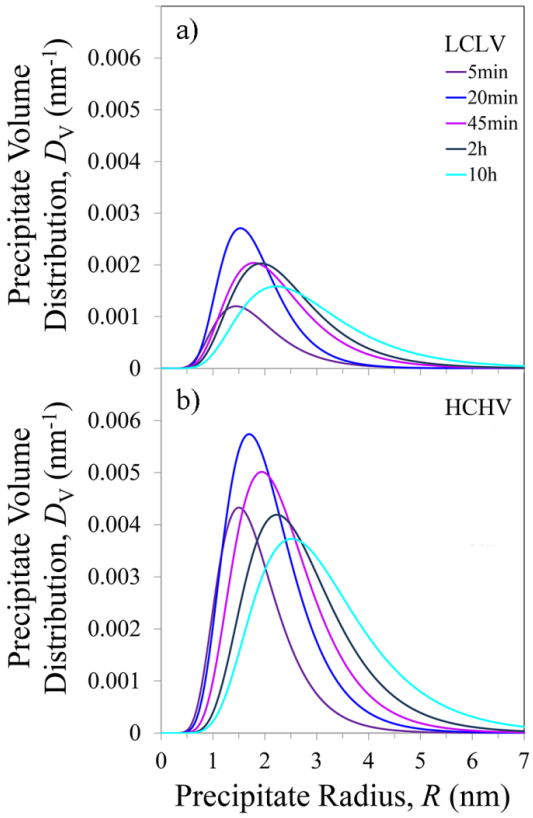

Fig. 2.10. Log-normal volume distribution, D_V, of the VC precipitates in the a) LCLV and b) HCHV steels during annealing at 650 °C for up to 10 h. The curves are based on the R_m, N_p and σ values resulted from the fitting of the experimental $Q^2(d\Sigma/d\Omega)_{NUC}$ results.

2.3.2.4. Precipitation characterization by TEM and APT at 650 °C

Fig. 2.11 shows a representative bright-field TEM image of the HCHV specimen annealed at 650 °C for 20 min and subsequently quenched to room temperature. The precipitates are represented in black while the ferritic matrix is represented in grey. The precipitates are arranged in rows, showing that interphase precipitation takes place during the austenite-to-ferrite phase transformation during the first 20 min of annealing. The average distance between the rows (inter-sheet spacing) in this condition is approximately 12 nm. The precipitates' average radius is measured to be around 1.1 nm, in agreement with the value 1.3 ± 0.6 nm derived from the SANS measurements. In addition, spherical (or slightly ellipsoidal) precipitates are observed, which a posteriori justifies our SANS data analysis based on the modelling of spherical precipitates. The fact that the precipitates' shape is spherical is in agreement to previous studies [18],[19],[24], in which spherical/ellipsoidal [18],[19] and spherical/disk-shaped [24] vanadium carbide precipitates were formed during isothermal annealing at the same temperature.

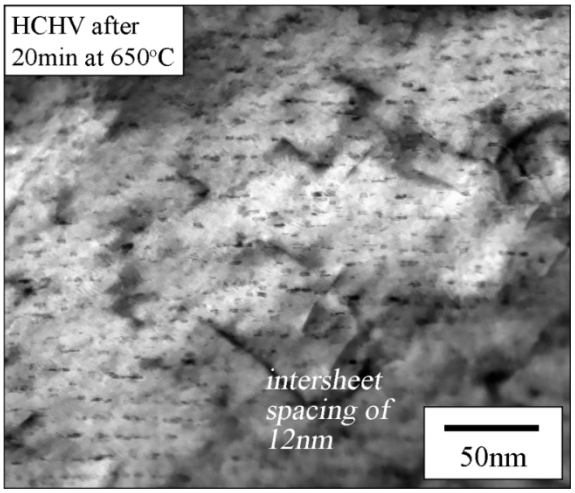

Fig. 2.11. Bright field TEM image illustrating interphase precipitation in the HCHV steel. It belongs to the specimen annealed for 20min at 650°C.

Representative 3D vanadium atom maps obtained by APT from samples of the LCLV and HCHV steels heat treated at 650 °C for holding times of 5 min, 45 min, and 10 h are shown in Fig. 2.12a-c and Fig. 2.12d-f, respectively. The V-rich regions can be clearly seen in all maps, which are superimposed with 2 at.%V iso-concentration surfaces. This threshold of vanadium concentration is set to a value much larger than the steel nominal composition in order to avoid local vanadium concentration fluctuations. The 3D maps can be rotated in any orientation, providing information regarding the precipitates' shape and arrangement. In all these maps and for both steels, spherical and ellipsoidal precipitates are observed. Small precipitates with a high number density can be seen in Fig. 2.12a and d after 5 min of annealing at 650 °C of a LCLV and a HCHV specimen, respectively. Their size increases with annealing time as a result of growth and/or coarsening as shown in Fig. 2.12b, c, e and f, while their number continuously decreases. Moreover, precipitates aligned in parallel rows are observed in both steels (Fig. 2.12a and d), denoting interphase precipitation. Randomly distributed precipitates in the ferritic matrix are also present, as shown in Fig. 2.12c.

From the vanadium maps, we deduced the inter-sheet spacing of interphase precipitation, determined by the velocity of the migrating α/γ interface during the austenite-to-ferrite phase transformation. The inter-sheet spacing is measured in the 5 min annealing condition in both steels, where coarsening has not started yet and the precipitates arrangement is relatively clear. It is found to be in the range of 12 - 17 nm in both steels, in agreement with our TEM measurements.

A quantitative characterization of vanadium carbide precipitates is obtained through a detailed cluster analysis. The cluster analysis is performed following the maximum separation method [55] based on solute vanadium atoms. Carbon enrichment is observed in the V-rich regions, indicating the presence of vanadium carbide precipitates. The maximum distance between two solute atoms that belong to the same cluster, d_{max}, and the minimum number of atoms in a cluster, N_{min}, are chosen as 1 nm and 20, respectively, after a trial and error procedure. The same d_{max} and N_{min} parameters are selected for all the measured specimens of LCLV and HCHV alloys. Clusters containing fewer atoms than N_{min} are not considered in the analysis to avoid the contribution of possible local fluctuations of vanadium concentration within the matrix. The d_{max} is determined based on the nearest neighbor distance (NN) distribution of 3 nearest neighbors.

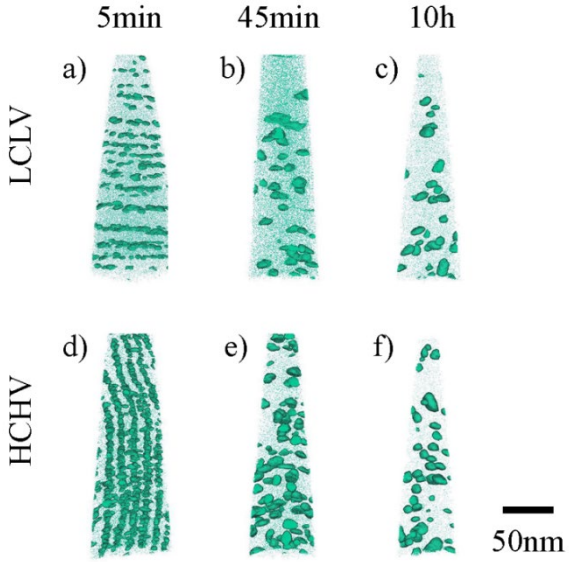

Fig. 2.12. 3D APT atom maps of V of a)-c) LCLV steel and d)-f) HCHV steel specimens previously treated in different conditions. The maps are superimposed with iso-concentration surfaces of 2at%V. The arrangement of the precipitates and their evolution during annealing is shown.

The cluster analysis provides information regarding the precipitate size distribution, number density and volume fraction in the analyzed tips. The precipitate number density is the number of precipitates divided by the analyzed volume (volume of the tip), and the precipitate volume fraction is the total precipitate volume divided by the analyzed volume. The precipitate volume is calculated from the number of vanadium atoms in each precipitate taking into account the unit cell volume of the VC and the number of vanadium atoms per unit cell. Four vanadium atoms are in one VC unit cell and its lattice parameter is 0.415 nm [31]. The radius of each precipitate is then calculated by assuming spherical precipitates. The detection efficiency of the instrument is 36% and it is considered in the above calculations to obtain the real number of the detected atoms.

Table 2.2 summarizes the precipitate radius, number density and volume fraction derived from APT measurements. The results obtained from the specimens of both steels, heat-treated for the three annealing conditions, are compared to the corresponding values obtained from the SANS data analysis. The number of tips measured per condition by APT is given and R_m, N_p and f_V presented are the calculated average values of all the analyzed tips per condition. Precipitates are detected in all the analyzed tips of both alloys, except for 3 tips of the LCLV specimen annealed for 5 min. This is attributed to the low precipitate volume fraction (0.13%) in the LCLV steel after 5 min of annealing at 650 °C, and suggests non- homogeneous precipitate distribution over the entire specimen volume.

The precipitate mean radius, number density and volume fraction values obtained from the APT cluster analysis are in good agreement with the corresponding values derived from the SANS analysis as shown in Fig. 2.8a, b and c. The precipitate mean radius and volume fraction are continuously increasing in both steels during annealing at 650 °C, while the precipitate number density is decreasing from 45 min to 10 h due to precipitate coarsening.

The fraction of vanadium atoms in solid solution in ferrite during annealing can be also obtained from the APT cluster analysis. The fraction of vanadium in solid solution, $f_{vanadium,ss}$, is calculated for each tip as:

$$f_{vanadium,ss} = (N_{V,total} - N_{V,precip}) / N_{V,total} = N_{V,\alpha\text{-}Fe} / (N_{V,\alpha\text{-}Fe} + N_{V,precip}) \quad \text{(Eq. 2.7)}$$

Table 2.2. Precipitate mean radius, R_m (nm), number density, N_p ($10^{23}m^{-3}$) and volume fraction, f_V (%), comparison between SANS and APT. The tip volume analysed by APT and the vanadium in solid solution measured in each condition are presented as well.

Steel	Holding time	R_m (nm)		N_p ($10^{23}m^{-3}$)		f_V (%)		no. of tips and total tip volume analyzed by APT	$f_{vanadium,ss}$ (%) by APT
		SANS	APT	SANS	APT	SANS	APT		
LCLV	5 min	1.05 ± 0.22	1.09 ± 0.03	1.90 ± 1.95	1.85 ± 0.83	0.13 ± 0.07	0.14 ± 0.07	6 tips (3.8E6 nm^3)	79 ± 9.43
	45 min	1.30 ± 0.05	1.36 ± 0.07	2.10 ± 0.38	1.57 ± 0.39	0.31 ± 0.04	0.31 ± 0.04	7 tips (5.9E6 nm^3)	41 ± 4.85
	10 h	1.53 ± 0.02	2.07 ± 0.15	1.20 ± 0.08	0.59 ± 0.08	0.37 ± 0.09	0.36 ± 0.05	8 tips (5.5E6 nm^3)	25 ± 1.88
HCHV	5 min	1.14 ± 0.14	1.62 ± 0.17	5.60 ± 3.44	3.60 ± 0.89	0.44 ± 0.10	0.74 ± 0.05	7 tips (4.0E6 nm^3)	28 ± 4.08
	45 min	1.47 ± 0.04	1.79 ± 0.14	3.88 ± 0.53	2.85 ± 0.75	0.73 ± 0.06	0.92 ± 0.04	10 tips (6.6E6 nm^3)	20 ± 2.11
	10 h	1.85 ± 0.03	2.11 ± 0.08	1.86 ± 0.11	1.37 ± 0.13	0.93 ± 0.16	0.90 ± 0.04	12 tips (5.4E6 nm^3)	12 ± 0.72

In Eq. 2.7, $N_{V,total}$ is the total number of vanadium atoms detected, $N_{V,precip}$ is the number of vanadium atoms in precipitates and $N_{V,\alpha\text{-}Fe}$ is the calculated number of vanadium atoms in ferrite ($N_{V,total}$ - $N_{V,precip}$). The fraction of vanadium in solid solution is averaged over the tips of the same specimen and is presented in the last column of Table 2.2. The 3D-APT measurements reveal that the total fraction of solute vanadium atoms in ferrite decreases during isothermal annealing in both steels due to continuous precipitation. However, it is not completely eliminated even after 10 h of annealing in any of the steels, indicating that the maximum volume fraction of precipitates is not reached. This is in agreement with the SANS results (see Fig. 2.8d) and the ThermoCalc [41] predictions for the equilibrium precipitate volume fraction stated earlier.

Note that APT allows for a local precipitation analysis over an average tip volume in the order of ~10^6 nm^3 while SANS measurements are performed in large samples with dimensions 10 x 10 x 1 mm^3 (= 10^{20} nm^3), leading to better statistics. Additionally, the nature of the APT technique introduces deviations in the mean atom-atom distance between reality and reconstructed data which consequently affect the cluster analysis. Based on these considerations, it is reasonable to expect small deviations between the results obtained by the two techniques. Nevertheless, the good agreement between the results obtained from these two very different techniques supports the validity of our analysis.

The precipitate size distribution derived from the APT cluster analysis for the LCLV and HCHV specimens annealed for 5 min, 45 min and 10 h is plotted in Fig. 2.13. The total number of precipitates measured in all tips for each thermal condition is also presented. A larger number of precipitates is measured in the HCHV specimens compared to the corresponding LCLV specimens that have undergone the same heat treatment due to the higher vanadium and carbon concentration. The time evolution of the distribution is found to have the same behavior as the one measured by SANS (Fig. 2.10a and b). Smaller precipitates are present in the first 5 min of annealing. As the isothermal annealing proceeds, the peak of the distribution is moving towards higher radii and the distribution broadens, indicating growth and coarsening as the dominant phenomena in these steps. Isothermal holding at 650 °C from 45 min to 10 h leads to a decrease of the total number of precipitates in both steels while coarse particles are formed. Only a few precipitates with a radius of more than 3 nm are found in both steels and the precipitate radius does not exceed 5.5 nm.

The precipitates' chemical composition profile is derived from the Proximity Diagrams (Proxigrams) [56], which are calculated based on iso-concentration surfaces (iso-surfaces) of 2 at% vanadium. The evolution of the precipitates' chemical composition during annealing is presented in 1D composition profile in Fig. 2.14a and c for the LCLV steel and in Fig. 2.14b and d for the HCHV steel. A comparison is shown between the precipitate chemical composition after 5 min and 10 h of annealing in both steels. The concentration profiles are calculated in one representative precipitate for each condition. The precipitate composition evolution during annealing shows the same behavior for both steels and is dependent on the precipitate size. It is observed that the matrix/precipitate interface is not sharp (on a nm-length scale) and that there is a gradual increase of vanadium and carbon along with a decrease of Fe concentration from the surface to the precipitate core for all the annealing conditions. The smaller precipitates formed after 5 min at 650 °C are Fe-rich despite a decrease in Fe content from their surface to their core. A drop in the fraction of Fe in the core is observed in the larger precipitates observed after 10 h and the core consists only of vanadium and carbon atoms in a stoichiometric ratio. Our results suggest no manganese enrichment in the precipitates, which is in agreement with Ref. [13], [19], [26] and [27], but in contrast to Ref. [25], in which manganese enrichment was observed only in the interphase precipitates and not in the randomly distributed ones.

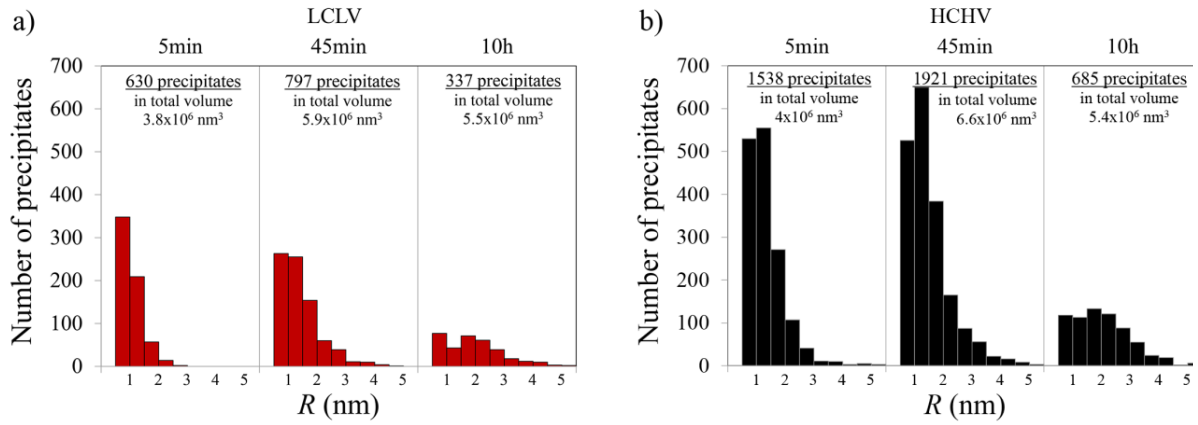

Fig. 2.13. Precipitate size distribution based on APT cluster analysis in a) LCLV and b) HCHV steels. The cluster analysis is performed in all the tips presented in Table 2.2.

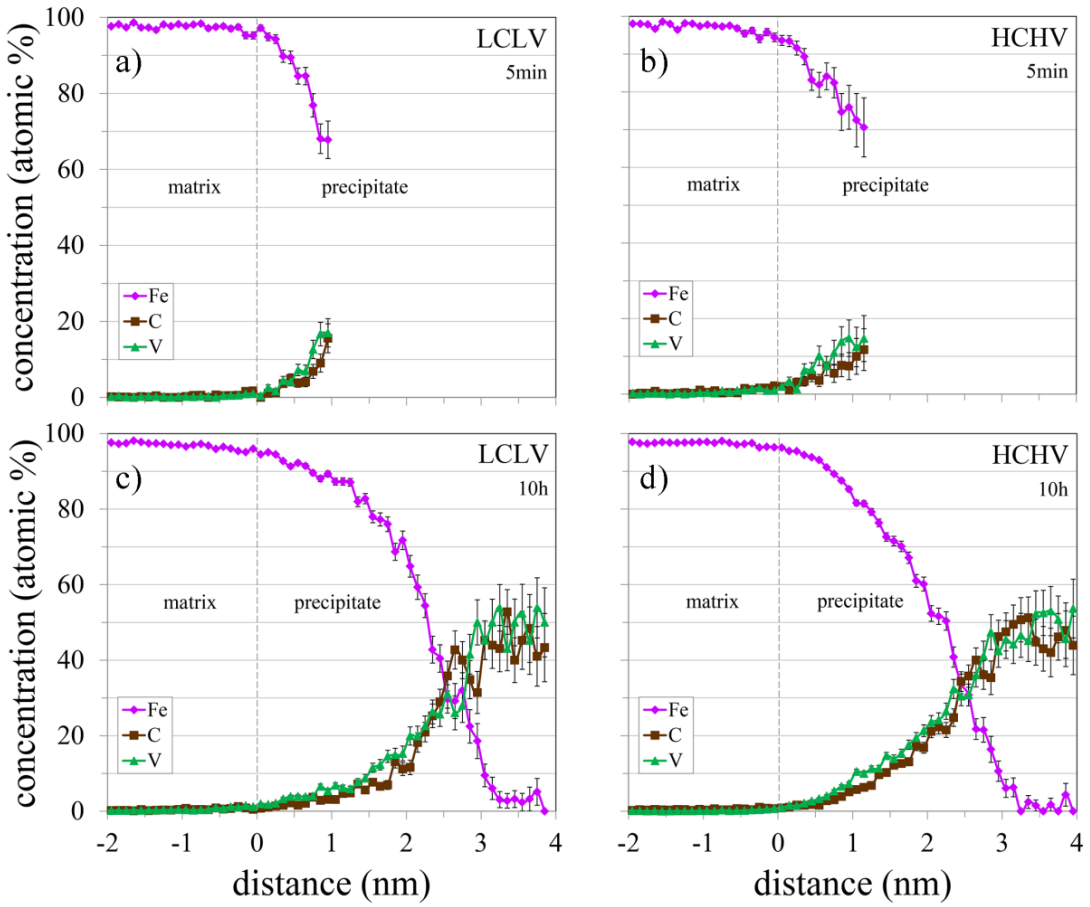

Fig. 2.14. Proxigrams showing the precipitate chemical composition evolution during isothermal holding at 650 °C. a) LCLV and b) HCHV steel annealed for 5min, c) LCLV and d) HCHV steel annealed for 10h. They are based on iso-concentration surfaces of 2at%V and belong to one representative precipitate of this condition.

2.3.2.5. Precipitate growth / coarsening at 650 °C

The average growth of the precipitate after the austenite/ferrite transformation front has passed can be described by the model developed by Öhlund et al. [21], in which the growth is controlled by volume diffusion of atoms, i.e. in our case of vanadium atoms. During precipitate growth, the diffusion field is assumed to have a linear concentration profile with length, L, which can be calculated by [21]:

$$L = \left\{ \frac{1}{3}\left(44 + 54B + 6\sqrt{54 + 132B + 81B^2}\right)^{1/3} - \frac{2}{3\left(44 + 54B + 6\sqrt{54 + 132B + 81B^2}\right)^{1/3}} - \frac{4}{3} \right\} R \ , \qquad \text{(Eq. 2.8)}$$

where R is the precipitate radius and $B = (c_0^m - c_{equil}^{VC})/(c_{equil}^m - c_0^m)$. c_0^m is the concentration of vanadium in the matrix obtained from the nominal steel composition. c_{equil}^m and c_{equil}^{VC} are the equilibrium concentrations of vanadium atoms in the matrix and in the vanadium carbide precipitates, respectively, and both quantities can be derived from ThermoCalc [41]. For the LCLV steel these are c_{equil}^m = 0.011 wt.% and c_{equil}^{VC} = 68 wt.%, while for the HCHV steel c_{equil}^m = 0.014 wt.% and c_{equil}^{VC} = 70 wt.%. According to ThermoCalc, the c_{equil}^{VC} is slightly different between the 2 alloys and also deviates from the theoretical calculated value for pure VC of 1:1 stoichiometric ratio, i.e. $c_{theoretical,equil}^{VC}$ = atomic mass of vanadium / (atomic mass of vanadium + atomic mass of carbon) = 50.9/62.9 = 81%. This indicates that possibly a small amount of Fe is included in the precipitates. In particular, ThermoCalc predicts a precipitate equilibrium composition of 45mol%V, 47mol%C and 8mol%Fe in both steels.
Coarsening is possible only when the diffusion fields of neighboring precipitates overlap. The length of the linear concentration profile, L, is calculated for both steels for the specimens annealed for times longer than 20 min, using the experimental mean radius values, R_m, derived by SANS. The average distance between two randomly distributed precipitates, d, is obtained by using the experimental number density values from SANS measurements and is equal to $N_p^{-1/3}$. For the case of the growth of spherical precipitates of the same size, the diffusion fields overlap when $2R+2L>d$. This criterion is fulfilled for both steels for all the samples annealed for longer than 20 min at 650°C and the results are summarized in Table 2.3. Combining the fact that the diffusion fields overlap with the experimental observations that the precipitate number density decreases (Fig. 2.8b), the volume fraction increases (Fig. 2.8c), and the amount of vanadium in solid solution decreases (Fig. 2.8d) with time, proves that the observed increase in average precipitate radius (Fig. 2.8a) after 20 min of annealing is the result of both growth with soft impingement (overlapping diffusion fields) and coarsening.

Table 2.3. Overlap of the diffusion fields of the VC precipitates.

Steel	Holding time	R_m (nm) by SANS	L (nm)	$d = N_p^{-1/3}$ (nm)	Overlap of diffusion fields $2R_m + 2L > d$
LCLV	20min	1.20	10.3	14.6	Yes
	45min	1.24	10.6	15.7	Yes
	2h	1.35	11.6	16.8	Yes
	10h	1.53	13.2	20.3	Yes
HCHV	20min	1.29	8.5	11.9	Yes
	45min	1.48	9.8	13.9	Yes
	2h	1.58	10.4	14.4	Yes
	10h	1.80	11.9	16.8	Yes

2.4. Conclusions

The vanadium carbide precipitation kinetics and the austenite-to-ferrite phase transformation kinetics are studied in two vanadium micro-alloyed steels, which are isothermally heat-treated at different temperatures for various holding times, by combining dilatometry, SANS, TEM and 3D-APT measurements. The conclusions are summarized as follows:
(1) Thermodynamic equilibrium calculations predict that vanadium carbide precipitates are present at 900, 750 and 650 °C. However, experiments show that neither precipitation nor phase transformation takes place in both steels when isothermally treated at 900 and 750 °C for holding times up to 10 h (except for the formation of a small fraction of ferrite at 750 °C in the LCLV steel).
(2) Experiments at 650 °C show that precipitation of vanadium carbides does take place after the onset of the austenite-to-ferrite phase transformation. This indicates that the austenite-to-ferrite phase transformation initiates the vanadium carbide precipitation. Nucleation and growth are dominant during the first 20 min, while later precipitate growth with soft impingement (overlapping diffusion fields) and coarsening take place. The steel with two times higher vanadium and carbon concentrations (HCHV) exhibits about two times higher volume fraction and number density of the precipitates after 10 h of annealing.
(3) After 10 h of annealing at 650 °C there is still some vanadium in solid solution in both steels and the precipitate volume fraction has not reached the maximum theoretical value corresponding to thermodynamic equilibrium.
(4) Spherical (and slightly ellipsoidal) precipitates that are ordered in rows as a result of interphase precipitation as well as randomly distributed precipitates are observed by TEM and APT. The precipitate chemical composition evolution during annealing is strongly correlated to their size. The smaller vanadium carbide precipitates detected for shorter holding times are Fe-rich. The larger precipitates in the later stages of annealing are Fe-rich near the matrix/precipitate interface, but are composed of vanadium and carbon in a stoichiometric ratio of 1:1 in the core of the precipitate, with possibly a small amount of Fe, consistent with the ThermoCalc calculations.
Overall, our findings provide quantitative information focused on the kinetics of the vanadium carbides in low-carbon steels, on its interaction with austenite-to-ferrite phase transformation and on the evolution of the precipitate chemical composition during annealing at 650 °C. The acquired quantitative results can be used as input parameters for modelling the precipitation kinetics in vanadium micro-alloyed steels, which may lead to improved steel design and performance for automotive applications.

Acknowledgements

This research was carried out under project number S41.5.14548 in the framework of the Partnership Program of the Materials innovation institute M2i (www.m2i.nl) and the Technology Foundation TTW (www.stw.nl), which is part of the Netherlands Organization for Scientific Research (www.nwo.nl). The authors wish to acknowledge the use of the Larmor beamline at ISIS (experiment number RB1669000) [57]. The experiments at ISIS pulsed neutron and muon source were supported by beam-time allocation from the Netherlands Organisation for Scientific Research (NWO) through the project 721.012.102 (LARMOR). The authors are grateful to Tata Steel for providing the materials for the experiments and would like to thank N. Geerlofs (TU Delft) for his assistance to the dilatometry treatments.

References

[1] European Commission, “A resource-efficient Europe – Flagship initiative under the Europe 2020 Strategy”, COM (2011) 21.
[2] Regulation EU No 333/2014, Amending Regulation (EC) No 443/2009 to define the modalities for reaching the 2020 target to reduce CO2-emissions from new passenger cars, 11 March 2014.
[3] K. Seto, Y. Funakawa, and S. Kaneko, Hot rolled high strength steels for suspension and chassis parts “NanoHiten” and “BHT” steel, JFE Technical Report, No. 10, (2007).
[4] A. Rijkenberg, A. Blowey, P. Bellina, and C. Wooffindin, Advanced high stretch-flange formability steels for chassis & suspension applications, Conference proceedings of the 4th International Conference on Steels in Cars and Trucks (SCT2014), Braunschweig (Germany), (2014) 426.
[5] Y. Funakawa, T. Shiozaki, K. Tomita, T. Yamamoto and E. Maeda, Development of High Strength Hot-rolled Sheet Steel Consisting of Ferrite and Nanometer-sized Carbides, ISIJ International 44 (2004), No. 11 1945–1951.
[6] T. N. Baker (2016) Microalloyed steels, Ironmaking & Steelmaking, 43:4, 264-307.
[7] WO2013167572 (A1), “Automotive chassis part made from high strength formable hot rolled steel sheet”, Tata Steel Europe.
[8] WO2014122215 (A1), A high-strength hot-rolled steel strip or sheet with excellent formability and fatigue performance and a method of manufacturing said steel strip or sheet, Tata Steel Europe.
[9] EP1338665 (A1), High tensile hot rolled steel sheet and method for production thereof, JFE Steel Corporation.
[10] European Commission, Report on critical raw materials for the EU, Report of the Ad hoc Working Group on defining critical raw materials, May 2014.
[11] W. B. Lee, S. G. Hong, C. G. Park, K. H. Kim, and S. H. Park, Influence of Mo on precipitation hardening in hot rolled HSLA steels containing Nb, Scr. Mater. 43 (2000) 319-324.
[12] H.-W. Yen, P.-Y. Chen, C.-Y. Hunag, and J.-R. Yang, Interphase precipitation of nanometer-sized carbides in a titanium-molybdenum-bearing low-carbon steel, Acta Mater. 59 (2011) 6264-6274.
[13] P. Gong, X. G. Liu, A. Rijkenberg, W. M. Rainforth, The effect of molybdenum on interphase precipitation and microstructures in microalloyed steels containing titanium and vanadium, Acta Mater. 161 (2018) 374-387.
[14] S. Dhara, R. K. W. Marceau, K. Wood, T. Dorina, I. B. Timokhina, P.D. Hodgson, Precipitation and clustering in a Ti-Mo steel investigated using atom probe tomography and small-angle neutron scattering, Mat. Sc. & Eng. A 718 (2018) 74–86.
[15] R. Lagneborg, T. Siwecki, S. Zajac, B. Hutchinson, The role of vanadium in microalloyed steels, Scand. J. Metall. 28 (5) (1999) 186-241.
[16] T. N. Baker (2009) Processes, microstructure and properties of vanadium microalloyed steels, Mater. Sc. and Tech., 25:9, 1083-1107.
[17] M.-Y. Chen, M. Goune, M. Verdier, Y. Brechet, J.-R. Yang, Interphase precipitation in vanadium-alloyed steels: strengthening contribution and morphological variability with austenite to ferrite transformation, Acta Mater. 64 (2014) 78-92.
[18] G. Miyamoto, R. Hori, B. Poorganji, T. Furuhara, Interphase precipitation of VC and resultant hardening in V-added medium carbon steels, ISIJ Int. 51 (10) (2011) 1733-1739.
[19] Y.-J. Zhang, G. Miyamoto, K. Shinbo, T. Furuhara, T. Ohmura, T. Suzuki and K. Tsuzaki, Effects of transformation temperature on VC interphase precipitation and resultant hardness in low-carbon steels, Acta Mater. 84 (2015) 375-384.

[20] Y. Q. Wang, S. J. Clark, V. Janik, R. K. Heenan, D. Alba Venero, K. Yan, D. G. Mc Cartney, S. Sridhar, P. D. Lee, Investigating nano-precipitation in a V-containing HSLA steel using small angle neutron scattering, Acta Mater. 145 (2018) 84-96.
[21] C. E. I. C. Öhlund, J. Weidow, M. Thuvander and S. E. Offerman, Effect of Ti on Evolution of Microstructure and Hardness of Martensitic Fe–C–Mn Steel during Tempering, ISIJ Intern. 54 (2014), No. 12, 2890-2899.
[22] N. H. van Dijk, S. E. Offerman, W. G. Bouwman, M.Th. Rekveldt, J. Sietsma, S. van der Zwaag, A. Bodin, and R.K. Heenan, High Temperature SANS Experiments on Nb(C,N) and MnS Precipitates in HSLA Steel, Metallurgical and Mater. Trans. A 33 (2002) 1883-1891.
[23] C. Ioannidou, Z. Arechabaleta, A. Rijkenberg, R. M. Dalgliesh, A. A. van Well and S. E. Offerman, VC-precipitation kinetics studied by Small-Angle Neutron Scattering in Nano-Steels, Materials Science Forum 941 (2018) 236-244.
[24] Y. Oba, S. Koppoju, M. Ohnuma, T. Murakami, H. Hatano, K. Sasakawa, A. Kitahara and J. Suzuki, Quantitative Analysis of Precipitate in Vanadium-microalloyed Medium Carbon Steels Using Small-angle X-ray and Neutron Scattering Methods, ISIJ International, Vol. 51 (2011), No. 11, pp. 1852-1858.
[25] M. Nöhrer, S. Zamberger, S. Primig and H. Leitner, Atom probe study of vanadium interphase precipitates and randomly distributed vanadium precipitates in ferrite, Micron 54-55 (2013) 57-64.
[26] Y.-J. Zhang, G. Miyamoto, K. Shinbo, T. Furuhara , Quantitative measurements of phase equilibria at migrating α/γ interface and dispersion of VC interphase precipitates: Evaluation of driving force for interphase precipitation, Acta Mater. 128 (2017) 166-175.
[27] Y. S. Shanmugam, M. Tanniru, R. D. K. Misra, D. Panda and S. Jansto, Microalloyed V–Nb–Ti and V steels Part 2, Precipitation behaviour during processing of structural beams, Mater. Sc. and Tech., 21:2, (2005) 165-177.
[28] T. Epicier, D. Acevedo and M. Perez, Crystallographic structure of vanadium carbide precipitates in a model Fe-C-V steel, Philosophical Magazine, Vol. 00, No. 00, August 2007, 1-14.
[29] N. Kamikawa, K. Sato, G. Miyamoto, M. Murayama, N. Sekido, K. Tsuzakie and T. Furuhara, Stress–strain behavior of ferrite and bainite with nano-precipitation in low carbon steels, Acta Mater. 83 (2015) 383-396.
[30] R. G. Baker and J. Nutting: in 'Precipitation processes in steels', Special report no. 64, 1–22; 1959, London, The Iron and Steel Institute.
[31] Y.-J. Zhang, G. Miyamoto, K. Shinbob and T. Furuhara, Effects of α/γ orientation relationship on VC interphase precipitation in low-carbon steels, Scr. Mater. 69 (2013) 17-20.
[32] G. Miyamoto, R. Hori, B. Poorganji, and T. Furuhara, Crystallographic Analysis of Proeutectoid Ferrite/Austenite Interface and Interphase Precipitation of Vanadium Carbide in Medium-Carbon Steel, Metallurgical and Mater. Trans. A 44A (2013) 3436-3443.
[33] S. Jiang, H. Wang, Y. Wu, X. Liu, H. Chen, M. Yao, B. Gault, D. Ponge, D. Raabe, A. Hirata, M. Chen, Y. Wang and Z. Lu, Ultrastrong steel via minimal lattice misfit and high-density nanoprecipitation, Nature, Volume 544 (2017) 460-464.
[34] E. A. Marquis, J. M. Hyde, Applications of atom-probe tomography to the characterisation of solute behaviours, Mater. Sc. and Eng. R 69 (2010) 37-62.
[35] Wiedenmann, Small Angle Scattering Investigations of Magnetic Nanostructures, in T. Chatterji (Ed.), Neutron Scattering from Magnetic Materials, Elsevier (2006) 473-519.
[36] F. Perrard, A. Deschamps, F. Bley, P. Donnadieua and P. Maugis, A small-angle neutron scattering study of fine-scale NbC precipitation kinetics in the a-Fe–Nb–C system, J. Appl. Cryst. (2006) 39 473-482.
[37] S. M. He, N. H. van Dijk, M. Paladugu, H. Schut, J. Kohlbrecher, F. D. Tichelaar, and S. van der Zwaag, In situ determination of aging precipitation in deformed Fe-Cu and Fe-Cu-B-

N alloys by time-resolved small-angle neutron scattering, Phys. Rev. B 82 (2010) 174111 1-14.
[38] S. Zhang, J. Kohlbrecher, F.D. Tichelaar, G. Langelaan, E. Bruck, S. van der Zwaag, N. H. van Dijk, Defect-induced Au precipitation in Fe–Au and Fe–Au–B–N alloys studied by in situ small-angle neutron scattering, Acta Materialia 61 (2013) 7009-7019.
[39] T. H. Simma, L. Sunb, D.R. Galvina, E. P. Gilbertc, D. Alba Venerof, Y. Lia, T. L. Martine, P. A. J. Bagote, M. P. Moodye, P. Hilld, H. K. D. H. Bhadeshia, S. Biroscaa, M.J. Rawsond, K.M. Perkins, A SANS and APT study of precipitate evolution and strengthening in a maraging steel, Mater. Sc. & Eng. A 702 (2017) 414-424.
[40] B. S. Seong, E. Shin, S. Choi, Y. Choi, Y. S. Han, K. H. Lee, Y. Tomota, Quantitative analysis of fine nano-sized precipitates in low-carbon steels by small angle neutron scattering, Appl. Phys A (2010) 99: 613-620.
[41] J. O. Andersson, T. Helander, L. Höglund, P. F. Shi, and B. Sundman, Thermo-Calc and DICTRA, Comp. tools for Mater. Sc., Calphad, 26 (2002) 273-312.
[42] C. A. Schneider, W.S. Rasband, and K.W. Eliceiri, "NIH Image to ImageJ: 25 years of image analysis", Nature methods 9 (7) (2012): 671-675, PMID 22930834.
[43] O. Arnold, J.C. Bilheux, J.M. Borreguero, A. Buts, S.I. Campbell, L. Chapon, M. Doucet, N. Draper, R. Ferraz Leal, M.A. Gigg, V.E. Lynch, A. Markvardsen, D.J. Mikkelson, R.L. Mikkelson, R. Miller, K. Palmen, P. Parker, G. Passos, T.G. Perring, P.F. Peterson, S. Renc, M.A. Reuter, A.T. Savici, J.W. Taylor, R.J. Taylor, R. Tolchenov, W. Zhou and J. Zikovsky, Mantid-Data analysis and visualization package for neutron scattering and μ SR experiments, Nuc. Inst. and Meth. in Phys. Research A 764 (2014) 156-166.
[44] D. J. Larson, D. T. Foord, A. K. Petford-Long, T. C. Anthony, I. M. Rozdilsky, A. Cerezo and G. W. D. Smith, Focused ion-beam milling for field-ion specimen preparation: preliminary investigations, Ultramicroscopy 75 (1998) 147-159.
[45] R. Córdoba, N. Sharma, S. Kölling, P. M. Koenraad and B. Koopmans, High-purity 3D nano-objects grown by focused-electron-beam induced deposition, Nanotechnology 27 (2016) 355301.
[46] B. Gault, F. Danoix, K. Hoummada, D. Mangelinck and H. Leitner, Impact of directional walk on atom probe microanalysis, Ultramicroscopy 113 (2012) 182-191.
[47] M. Thuvander, J. Weidow, J. Angseryd, L. K. Falk, M. Sonestedt, K. Stiller and H. O. Andrén, Quantitative atom probe analysis of carbides, Ultramicroscopy 111 (2011) 604.
[48] M. Enemoto, N. Nojiri and Y. Sato, Effects of Vanadium and Niobium on the Nucleation Kinetics of Proeutectoid Ferrite at Austenite Grain Boundaries in Fe-C and Fe-C-Mn Alloys, Mater. Trans. JIM 35 (1994) Issue 12 859-867.
[49] M.J. Peet, H.K.D.H. Bhadeshia: mucg83. (University of Cambridge, 2006), http://www.msm.cam.ac.uk/ map/steel/programs/mucg83.html.
[50] T. Narayanan, Synchrotron Small-Angle X-Ray Scattering, in R. Borsali, R. Pecora (Eds.), Soft-Matter Characterization, Springer, (2008) 899-948.
[51] L. A. Feigin, Structure Analysis by small-angle X-ray and neutron scattering, New York, 1987.
[52] M. Perez, Gibbs–Thomson effects in phase transformations, Scripta Materialia 52 (2005) 709-712.
[53] Q. Yong, X. Sun, Z. Li, Z. Wang and K. Zhang. Physical Metallurgical Principles of Titanium Microalloyed Steel-Dissolution and Precipitation of Titanium-Bearing Secondary Phases. In: Xinping Mao, editor. Titanium Microalloyed Steel: Fundamentals, Technology, and Products, Springer 2019, p. 94.
[54] G. G. Long, L. E. Levine, Ultra-small-angle X-ray scattering from dislocation structures, Acta Crystallogr. A61 (2005) 557-567.

[55] D. Vaumousse, A. Cerezo and P.J. Warren, A procedure for quantification of precipitate microstructures from three-dimensional atom probe data, Ultramicroscopy 95 (2003) 215-221.
[56] O. C. Hellman, J. A. Vandenbroucke, J. Rusing, D. Isheim, and D. N. Seidman, Analysis of Three-dimensional Atom-probe Data by the Proximity Histogram, Microsc. Microanal. 6 (2000) 437-444.
[57] A. A. van Well, R. M. Dalgliesh, S. E. Offerman, C. Ioannidou and Z. Arechabaleta Guenechea, (2016): 1669000, STFC ISIS Facility, doi:10.5286/ISIS.E.83552069.

Chapter 3 - Furnace for in-situ simultaneous studies of nano-precipitates and phase transformations in steels by SANS and neutron diffraction

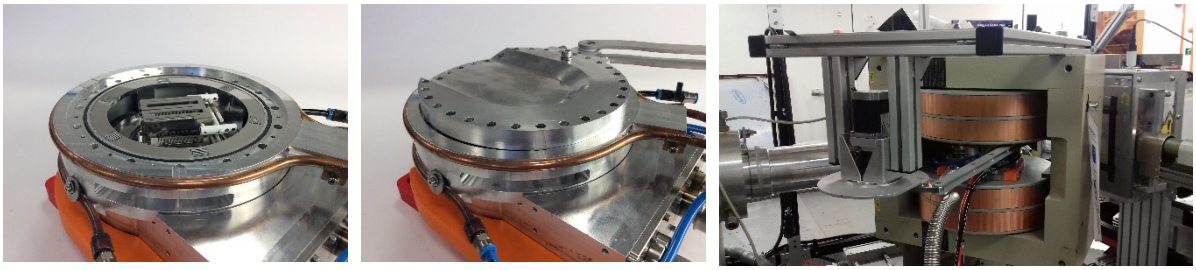

Abstract

Interphase precipitation occurring during solid-state phase transformations in micro-alloyed steels is generally studied through Transmission Electron Microscopy (TEM), Atom Probe Tomography (APT), and ex-situ Small-angle Neutron Scattering (SANS) measurements. The advantage of SANS over the other two characterization techniques is that SANS allows for the quantitative determination of size distribution, volume fraction, and number density of a statistically significant number of precipitates within the resulting matrix at room temperature. However, ex-situ SANS measurements alone do not provide information regarding the possible correlation between precipitation and phase transformations, and therefore, SANS should be coupled to another technique that monitors the phase-transformation kinetics. Moreover, the background subtraction is challenging in the ex-situ SANS experiments as explained in this chapter. Based on the above, it is necessary to perform in-situ and simultaneous studies on precipitation and phase transformations in order to gain an in-depth understanding of the nucleation and growth of precipitates in relation to the evolution of austenite decomposition at high temperatures. A furnace is, thus, designed and developed for such in-situ studies in which SANS can be simultaneously performed to neutron diffraction measurements during high-temperature thermal treatments. The furnace is capable of carrying out thermal treatments involving fast heating and cooling as well as high operation temperatures (up to 1200 °C) for a long period of time with accurate temperature control in a protective atmosphere and in a magnetic field of up to 1.5 T. The characteristics of this furnace open the possibility of developing new research studies for better insight of the relationship between phase transformations and precipitation kinetics in steels and also in other types of materials containing nano-scale microstructural features.

Reproduced from: "A. Navarro-López, C. Ioannidou, E. M. van der Wal, Z. Arechabaleta, R. van den Oever, M. N. Verleg, R. M. Dalgliesh, J. Sykora, F. A. Akeroyd, N. Geerlofs, J. Sietsma, C. Pappas, A. A. van Well, S. E. Offerman, "Furnace for In-situ and Simultaneous Studies of Nano-Precipitates and Phase Transformations in Steels by SANS and Neutron Diffraction", Review of Scientific Instruments 91 (2020), 123903."

3.1. Introduction

Precipitation in steels has been extensively studied over the years since the formation of precipitates within the steel microstructure often entails an enhancement of its mechanical behavior. The improvement of steel strength due to precipitation can occur via different mechanisms in which precipitates reduce the mobility of dislocations, inhibit grain growth, or even suppress recrystallization via the pinning of dislocations and grain boundaries [1],[2].
In micro-alloyed steels, the process of formation and growth of precipitates can typically take place in different phases: (I) precipitation in the fcc phase (austenite) [3], (II) precipitation in bcc phases (generally, ferrite or martensite) [4–6], and (III) precipitation during fcc-to-bcc transformation (mainly austenite-to-ferrite) [7–10]. The last one is commonly known as interphase precipitation.
The complex processes of nucleation and growth of precipitates of different sizes and morphologies inherent to each type of precipitation make it necessary to use several advanced characterization techniques for a better understanding of the underlying precipitation mechanisms. Small-angle Neutron Scattering (SANS) is one of the most powerful characterization techniques extensively used to study the precipitation phenomenon in a wide range of steel compositions [3],[4],[6],[8–13]. This non-destructive technique provides statistically relevant and quantitative information concerning the size distribution, volume fraction, and number density of precipitates. The SANS measurements can be performed in-situ at a specific temperature range where precipitation takes place or ex-situ at room temperature after the application of a thermal treatment. For ferromagnetic materials, a strong magnetic field may need to be applied in both types of SANS measurements to avoid any contribution from magnetic-domain scattering.
Precipitation in austenite has been studied by in-situ SANS measurements at high temperature ranges where austenite is present in the steel microstructure [3], without the need for a strong magnetic field since austenite is in the paramagnetic state. On the other hand, precipitation in ferritic (or martensitic) steels is mainly studied by ex-situ SANS measurements after the application of annealing (or aging) treatments at intermediate temperatures [4],[6]. These measurements require a magnetic field able to magnetically saturate the sample, in order to avoid the magnetic-domain scattering from ferromagnetic phases, such as ferrite (or martensite). However, both in-situ and ex-situ SANS measurements present certain limitations: (1) the need for the combination of a furnace and an electromagnet to perform in-situ SANS measurements of precipitation in ferro-magnetic materials and (2) in the ex-situ measurements, the interference of the SANS-signal from precipitates with the SANS-signal from other microstructural features, such as the dislocations contained in a martensitic microstructure.
Interphase precipitation during austenite-to-ferrite phase transformation is generally studied by ex-situ SANS performed at room temperature under an external magnetic field to prevent magnetic-domain scattering [8–10]. The progress of the nucleation and growth of precipitates during the austenite-to-ferrite phase transformation is, thus, studied from a series of partially transformed (and partially precipitated) microstructures after being annealed for several holding times followed by subsequent rapid cooling to room temperature. This implies the formation of a certain volume fraction of ferrite, depending on the holding time, as well as the formation of other phases, generally martensite, during the final cooling. The limitations of these ex-situ SANS measurements are (1) the overlapping of the SANS-signals from the precipitates and from other microstructural features, generally from the high density of dislocations formed in martensite, and (2) the difficulty in obtaining an accurate background from a reference microstructure free of precipitates and other microstructural features that contribute to the SANS-signal.

Due to the limitations of the ex-situ SANS measurements, precipitation occurring during austenite-to-ferrite phase transformation in steels may be studied more accurately by in-situ SANS during the application of thermal treatments at relatively high temperatures where both phenomena take place. This implies that the use of a furnace as well as an electromagnet is essential to perform such in-situ measurements and overcome the corresponding limitations. Furthermore, an additional simultaneous characterization technique shall be used, together with SANS, to track the progress of the phase transformation and relate it with the precipitation kinetics. Neutron Diffraction (ND) is the most appropriate characterization technique to be used for such studies since it is also a non-destructive technique capable of providing quantitative information regarding the evolution of volume fraction of phases during phase transformations.

Several furnaces were developed with the objective of performing experimental measurements through SANS, high-energy X-ray diffraction (HE-XRD), or ND for the in-situ study of precipitation, phase transformations, and/or mechanical performance at high temperatures in different types of metals [14–22]. Most of these furnaces were able to operate at temperatures up to 1300 °C under a protective atmosphere by either vacuum or an inert gas. However, none of the referenced furnaces were designed for in-situ and simultaneous studies of both precipitation and phase-transformation kinetics by the use of two of the characterization techniques previously mentioned (SANS, HE-XRD, and ND). In the case of steels, the need for applying a magnetic field when studying precipitation in a ferro-magnetic material by using neutrons entails a limiting design criterion, since the furnace should fit between the poles of an electromagnet, which is not the case for the referenced furnaces.

In a research study of the formation of precipitates and dislocations in a micro-alloyed steel, in-situ diffraction and small-angle scattering measurements were carried out in a multi-purpose furnace using X-rays [5],[23]. Although high-energy X-ray radiation is used in such studies, the contrast given by X-rays between the precipitates and the matrix may be insufficient for an accurate precipitation analysis in the case of similar electron densities between the matrix and the precipitate. An alternative solution to overcome this limitation is the use of neutrons since they are more suitable than X-rays for studying precipitation in cases where the electron density difference between the precipitate and the matrix is small. Neutrons can give a larger contrast than X-rays between the precipitates and the matrix, resulting in higher quality measurements, because the neutron scattering length densities may be significantly different between the precipitate and the matrix. In addition, the use of neutrons in in-situ measurements allows the monitoring of the evolution of the chemical composition of the precipitates together with the progress of the phase transformation through the analysis of the nuclear and magnetic contributions of the neutrons scattering signal [24].

The combination of SANS and ND for in-situ measurements during the application of thermal treatments is, thus, the most promising alternative for further in-depth research on interphase precipitation in micro-alloyed steels. Within Europe, the Larmor Instrument placed at ISIS STFC Rutherford Appleton Laboratory (UK) is the only facility in which both techniques can simultaneously be used for such studies. In the near future, the European Spallation Source (ESS) will also give the opportunity of carrying out this type of research studies with the combined use of both techniques [25]. With this aim, the development of a furnace suitable for the simultaneous study with neutrons of precipitation and phase-transformations in steels is needed and, in turn, is expected to contribute to a better insight of both phenomena. The furnace will also be suitable for the study of any material with nano-scale microstructural features in a magnetic or non-magnetic matrix. This research work describes the general design requirements as well as the main components of a furnace specially designed and developed to perform in-situ and simultaneous SANS and ND measurements. The design of the control system needed to use the furnace successfully is also described. Furthermore, a basic analysis

of the first in-situ SANS in combination to ND measurements during the application of thermal treatments with the designed furnace is presented in order to establish the performance of the furnace and highlight this new research possibility of studying the relationship between phase transformation and precipitation kinetics in-situ and simultaneously.

3.2. Design Requirements

The design requirements for a furnace to be developed for simultaneous studies of interphase precipitation and phase transformations in micro-alloyed steels are defined not only by the thermal treatments necessary in such studies, but also by the spatial and geometrical limitations imposed by the Larmor Instrument at ISIS STFC Rutherford Appleton Laboratory (UK), which is used for the SANS and ND measurements in combination with an electromagnet. Table 3.1 shows a summary of the main requirements for the furnace design.

Table 3.1. General requirements for the furnace design.

Furnace Height	- Maximum height of 44 mm, which is the maximum distance between the available electromagnet poles to reach magnetic saturation (1.5 T) of steel specimens at elevated temperature.
Material of the furnace	- Non-magnetic material. - Machine-able. - Minimum yield strength 100 MPa to resist the pressure difference between vacuum in furnace and ambient pressure.
Windows	- Vacuum tight. - Resist the pressure difference between vacuum in furnace and ambient pressure. - Non-magnetic material. - Neutron transparent. - Same thermal expansion coefficient with furnace material. - Size and position depends on beam size, and position of the SANS and ND detectors.
Heat Shields	- Non-magnetic material. - Resist a minimum temperature of 1200 °C. - High heat reflection coefficient (reflectance).
Temperature Control	- High temperature (up to 1200°C) to dissolve all carbides/carbonitrides. - Accurate control (± 1 °C). - Temperature gradient in the irradiated volume less than 0.3 °C/mm. - Heating rate (~10 °C/s), but not critical. - Necessary to reach cooling rates higher than 15 °C/s to avoid phase transformation and precipitation before annealing.
Atmosphere Control	- Minimum vacuum of the order of 10^{-4} mbar (for avoiding oxidation and decarburization of steel specimens). - Gas for specimen cooling (He).
Specimen	- I-shaped (approx. gauge dimensions 10 mm x 14 mm x 1 mm).
Specimen Holder	- Allow sample thermal expansion without deformation.
Specimen Change	- Fast and easy.
Specimen Rotation	- Maximum rotation angle of 20 °. - Accurate and user-friendly control system. - According to the reduced room available in the set-up.

One of the main criteria for the furnace design is related to the spatial and geometrical requirements. The use of a steel specimen requires, for SANS data collection, that it is magnetically saturated during the application of thermal treatments to prevent small-angle scattering from magnetic domains and to separate the nuclear and magnetic small-angle scattering components. The magnetic field (1.5 T) needed to reach magnetic saturation is directly related to the gap between the 75 mm diameter pole shoes of a GMW-3473 dipole electromagnet [26]. This gap is limited to a maximum of 44 mm for the previously mentioned magnetic field. The electromagnet is placed in a vertical configuration with the furnace between its pole shoes, as shown in Fig. 3.1a. The longest dimension of the specimen should be parallel to the magnetic field since, in this case, the demagnetization factor is the smallest.

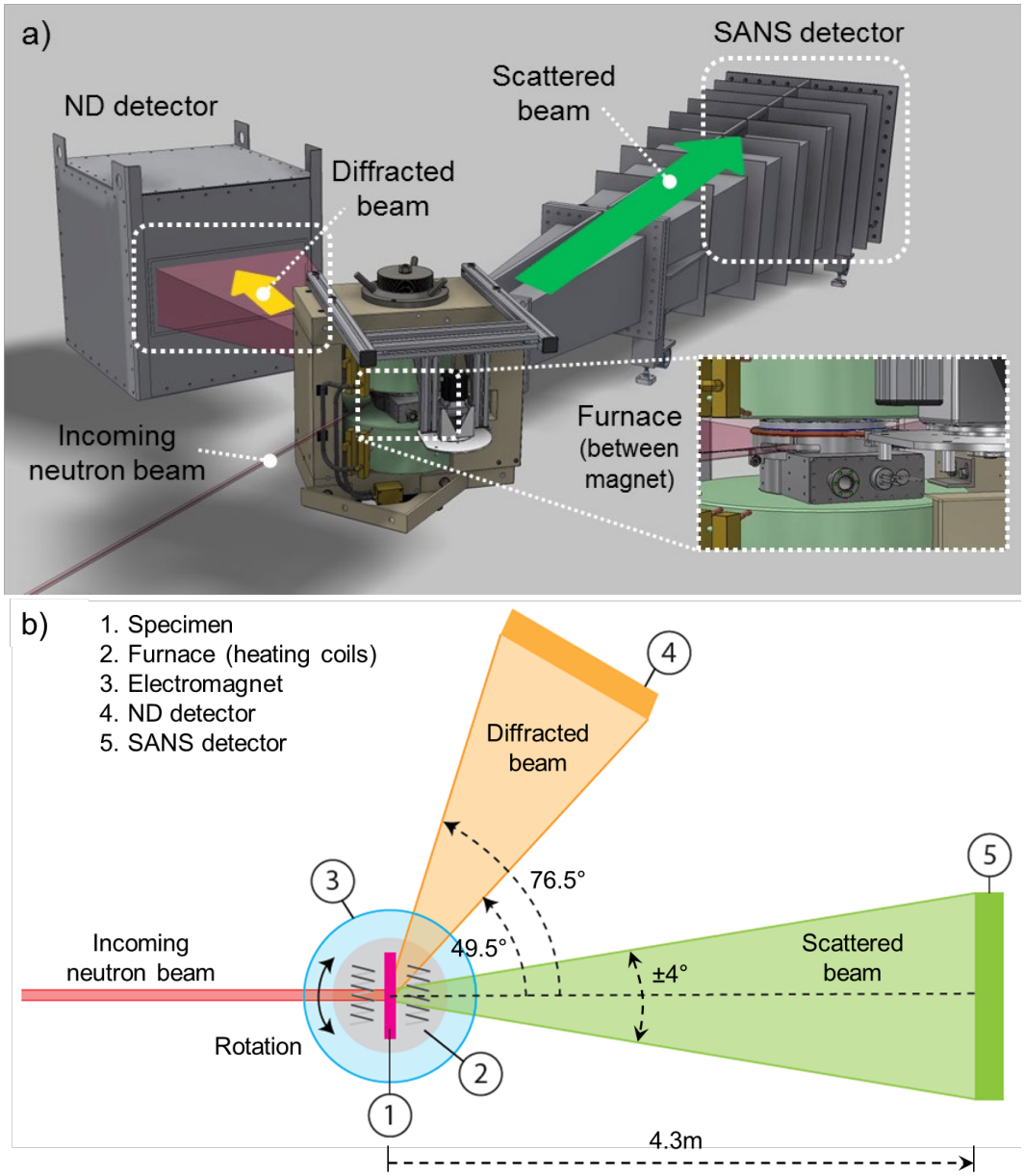

Fig. 3.1. a) Initial design of the general experimental setup and b) schematic top view (not on scale) of the experimental setup with the position of main elements. The shown specimen orientation corresponds with the 0° position of the steel specimen with respect to the incoming neutron beam.

Another important design criterion is related to the thermal treatment with an accurate control of the time-temperature profile to obtain the desired final microstructure. The furnace should be able to heat the steel specimen at moderate rates (between 1 °C/s and 20 °C/s) up to a maximum temperature of 1200 °C, at which the specimen can be held for a certain time (up to 15-20 min) to assure that all alloying elements are in solid solution. During cooling, the maximum rate should be rapid enough (up to 20 °C/s) to ensure the application of thermal treatments without any phase transformation during cooling. After the interrupted cooling, isothermal holdings in a wide range of temperatures should be possible to be applied for long periods of time (up to 10 h), maintaining the capability and feasibility of the furnace.
Both criteria (the geometrical limitation due to the use of a magnet and the limitations due to thermal treatments) are the basis of the furnace design since the material used to build the furnace should be, on one hand, a machine-able non-magnetic material and, on the other hand, a material with high resistance to high temperatures and good thermal conductivity. Moreover, the furnace size should be kept small so that it fits in between the pole shoes of the electromagnet.
Apart from these requirements, the windows of the furnace, i.e., the furnace areas interfering with the incoming and scattered neutron beams, should be as thin as possible to minimize the interaction with the neutron beams. In addition, the furnace windows have to be made of a material that is not significantly activated by the neutron beam and has minimum absorption of the neutron signal (<10%). For SANS measurements, the material of the furnace windows should give a small background signal compared to that given by the specimen. The background signal should also be constant to ensure that no microstructural changes occur in the window material during the application of thermal treatments. For ND measurements, the main requirement lies in preventing the overlap, insofar as possible, of the diffraction peaks corresponding to the windows' material with the ones obtained from the specimen.
Another important design criterion to be considered is related to the temperature distribution along the specimen, as high temperature gradients could cause local differences in phase transformation and precipitation starting at different specimen areas. The thermal gradient along the area probed by the incident neutron beam should be as small as possible to ensure that the temperature measured with a spot-welded thermocouple close to that area is the same as the temperature defined in the programmed thermal treatment.
Reaching and maintaining a high temperature at the specimen require the introduction of heat shields within the furnace chamber, which are made of a non-magnetic, high-temperature resistant, and heat-reflective material. Moreover, the furnace should be able to hold the pressure difference between the ambient pressure and the vacuum level within the furnace chamber during the heating and holding stages as well as the expansive effect caused by the introduction of pressurized gas during cooling. An appropriate level of vacuum within the furnace chamber is necessary to prevent decarburization and oxidation of the steel specimen during the application of the thermal treatment, but also neutron scattering from air. The furnace design should also allow fast and easy insertion/extraction of the specimen as well as possible thermal expansion without deformation during the thermal treatment.
Rotating the specimen around its vertical axis is the last main design criterion. Specimen rotation is needed in order to bring more grains in the diffraction condition when determining the mass fractions of ferrite and austenite. In this way, the effects of possible specimen texture induced by the pre-application of processes such as hot-rolling can be minimized. Ideally, the specimen should be rotated over 360° during the in-situ measurements to minimize texture effects in the resulting neutron diffraction patterns, although smaller rotations are also possible [27]. This would imply the use of a cylindrical specimen. However, flat specimens are better suited for SANS measurements and, in this geometry, the rotation of the specimen is limited because the illuminated volume by the incident neutron beam varies with rotation. This

limitation affects both the SANS and the ND measurements, becoming a challenge to the post-processing of the generated experimental data. As a compromise, the specimen should be rotated over 20° during the application of the thermal treatment. The possibility of rotating solely the specimen holder inside the furnace is discarded due to the limited space of the furnace chamber. The rotation of the whole furnace is, thus, the only option, although rotation is limited by the electromagnet. To facilitate the rotating movement of the furnace that is placed between the pole shoes of the electromagnet, the furnace geometry should be cylindrical. A schematic top view of the experimental setup is depicted in Fig. 3.1b, showing the 0° position of the specimen (perpendicular to the incident neutron beam) and the position of the SANS and ND detectors. For SANS measurements, the extension of the furnace windows is defined by the angular range covered by the SANS detector, limited to ± 4°, and the rotation angle selected to reduce texture effects. For ND measurements, the specimen material determines the ND angle and, as a result, the position of the furnace windows.
Calculations of the diffraction angles for ferritic and austenitic steel specimens indicated that, for a wavelength range of 0.10 - 0.35 nm, a 45°–80° angle range with respect to the incoming neutron beam is sufficient for detecting the first four diffraction peaks of each of the fcc and bcc phases. Thus, the size of the furnace windows is also defined by this angle range.

3.3. Furnace design

The final furnace design consists of the following components: the outer furnace (lids, central section and windows), a heating cell and several heat shields. Depending on the requirements to fulfill, distinct materials are chosen to make each component. The material selection made for each of these components is described below. Moreover, a brief description is included a) on how the temperature and the protective atmosphere are controlled during the application of thermal treatments as well as b) on the specimen rotation.

3.3.1. Outer furnace (lids, central section and windows)

The material used for the upper/bottom lids as well as the central section of the furnace is the Al–Mg–Si_1 aluminum alloy. This material is chosen because it is paramagnetic, thus non-(ferro)magnetic. It is easily machine-able, so that the central section including the windows can be made out of one piece with reasonable strength. The selected material also provides a reasonably good compromise between strength and stiffness, which is crucial to maintain all parts of the outer furnace non-altered in shape, supporting the pressure difference when vacuum is made within the furnace chamber. In addition, this material is characterized by good thermal conductivity, which limits the deformation of the outer furnace throughout the fast heat dissipation during the thermal treatments.
The same aluminum Al–Mg–Si_1 alloy is also selected for the furnace windows. The use of the same material eliminates the need for welding or clamping the windows to the central section. Although the selected material is transparent, to some extent, to neutrons, the windows are chosen to be 1 mm thick to minimize their interference with the incoming and scattered neutron beams without compromising the robustness of the entire furnace. Note that, for this alloy, precipitation hardening can occur due to aging at temperatures higher than 80 - 90 °C. The temperature of the furnace windows during the application of thermal treatments should, thus, be kept below this temperature in order to avoid the formation of precipitates in the aluminum windows, which could interfere with the SANS measurements. Last but not least, the diffraction peaks from these Al-windows do not interfere with the diffraction peaks of the steel for the experimental conditions used at Larmor Instrument.

3.3.2. Heating cell

The heating cell is placed in the center of the furnace and consists of a titanium frame, four molybdenum heat shields, and four boron-nitride cylinders with their respective molybdenum–lanthanum windings. The titanium frame does not interfere with the incident neutron beam. Two molybdenum heat shields are inserted at both sides in the titanium frame close to the specimen to reduce the heat loss as well as the thermal gradient along the specimen gauge. Two heating coils are placed at both specimen sides at the upper and bottom parts of the frame. A molybdenum–lanthanum wire of 0.5 mm diameter is selected for windings of the heating coil. This type of wire resists temperatures up to 2000 °C and exhibits better electrical behavior compared to other materials such as platinum, platinum-10%rhodium, or even molybdenum. The molybdenum–lanthanum wire is wound around a boron-nitride cylinder to give the coil good mechanical and thermal stability. Four heating coils are used to heat the specimen during the application of the thermal treatment. The titanium frame and the configuration of the heating system are shown in Figs. 3.2a and b.

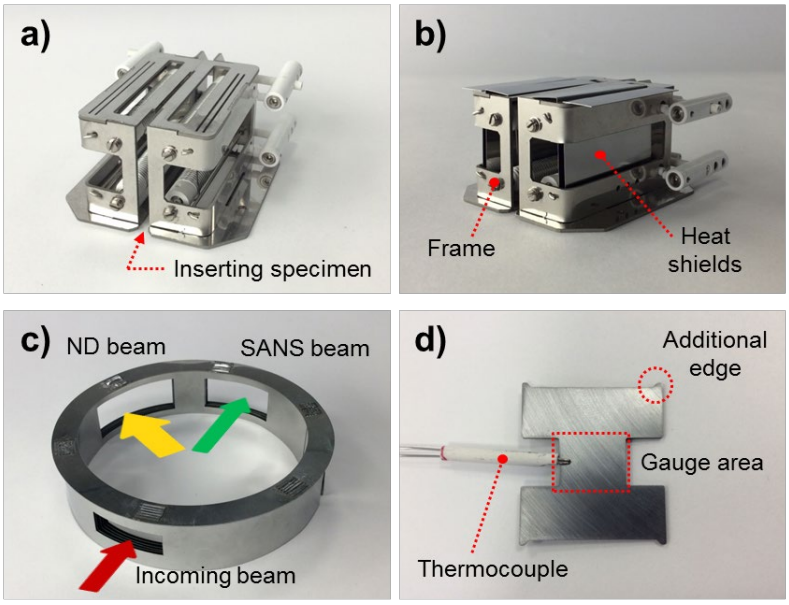

Fig. 3.2. a) Heating cell containing the four boron-nitride cylinders with heating coils without the direct shielding system, and b) heating cell with the two heat shields at both sides of the cell. The replacement of specimens is performed through the opposite side to the one in which all connections are placed. c) Concentric molybdenum heat shields placed within the furnace chamber surrounding the heating cell. There are openings to allow the neutron incident beam as well as the scattered and diffracted beams to pass through without interference. d) Steel specimen used in the in-situ experiments.

3.3.3. Outer heat shields

Several heat shields are concentrically placed between the heating cell and the furnace in order to reduce the heat loss and keep the temperature of the outer furnace as low as possible for safety reasons, and also to avoid possible precipitation in the Al windows. Molybdenum is selected as the optimum material for heat shields since it is easily machine-able, resists high temperatures, and is not activated by neutron irradiation. The use of molybdenum heat shields allows higher temperatures to be reached in the steel specimen during heating than those reached when no heat shields are used, using the same power. Considering the room available

between the heating cell and the outer furnace, seven heat shields of 0.15 mm thickness are placed within the furnace chamber. All heat shields have rectangular windows, as shown in Fig. 3.2c, at locations that coincide with the angular openings for the incoming and scattered neutron beams indicated in Section 3.2.

3.3.4. Specimen

I-shaped specimens with total dimensions of 32 mm height, 30 mm width, and 1 mm thickness are used for in-situ and simultaneous SANS-ND measurements (see Fig. 3.2d). The dimensions of the gauge area are 10 mm x 14 mm (height x width). This specimen shape minimizes the heat thermal gradient in the gauge area. The stability of the specimen inside the titanium frame of the heating cell is achieved by the use of horizontal reels in the upper and bottom parts of the frame. The specimen has four additional edges to maintain its horizontal position within the frame and reduce the thermal conduction to the surroundings. Figs. 3.3a-d show the different components of the furnace, such as the heating cell, the heat shielding system, the furnace chamber as well as a general overview of the final design of the multi-purpose furnace and the setup of all parts. As observed in Fig. 3.3a, the heating cell is fixed within the furnace chamber in a position at which the incident neutron beam is perpendicular to the steel specimen. Fig. 3.3b shows the final position of the concentrically disposed molybdenum heat shields as well as the central section of the furnace chamber. This section shows a gap in its center corresponding to the window of the incident neutron beam. Once the specimen is inserted in the heating cell, two replaceable molybdenum discs are placed at the top of the furnace chamber as additional heat shields (Fig. 3.3c). Fig. 3.3d shows the final assembling of all parts of the furnace as well as a water cooling system consisted of two tubes wrapped around the upper and bottom part of the central section in order to cool down the furnace during the application of thermal treatments.

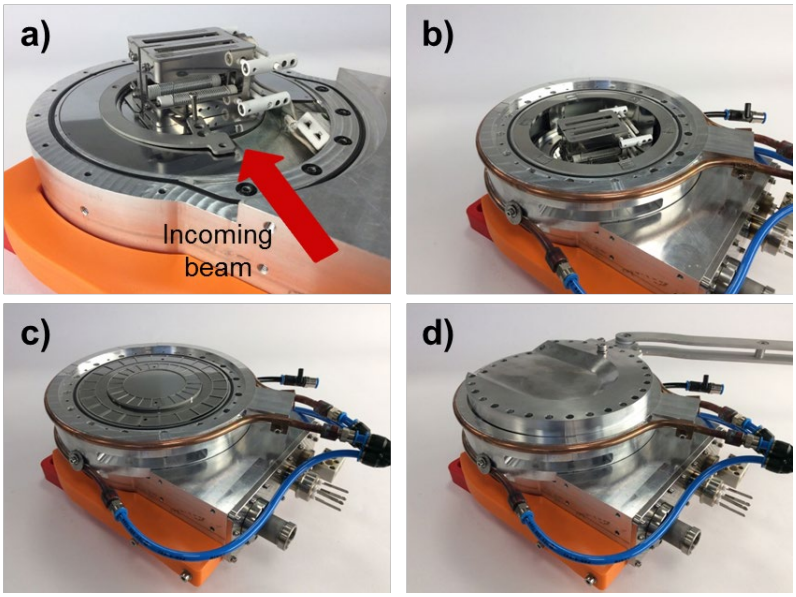

Fig. 3.3. Final design and set-up of the heating cell, shielding system, and other additional parts of the furnace with 200 mm diameter and 44 mm height. a) Placement and fixation system of the heating cell, b) heating cell and shielding system within the furnace chamber, c) additional molybdenum shielding on top of the heating cell and d) placement of the furnace lid with rotation system.

3.3.5. Temperature control

The specimen temperature at any time during the application of the thermal treatment is measured by two K-type thermocouples made of chromel–alumel wires of 0.5 mm each. Both thermocouples are spot-welded to the specimen. The main thermocouple, which is used for the temperature control, is placed at the side of the center of the specimen gauge. The second thermocouple, which gives insight of the possible temperature gradient, is placed in the center at the edge of the specimen gauge. Both thermocouple wires are isolated by an initial alumina tube followed by a fiberglass cover. After having determined a thermal gradient of $\Delta T \leq 0.3$ °C/mm along the specimen gauge, one thermocouple is only used for the temperature control, as shown in Fig. 3.2d, simplifying the experimental setup.

3.3.6. Atmospheric control

An inert atmosphere is created during the heating and holding stages of the thermal treatment by creating a vacuum inside the furnace chamber using a rotary pump. The airtight sealing is achieved by placing a rubber O-ring between the central section and the upper/bottom parts of the furnace (see Fig. 3.3a), which allows us to reach a vacuum level of the order of 10^{-4} mbar within the furnace chamber. The air within the chamber is extracted before the beginning of each in-situ measurement, in order to avoid the oxidation and decarburization of the specimen at high temperatures and to minimize the heat transfer between the heating elements and the furnace frame (so that undesired warming up is prevented). During cooling, an inert atmosphere is created by flushing helium through a gas system controlled by a mass-flow controller.

3.3.7. Specimen rotation

The optimum range of the specimen rotation angle is established between 0° and +20° (counter-clockwise direction), taking into consideration all the limitations derived from the use of an electromagnet and the specimen geometry. The asymmetric rotation of the furnace during in-situ measurements reduces the possible attenuation of the diffracted neutron beam from the specimen with a flat geometry (needed for SANS), since the neutron diffraction detector is positioned laterally with respect to the direction of the incident neutron beam. The 0° position corresponds with that in which the specimen gauge area is perpendicular to the incident neutron beam, as depicted in Fig. 3.1b. The rotation is performed by a stepper motor (0.025°/step) connected with an arm to the furnace. Fig. 3.3d shows this connection system where the arm of the rotation system is attached to one side of the upper lid of the furnace. The rotating movement consists of a forward–backward rotation over the specimen longitudinal axis within the selected rotation angle range.
Although this rotation range does not allow the measurement of the full texture of the specimen, the volume fraction of fcc and bcc phases can still be determined from the diffraction peaks if it is experimentally proved that there is no change in texture during phase transformations.

3.4. Control system design

The design characteristics of the furnace as well as the several requirements (heating, cooling, and rotation) needed to successfully achieve the desired results are considered in order to develop the final experimental setup for the performance of in-situ SANS and ND measurements. In brief, the equipment included in the experimental setup is the following:

- Furnace (with all components described above).
- Temperature controller (Eurotherm 3504).

- Power supply (to provide power to the heating coils).
- Rotary pump (to make vacuum).
- Mass-flow controller (to cool down samples by helium gas).
- Stepper motor (including the rotation system).
- Local laptop (to control the entire setup).
- CompactRIO (interface with ISIS control systems [28], data acquisition and motor control).

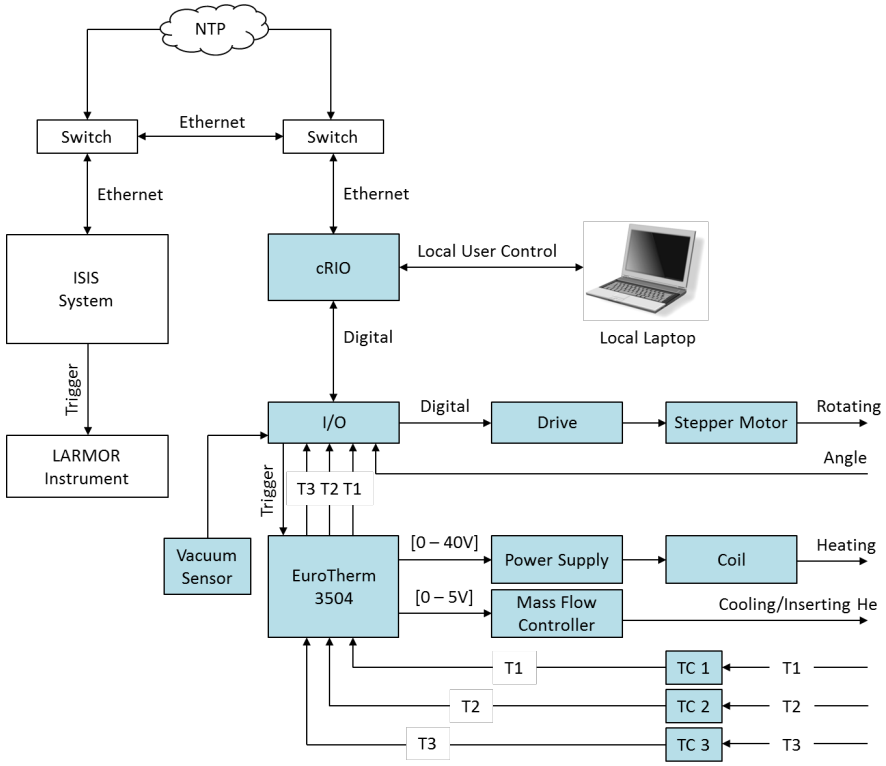

Fig. 3.4. Schematic illustration of the general control system set-up and the connection diagram between all equipment needed to successfully perform the in-situ SANS-ND measurements as well as the connection between this equipment and the ISIS control system.

All equipment needs to be interconnected and also connected with the instrument control system of the ISIS Neutron Research Center in order to correctly perform the desired thermal treatments and exchange the resulting data. The general data acquisition and control system setup including all the connections is shown in Fig. 3.4. The components of the local control system are highlighted in blue color. A network time protocol (NTP) is used to ensure that the time reference of both systems is the same. This is crucial since the experimental data forwarded to the ISIS system are time-stamped. The start of each in-situ SANS–ND measurement is defined by a hardware trigger signal, which is generated by the Larmor instrument control system. On the other hand, the start of the programmed thermal treatment, asynchronous to the Larmor instrument, is initiated by a manual action via the user interface of the local control system.

The Eurotherm controller is programmed with a predefined thermal profile that can be parameterized by the user. The control topology in the Eurotherm is implemented as a cascade proportional-integral-derivative (PID) control topology and is fine tuned to the system characteristics of the used peripheral system components. According to the programmed thermal treatment, the Eurotherm component controls the power supplied to the molybdenum–

lanthanum windings for heating the specimen and the flow of helium gas necessary to flush into the furnace chamber for cooling the specimen. The maximum power given by the power supply is limited to 400 W (40 V–10 A). The pressure inside the furnace chamber is controlled by a pressure sensor and a valve.
Furthermore, the Eurotherm controller receives as input signals the temperatures measured by three thermocouples placed in the specimen gauge center (TC1), at the edge of the specimen gauge (TC2), and at the upper lid of the furnace (TC3). All signals are also sent to the CompactRIO (cRIO) controller, which acts as the primary data interface to the in-place ISIS control system. For safety reasons, the CompactRIO controller switches off the power supply as soon as the temperature of the upper lid of the furnace, measured by the K-type thermocouple (TC3), exceeds the temperature of 100 °C.

3.5. In-situ simultaneous SANS and ND experiments

The first in-situ SANS in combination with ND measurements during thermal treatments with the described furnace are carried out in the Larmor instrument at ISIS Neutron and Muon Source, at Rutherford Appleton Laboratory (UK). The final experimental setup is shown in Fig. 3.5. The size of the incident neutron beam is 8 × 8 mm^2 allowing the measurement of a significant specimen volume and obtain good statistics in the resulting measurements. The specimen rotation is continuous during the application of the thermal treatments with a maximum rotation angle range of +18° (counter-clockwise direction).

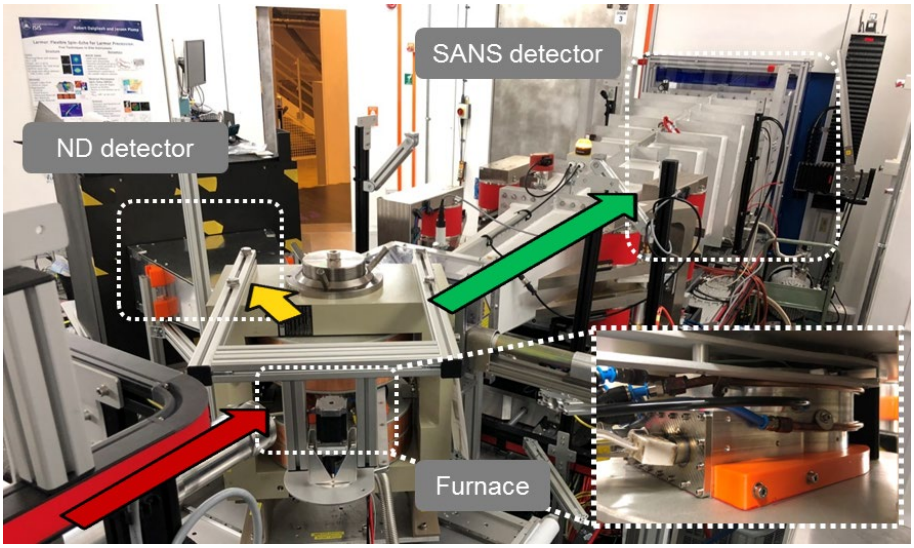

Fig. 3.5. Experimental set-up installed in the Larmor instrument.

3.5.1. Thermal treatments

Isothermal holding measurements at high temperatures are successfully applied in micro-alloyed steel specimens with distinct chemical compositions. Fig. 3.6a shows an example of a thermal treatment applied by means of the developed furnace on a steel specimen with composition 0.071C–1.84Mn–0.29V (wt. %). This thermal treatment consists of continuous heating until full austenitization at a temperature (in this case, 1050 °C) at which all precipitates are completely dissolved. After austenitization for several minutes, a rapid cooling process is applied by using helium gas for a short time followed by isothermal holding at 650 °C in vacuum (of the order of 10^{-4} mbar) for a certain period of time.

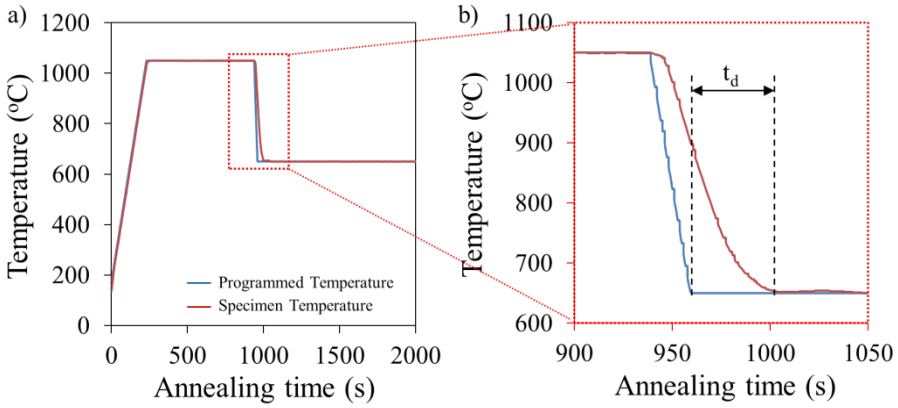

Fig. 3.6. Example of thermal treatment performed with the developed furnace during in-situ and simultaneous SANS-ND measurements. A comparison between the programmed thermal profile and the specimen temperature recorded by a thermocouple is shown.

The response of the furnace is smooth in all stages of the programmed thermal profile due to previous optimization of the PID values of the furnace control system. Only a small delay, t_d, is detected during the cooling stage, as observed in the enlarged image presented in Fig. 3.6b. No large undercooling is detected during rapid cooling from the austenitization to the isothermal temperature, aiming to avoid possible formation of precipitates before the isothermal holding.

3.5.2. Neutron diffraction

Fig. 3.7 shows a comparison between the diffraction patterns of the empty furnace and the steel specimen after the background is subtracted, at a random time during isothermal holding at 650 °C. Both diffraction patterns are obtained through a neutron diffraction detector especially developed for these measurements. The diffraction pattern obtained from the empty furnace is recorded at room temperature. This pattern is considered to be the background signal and is subtracted from the diffraction signals obtained from the steel specimen. As observed in Fig. 3.7, several α-ferrite and γ-austenite diffraction peaks are observed during the austenite-to-ferrite phase transformation occurring in the steel specimen. After background subtraction, the evolution of the volume fractions of both phases as a function of holding time is calculated from the integrated intensity of these diffraction peaks. In this case, the intensity ratio between diffraction peaks of each phase remains constant as a function of time, indicating that the texture of the material remains unaltered during phase transformations. Fig. 3.8 shows the evolution of the {110}, {200}, and {211} α-ferrite diffraction peaks and the {111}, {200}, and {220} γ-austenite diffraction peaks obtained from a series of neutron diffraction measurements during the application of one-hour isothermal holding at 650 °C on the micro-alloyed steel specimen. The evolution of these diffraction peaks with time reveals the isothermal transformation of austenite into ferrite during holding. The austenite-to-ferrite transformation kinetics can be quantitatively analyzed from this series of neutron diffraction patterns.

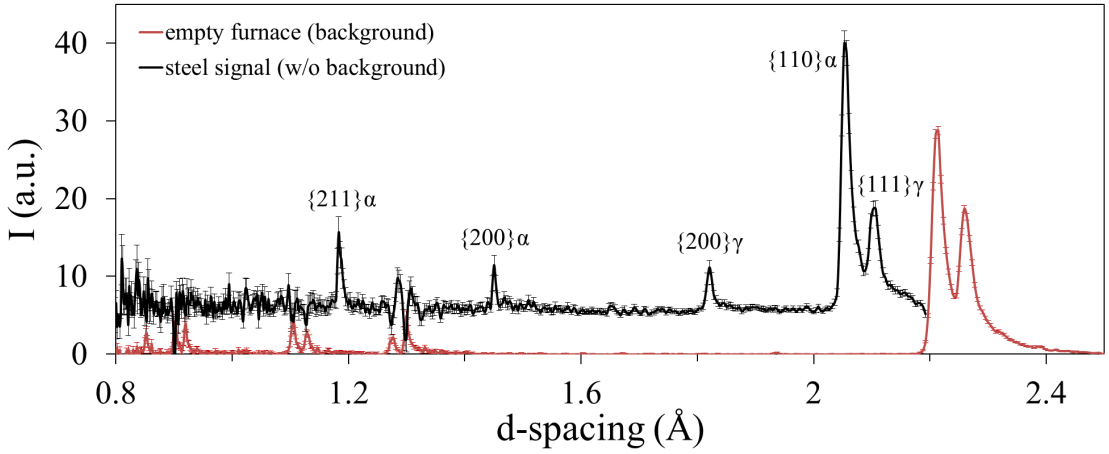

Fig. 3.7. Comparison between diffraction signals of the empty furnace and the steel specimen (after background subtraction) from a neutron diffraction measurement at a random time during isothermal holding at 650 °C.

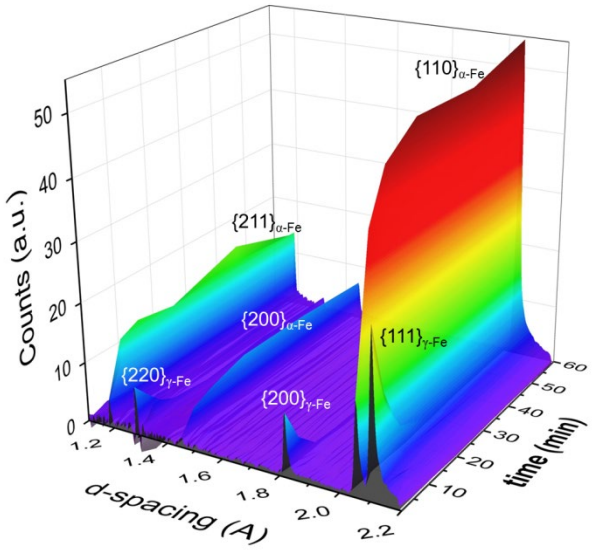

Fig. 3.8. Tine evolution of the diffraction peaks of α-ferrite and γ-austenite during 1 h of isothermal holding of a steel specimen, obtained from neutron diffraction measurements.

3.5.3. Small-angle neutron scattering

An example of a SANS pattern measured at a random time during the one-hour isothermal holding performed at 650 °C on a micro-alloyed steel specimen is shown in Fig. 3.9. The pattern includes the nuclear and magnetic contributions of the steel specimen. Sectors of 30° parallel and perpendicular to the applied magnetic field, *B*, are used to separate the nuclear and magnetic contributions to the scattering. From these intensities, the precipitation kinetics, i.e., nucleation, growth, coarsening, and chemical composition of precipitates, is quantified following the procedure described in Ref. [10].

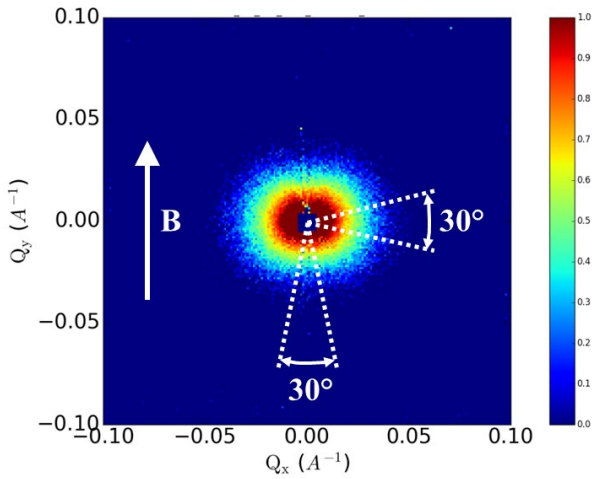

Fig. 3.9. Data obtained from a SANS measurement at a random time during isothermal holding. The SANS pattern includes the nuclear and magnetic contributions of the steel sample.

Fig. 3.10a shows an example of the in-situ nuclear SANS intensity as a function of wave-vector transfer *Q* measured at specific times during the isothermal holding of the micro-alloyed steel specimen at 650 °C. As a comparison, Fig. 3.10b shows the corresponding ex-situ nuclear SANS intensities measured at room temperature after the application of different holding times in the same type of steel specimens [10]. The intensity curves plotted in both figures are the result of the scattering originated only from the steel. In the case of the in-situ measurements, the SANS intensity is corrected using the high-temperature SANS signal. The intensity curves of the in-situ and ex-situ SANS are measured at the same temperature–time conditions. For short measuring times (5 min–10 min curve), larger error bars are observed in the in-situ SANS indicating a limitation to obtain good statistics for short isothermal treatments. This limitation can be avoided in the ex-situ measurements where a measuring time of 35 min is used to obtain good statistics.

On the other hand, the background subtraction is less challenging in the in-situ measurements than in the ex-situ ones. For the in-situ SANS measurements, the background is considered as an intensity curve that includes no precipitate signal. This curve corresponds to the scattering signal of the fully austenitic microstructure obtained at high temperature, where precipitates are totally dissolved. This intensity curve is used as a reference and subtracted from the intensity curves obtained at distinct times during the isothermal holding in order to obtain the pure precipitate signal. For the ex-situ SANS measurements, it is not possible to obtain a microstructure without dislocations to be used as a background reference. In this case, the intensity curve of the steel specimen directly quenched from the austenitization temperature to room temperature, whose microstructure consists of martensite with a high density of dislocations, should be considered as a (non-ideal) background signal. However, as shown in Fig. 3.10b, this curve exhibits a higher intensity in the low-*Q* range than those curves obtained even after 10 h of holding time when the phase transformations and precipitation have already occurred. The different background signal obtained in in-situ and ex-situ SANS measurements is a consequence of the different microstructure obtained in both steel specimens. Fig. 3.10c shows a comparison of both background signals. The intensity difference (ΔI) at a lower-*Q* range between both specimens is related to the contribution to the SANS signal of the high dislocation density and iron carbides contained in the fully martensitic microstructure of the as-quenched specimen. Consequently, isolating the precipitate signal during the isothermal holding has proved to be more challenging in the case of ex-situ SANS since a more complicated procedure (including calculations of the background for different *Q* ranges) has to be followed. The discussion strongly supports performing in-situ SANS experiments to study quantitatively the precipitation phenomenon and its kinetics in steels with higher accuracy.

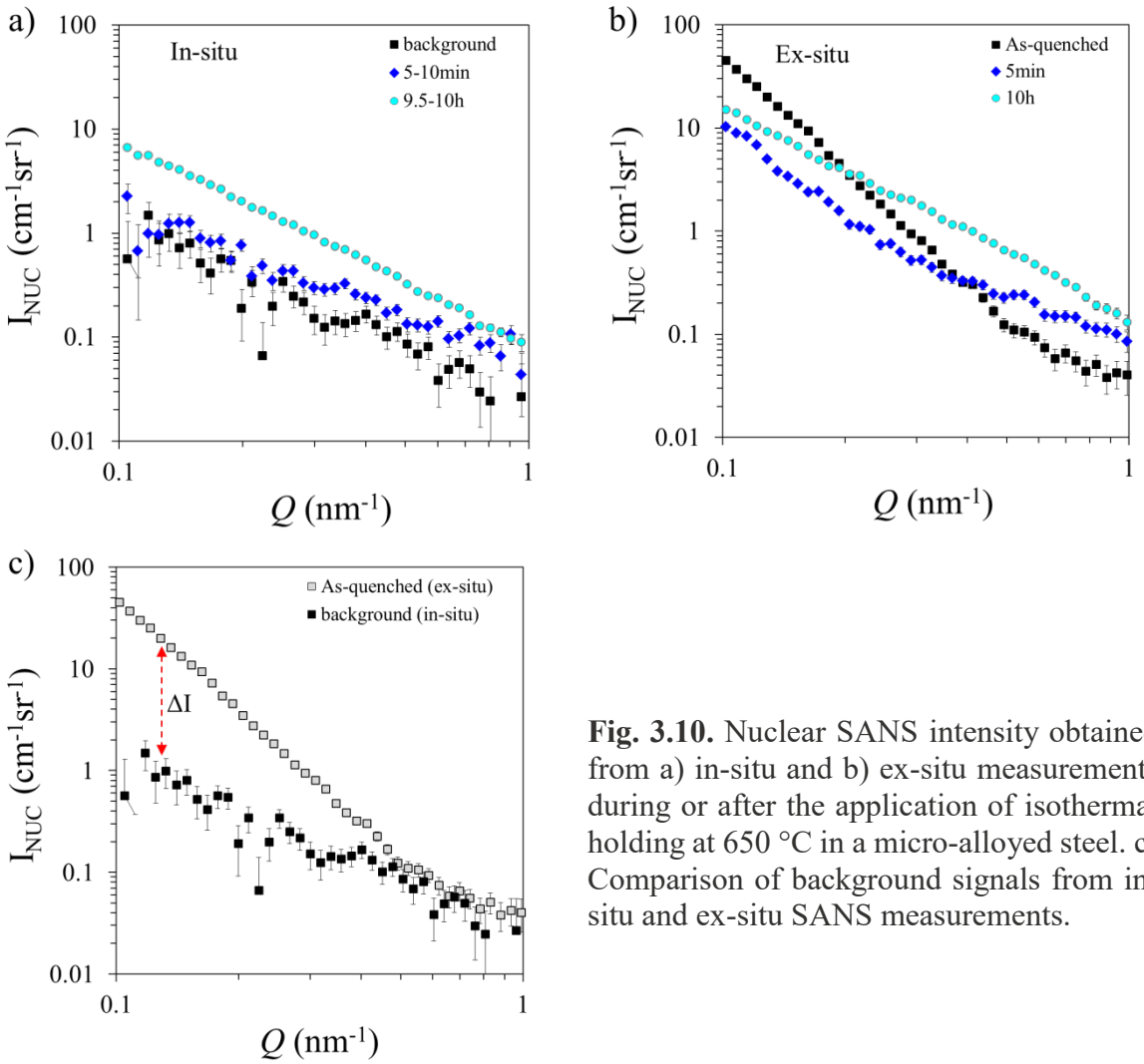

Fig. 3.10. Nuclear SANS intensity obtained from a) in-situ and b) ex-situ measurements during or after the application of isothermal holding at 650 °C in a micro-alloyed steel. c) Comparison of background signals from in-situ and ex-situ SANS measurements.

3.6. Conclusions

A furnace is designed and developed to perform in-situ and simultaneous small-angle neutron scattering and neutron diffraction measurements in micro-alloyed steels containing nano-precipitates. The furnace fulfills all the requirements needed to successfully carry out thermal treatments involving fast heating and cooling as well as high operation temperatures (up to 1200 °C), for a long period of time with an accurate control of the specimen temperature in a protective atmosphere and in a magnetic field. The development of this furnace allows the in-situ study of interphase precipitation in steels by relating the nucleation, growth, and coarsening of precipitates to the kinetics of phase transformations occurring during the application of thermal treatments. This achievement not only opens new ways of research of the precipitation phenomenon in steels but may also stimulate developments of other furnaces for advanced research studies.

Acknowledgements

This work was financially supported equally by the Technology Foundation TTW, as part of the Netherlands Organization for Scientific Research (NWO), and Tata Steel Europe through the Grant No. 14307 under the Project No. S41.5.14548 in the framework of the Materials Innovation Institute (M2i) Partnership Program. The experiments performed at ISIS Neutron and Muon Source were supported by beam-time allocation from the Netherlands Organization for Scientific Research (NWO) through Project No. 721.012.102 (LARMOR) with Experiment No. RB1869024 [29].

References

[1] H. Halfa, "Recent trends in producing ultrafine grained steels," J. Miner. Mater. Charact. Eng. 02, 428–469 (2014).
[2] H. J. Kong and C. T. Liu, "A review on nano-scale precipitation in steels," Technologies 6(1), 36 (2018).
[3] N. H. van Dijk, W. G. Bouwman, S. E. Offerman, M. T. Rekveldt, J. Sietsma, S. van der Zwaag, A. Bodin, and R. K. Heenan, "High temperature SANS experiments on Nb(C,N) and MnS precipitates in HSLA steel," Metall. Mater. Trans. A 33, 1883–1891 (2002).
[4] K. Osamura, H. Okuda, K. Asano, M. Furusaka, K. Kishida, F. Kurosawa, and R. Uemori, "SANS study of phase decomposition in Fe-Cu alloy with Ni and Mn addition," ISIJ Int. 34, 346–354 (1994).
[5] E. G. Dere, H. Sharma, R. M. Huizenga, G. Portale, W. Bras, V. Bliznuk, J. Sietsma, and S. E. Offerman, "Formation of (Fe,Cr) carbides and dislocation structures in low-chromium steel studied in situ using synchrotron radiation," J. Appl. Cryst. 46, 181–192 (2013).
[6] T. H. Simm, L. Sun, D. R. Galvin, E. P. Gilbert, D. Alba Venero, Y. Li, T. L. Martin, P. A. J. Bagot, M. P. Moody, P. Hill, H. K. D. H. Bhadeshia, S. Birosca, M. J. Rawson, and K. M. Perkins, "A SANS and APT study of precipitate evolution and strengthening in a maraging steel," Mater. Sci. Eng.: A 702, 414–424 (2017).
[7] R. Okamoto, A. Borgenstam, and J. Ågren, "Interphase precipitation in niobiummicroalloyed steels," Acta Mater. 58, 4783–4790 (2010).
[8] Y. Oba, S. Koppoju, M. Ohnuma, T. Murakami, H. Hatano, K. Sasakawa, A. Kitahara, and J.-i. Suzuki, "Quantitative analysis of precipitate in vanadium microalloyed medium carbon steels using small-angle X-ray and neutron scattering methods," ISIJ Int. 51, 1852–1858 (2011).
[9] Y. Q. Wang, S. J. Clark, V. Janik, R. K. Heenan, D. A. Venero, K. Yan, D. G. McCartney, S. Sridhar, and P. D. Lee, "Investigating nano-precipitation in a V containing HSLA steel using small angle neutron scattering," Acta Mater. 145, 84–96 (2018).
[10] C. Ioannidou, Z. Arechabaleta, A. Navarro-López, A. Rijkenberg, R. M. Dalgliesh, S. Kölling, V. Bliznuk, C. Pappas, J. Sietsma, A. A. van Well, and S. E. Offerman, "Interaction of precipitation with austenite-to-ferrite phase transformation in vanadium micro-alloyed steels," Acta Mater. 181, 10–24 (2019).
[11] F. Perrard, A. Deschamps, F. Bley, P. Donnadieu, and P. Maugis, "A small-angle neutron scattering study of fine-scale NbC precipitation kinetics in the α-Fe–Nb–C system," J. Appl. Cryst. 39, 473–482 (2006).
[12] B. S. Seong, E. Shin, S.-H. Choi, Y. Choi, Y. S. Han, K. H. Lee, and Y. Tomota, "Quantitative analysis of fine nano-sized precipitates in low-carbon steels by small angle neutron scattering," Appl. Phys. A 99, 613–620 (2010).

[13] S. Dhara, R. K. W. Marceau, K. Wood, T. Dorin, I. B. Timokhina, and P. D. Hodgson, "Precipitation and clustering in a Ti-Mo steel investigated using atom probe tomography and small-angle neutron scattering," Mater. Sci. Eng.: A 718, 74–86 (2018).
[14] M. G. Bowman, D. E. Hull, W. G. Witteman, G. P. Arnold, and A. L. Bowman, "High temperature neutron diffraction furnace," Rev. Sci. Instrum. 37, 1543–1544 (1966).
[15] F. P. Bailey and C. E. G. Bennett, "A simple furnace for neutron diffraction studies," J. Appl. Cryst. 12, 403–404 (1979).
[16] S. Katano, H. Motohashi, and M. Iizumi, "Furnace for rapid change of temperature for neutron diffraction," Rev. Sci. Instrum. 57, 1409–1412 (1986).
[17] T. Flottmann, W. Petry, R. Serve, and G. Vogl, "A combined furnace for crystal growth and neutron scattering," Nucl. Instrum. Methods Phys. Res., Sect. A 260, 165–170 (1987).
[18] L. Margulies, M. J. Kramer, R. W. McCallum, S. Kycia, D. R. Haeffner, J. C. Lang, and A. I. Goldman, "New high temperature furnace for structure refinement by powder diffraction in controlled atmosphere using synchrotron radiation," Rev. Sci. Instrum. 70, 3554–3561 (1999).
[19] P. Staron, E. Eidenberger, M. Schober, M. Sharp, H. Leitner, A. Schreyer, H. Clemens, "In situ small-angle neutron scattering study of the early stages of precipitation in Fe-25 at.% Co-9 at.% Mo and Fe-1 at.% Cu at 500 °C," J. Phys.: Conf. Ser. 247, 012038 (2010).
[20] H. M. Reiche, S. C. Vogel, P. Mosbrucker, E. J. Larson, and M. R. Daymond, "A furnace with rotating load frame for in situ high temperature deformation and creep experiments in a neutron diffraction beam line," Rev. Sci. Instrum. 83, 053901 (2012).
[21] P. A. Shade, B. Blank, J. C. Schuren, T. J. Turner, P. Kenesei, K. Goetze, R. M. Suter, J. V. Bernier, S. F. Li, J. Lind, U. Lienert, and J. Almer, "A rotational and axial motion system load frame insert for in-situ high-energy X-ray studies," Rev. Sci. Instrum. 86, 093902 (2015).
[22] D. C. Pagan, J. V. Bernier, D. Dale, J. Y. P. Ko, T. J. Turner, B. Blank, and P. A. Shade, "Measuring Ti-7Al slip system strengths at elevated temperature using high-energy X-ray diffraction," Scr. Mater. 142, 96–100 (2018).
[23] H. Sharma, A. C. Wattjes, M. Amirthalingam, T. Zuidwijk, N. Geerlofs, and S. E. Offerman, "Multipurpose furnace for in situ studies of polycrystalline materials using synchrotron radiation," Rev. Sci. Instrum. 80, 123301 (2009).
[24] C. Ioannidou, A. Navarro-López, A. Rijkenberg, R. M. Dalgliesh, S. Kölling, C. Pappas, J. Sietsma, A. A. van Well, and S. E. Offerman, "Evolution of the precipitate chemical composition during annealing of vanadium micro-alloyed steels by in-situ SANS," Acta Mater. 201, 217 (2020).
[25] J. Fenske, M. Rouijaa, J. Šaroun, R. Kampmann, P. Staron, G. Nowak, J. Pilch, P. Beran, P. Šittner, P. Strunz, H.-G. Brokmeier, V. Ryukhtin, L. Kadeˇrávek, M. Strobl, M. Müller, P. Lukáš, and A. Schreyer, "BEER – The beamline for European materials engineering research at the ESS," J. Phys.: Conf. Ser. 746, 012009 (2016).
[26] http://www.gmw.com/electromagnets/dipole/3473/3473_Specs .
[27] T. Gnäupel-Herold and A. Creuziger, "Diffraction study of the retained austenite content in TRIP steels," Mater. Sci. Eng.: A 528, 3594–3600 (2011).
[28] F. A. Akeroyd, K. V. L. Baker, M. J. Clarke, J. R. Holt, G. D. Howells, D. P. Keymer, T. Löhnert, C. M. Moreton-Smith, D. E. Oram, A. Potter, I. H. Rey, T. A. Willemsen, and K. Woods, "IBEX - an EPICS based control system for the ISIS pulsed neutron and muon source," J. Phys.: Conf. Ser. 1021, 012019 (2018).
[29] S. E. Offerman, E. van der Wal, A. A. van Well, A. Navarro-López, C. Ioannidou, and R. M. Dalgliesh, "In-situ and simultaneous SANS and ND to study the precipitation and phase transformation kinetics in V-containing nano-steels," STFC ISIS Neutron and Muon Source, 2019, https://doi.org/10.5286/ISIS.E.RB1869024.

Chapter 4 - Evolution of the precipitate composition during annealing of vanadium micro-alloyed steels by in-situ SANS

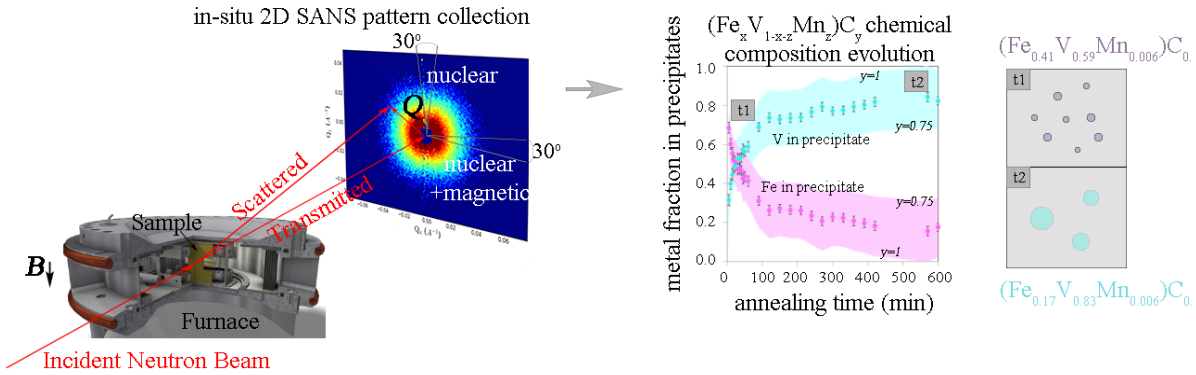

Abstract

In-situ Small-angle Neutron Scattering (SANS) is used to determine the time evolution of the chemical composition of precipitates at 650 °C and 700 °C in three micro-alloyed steels with different vanadium (V) and carbon (C) concentrations. Precipitates with a distribution of sub-stoichiometric carbon-to-metal ratios are measured in all steels. The precipitates are initially metastable with a high iron (Fe) content, which is gradually being substituted by vanadium during isothermal annealing. Eventually a plateau in the composition of the precipitate phase is reached. Faster changes in the precipitate chemical composition are observed at 700 °C in all steels. At both temperatures, the addition of more vanadium and more carbon to the steel has an accelerating effect on the evolution of the precipitate composition. Addition of vanadium to the nominal composition of the steel leads to more vanadium rich precipitates with less iron. Atom Probe Tomography (APT) shows the presence of precipitates with a distribution of carbon-to-metal ratios, ranging from 0.75 to 1, after 10 h of annealing at 650 °C or 700 °C in all steels. These experimental results are coupled to ThermoCalc equilibrium calculations and literature findings to support the Small-Angle Neutron Scattering results.

Reproduced from: "C. Ioannidou, A. Navarro-López, A. Rijkenberg,R. M. Dalgliesh, S. Koelling, C. Pappas, J. Sietsma, A. A. van Well, S. E. Offerman, "Evolution of the precipitate composition during annealing of vanadium micro-alloyed steels by in-situ SANS", Acta Materialia 201 (2020) 217–230."

4.1. Introduction

High-performance steels with high strength, ductility and stretch flange-ability are required nowadays in lightweight automotive parts for low fuel consumption, reduced CO_2 emission and little use of raw materials [1]. Nano-steels have attracted both industrial and technological interest due to their high potential to meet these demands [2-8]. Their outstanding mechanical properties arise from the combination of a ferritic matrix with nano-sized precipitates. The ferritic phase offers high ductility while a substantial degree of strengthening originates from the presence of precipitates. Vanadium carbide precipitates are well known for precipitation strengthening [5],[9], therefore, much research has been conducted on their effect on the mechanical properties of steels with various compositions that are processed under different conditions [9-13].

The chemical composition of the precipitates is a key factor for the precipitation strengthening since it drives the precipitation kinetics through the chemical driving force and the precipitate-matrix lattice misfit which control the precipitates nucleation and growth [14-16], eventually affecting the precipitate size distribution and the resulting mechanical properties. A high iron concentration in the vanadium carbides at the early stage of precipitation can reduce the lattice misfit and the strain energy between the precipitate and the matrix and, therefore, reduce the activation energy for the nucleation of the precipitate [15],[16]. In turn, this leads to a high number density of precipitates, which is beneficial for the strength of the steel. In addition, the fraction of vanadium and the carbon-to-vanadium ratio in the precipitates can be important for the strengthening since it can affect the shear modulus of the precipitates [17-19] and eventually the modulus hardening which is caused by a modulus difference between the precipitates and the matrix (even though it is weak compared with other mechanisms of precipitation strengthening) [20]. It is reported in the literature that vanadium carbides with different carbon-to-metal atomic ratio show different mechanical properties such as Young's modulus, shear modulus and hardness [17-19], because of the different atomic configuration in the precipitates [17]. The abovementioned material properties are promoted for precipitates with a composition closer to stoichiometry [17]. The binding energy between the vanadium and carbon atoms in nano-sized precipitates can be influenced by the ferrite matrix. The presence of vacancies in the precipitates can reduce their interfacial energy and increase their stability [14]. Knowledge on the chemical composition evolution of the precipitates during processing can contribute to an improved commercial steel design, optimized manufacturing and optimum use of critical raw materials.

The vanadium carbide precipitates have a Baker Nutting orientation relationship with the ferrite matrix [5] and they form in different shapes (spherical, disk-like, ellipsoidal, rod-like, needle-like or cuboid) with their shape and composition being dependent on steel composition and thermo-mechanical treatment conditions. Based on literature data, the vanadium carbides in low-carbon steels have a NaCl-type crystal structure with chemical formula: VC [21], V_4C_3 [5],[21], $VC_{0.9}$ [13], $VC_{0.81}$ [22] or $VC_{0.75\text{-}0.92}$ [23]. In medium-carbon vanadium micro-alloyed steels the precipitates can be either NaCl-type of composition $VC_{0.72\text{-}0.9}$, depending on the processing temperature [24], V_6C_5 monoclinic or hexagonal [25] or V_4C_3 trigonal [25].

Earlier studies on the chemical composition of precipitates by means of Atom Probe Tomography (APT) in vanadium micro-alloyed steels [26] but also in titanium micro-alloyed steels [27],[28] and in nickel-aluminium-molybdenum steels confirm the presence of iron in the precipitates [29]. APT measurements show gradual changes in the precipitate chemical composition during isothermal annealing at 650 °C [26], while the precipitate chemical composition evolution is strongly correlated to the precipitate size [26],[34]. In Ref. [26], the smaller vanadium carbides are found to be iron-rich and the larger precipitates in the later stages of annealing are rich in iron only near the matrix/precipitate interface. Possibly a small

fraction of iron is present in the core of the larger precipitates but they mainly consist of vanadium and carbon. Similar findings are presented in Ref. [27] and in Ref. [29], where it is stated that the iron content decreases across the particle interface from the surface to the core but still a considerable fraction of iron is measured in the precipitate core.

Transmission Electron Microscopy (TEM) and other TEM-based and spectroscopy techniques are often being used for precipitate characterisation [4],[10-13],[21-22],[24-42]. These techniques are performed at room temperature, in a limited number of treated samples sampling a small area. Consequently, the sample preparation and treatment is time-consuming when aiming for results with good statistics. If the precipitate composition evolution needs to be measured, the characterisation procedure requires time and preparation [30]. In addition, quantitative analysis of the precipitates' chemical composition is challenging in the case of APT measurements because of the technique's limitations. By APT, the stoichiometry of the precipitates cannot be accurately quantified due to the directional walk effect that lowers the accuracy in the measured carbon concentration [43]. Moreover, the local magnification effect, caused by the field evaporation potential being different between the iron matrix and the precipitates, deteriorates the spatial resolution in the vicinity of small clusters and makes it difficult to quantify the iron content in the precipitates [28],[39].

Small-angle Neutron Scattering is a non-destructive technique for quantitative and statistically relevant precipitate characterization in steels [26],[27],[44-48]. By the separation of the nuclear and magnetic precipitate scattering contributions, it is possible to obtain information on the magnetic and chemical properties of the precipitates [48]. Earlier studies on the precipitation kinetics of vanadium carbides on interphase boundaries by ex-situ SANS [13],[26] have been performed in low-carbon steels at room temperature. In these ex-situ SANS experiments, the microstructure is transforming from austenite to ferrite and the vanadium carbide precipitation takes place simultaneous to the phase transformation. Subsequent quenching of the steel to room temperature results in a complex microstructure of ferrite, vanadium carbides, martensite, iron carbides and dislocations. In such ex-situ SANS measurements, it is challenging to accurately separate the precipitate signal from the interfering signal from the dislocations of the martensite.

The major advantages of performing in-situ SANS measurements which we demonstrate in this work, are: 1) the SANS signal of the precipitates is free from interference from the dislocations of the martensite and 2) an optimum background of the matrix without the presence of precipitates can be measured at temperatures where all precipitates are dissolved in the matrix. In this way, the precipitate signal can be isolated and the precipitate chemical composition can be determined. In addition, in the in-situ experiments the real-time evolution of the precipitate chemical composition can be measured. However, the SANS technique, either ex-situ or in-situ, does not provide direct information on the precipitate crystal structure, therefore, complementary techniques such as TEM or literature data are necessary to support the SANS measurements.

In this work, we study quantitatively and in real-time the chemical composition evolution of precipitates in low-carbon vanadium micro-alloyed steels using in-situ SANS. The results are supported by APT, literature data as well as ThermoCalc equilibrium calculations. The effects of the processing temperature and different vanadium and carbon concentrations of each steel composition on the precipitate chemical composition evolution are investigated. The chemical composition evolution of the precipitates is determined irrespective of the precipitate shape and size distribution. The time evolution of the fraction of iron in the vanadium carbide lattice, for which limited experimental investigation has been reported so far, is derived from the in-situ SANS, together with the stoichiometry of the precipitates.

4.2. Experimental

The precipitate chemical composition evolution is studied in three vanadium micro-alloyed steels. The steels were provided by Tata Steel in Europe as hot-rolled plates. The chemical composition of the alloys is given in wt.% and at.% in Table 4.1. The steels differ in vanadium and carbon content. The first two steels have the same carbon but different vanadium contents and are referred to hereafter as LCLV (low carbon - low vanadium alloy) and LCHV (low carbon - high vanadium alloy). The third steel has a double amount of vanadium and carbon compared to the LCLV steel and is called HCHV (high carbon - high vanadium alloy). The atomic ratio of vanadium to carbon is 1 in the LCLV and HCHV steels. All steels have the same manganese concentration and the amount of the other elements is as low as possible. The LCLV and HCHV steels will provide information on the vanadium and carbon effects when the atomic ratio of these elements is 1, whereas the LCHV steel will clarify how the excess of solute vanadium atoms influences the kinetics of the evolution of the precipitate chemical composition.

Table 4.1 Chemical composition of the steels in weight percent (wt.%) and atomic percent (at.%) with balance Fe.

Steel		C	Mn	V	Si	P	Cr	Al
LCLV	wt.%	0.071	1.84	0.29	0.010	0.0010	0.010	0.004
	at.%	0.330	1.86	0.32	0.026	0.0018	0.011	0.008
LCHV	wt.%	0.075	1.83	0.57	0.014	0.0010	0.006	0.006
	at.%	0.350	1.85	0.62	0.028	0.0018	0.011	0.012
HCHV	wt.%	0.140	1.83	0.57	0.013	0.0010	0.007	0.008
	at.%	0.620	1.85	0.62	0.026	0.0018	0.007	0.002

I-shaped specimens of 1mm thickness were machined from the centre of the hot-rolled plates as in Ref. [26]. The specimen shape and size was designed to fit in a furnace [50], which was used for heat-treating the specimens during the in-situ SANS measurements. The furnace was custom made at Delft University of Technology, and specially designed to fit to the sample area of the Larmor Instrument at the ISIS Neutron and Muon Source (at the STFC Rutherford Appleton Laboratory, UK), in order to perform in-situ SANS measurements. A detailed description of the instrumentation is provided in Ref. [50] (and in Chapter 3).

The thermal cycle followed during the in-situ SANS measurements is schematically illustrated in Fig. 4.1. The specimens are heated up with a rate of 5 °C/s to a temperature of 1050 °C (for LCLV specimens) or 1100 °C (for LCHV and HCHV specimens) and are held there for 15 min. These temperatures are chosen to be ~50 °C higher than the respective precipitate dissolution temperatures calculated by ThermoCalc. At these soaking temperatures all elements are therefore in solid solution and the specimens are fully austenitic. Subsequently, the specimens are cooled to 650 °C or 700 °C with a rate of 15°C/s where austenite-to-ferrite phase transformation and precipitation are taking place during a 10-hour isothermal annealing treatment. Finally, the samples are cooled to room temperature.

The furnace is placed between the pole shoes of a 3473-70 GMW electromagnet, which is used to generate a vertical magnetic field of 1.5T perpendicular to the neutron beam. This magnetic field is strong enough to saturate the magnetization of the specimens. In this way we eliminate the scattering of domains and we can separate the nuclear contribution to the SANS pattern from the magnetic contribution.

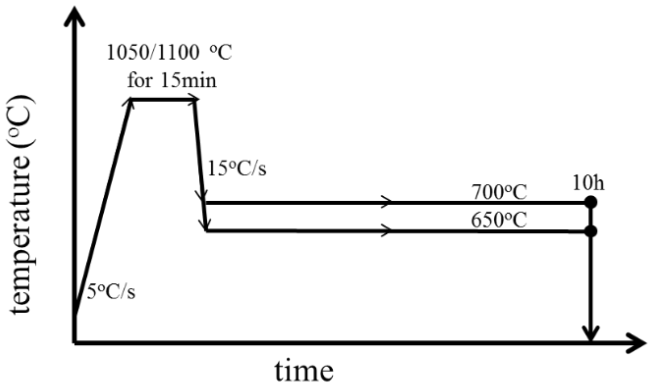

Fig. 4.1. Schematic illustration of the thermal cycles conducted in the furnace [50] during the in-situ SANS measurements.

The size of the incident neutron beam is 8 x 8 mm^2, the wavelength range for SANS is 0.42-1.33 nm and the SANS detector is a 600 x 600 mm^2 ^{3}He tube array with an 8 x 8 mm^2 pixel size, located 4.3 m from the sample. The reduction of SANS raw data is done using the Mantid software [51].

The specimens for APT are heat-treated in a dilatometer prior to the APT investigations. The dilatometry specimens are rectangular with dimensions 14 x 10 x 1 mm^3. The equipment used is a DIL-805 A/D dilatometer with inductive heating under a low pressure of 10^{-4} mbar and cooling is achieved by helium gas. An S-type thermocouple is spot-welded in the centre of the specimen to control the temperature and monitor the thermal cycle. The same heat-treatments as the ones conducted with the use of the SANS furnace (Fig. 4.1) are applied, i.e., holding at 1050 °C or 1100 °C for 15min followed by a 10 h isothermal annealing at 650 ºC or 700ºC and finally quenching to room temperature.

APT measurements are performed on samples taken from the dilatometry pre-treated specimens. More than 8 tips from each condition are tested aiming for good statistics and representative results. The specimens are prepared by the lift-out method using Focussed Ion Beam milling (FIB) [52]. A LEAP 4000X-HR system from CAMECA Instruments is used for the measurements. The preparation procedure of the APT tips is described in detail in Refs. [26],[53]. The APT data reconstruction is performed using the IVAS 3.8.0 software from CAMECA Instruments, in which elemental ions are identified based on their isotope distribution in a time of flight mass spectrum and then the atomic arrangement of the analysed volume is reconstructed following the standard protocol [53-55].

4.3. Method for calculating the precipitate chemical composition evolution from the in-situ Small-Angle Neutron Scattering data

The magnetic scattering of neutrons originates only from the magnetization components that are perpendicular to the scattering vector **Q**. In our experiment we use this selection rule to separate the magnetic from the nuclear neutron scattering. We apply in the detector plane, along the vertical direction (see Graphical Abstract and Fig. B1 in Appendix B), a magnetic field **B** strong enough to accomplish magnetic saturation of the sample. The magnetic scattering for **Q** // **B** is zero whereas it is maximum for **Q** ⊥ **B**. The macroscopic differential scattering cross-section, $(d\Sigma/d\Omega)(Q)$, which is the background-corrected and calibrated SANS intensity [56], can be written as [46]:

$$\left(\frac{d\Sigma}{d\Omega}\right)(\mathbf{Q}) = \left(\frac{d\Sigma}{d\Omega}\right)_{NUC}(Q) + \left(\frac{d\Sigma}{d\Omega}\right)_{MAG}(Q)\cdot\sin^2\alpha \quad (4.1)$$

where $(d\Sigma/d\Omega)_{NUC}(Q)$ and $(d\Sigma/d\Omega)_{MAG}(Q)$ stand for the nuclear and the magnetic scattering cross-sections respectively, Q is the magnitude of **Q**, and α is the angle between **Q** and **B**. $(d\Sigma/d\Omega)_{NUC}(Q)$ and $(d\Sigma/d\Omega)_{NUC}(Q)+(d\Sigma/d\Omega)_{MAG}(Q)$ are determined from the intensity integrated over sectors of 30° parallel and perpendicular to ***B***, respectively. In our case $(d\Sigma/d\Omega)_{NUC}(Q)$ is obtained from the vertical sectors and $(d\Sigma/d\Omega)_{NUC}(Q)+(d\Sigma/d\Omega)_{MAG}(Q)$ from the horizontal ones. $(d\Sigma/d\Omega)_{MAG}(Q)$ is then calculated as the difference between the above terms.
For a dilute system of precipitates within a homogeneous matrix, $(d\Sigma/d\Omega)_i(Q)$ is [56]:

$$\left(\frac{d\Sigma}{d\Omega}\right)_i(Q) = (\Delta\rho_i)^2 \int D_N(R)\cdot V^2(R)\cdot P^2(Q,R)\,dR, \tag{4.2}$$

where i can be either the nuclear or the magnetic term. R and V are the precipitate spatial coordinate in three dimensions and the precipitate volume, respectively. $D_N(R)$ is the log-normal size distribution of the precipitates and $P(Q,R)$ is the form factor reflecting the precipitate shape[56,57]. $\Delta\rho_i$ is the difference in scattering length density (scattering contrast) between the matrix and the precipitates, nuclear or magnetic. When the steel has reached magnetic saturation, the ratio of the nuclear to the magnetic SANS component is proportional to the squared ratio of the nuclear to magnetic scattering contrast:

$$\frac{\left(\frac{d\Sigma}{d\Omega}\right)_{NUC}(Q)}{\left(\frac{d\Sigma}{d\Omega}\right)_{MAG}(Q)} = \frac{(\Delta\rho_{NUC})^2}{(\Delta\rho_{MAG})^2} \tag{4.3}$$

This ratio is related to the composition of the microstructural features present in the sample. In the case of precipitates in a steel matrix and only if the magnetic saturation is reached, so that the integral in Eq. (4.2) has the same Q-dependence for nuclear and for the magnetic scattering (same nuclear and magnetic distribution), the ratio is determined by the chemical composition of the precipitates and the presence of different types of precipitates [48]. It has been reported that the vanadium carbide precipitate composition is size dependent [21],[26] and, consequently, the ratio is influenced by changes in the precipitate size distribution. APT measurements performed earlier [26-29] show the presence of iron in the precipitates, being more pronounced in the smaller precipitates. In addition, vanadium carbides with a sub-stoichiometric ratio of carbon to vanadium have been reported in the literature [5],[13],[21-24]. By in-situ SANS and using Eq. (4.3), we are able to quantify the evolution of the iron content and the stoichiometry of the precipitates during annealing.
It is important to note here that since the ratio is sensitive to all microstructural features, it is critical that the experimentally determined values of both the nuclear and magnetic scattering are free from any contributions other than from the vanadium carbide precipitates (same Q-dependence of nuclear and magnetic scattering of the integral, Eq. (4.2)). Thus, for a quantitative analysis of the chemical composition of precipitates by SANS, it is important to fulfil the two following experimental conditions. First, measure at temperatures high enough to avoid the formation of cementite, of pearlite and in particular of martensite because in that case the SANS signal from the dislocations would interfere with the signal from the precipitates. Second, determine the SANS signal originating from the matrix without any precipitates. Both conditions have been fulfilled by our in-situ SANS measurements, as we measured at the isothermal holding temperatures of 650/700 °C and obtained the matrix

background at the soaking temperatures of 1050/1100 °C, where all elements are in solid solution.

The scattering events at the Larmor instrument at ISIS can be recorded using event-mode data acquisition, where each neutron detection event has its own time stamp. This feature is very convenient for kinetics measurements, because it allows to re-bin the data over time slices that can be chosen after the measurement. Larger time slices provide good measuring statistics, however, shorter time slices allow the following of the kinetics with a higher temporal resolution. As the first hour of annealing is more critical for the kinetics, consecutive 5 minute time slices are chosen during the first hour at the isothermal holding temperature, while consecutive 30 minute time slices are chosen for annealing times longer than 1 h.

As a first step for determining the precipitate chemical composition evolution by in-situ SANS, the experimental $(d\Sigma/d\Omega)_{NUC}(Q)/(d\Sigma/d\Omega)_{MAG}(Q)$ ratio is calculated for all Q values in each time slice during the isothermal annealing at 650 °C and at 700 °C of the three alloy steels of interest. Due to the aforementioned advantages that the in-situ SANS measurements allow for, no considerable Q dependence of the $(d\Sigma/d\Omega)_{NUC}/(d\Sigma/d\Omega)_{MAG}$ ratio is observed in each individual time slice (see Fig. 4.3). A weighted average value for the $(d\Sigma/d\Omega)_{NUC}/(d\Sigma/d\Omega)_{MAG}$ is calculated for each time slice and eventually the $(d\Sigma/d\Omega)_{NUC}/(d\Sigma/d\Omega)_{MAG}$ over time is obtained.

As a second step, we assume that the SANS signal arises from precipitates with a chemical formula $(Fe_xV_{1-x-z}Mn_z)C_y$ and a NaCl type crystal structure during the entire annealing process. This hypothesis is based on literature studies of the VC_y crystal structure in low-carbon steels [5],[13],[21-23]. Other crystal structures for the precipitates rather than NaCl are not considered, even though they have been reported for medium carbon steels [25]. It is also possible that in the very early stage of the nucleation process, the embryos have a different crystal structure than NaCl [24], however, this is not taken into account. In the NaCl crystal structure, the Fe, V and Mn atoms can occupy the metal positions in the lattice with fractions of x, $1-x-z$ and z, respectively. The manganese fraction, z, is very small compared to the iron and vanadium fractions. Therefore, it is considered constant and, for each steel at a specific temperature, its value is the same as the equilibrium manganese fraction in the precipitates as derived from ThermoCalc calculations. The parameter y is the ratio of carbon, C, to metal, M, atoms, in the precipitate, i.e., C:M, and indicates deviations from the stoichiometric ratio of the carbides. For stoichiometric precipitates $y = 1$, but if vacancies are present at the carbon positions in the precipitate lattice, y is smaller than 1. In addition, if there is a single type of precipitate present in the steel with different stoichiometric ratios of carbon-to-metal, y represents the weighted average of the distribution of the carbon-to-metal ratios. The carbon-to-metal ratio is found to be related to the precipitate size distribution. For instance, in Ref. [21], fine stoichiometric VC precipitates ($y = 1$) and coarse V_4C_3 ($y = 0.75$) precipitates were identified by TEM. Based on such literature findings [5],[13],[21-23], we consider $0.75 \leq y \leq 1$. For the ferritic matrix, z_{matrix} is the atomic fraction of manganese in the matrix which is assumed constant during annealing and equal to its nominal concentration in the alloys.

The ratio $\Delta\rho^2_{NUC}/\Delta\rho^2_{MAG}$ is theoretically calculated as a function of the precipitate chemical composition, i.e., as a function of the x and y parameters, with constant z.

The difference in the scattering length densities between the precipitates and the iron matrix is $\Delta\rho_{NUC} = \rho_{NUC\_matrix} - \rho_{NUC\_precip}$. The scattering length density of the matrix is:

$$\rho_{NUC\_matrix} = \frac{\sum_j \left(f_j^m \cdot b_j \right)}{V_{bcc}} \approx \frac{(1 - z_{matrix}) \cdot b_{Fe} + z_{matrix} \cdot b_{Mn}}{V_{bcc}}, \tag{4.4}$$

and the precipitates' scattering length density is:

$$\rho_{\mathrm{NUC\_precip}} = \frac{\sum_j \left(f_j^p \cdot b_{\mathrm{j}} \right)}{V_{\mathrm{precip}}} \approx \frac{x \cdot b_{\mathrm{Fe}} + (1-x-z) \cdot b_{\mathrm{V}} + z \cdot b_{\mathrm{Mn}} + y \cdot b_{\mathrm{C}}}{V_{\mathrm{precip}}}, \tag{4.5}$$

where j stands for each individual element in the phase: j = Fe, Mn, V or C, and f_j^{m} and f_j^{p} are the atomic fractions of each element in the matrix and the precipitate unit cell, respectively. The V_{bcc} is the atomic volume of the matrix and the V_{precip} the atomic volume of the substitutional elements in the precipitates. They are calculated as: $V_{\mathrm{bcc}} = a^3{}_{\mathrm{bcc}}/2$ and as $V_{\mathrm{precip}} = a^3{}_{\mathrm{precip}}/4$. The a_{bcc} and the a_{precip} are the lattice parameters of the ferrite unit cell and of the precipitate unit cell. The lattice parameter dependence on temperature is considered for both precipitates [58] and matrix [59]. For the precipitates, the additional dependence of the lattice parameter on the precipitate stoichiometry, i.e. on the carbon vacancies fraction, is also taken into account in the calculations [60]. The numbers 2 and 4 used for the atomic volume of the matrix and the precipitates calculation, respectively, are the total number of metal atoms in the BCC ferrite matrix unit cell and in the precipitate unit cell. The b_{j} is the coherent scattering length of each element j [61]. The coherent scattering lengths are $b_{\mathrm{Fe}} = 9.45 \times 10^{-15}$ m for iron, $b_{\mathrm{C}} = 6.646 \times 10^{-15}$ m for carbon, $b_{\mathrm{V}} = -0.3824 \times 10^{-15}$ m for vanadium and $b_{\mathrm{Mn}} = -3.73 \times 10^{-15}$ m for manganese. The vanadium and carbon fractions in solid solution in the matrix are excluded from the matrix contrast calculation because of their insignificant numerical contribution.

Similar to the nuclear contrast between the matrix and the precipitates, the magnetic contrast is $\Delta\rho_{\mathrm{MAG}} = \rho_{\mathrm{MAG\_matrix}} - \rho_{\mathrm{MAG\_precip}}$. The matrix magnetic scattering length is:

$$\rho_{\mathrm{MAG\_matrix}} = \frac{p}{V_{\mathrm{bcc}}} \tag{4.6}$$

In the ferritic matrix only the Fe is magnetic and the p parameter in Eq. (4.6) is its magnetic scattering length given by $p = 2.699 \times 10^{-15}\text{-m} * \mu$, where μ is the saturation per iron atom in μ_{B} units. The magnetization saturation temperature dependence is taken into consideration as in Ref. [62] and is equal to 1.47 μ_{B} at 650 ºC (corresponding to $\mu_0 * M \sim 1.45$ T, where μ_0 is the magnetic permeability of the vacuum and M the magnetization) and to 1.26 μ_{B} at 700 °C (corresponding to $\mu_0 * M \sim 1.24$ T) resulting to a magnetic scattering length of 3.97×10^{-15} m at 650 ºC and 3.39×10^{-15} m at 700 °C.

The magnetic scattering from the precipitates depends on the fraction of Fe in the precipitates and the corresponding magnetic scattering length is:

$$\rho_{\mathrm{MAG\_precip}} = x \cdot \frac{p}{V_{\mathrm{precip}}} \tag{4.7}$$

By combining Eq. (4.4)-(4.7), for each steel composition and for a specific temperature, 650 °C or 700 °C, the $\Delta\rho^2{}_{\mathrm{NUC}}/\Delta\rho^2{}_{\mathrm{MAG}}$ is obtained as a function of the x and y, i.e., as a function of the precipitate chemical composition. Following Eq. (4.3), the experimental intensity ratio evolution for each time slice is thus obtained as a function of x and y:

$$\frac{\left(\frac{d\Sigma}{d\Omega}\right)_{NUC}}{\left(\frac{d\Sigma}{d\Omega}\right)_{MAG}} = \frac{\left(\frac{(1-z_{matrix})\cdot b_{Fe} + z_{matrix}\cdot b_{Mn}}{V_{bcc}} - \frac{x\cdot b_{Fe} + (1-x-z)\cdot b_{V} + z\cdot b_{Mn} + y\cdot b_{C}}{V_{precip}}\right)^2}{\left(\frac{p}{V_{bcc}} - x\cdot\frac{p}{V_{precip}}\right)^2} = f(x,y) \quad (4.8)$$

The presence of iron in the precipitates reduces both $\Delta\rho^2_{NUC}$ and $\Delta\rho^2_{MAG}$. However, the decrease in $\Delta\rho^2_{NUC}$ is much larger, causing an overall reduction of $\Delta\rho^2_{NUC}/\Delta\rho^2_{MAG}$. On the other hand, the presence of carbon vacancies leads to an increase of $\Delta\rho^2_{NUC}/\Delta\rho^2_{MAG}$. Consequently, different combinations of x and y can result in the same ratio of the nuclear-to-magnetic macroscopic differential scattering cross-sections as given by Eq. (4.8). In order to overcome this complication and due to the fact that the precipitate composition can be assumed to reach a plateau after 10 h of annealing according to the experimental SANS intensity ratios (as will be shown in the Figs. 4.4-4.6 of the present study), the ThermoCalc software is used to determine the equilibrium precipitate stoichiometry.

ThermoCalc equilibrium calculations of the precipitates chemical composition are performed for the three alloys at 650 °C and at 700 °C. The results are listed in Table 4.2. In equilibrium, in all alloys and at both temperatures, the precipitates are mainly vanadium carbides with less than 8.5% of iron and an even smaller fraction of manganese (less than 0.5%) present. According to ThermoCalc, the equilibrium precipitate chemical composition in LCLV and HCHV steels is very similar. In the LCHV steel at both temperatures the concentration of iron and manganese in the precipitates is less than the corresponding concentrations in the precipitates in the LCLV and HCHV steels.

In the last column of Table 4.2, the precipitate stoichiometry is presented based on the carbon-to-metal fraction as derived from ThermoCalc. For solving Eq. (4.8), the y value for each steel at a specific temperature is assumed to be constant during annealing, and equal to the equilibrium value given by ThermoCalc. Then the fraction of iron in the precipitates during annealing is obtained from Eq. (4.8) and the fraction of vanadium is the remaining metallic fraction after the subtraction of iron and manganese fractions.

Table 4.2. Equilibrium precipitate chemical composition predicted by ThermoCalc.

Steel	annealing temperature (°C)	at.% of atoms in the precipitates				precipitates' chemical formula
		at.%V	at.%C	at.%Fe	at.%Mn	$(Fe_xV_{1-x-z}Mn_z)C_y$
LCLV	650	44.75	46.58	8.35	0.31	$(Fe_{0.156}V_{0.84}Mn_{0.006})C_{0.872}$
	700	46.18	46.49	7.10	0.23	$(Fe_{0.133}V_{0.86}Mn_{0.004})C_{0.869}$
LCHV	650	51.65	45.62	2.66	0.06	$(Fe_{0.049}V_{0.95}Mn_{0.001})C_{0.839}$
	700	51.39	45.74	2.80	0.07	$(Fe_{0.050}V_{0.95}Mn_{0.001})C_{0.843}$
HCHV	650	45.72	46.54	7.48	0.25	$(Fe_{0.140}V_{0.86}Mn_{0.005})C_{0.871}$
	700	46.29	46.49	6.99	0.23	$(Fe_{0.130}V_{0.87}Mn_{0.004})C_{0.869}$

However, the validity of the assumption that y remains overall constant during annealing, is questionable because it basically implies that the precipitate (sub-)stoichiometry distribution is time-independent. Furthermore, y may also change with time because it may be dependent on the size of the precipitates and the size distribution changes with time. The time evolution of the precipitate sub-stoichiometry distribution is included in the final chemical composition calculations by calculating boundaries for the iron and vanadium fractions. Since a decrease of y and a decrease in the amount of iron in the precipitates both result in an increase in the

$\Delta\rho^2_{NUC}/\Delta\rho^2_{MAG}$ ratio, by solving Eq. (4.8) for a given experimental ratio, $y_{min} = 0.75$ will determine the upper boundary for the Fe fraction. Accordingly, $y_{max} = 1$ will yield the lower boundary for the Fe fraction. The boundaries in the fraction of vanadium are calculated as the boundaries of iron subtracted from 1 for each moment of annealing.
Summarizing, following this method, the precipitate chemical composition evolution can be calculated for any steel composition and for all possible precipitate sizes and shapes without fitting of any parameters other than the composition parameters (e.g. parameters related to the precipitates size distribution). The complexity, however, of the analysis increases when more alloying elements that can partially substitute vanadium in the vanadium carbide precipitate are included, or when different types of precipitates with different size distribution evolution are present. Moreover, a limitation of the SANS technique is that it cannot directly provide information on the precipitate crystal structure and on the spatial distribution of the metal atoms within the precipitate. For these reasons, complementary techniques like TEM and APT should accompany and complement the SANS measurements.

4.4. Results and Discussion

4.4.1. Small-Angle Neutron Scattering

Nuclear and magnetic differential scattering cross-sections of the LCLV, LCHV and HCHV steels obtained by in-situ SANS during annealing at 650 °C and at 700 °C are presented in the Appendix B (Fig. B2). Because of space limitations, only an example, the differential scattering cross-section evolution in the LCLV during annealing at 650 °C is shown in Figs. 4.2a and b for the nuclear and the magnetic components, respectively. These curves are obtained after background subtraction, and therefore consist only of the precipitation scattering contribution. The subtracted background signal consists of the furnace scattering contribution and the scattering from a steel without precipitates (obtained from the scattering of the samples at the soaking temperature, 1050 °C or 1100 °C). The SANS intensity during cooling (obtained by using 1 minute time slices) is compared to the SANS signal at high temperatures and the curves are identical, indicating that no precipitation takes place before the isothermal annealing temperature is reached.
Four representative time slices are chosen and the SANS intensity time evolution during isothermal holding is shown in Fig. 4.2. Both nuclear and magnetic intensities are increasing with time due to precipitation, and the magnitude of intensity increase depends on the volume fraction of the precipitates formed. The intensity increases more rapidly during the first hour of annealing, indicating faster precipitation kinetics at the beginning of annealing than at later stages. The intensity curves corresponding to shorter annealing times have larger error bars due to the re-binning of data over shorter time slices than for the long annealing times.
Note that for short annealing times the precipitate size and volume fraction are small, therefore the measured scattering intensity is low. In addition, the Q-range of the Larmor instrument is limited, affecting the accuracy in resolving the smallest precipitates. However precipitates of size of ~1 nm can be detected as stated in Ref. [26].

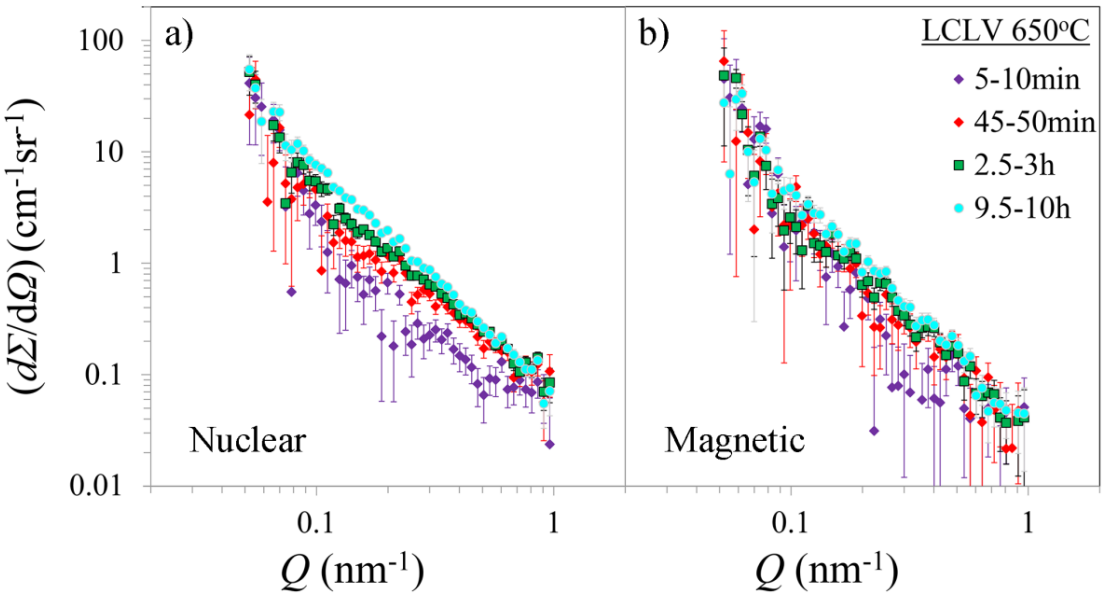

Fig. 4.2. a) Nuclear and b) magnetic differential scattering cross sections obtained during annealing of LCLV steel at 650 °C as a function of Q. The scattering curves of some selected annealing times are shown.

Fig. 4.3 provides the $(d\Sigma/d\Omega)_{NUC}/(d\Sigma/d\Omega)_{MAG}$ ratios obtained by in-situ SANS measurements on the LCLV steel annealed at 650 °C. The ratio is calculated from the scattering curves of Figs. 4.2a and b. Note that the errors for short annealing times are relatively large due to the limited counting statistics. Since we observe no significant Q-dependence we calculate the weighted average for the $(d\Sigma/d\Omega)_{NUC}/(d\Sigma/d\Omega)_{MAG}$ ratio over Q for each time slice. The weighted average is calculated as the $\sum_{n=1}^{npts}\left(\left(1/ratio\_error_n^{\,2}\right)\cdot ratio_n\right)\Big/\sum_{n=1}^{npts}\left(1/ratio\_error_n^{\,2}\right)$, where n stands for each individual data point in Fig. 4.3, $ratio_n$ and $ratio\_error_n$ are the experimental $((d\Sigma/d\Omega)_{NUC}/(d\Sigma/d\Omega)_{MAG})(Q)$ ratio and its error for each Q, respectively, and *npts* is the number of the experimental data points. The dotted lines in Fig. 3 represent the calculated weighted average of the nuclear to magnetic intensity ratio for each time slice. The ratio is increasing during annealing of all the steels at both 650 °C and 700 °C and it is presented later in Figs. 4.4a-b, 4.5a-b and 4.6a-b.

Examples of nuclear and magnetic differential scattering cross sections vs Q of all steels annealed at 650 °C and 700 °C are provided in Appendix B (Fig. B3), showing the Q independence of the $(d\Sigma/d\Omega)_{NUC}/(d\Sigma/d\Omega)_{MAG}$ ratio.

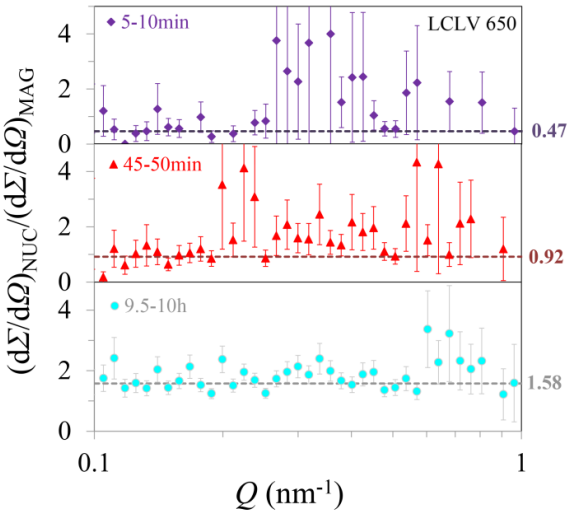

Fig. 4.3. Ratios of the nuclear to magnetic scattering cross sections plotted versus the scattering vector, Q, on a logarithmic scale, for LCLV alloy samples annealed at 650 °C for different annealing times from the in-situ scattering curves of Figs. 4.2a and b.

The experimental, weighted averaged, $(d\Sigma/d\Omega)_{NUC}/(d\Sigma/d\Omega)_{MAG}$ ratio evolution during annealing at 650 °C and at 700 °C is presented for the LCLV, LCHV and HCHV steels in the graphs of Figs. 4.4a-b, 4.5a-b and 4.6a-b, respectively. The missing points in the graphs are due to an interruption of the neutron beam. The errors in the experimental $(d\Sigma/d\Omega)_{NUC}/(d\Sigma/d\Omega)_{MAG}$ ratio are statistical errors originating from the neutron measurements. For all steels and at both temperatures, the $(d\Sigma/d\Omega)_{NUC}/(d\Sigma/d\Omega)_{MAG}$ ratio increases during annealing, indicating changes in the precipitate chemical composition with time. As shown in Figs. 4.4-4.6, the first 4 hours are the most critical for the precipitate chemical composition evolution while at the later stages of annealing, the $(d\Sigma/d\Omega)_{NUC}/(d\Sigma/d\Omega)_{MAG}$ ratio reaches a plateau value suggesting that the (metastable) equilibrium precipitate composition is reached. The smaller experimental $(d\Sigma/d\Omega)_{NUC}/(d\Sigma/d\Omega)_{MAG}$ ratio in the first hours of annealing is mainly attributed to the presence of iron in the precipitates which, as explained in the previous section, leads to a lower $\Delta\rho^2_{NUC}/\Delta\rho^2_{MAG}$.

The black dashed horizontal line plotted in Figs. 4.4a-b, 4.5a-b and 4.6a-b is the $\Delta\rho^2_{NUC}/\Delta\rho^2_{MAG}$ ratio that corresponds to the equilibrium precipitate chemical composition according to ThermoCalc (presented in Table 4.2). The green dashed horizontal line is the theoretically calculated $\Delta\rho^2_{NUC}/\Delta\rho^2_{MAG}$ ratio for stoichiometric vanadium carbides that do not contain any iron but only a small fraction of manganese given by ThermoCalc. This ratio (for stoichiometric vanadium carbides) is temperature dependent and is equal to 1.69 at 650 °C and 2.33 at 700 °C. Both $\Delta\rho^2_{NUC}$ and $\Delta\rho^2_{MAG}$ are lower at 700 °C than at 650 °C, but the $\Delta\rho^2_{MAG}$ reduction from 650 to 700 °C is stronger due to the reduction in the magnetization of the iron matrix at 700 °C compared to that at 650 °C. ThermoCalc indicates a sub-stoichiometric equilibrium precipitate composition for all steels ($y < 1$) and this is graphically shown by the black line having a higher value than the green stoichiometric line for which $y = 1$. The fact that we measure ratios above the corresponding ratio for pure vanadium carbide (green lines), especially in the cases of LCHV and HCHV at both temperatures, is a strong indication for the presence of sub-stoichiometric carbides.

For the HCHV steel at both annealing temperatures, the experimental $(d\Sigma/d\Omega)_{NUC}/(d\Sigma/d\Omega)_{MAG}$ ratio is larger than the equilibrium and the stoichiometric ratios (Figs. 4.6a and 4.6b), implying that the carbon-to-metal ratio in the precipitates of this steel is smaller than the ThermoCalc results. For this steel, a red dashed horizontal line is plotted corresponding to $(V,Fe,Mn)_4C_3$ for comparison.

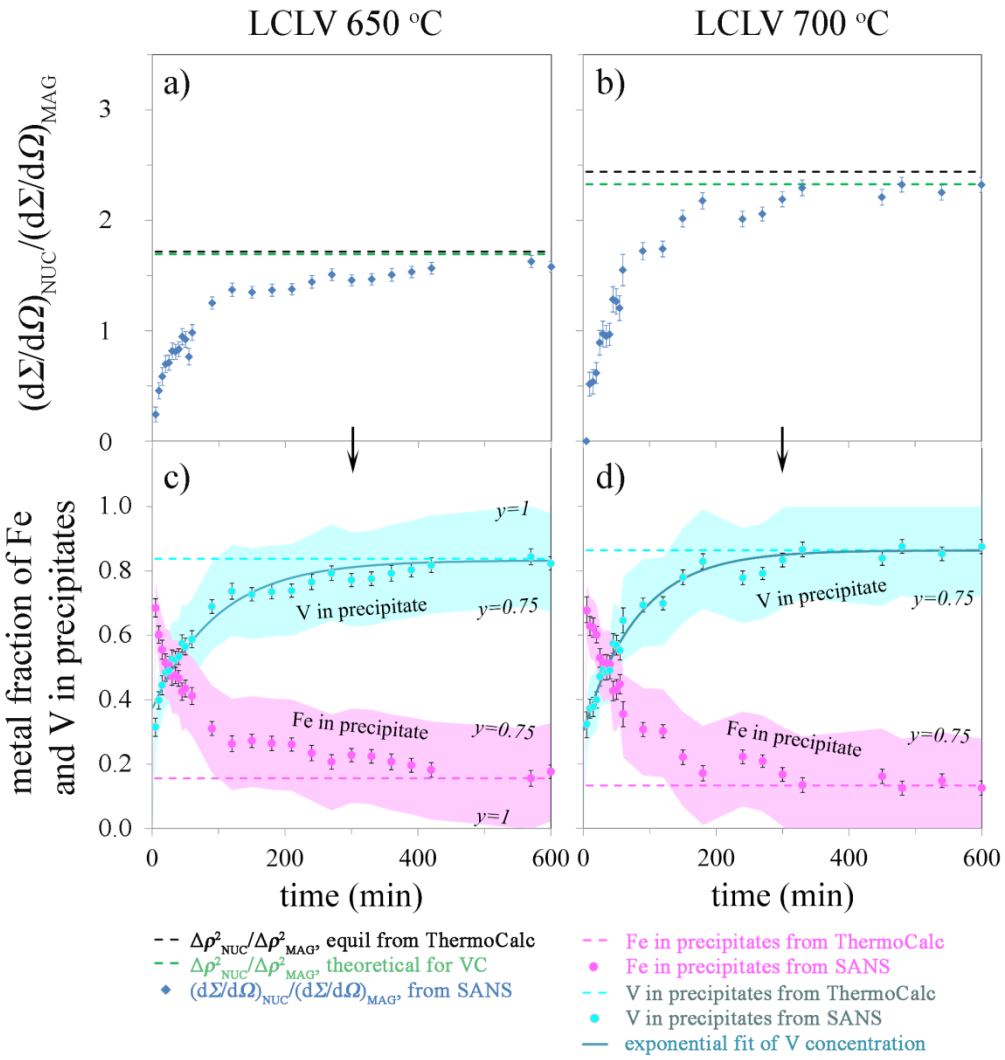

Fig. 4.4. Experimentally observed evolution of the ratio of the nuclear to magnetic scattering cross section of the LCLV steel during annealing a) at 650 °C and at b) 700 °C. The derived precipitate composition evolution is shown in c) and d), respectively. The solid lines in c and d are fits with Eq. (4.9).

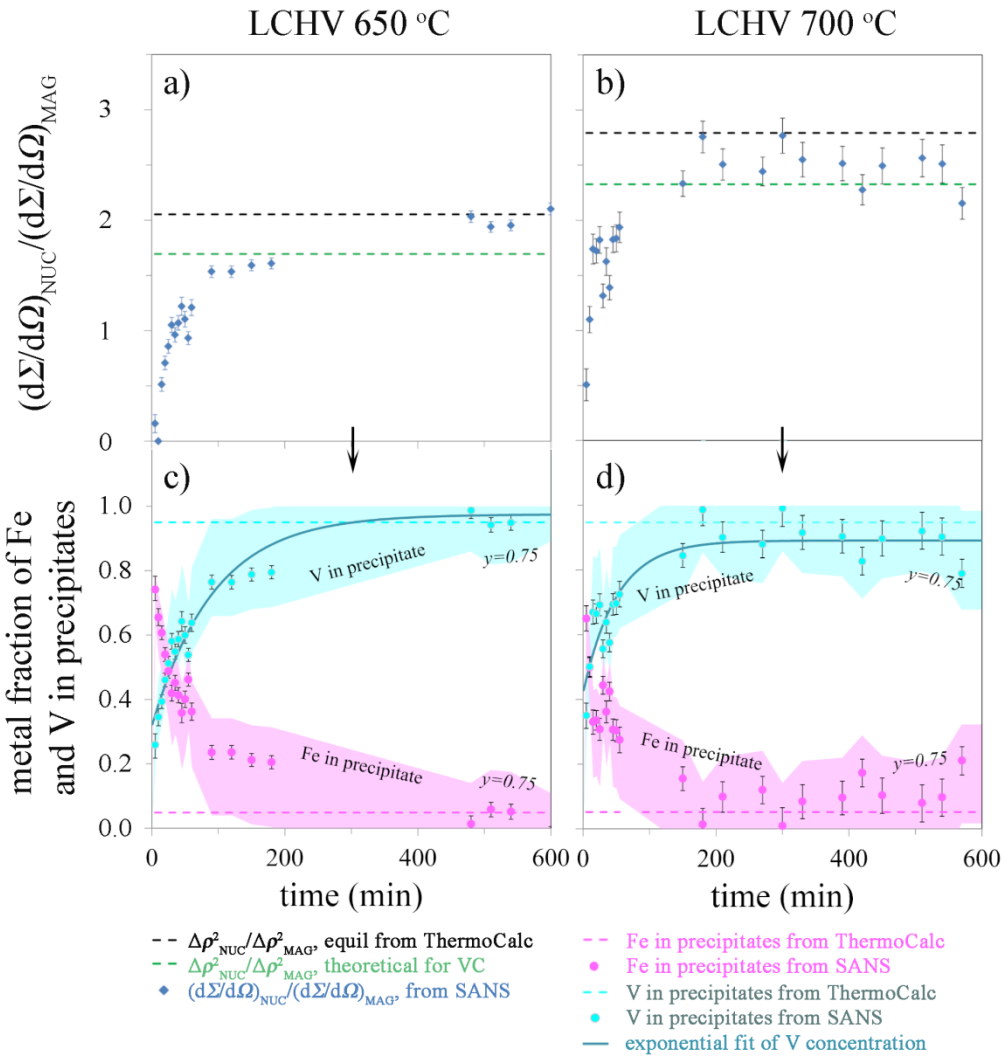

Fig. 4.5. Experimentally observed evolution of the ratio of the nuclear to magnetic scattering cross section of the LCHV steel during annealing a) at 650 °C and at b) 700 °C. The derived precipitate composition evolution is shown in c) and d), respectively. The solid lines in c and d are fits with Eq. (4.9).

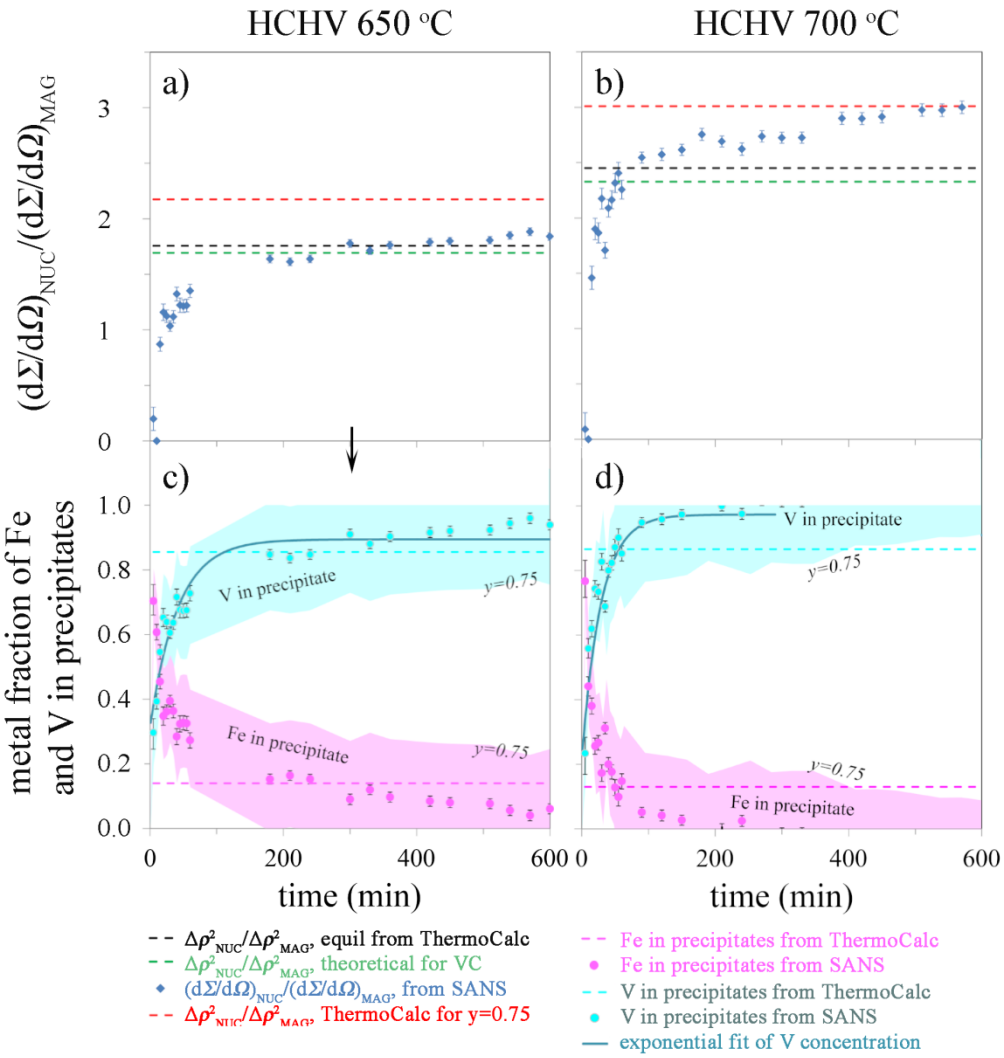

Fig. 4.6. Experimentally observed evolution of the ratio of the nuclear to magnetic scattering cross section of the HCHV steel during annealing a) at 650 °C and at b) 700 °C. The derived precipitate composition evolution is shown in c) and d), respectively. The solid lines in c and d are fits with Eq. (4.9).

In order to quantify the evolution of iron and vanadium fractions in the precipitates, we follow the method described in Section 4.3. The results are presented in Figs. 4.4c-d, 4.5c-d and 4.6c-d for the three steels. The marker dots for the iron and vanadium fractions result from the solution of Eq. (4.8) using y from ThermoCalc for each steel at each temperature. The error bars reflect the statistical error from the SANS measurements. They are calculated from the experimental $(d\Sigma/d\Omega)_{NUC}/(d\Sigma/d\Omega)_{MAG}$ ratio errors, after solving Eq. (4.8). The shaded areas in the iron and vanadium fractions reflect the spread in the iron and vanadium fractions in the precipitates during annealing when the upper ($y_{max} = 1$) and lower ($y_{min} = 0.75$) values for y are applied to Eq. (4.8). The iron and vanadium fractions can vary between 0 and 1, setting the upper boundary for y during annealing (boundaries in the shaded areas in Figs. 4.4-4.6). According to Figs. 4.4-4.6, the precipitates in the LCLV steel at both temperatures tend to a more stoichiometric distribution than the LCHV and HCHV steels, indicated by the larger y values.

For the HCHV steel annealed at 700 °C, y = 0.869 is given by ThermoCalc. However, by applying our method, the calculated iron and vanadium fractions in the precipitates are physically possible only for the first hours of annealing. y = 0.869 yields a negative iron fraction and a vanadium fraction larger than 1 after 300 min of annealing (Fig. 4.6d). This means that, either ThermoCalc gives a larger value for y than the experimental one from SANS (the final experimental $(d\Sigma/d\Omega)_{NUC}/(d\Sigma/d\Omega)_{MAG}$ ratio can be reached if the carbon-to-metal ratio is set to y = 0.75 in the model – Fig. 4.6d), or that in the HCHV steel the precipitates possibly have a different crystal structure than that of the precipitates in the steels with the lower carbon concentration (LCLV and LCHV steels). However, evidence of a different precipitate crystal structure in the precipitates of the HCHV steel is not pronounced at 650 °C. The evolution of the iron and vanadium content in the precipitates in the HCHV steel at 700 °C is calculated only for the first 300 min of annealing. The presence of precipitates that have not yet reached the equilibrium precipitate composition is a possible reason for the difference between the precipitate chemical composition measured experimentally and the one given by ThermoCalc. The iron fraction in the precipitates decreases with time, with the iron being substituted by vanadium in the precipitate lattice, so that the fraction of vanadium in the precipitates is increasing with time. Since the precipitate size is becoming larger during isothermal holding (precipitate growth and coarsening), our analysis confirms the presence of iron in small vanadium carbides, in agreement with Ref. [26]. Comparing the precipitate chemical composition evolution plots for the precipitates in the LCLV and LCHV steels (Figs. 4.4 and 4.5), we conclude that the addition of vanadium to the steel nominal composition leads to the formation of precipitates with a higher vanadium concentration. At both temperatures, more vanadium is included in the precipitates of LCHV and HCHV steels than in the LCLV steel as there is twice the amount of vanadium in the steels' nominal composition. Consequently, the addition of vanadium to the steel nominal composition promotes the presence of vanadium rich precipitates, with less iron and a smaller carbon to metal ratio.

These precipitates are initially metastable with a high iron concentration and their composition gradually evolves towards equilibrium during annealing. Similar conclusions are reported in [15],[16] regarding the presence of iron in niobium carbides. A possible reason for the presence of iron is that it lowers the precipitate strain energy through the precipitate-matrix lattice misfit reduction, resulting in a higher net driving force (the sum of the chemical free energy difference and the strain energy) and therefore reduced activation energy for precipitate nucleation as explained in [29] for (Ni,Al,Mo) precipitates and in [15],[16] for niobium carbides. Quantitatively, the average metal fraction of iron in the precipitates in all steels reduces from a value larger than 0.65 in the initial stage of precipitation to a value smaller than 0.15 in the later stages. In the LCHV steel, both at 650 and at 700 °C, the final fraction of iron in the precipitates is much less (and the amount of vanadium is much higher) than the corresponding fraction in the LCLV steel. This composition effect is a purely thermodynamic effect, as it is also shown in the equilibrium precipitate composition provided by ThermoCalc (Table 4.2).

It is important to note that, despite the fact that in the LCLV and HCHV steel the vanadium and carbon have the same atomic ratio (equal to 1) in the nominal composition and that ThermoCalc predicts the same precipitate composition in these two steels, the experimentally measured precipitate composition differs between the LCLV and HCHV alloys. This, in turn, could affect the resulted precipitation and modulus strengthening of the steel.

4.4.2. Rate of change in the precipitate chemical composition evolution by SANS

In order to calculate the rate of change in the precipitate chemical composition in the three steels, the calculated fraction of vanadium in the precipitates is fitted to the following equation:

$$V_{metal\_fraction}(t) = A - B \cdot \exp(-k \cdot t), \quad (4.9)$$

where A and B are fitting parameters dependent on the matrix and precipitate composition and on the annealing temperature. The k factor describes the rate of change in the precipitate chemical composition and t is the time. The fitting curves are shown in Fig. 4.4c-d, 4.5c-d, 4.6c-d and in Fig. 4.7a-b and the k factor is graphically presented for the three steels annealed at 650 °C and at 700 °C in Fig.4. 8.

Figs. 4.7a and b show the evolution of the metal fraction of vanadium in the precipitates during annealing at 650 °C and at 700 °C, respectively. The individual points are obtained from the experimental data after solving Eq. (4.8) using the y-value from ThermoCalc as explained above. These points are also presented in Figs. 4.4c-d, 4.5c-d and 4.6c-d. The dashed lines result from the fitting of these data points, i.e., from the fitting of the fraction of vanadium in the precipitates (Eq. (4.9)).

At a fixed temperature, 650 °C or 700 °C (Fig. 4.7a and b, respectively), changes in the precipitate chemical composition are faster in the LCHV and HCHV steels due to their excess of vanadium with respect to LCLV steel. This is also reflected in the larger k factor for LCHV and HCHV compared to the LCLV steel at a specific temperature (Fig. 4.8). The carbon also has an accelerating effect on the kinetics of evolution of the precipitate chemical composition at both temperatures (Figs. 4.7a and b). This is visible also by the larger k factor in the HCHV than in the LCLV and LCHV steels – Fig. 4.8.

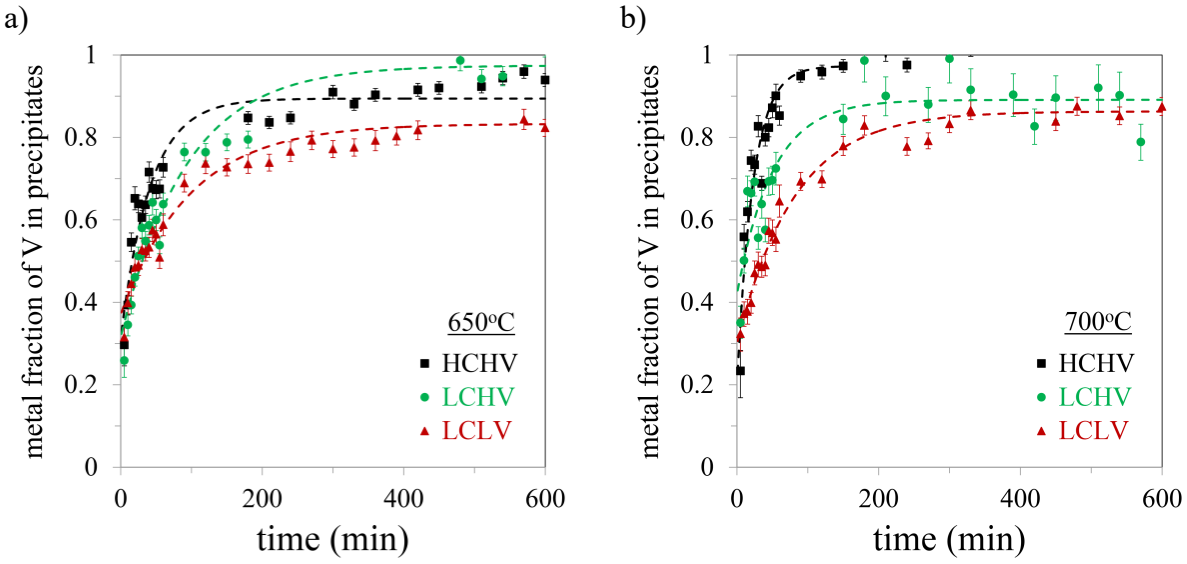

Fig. 4.7. Evolution of the metal fraction of vanadium in the precipitates in the LCLV(▲), LCHV(●) and HCHV(■) steels during annealing at a) 650 °C and b) 700 °C. The marker dots are obtained from the experimental data after solving Eq. (4.8) using the y from ThermoCalc (they are also presented in Figs. 4.4c-d, 4.5c-d and 4.6c-d), and the dashed lines result from the fitting of these data points, i.e., from the fitting of the amount of vanadium in the precipitates.

As shown in Fig. 4.8, the k factor is larger at 700 °C than at 650 °C for all steels corresponding to faster changes in the precipitate chemical composition at 700 °C, which can be attributed to a faster –thermally activated– vanadium diffusion. According to Fig. 4.8, the influence of temperature in the rate of change in the precipitate chemical composition in the LCHV and HCHV steels clearly increases with increasing temperature. In the LCLV steel, the rate of

change in the precipitate chemical composition increases with increasing temperature as well, however, the influence of temperature is smaller in this steel, suggesting that the impact of the increased vanadium diffusion is more evident in steels with a higher vanadium fraction.

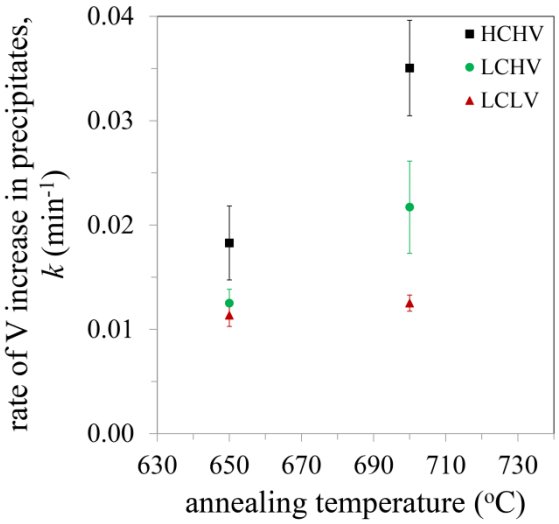

Fig. 4.8. Precipitate chemical composition evolution rate at 650 °C and at 700 °C for the precipitates in the LCLV, LCHV and HCHV.

The driving force for the precipitation of vanadium carbides in ferrite at 650 °C and at 700 °C is calculated using ThermoCalc ortho-equilibrium calculations. The results are listed in Table 4.3. For each steel, the driving force for precipitation is smaller at 700 °C than at 650 °C as expected due to the increase in the solubility of the precipitates when the temperature increases [9],[63], and comparable to the values reported in [63].

Table 4.3 Driving force for precipitation in ferrite and precipitate dissolution temperature in the three steels of interest according to ThermoCalc.

	driving force for precipitation in ferrite, ΔG_V		precipitate dissolution temperature in °C
Steel	annealing at 650 °C	annealing at 700 °C	
LCLV	24.3 kJ/mol (=2229 MJ/m^3)	21.0 kJ/mol (=1925 MJ/m^3)	990
LCHV	26.9 kJ/mol (=2462 MJ/m^3)	23.7 kJ/mol (=2173 MJ/m^3)	1060
HCHV	28.8 kJ/mol (=2642 MJ/m^3)	25.8 kJ/mol (=2361 MJ/m^3)	1069

The nucleation rate of the precipitates depends on the driving force for precipitation as described by [64]:

$$\dot{N} \propto \exp\left(-\frac{\Delta G^* + Q_D}{k_B T}\right) \tag{4.10}$$

In Eq. (4.10), Q_D is the activation energy for vanadium diffusion, T is the temperature, k_B is the Boltzmann constant and ΔG^* is the activation energy for the nucleation of the precipitates given by:

$$\Delta G^* = \frac{\Psi}{\left(\Delta G_V - g_s\right)^2}, \tag{4.11}$$

where ΔG_V is the chemical driving force for the nucleation of the precipitates and g_s is the misfit strain energy between the precipitates and the matrix. The Ψ parameter is equal to [65]:

$$\Psi = \frac{4}{27 z_V^2}\left(\sum_l z_A^l \sigma_l\right)^3 \tag{4.12}$$

and it contains information about the energies, σ, between the interfaces l that are involved in the nucleation process and the shape of the critical nucleus (reflected by the coefficients z_A^l and z_V^l) [65]. The Ψ parameter is dependent on the coherency of the precipitate/matrix interface, therefore, dependent on the iron content in the precipitates due to the fact that the presence of iron in the precipitates can reduce the precipitate/matrix lattice misfit [15],[16]. Consequently, because a higher fraction of iron in the precipitates increases the coherency of the precipitates and thus reduces the interfacial energy between the precipitates and the matrix, it eventually reduces Ψ. This leads to a decrease in the activation energy for the precipitate nucleation, ΔG^*, and consequently to an increase in the nucleation rate, $\dot{N}$ (Eq. (4.10)-(4.12)). In addition, the presence of iron in the precipitates reduces the strain energy between the precipitate and the matrix, g_s, which, based on Eq. (4.11), also reduces the activation energy for the precipitate nucleation, ΔG^*, and, increases $\dot{N}$, explaining that the presence of iron in the precipitates in the first stages of annealing is critical for the entire nucleation process. The presence of iron in the precipitates affects also the chemical driving force for the nucleation, ΔG_V. Iron in the precipitates reduces ΔG_V and consequently the nucleation rate, $\dot{N}$ (Eqs. (4.10) and (4.11)). Our observations seem to favour iron-rich precipitates in the beginning of annealing, indicating that the latter effect of iron on reducing the chemical driving force and consequently reducing the $\dot{N}$ is minor compared to its effect on reducing the lattice misfit and the strain energy and consequently increasing the $\dot{N}$. The presence of carbon vacancies in the precipitates has also an influence on the driving force for precipitation and the nucleation rate through the parameters of Eq. (4.10), (4.11) and (4.12), however, these effects are not quantified here because of the lack of sufficient data.

Based on Eqs. (4.10) and (4.11), the smaller driving force for precipitation, ΔG_V, at 700 ºC in all steels (Table 4.3) results in a higher activation energy for the precipitate nucleation, ΔG^*, and therefore to a reduced nucleation rate, $\dot{N}$.

Precipitates nucleate at a lower rate at 700 °C than at 650 °C [63] (see also the APT results below) but due to the larger mobility of the precipitating elements at 700 °C, the precipitate growth rate is larger at 700 °C and therefore faster changes in the precipitate chemical composition are observed at this temperature (the k factor is larger Fig. 4.8).

By increasing the vanadium content in the steel at a certain temperature (see the comparison between LCLV and LCHV steels in Table 4.3), the driving force for vanadium carbide precipitation becomes larger (in agreement with [22] and [63]) at both temperatures. This is attributed to the fact that the addition of vanadium to the steel results in an increased concentration of vanadium at the α/γ interface due to the solute drag effect.

We observe that an increase in the overall carbon concentration leads to an increase in the rate of change in the precipitate chemical composition. A possible explanation for this observation is as follows. The bulk carbon content also affects the precipitation driving force. The carbon

addition also increases the precipitate dissolution temperature (Table 4.3 – comparison between LCHV and HCHV, consistent with [63]). However, a larger carbon content in the steel composition may retard the austenite-to-ferrite phase transformation due to the carbon enrichment in austenite [26] and consequently it might be possible that the vanadium segregation and supersaturation at the α/γ interface is enhanced, causing an increase in the driving force for precipitation (Table 4.3 – comparison between LCHV and HCHV) and consequently an increase in the rate of change in the precipitate chemical composition. More information is presented in Chapter 5.
The values for the driving force for precipitation presented in Table 4.3 are based on the assumption that the vanadium carbide precipitation takes place in the bulk ferrite. In reality, these values can be different when the precipitates nucleate during the austenite-to-ferrite phase transformation in the moving α/γ boundary, in which the local concentration of the elements is somewhat different.
Summarizing, the alloying additions of vanadium or carbon to the steel nominal composition can increase the driving force for precipitation at a specific temperature. The rate of change in the precipitate chemical composition depends on the driving force for precipitation (which is influenced by the alloy composition, the concentration of elements at the α/γ interface, the solute drag effect and the precipitate chemical composition) as well as on the diffusivity of the precipitating elements such as vanadium through their effect on the precipitate/matrix interface velocity. For each steel annealed at a specific temperature, the parameter that has the dominant effect over the others is the one that eventually controls the rate of change in the precipitate chemical composition.

4.4.3. Precipitate chemical composition determined by Atom Probe Tomography

Fig. 4.9 shows representative 3D vanadium atom maps for LCLV, LCHV and HCHV steel tips measured by APT. All maps are superimposed with 2 at.%V iso-concentration surfaces. Vanadium rich regions are clearly distinguished in all tips and correspond to vanadium carbides since carbon enrichment is also measured in these regions (an example is provided in Fig. B4 in the Appendix B). The first three maps belong to LCLV, LCHV and HCHV specimens isothermally annealed in the dilatometer at 650 °C for 10 h. Spherical/slightly ellipsoidal precipitates larger than 2 nm have been formed after 10 h at 650 °C in all steels. Much larger precipitates are seen after 10 h at 700 °C in all steels. A representative example of a tip of a LCLV specimen annealed at 700 °C for 10 h is shown in the fourth tip of Fig. 4.9.
Proximity Diagrams (proxigrams) [66] calculated using iso-concentration surfaces (iso-surfaces) of 2 at.%V are used to provide the precipitates' chemical composition profile. After 10 h of isothermal holding at 650 °C or at 700 °C, the precipitates have reached a stable composition according to SANS (Figs. 4.4-4.6). The precipitate chemical composition analysis is performed by the use of proxigrams in all steels after 10 h of annealing.

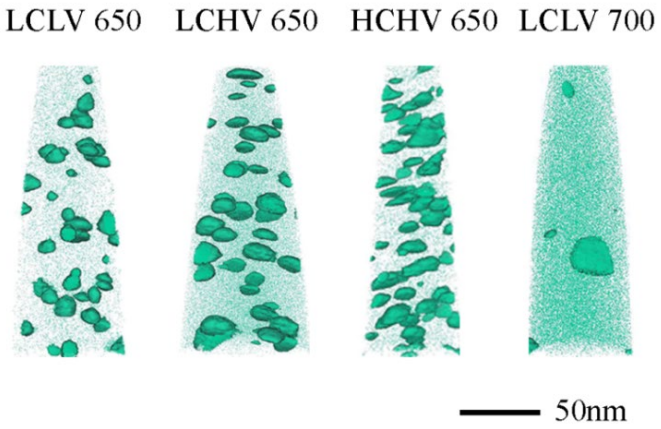

Fig. 4.9. From left to right: 3D APT maps of V atoms in LCLV, LCHV and HCHV after annealing at 650 °C for 10 h, and of LCLV after annealing at 700 °C for 10 h. The maps are superimposed with 2at.%V iso-surfaces.

As a representative example, the radially averaged 1D composition profiles of two precipitates in the LCHV steel annealed at 700 °C for 10 h are shown in Figs. 4.10a and b. More composition profiles of precipitates in LCLV, LCHV and HCHV steels can be found in the supplementary material (Figs. B5-7). No manganese enrichment is measured by APT in the precipitates in any of the three alloy steels in agreement with ThermoCalc calculations, therefore the amount of manganese is not plotted in the proxigrams for the sake of simplicity. Precipitates with a small and comparable fraction of iron in the core and with different sub-stoichiometric ratios are found in all steels.

The two precipitates in Figs. 4.10a and b are from two different APT tips extracted from the same sample area of the LCHV steel annealed at 700 °C. Fig. 4.10a shows the radially averaged 1D composition profile of a precipitate in which the carbon-to-metal ratio is close to the stoichiometric one while Fig. 4.10b shows the profile of a precipitate in which the carbon-to-metal ratio is much lower that the stoichiometric ratio. Such differences in the stoichiometry of the precipitates are found in all alloys. In both precipitates, iron is detected in the core in a fraction of a few at.% which is consistent with the equilibrium precipitate composition given by ThermoCalc.

A gradual increase of vanadium and carbon along with a decrease of iron concentration from the surface to the precipitate core is observed. However, inconsistencies in the concentration profile of the precipitates' surface are possible as a result of the local magnification effect [39] in APT, which causes misidentification of atoms close to the precipitate/matrix interface.

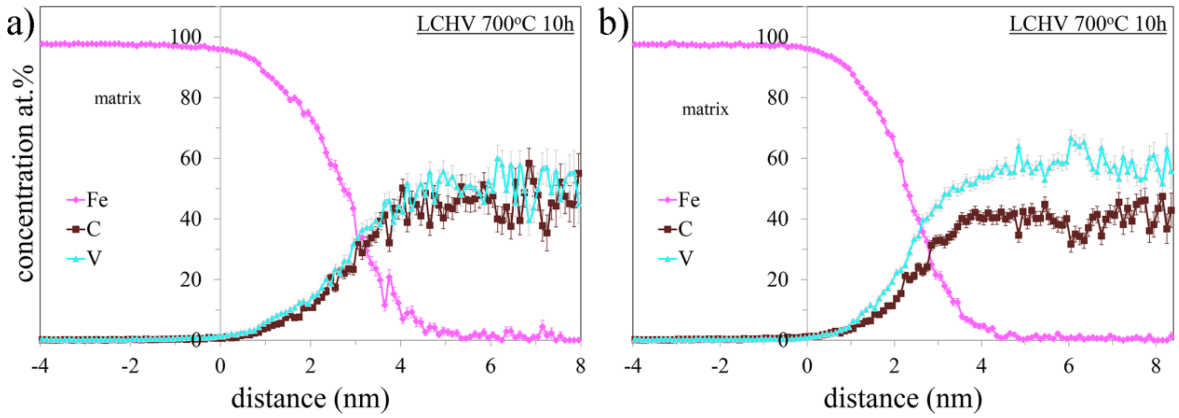

Fig. 4.10. Proxigrams of two representative precipitates with different stoichiometry in the LCHV steel annealed at 700 °C for 10 h. In a), the carbon-to-metal ratio is closer to the stoichiometric ratio than in b).

The proxigrams in Figs. 4.11a and b belong to precipitates in the LCLV steel annealed at 700 °C for 10 h. Like in Figs. 4.10a and b, the precipitates in Fig. 4.11 are from two different tips but from the same sample area of the LCLV steel. The precipitate in Fig. 11a has a composition closer to stoichiometry and the one in Fig. 11b has a lower carbon-to-metal ratio. APT therefore shows that sub-stoichiometric precipitates are also present in the LCLV steel, in which the presence of sub-stoichiometric precipitates is not obvious from the experimental SANS $(d\Sigma/d\Omega)_{NUC}/(d\Sigma/d\Omega)_{MAG}$ ratio evolution (Figs. 4a and b). In these figures, the experimental ratio does not reach the green dashed horizontal line which is the theoretical ratio that the precipitates would have if they were stoichiometric. The experimental $(d\Sigma/d\Omega)_{NUC}/(d\Sigma/d\Omega)_{MAG}$ values in the LCLV steel are lower than the theoretical stoichiometric ratio and this can explained by the presence of iron in the precipitates which reduces the $(d\Sigma/d\Omega)_{NUC}/(d\Sigma/d\Omega)_{MAG}$ ratio.

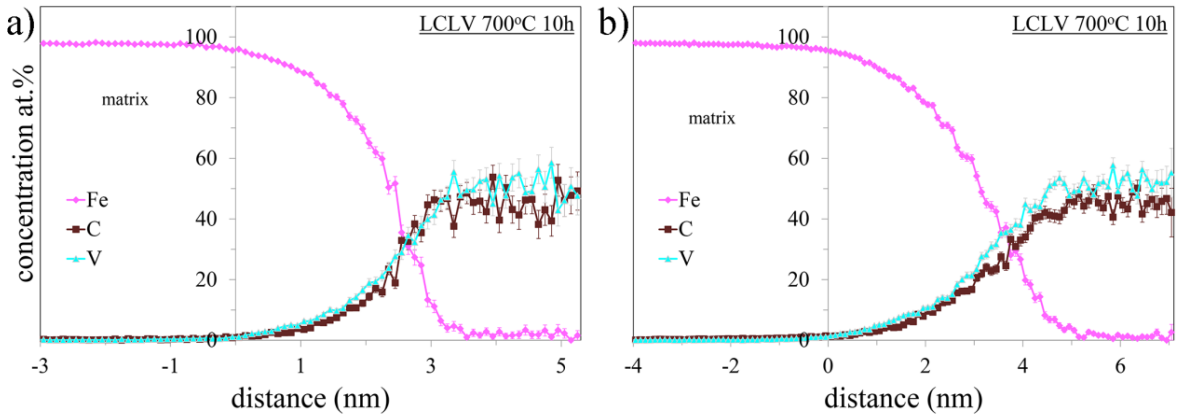

Fig. 4.11. Representative proximity diagrams of two precipitates differing in stoichiometry in the LCLV steel annealed at 700 °C for 10 h. In a), the carbon-to-metal ratio is closer to the stoichiometric ratio than in b).

The APT results confirm qualitatively the presence of a distribution of precipitates with different carbon-to-metal ratios, ranging from 0.75 to 1, in the same alloy treated at the same temperature. A quantitative analysis, which would lead to the determination of the sub-stoichiometric distribution of the precipitates, cannot be performed due to the local nature of the APT measurements which leads to limited statistics, due to the directional walk effect [43], which causes inconsistencies in the measured carbon concentration, and due to the limited effective spatial resolution of APT for small particles or precipitates [67].
The proxigrams also show that precipitates with a similar size can have different carbon-to-metal stoichiometry. This result suggests that the stoichiometry of a precipitate is not only size dependent but also a function of many other factors such as temperature, precipitate coherency, steel nominal composition and time of nucleation or growth/coarsening rate. Due to all these factors, the overall stoichiometry distribution can slightly vary during annealing. For instance, in the early stages of nucleation, iron-rich clusters coherent to the matrix are formed, which later transform into incoherent precipitates that may have different crystal structure [14],[68]. The lattice parameter and consequently the coherency of the precipitates is controlled by the solute elements fractions. During the transition from coherent to incoherent particles, the precipitate-matrix interfacial energy increases thus a larger fraction of vacancies is necessary for the precipitate stability, causing a slight gradual decrease in the carbon-to-vanadium ratio [14]. This could be an additional reason for a slight change in the precipitate stoichiometry during isothermal holding. Small inhomogeneities in the steel chemical composition or slight

temperature deviations between different specimen areas can also affect the precipitate chemical composition.
The in-situ SANS measurements are performed in a sample volume of ~10^{20} nm^3, which is approximately 14 orders of magnitude larger than the typical volume that is normally analysed by APT (~10^6 nm^3), consequently probing a larger number of precipitates and therefore providing better statistics on the chemical composition of the precipitates.

4.5. Conclusions

Our in-situ SANS investigation of the evolution of the precipitate chemical composition at 650 °C and at 700 °C in three vanadium micro-alloyed steels with different vanadium and carbon contents, provides unique insight into the time evolution of the precipitate chemical composition and opens up new possibilities for future investigations.
Our results indicate that precipitation of vanadium carbides takes place according to the following schemes. The precipitates are initially metastable with a high iron concentration and their composition gradually evolves during annealing. The initial high iron concentration in the precipitates can be explained by the ability of iron to reduce the precipitate-matrix misfit and reduce the activation energy for precipitate nucleation. The iron content in the precipitates depends on the steel composition, the annealing temperature, the precipitate size and the annealing time. The fraction of iron in the precipitate is gradually decreasing during annealing, being substituted by vanadium and leading to the formation of the vanadium carbide phase. The precipitates are sub-stoichiometric, i.e., the carbon-to-metal ratio in the precipitates is smaller than 1, possibly because the presence of carbon vacancies in their lattice can increase their stability. Addition of vanadium to the steel nominal composition leads to precipitates that are richer in vanadium and with less iron during the entire precipitation process, in case we assume that the carbon to metal ratio is given by ThermoCalc.
Faster changes in the precipitate chemical composition are observed at 700 °C in all steels because of the faster diffusion of vanadium at 700 °C than at 650 °C. At the same temperature, at 650 °C or 700 °C, an increase of both vanadium and carbon overall content accelerates the changes in the precipitate chemical composition during annealing as a result of a higher driving force for precipitation.
By in-situ SANS, the chemical composition evolution of the precipitates can be calculated in any steel irrespective of the precipitates shape and size distribution. Complementary APT measurements prove the presence of precipitates with a distribution of carbon-to-metal ratios, ranging from 0.75 to 1, after 10 h at 650 or 700 °C in all steels.

Acknowledgements

This work was supported by the Materials innovation institute M2i (www.m2i.nl), project S41.5.14548, in the framework of the M2i Partnership Program, and the Technology Foundation TTW (www.stw.nl), which is part of the Netherlands Organization for Scientific Research (www.nwo.nl). The authors greatly acknowledge the use of the Larmor beamline at ISIS (experiment number RB1869024 [69]) and the Nederlandse Organisatie voor Wetenschappelijk Onderzoek Groot grant no. LARMOR 721.012.102. The authors would like to thank Tata Steel in Europe for providing the materials as hot-rolled plates.

References

[1] European Commission, A resource-efficient Europe – Flagship initiative under the Europe 2020 strategy, COM (2011) 21.
[2] K. Seto, Y. Funakawa, and S. Kaneko, Hot rolled high strength steels for sus- pension and chassis parts “NanoHiten”and “BHT”steel, JFE Technical Report, No. 10, (2007).
[3] A. Rijkenberg, A. Blowey, P. Bellina, C. Wooffindin, Advanced high stretch-flange formability steels for chassis & suspension applications, in: Proceedings of the 4th International Conference on Steels in Cars and Trucks (SCT2014), Braunschweig (Germany), 2014, p. 426 .
[4] Y. Funakawa, T. Shiozaki, K. Tomita, T. Yamamoto, E. Maeda, Development of high strength hot-rolled sheet steel consisting of ferrite and nanometer-sized carbides, ISIJ Int. 44 (11) (2004) 1945–1951.
[5] T. N. Baker , Microalloyed steels, Ironmak. Steelmak. 43 (4) (2016) 264–307.
[6] WO2013167572 (A1), “Automotive Chassis Part Made from High Strength Formable Hot Rolled Steel Sheet”, Tata Steel.
[7] WO2014122215 (A1), A High-Strength Hot-Rolled Steel Strip Or Sheet With Excellent Formability and Fatigue Performance and a Method of Manufacturing Said Steel Strip Or Sheet, Tata Steel.
[8] EP1338665 (A1), High Tensile Hot Rolled Steel Sheet and Method For Produc- tion Thereof, JFE Steel Corporation.
[9] R. Lagneborg, T. Siwecki, S. Zajac, B. Hutchinson, The role of vanadium in microalloyed steels, Scand. J. Metall. 28 (5) (1999) 186–241.
[10] M.-.Y. Chen, M. Goune, M. Verdier, Y. Brechet, J.-.R. Yang, Interphase precipitation in vanadium-alloyed steels: strengthening contribution and morphological variability with austenite to ferrite transformation, Acta Mater. 64 (2014) 78–92.
[11] G. Miyamoto, R. Hori, B. Poorganji, T. Furuhara, Interphase precipitation of VC and resultant hardening in V-added medium carbon steels, ISIJ Int. 51 (10) (2011) 1733–1739.
[12] Y.-J. Zhang, G. Miyamoto, K. Shinbo, T. Furuhara, T. Ohmura, T. Suzuki, K. Tsuzaki, Effects of transformation temperature on VC interphase precipitation and resultant hardness in low-carbon steels, Acta Mater. 84 (2015) 375–384.
[13] Y.Q. Wang, S. J. Clark, V. Janik, R. K. Heenan, D. A. Venero, K. Yan, D.G. Mc Cartney, S. Sridhar, P.D. Lee, Investigating nano-precipitation in a V-containing HSLA steel using small angle neutron scattering, Acta Mater. 145 (2018) 84–96.
[14] J. Wang, M. Weyland, I. Bikmukhametov, M. K. Miller, P. D. Hodgson, I. Timokhina, Transformation from cluster to nano-precipitate in microalloyed ferritic steel, Scr Mater 160 (2019) 53–57.
[15] F. Danoix, E. Bémont, P. Maugis and D. Blavette, Atom Probe Tomography I. Early Stages of Precipitation of NbC and NbN in Ferritic Steels, Advanced Engineering Materials 8 (2006) No. 12, 1202-1205.
[16] R. P. Kolli and D. N. Seidman, Co-Precipitated and Collocated Carbides and Cu-Rich Precipitates in a Fe–Cu Steel Characterized by Atom-Probe Tomography, Microsc. Microanal. 20 (2014) 1727–1739.
[17] L. Wu, T. Yao, Y. Wang, J. Zhang, F. Xiao, B. Liao, Understanding the mechanical properties of vanadium carbides: Nano-indentation measurement and first-principles calculations, Journal of Alloys and Compounds 548 (2013) 60–64.
[18] W. Xing, F. Meng, R. Yu, A new type of vanadium carbide V_5C_3 and its hardening by tuning Fermi energy, Scientific Reports 6 (2016) 21794.
[19] X. Chong, Y. Jiang, R. Zhoua, J. Feng, Electronic structures mechanical and thermal properties of V–C binary compounds, RSC Adv., 4 (2014) 44959-44971.

[20] E. Nembach, Precipitation hardening caused by a difference in shear modulus between particle and matrix, Phys. Stat. Sol. (a) 78 (1984) 571-581.
[21] P. Gong, X. G. Liu, A. Rijkenberg , W. M. Rainforth , The effect of molybdenum on interphase precipitation and microstructures in microalloyed steels containing titanium and vanadium, Acta Mater 161 (2018) 374–387.
[22] Y.-J. Zhang, G. Miyamoto, K. Shinbo, T. Furuhara, Quantitative measurements of phase equilibria at migrating α/γ interface and dispersion of VC interphase precipitates: evaluation of driving force for interphase precipitation, Acta Mater. 128 (2017) 166–175.
[23] T. N. Baker, Processes, microstructure and properties of vanadium microalloyed steels, Materials Science and Technology, 25:9 (2009) 1083-1107.
[24] Y. Oba, S. Koppoju, M. Ohnuma, T. Murakami, H. Hatano, K. Sasakawa, A. Kitahara, J. Suzuki, Quantitative analysis of precipitate in vanadium-microalloyed medium carbon steels using small-angle X-ray and neutron scattering meth- ods, ISIJ Int. 51 (11) (2011) 1852–1858.
[25] T. Epicier, D. Acevedo, M. Perez, Crystallographic structure of vanadium carbide precipitates in a model Fe-C-V steel, Philos. Mag. 88 (1) (2007) 31–45.
[26] C. Ioannidou, Z. Arechabaleta, A. Navarro-López, A. Rijkenberg, R. M. Dalgliesh, S. Kölling, V. Bliznuk, C. Pappas, J. Sietsma, A. A. van Well, S. E. Offerman, Interaction of precipitation with austenite-to-ferrite phase transformation in vanadium micro-alloyed steels, Acta Mater 181 (2019) 10–24.
[27] S. Dhara, R. K. W. Marceau, K. Wood, T. Dorina, I. B. Timokhina , P. D. Hodgson, Precipitation and clustering in a Ti-Mo steel investigated using atom probe tomography and small-angle neutron scattering, Mat. Sci. Eng. A 718 (2018) 74–86.
[28] S. Dhara, R. K. W. Marceau, K. Wood b, T. Dorin, I. B. Timokhina, P. D. Hodgson, Atom probe tomography data analysis procedure for precipitate and cluster identification in a Ti-Mo steel, Data in Brief 18 (2018) 968–982.
[29] S. Jiang, H. Wang, Y. Wu, X. Liu, H. Chen, M. Yao, B. Gault, D. Ponge, D. Raabe, A. Hirata, M. Chen, Y. Wang, Z. Lu, Ultrastrong steel via minimal lattice misfit and high-density nanoprecipitation, Nature 544 (2017) 460–464.
[30] X. Zhang, C. loannidou, G. H. ten Brink, A. Navarro-López, J. Wormann, J. Campaniello, R. M. Dalgliesh, A. A. van Well, S. E. Offerman, W. Kranendonk, B. J. Kooi, Microstructure, precipitate and property evolution in cold-rolled Ti-V high strength low alloy steel, Materials and Design 192 (2020) 108720.
[31] H.-W. Yen, P.-Y. Chen, C.-Y. Hunag, J.-R. Yang, Interphase precipitation of nanometer-sized carbides in a titanium-molybdenum-bearing low-carbon steel, Acta Mater 59 (2011) 6264–6274.
[32] C. Ioannidou, Z. Arechabaleta, A. Rijkenberg, R. M. Dalgliesh, A. A . van Well, S. E. Offerman, VC-precipitation kinetics studied by small-angle neutron scattering in nano-steels, Mater. Sci. Forum 941 (2018) 236–244.
[33] M. Nöhrer, S. Zamberger, S. Primig, H. Leitner, Atom probe study of vanadium interphase precipitates and randomly distributed vanadium precipitates in ferrite, Micron 54-55 (2013) 57–64.
[34] Y. S. Shanmugam, M. Tanniru, R. D. K. Misra, D. Panda, S. Jansto, Microalloyed V–Nb–Ti and v steels part 2, precipitation behavior during processing of structural beams, Mater. Sci. Tech. 21 (2) (2005) 165–177.
[35] G. Miyamoto, R. Hori, B. Poorganji, T. Furuhara, Crystallographic analysis of proeutectoid ferrite/austenite interface and interphase precipitation of vanadium carbide in medium-carbon steel, Metall. Mater. Trans. A 44A (2013) 3436–3443.
[36] Y. Ishiguro and K. Sato, Determination of Non-Stoichiometric Composition of Complex Carbon-Nitrides in Steel by Measuring Plasmon Energy, Materials Transactions, JIM, Vol. 37, No. 4 (1996), 643-649.

[37] C. E. I. C. Öhlund, J. Weidow, M. Thuvander, S. E. Offerman, Effect of Ti on evolution of microstructure and hardness of martensitic fe–c–mn steel during tempering, ISIJ Intern. 54 (12) (2014) 2890–2899.
[38] Y.-J. Zhang, G. Miyamoto, K. Shinbob, T. Furuhara, Effects of α/γ orientation relationship on VC interphase precipitation in low-carbon steels, Scr Mater 69 (2013) 17–20.
[39] E. A. Marquis, J. M. Hyde, Applications of atom-probe tomography to the characterization of solute behaviours, Mater. Sci. Eng. R 69 (2010) 37–62.
[40] F. L. Alcântara, R. Barbosa, M. A. Cunha, Study of aluminum nitride precipitation in Fe-3%Si steel, Mater. Res. 16 (2013) 1039–1044.
[41] J. Lu, J. B. Wiskel, O. Omotoso, H. Henein, D. G. Ivey, Matrix dissolution techniques applied to extract and quantify precipitates from a microalloyed steel, Metall. Mater. Trans. A Phys. Metall. Mater. Sci. 42 (2011) 1767–1784.
[42] A. L. Rivas, E. Vidal, D. K. Matlock, J. G. Speer, Electrochemical extraction of microalloy carbides in Nb-steel, Rev. Metal. 44 (2008) 447–456.
[43] B. Gault, F. Danoix, K. Hoummada, D. Mangelinck, H. Leitner, Impact of directional walk on atom probe microanalysis, Ultramicroscopy 113 (2012) 182–191.
[44] F. Perrard, A. Deschamps, F. Bley, P. Donnadieua, P. Maugis, A small-angle neutron scattering study of fine-scale NbC precipitation kinetics in the a-Fe–Nb–C system, J. Appl. Cryst. 39 (2006) 473–482.
[45] N.H. van Dijk , S. E. Offerman , W. G. Bouwman , M. Th. Rekveldt , J. Sietsma, S. van der Zwaag, A. Bodin, R.K. Heenan, High Temperature SANS experiments on Nb(C,N) and MnS precipitates in HSLA steel, Metall. Mater. Trans. A 33 (2002) 1883–1891.
[46] Wiedenmann, Small angle scattering investigations of magnetic nanostructures, in: T. Chatterji (Ed.), Neutron Scattering from Magnetic Materials, Elsevier, 2006, pp. 473–519 .
[47] T. H. Simma, L. Sunb, D. R. Galvina, E. P. Gilbertc, D. A. Venerof, Y. Lia, T.L. Martine, P. A. J. Bagote, M.P. Moodye , P. Hilld , H. K. D. H. Bhadeshia , S. Biroscaa, M. J. Rawsond, K.M. Perkins, A SANS and APT study of precipitate evolution and strengthening in a maraging steel, Mater. Sci. Eng. A 702 (2017) 414–424.
[48] B. S. Seong, E. Shin, S. Choi, Y. Choi, Y. S. Han, K. H. Lee, Y. Tomota, Quantitative analysis of fine nano-sized precipitates in low-carbon steels by small angle neutron scattering, Appl. Phys. A 99 (2010) 613–620.
[49] J. O. Andersson, T. Helander, L. Höglund, P. F. Shi, B. Sundman, Thermo-Calc and Dictra, Comp. Tools Mater. Sci. Calphad 26 (2002) 273–312.
[50] A. Navarro-López, C. Ioannidou, E. van der Wal, Z. Arechabaleta, R. van der Oever, M. Verleg, R. Dalgliesh, J. Sykora, F. Akeroyd, J. Sietsma, C. Pappas, A. A. van Well, S. E. Offerman, Furnace for In-situ and Simultaneous Studies of Nano-Precipitates and Phase Transformations in Steels with by SANS and Neutron Diffraction, to be submitted to Review of Scientific Instruments.
[51] O. Arnold, J. C. Bilheux, J. M. Borreguero, A. Buts, S. I. Campbell, L. Chapon, M. Doucet, N. Draper, R. Ferraz Leal, M. A. Gigg, V. E. Lynch, A. Markvardsen, D. J. Mikkelson, R. L. Mikkelson, R. Miller, K. Palmen, P. Parker , G. Passos , T. G. Perring, P. F. Peterson, S. Renc, M. A. Reuter, A. T. Savici, J. W. Taylor, R. J. Taylor, R. Tolchenov, W. Zhou, J. Zikovsky, Mantid-Data analysis and visualization package for neutron scattering and μsr experiments, Nuc. Inst. Meth. Phys. Res. A 764 (2014) 156–166.
[52] D. J. Larson, D. T. Foord, A. K. Petford-Long, T. C. Anthony, I. M. Rozdilsky, A. Cerezo, G. W. D. Smith, Focused ion-beam milling for field-ion specimen preparation: preliminary investigations, Ultramicroscopy 75 (1998) 147–159.
[53] M. Thuvander, J. Weidow, J. Angseryd, L. K. Falk, M. Sonestedt, K. Stiller, H. O. Andrén, Quantitative atom probe analysis of carbides, Ultramicroscopy 111 (2011) 604-608.

[54] R. Córdoba, N. Sharma, S. Kölling, P.M. Koenraad, B. Koopmans, High-purity 3D nano-objects grown by focused-electron-beam induced deposition, Nanotechnology 27 (2016) 355301.
[55] P. Bas, A. Bostel, B. Deconihout, D. Blavette, A general protocol for the reconstruction of 3D atom probe data, Applied Surface Science 87/88 (1995) 298-304.
[56] T. Narayanan, Synchrotron small-angle X-Ray scattering, in: R. Borsali, R. Pec- ora (Eds.), Soft-Matter Characterization, Springer, 2008, pp. 899–948.
[57] L. A. Feigin, Structure Analysis by Small-Angle X-ray and Neutron Scattering, New York, 1987.
[58] E. K. Storms and C. P. Kempter, Thermal Expansion of Some Vanadium Carbides, Chem. Phys. 42 (1965) 2043-2045.
[59] M. Onink, C. M. Brakman, F. D. Tichelaar, E. J. Mittemeijer, S. van der Zwaag, J. H. Root, N. B. Konyer, The lattice parameters of austenite and ferrite in Fe-C alloys as functions of carbon concentration and temperature, Scr Metala et Mater Vol. 29, Issue 8 (1993) 1011-1016.
[60] Z. Sun, R. Ahuja, J. E. Lowther, Mechanical properties of vanadium carbide and a ternary vanadium tungsten carbide, Solid State Communications 150 (2010) 697-700.
[61] V. F. Sears, Neutron scattering lengths and cross sections, Neutron News, 3:3 (1992) 26-37.
[62] A. S. Arrott and B. Heinrich, Application of magnetization measurements in iron to high temperature thermometry, Journal of Applied Physics 52 (1981) 2113-2115.
[63] Y.-J. Zhang, G. Miyamoto, K. Shinbo, T. Furuhara, Weak influence of ferrite growth rate and strong influence of driving force on dispersion of VC interphase precipitation in low carbon steels, Acta Materialia 186 (2020) 533-544.
[64] H. Sharma, J. Sietsma, S. E. Offerman, Preferential Nucleation during Polymorphic Transformations, Scientific Reports 6 (2016) 30860.
[65] S. E. Offerman, N. H. van Dijk, J. Sietsma, S. van der Zwaag, E. M. Lauridsen, L. Margulies, S. Grigull, H. F. Poulsen, Reply to the discussion by Aaronson et al. to ‘‘Grain nucleation and growth during phase transformations’’ by S.E. Offerman et al., Science, 298, 1003 (November 1, 2002), Scr Mater 51 (2004) 937–941.
[66] O. C. Hellman , J. A. Vandenbroucke, J. Rusing, D. Isheim, D. N. Seidman, Analysis of three-dimensional atom-probe data by the proximity histogram, Microsc. Microanal. 6 (2000) 437–444.
[67] F. De Geusera, B. Gault, Metrology of small particles and solute clusters by atom probe tomography, Acta Mater 188 (2020) 406-415.
[68] H. Sawada, S. Taniguchi, K. Kawakami, T. Ozaki, Transition of the Interface between Iron and Carbide Precipitate From Coherent to Semi-Coherent, Metals 7 (2017) 277.
[69] S. E. Offerman, E. van der Wal, A. A. van Well, A. Navarro-López, C. Ioannidou, R. M. Dalgliesh, (2019): In-situ and simultaneous SANS and ND to study the precipitation and phase transformation kinetics in V-containing Nano-steels, STFC ISIS Neutron and Muon Source, https://doi.org/10.5286/ISIS.E.RB1869024.

Chapter 5 - Phase-transformation and precipitation kinetics in vanadium micro-alloyed steels by in-situ simultaneous neutron diffraction and SANS

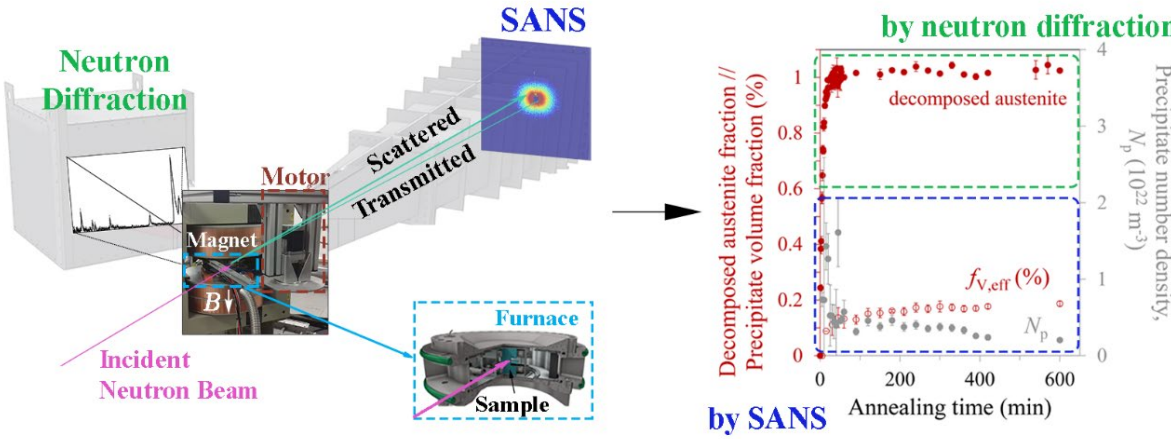

Abstract

In-situ Neutron Diffraction and Small-angle Neutron Scattering (SANS) are employed for the first time simultaneously in order to reveal the interaction between the austenite to ferrite phase transformation and the precipitation kinetics during isothermal annealing at 650 °C and at 700 °C in three steels with different vanadium (V) and carbon (C) concentrations. Austenite-to-ferrite phase transformation is observed in all three steels at both temperatures. The phase transformation is completed during a 10 h annealing treatment in all cases. The phase transformation is faster at 650 °C than at 700 °C for all alloys. Additions of vanadium and carbon to the steel composition cause a retardation of the phase transformation. The effect of each element is explained through its contribution to the Gibbs free energy dissipation. The austenite-to-ferrite phase transformation is found to initiate the vanadium carbide precipitation and the effect of the precipitation on the phase-transformation kinetics is discussed as well. Larger and fewer precipitates are detected at 700 °C than at 650 °C in all three steels, and a larger number density of precipitates is detected in the steel with higher concentrations of vanadium and carbon. After 10 h of annealing, the precipitated phase does not reach the equilibrium fraction as calculated by ThermoCalc. The external magnetic field applied during the experiments, necessary for the SANS measurements, causes a delay in the onset and time evolution of the austenite-to-ferrite phase transformation and consequently on the precipitation kinetics.

Reproduced from: "C. Ioannidou, A. Navarro-López, R. M. Dalgliesh, A. Rijkenberg, X. Zhang, B. Kooi, N. Geerlofs, C. Pappas, J. Sietsma, A. A. van Well, S. E. Offerman, "Phase-transformation and precipitation kinetics in vanadium micro-alloyed steels by in-situ, simultaneous neutron diffraction and SANS", Acta Materialia 220 (2021) 117317."

5.1. Introduction

Micro-alloyed steels containing nanometer-sized precipitates in a ferrite matrix have recently attracted a lot of interest due to their high performance when being used in lightweight automotive parts [1]–[4]. The combination of high strength, due to the presence of the precipitates, and ductility, originating from the ferritic matrix, makes their use promising in automotive applications, as these materials substantially reduce energy consumption and consequently CO_2 emission levels.

Vanadium carbide precipitates cause precipitation strengthening of steels [2], [5], [6]. Therefore, several studies have been focused on the microstructure and mechanical behavior of various steels that contain such precipitates and have undergone different treatments [5], [7]–[10]. Vanadium carbide precipitation takes place either during the austenite-to-ferrite phase transformation at the migrating austenite/ferrite interface, or in the ferrite phase. The former is called interphase precipitation. The vanadium and carbon solubility is high in austenite but low in the ferrite phase, and their solubility drop when austenite transforms to ferrite drives the interphase precipitation [6]. Understanding the vanadium carbide precipitation and its interaction with the austenite-to-ferrite phase transformation are key factors for achieving an optimum performance of lightweight steels, while minimizing the use of vanadium as alloying element.

The steel composition and the applied thermal treatment determine the vanadium carbide precipitation features. At a temperature range from 600 °C to 700 °C, the composition of the vanadium carbides can be VC, $VC_{0.9}$, V_4C_3, V_6C_5 [5], [7], [10]–[13], while the precipitates may also contain iron (Fe) [14] or manganese (Mn) [15]. These vanadium carbides have been observed as spheres, ellipsoids, disks, rods, needles or cuboids [7]–[12], [16]–[18]. Their nucleation is favorable at non-KS (Kurdjumov-Sachs) ferrite/austenite interfaces [19], [20], while they mainly have a Baker-Nutting orientation relation with the ferritic matrix [5].

Transmission Electron Microscopy (TEM), Atom Probe Tomography (APT) and several spectroscopy techniques have been used to characterize the precipitates [8]–[10], [12]–[16], [18]–[23]. Nevertheless, the results obtained by these techniques have to be complemented by other types of measurements in order to obtain more accurate statistical information. Moreover, TEM and APT cannot be used to follow the precipitation kinetics in-situ during an applied heat-treatment. These limitations can be overcome by Small-angle Neutron Scattering (SANS), which is a non-destructive technique for quantitative precipitation characterization in steels, allowing in-situ analysis and providing information from a more statistically representative volume. However, a quantitative analysis of the SANS data requires input from other techniques such as TEM and APT, which can thus complement the SANS measurements.

Interphase precipitation during the austenite-to-ferrite phase transformation has been studied by ex-situ SANS at room temperature in previously heat-treated vanadium micro-alloyed steels, while TEM and APT have been used to reveal the precipitate shape, size and chemical composition, supporting the SANS data analysis [10], [16], [17]. In these ex-situ SANS experiments, the precipitate evolution during the austenite-to-ferrite phase transformation is measured using a series of samples that have been annealed for different holding times followed by rapid cooling to room temperature. Therefore, these samples consist of complex microstructures with different ferrite, martensite and precipitate fractions. Consequently, it is challenging to accurately separate the precipitate signal from the strong signal arising from the dislocations of the martensite [16].

In the present study we chose to perform in-situ SANS measurements in steels as this approach offers the following major advantages. a) The precipitation kinetics can be measured real-time. b) The SANS signal from the dislocations in the martensite is avoided since martensite is not present at the high annealing temperatures (>higher than 600 °C). As a result, the SANS signal

from the precipitates can be more easily isolated. c) A SANS background signal can be determined, i.e. a SANS signal from a steel matrix without the presence of precipitates. This background signal can be obtained when measuring at the soaking temperatures that are normally applied in this kind of steels before the isothermal annealing treatments. The soaking temperatures are chosen to be higher than the precipitate dissolution temperatures to assure the absence of any precipitates. The advantages of in-situ SANS are manifold and in a recent study we employed the most of them by monitoring the evolution of the precipitate composition in vanadium micro-alloyed steels during annealing at either 650 or 700 °C [14].
The precipitation is closely related to the austenite-to-ferrite phase transformation and the investigation of the interplay between these two phenomena requires measuring the phase-transformation kinetics together with the precipitation kinetics. This can be achieved by combining in-situ SANS with neutron diffraction (ND), which can be used for phase identification and quantification. As will be discussed in the following, the combination of in-situ SANS and ND offers several advantages over other types of measurements of phase transformation and precipitation. Nevertheless, such a combination has not been reported in the literature so far and in this respect our study sets the direction for future investigations.
In the present study, in-situ and simultaneous ND and SANS measurements are performed in steel samples, which are being heat-treated in a furnace. The aim of our study is to provide real-time quantitative information on the interplay between austenite-to-ferrite phase transformation and the vanadium carbide precipitation kinetics in low-carbon steels. These steels have different vanadium and carbon contents and have been heat-treated at different isothermal annealing temperatures (650 or 700 °C). The effects of the annealing temperature and the different vanadium and carbon additions to the steel composition on the phase transformation and precipitation kinetics are investigated. TEM is used to support the SANS data analysis by providing information on the precipitate size and shape.
During the SANS measurements, an external magnetic field of 1.5 T is applied in order to magnetically saturate the steel specimens. In this way we suppress the magnetic-domain scattering and separate the nuclear and the magnetic SANS components, allowing for a quantitative analysis of the precipitation kinetics. The ND measurements show that this external magnetic field affects the phase-transformation kinetics. We thus deduce that the magnetic field would eventually also affect the precipitation kinetics. These observations are supported by in-situ magnetometer measurements, which also reveal a modification of the austenite-to-ferrite phase-transformation kinetics when an external magnetic field is applied.
Based on the experimental findings, first the phase-transformation kinetics in the different steels is analyzed, and the delay in the transformation kinetics due to the external magnetic field is presented. Next, the precipitation kinetics is quantified and finally the coupling between phase transformation and precipitation kinetics is explained.

5.2. Experimental

The phase-transformation and precipitation kinetics are studied in three vanadium micro-alloyed steels with different vanadium and carbon contents. The model alloys were provided by Tata Steel in Europe and their chemical composition is given in Table 5.1. We refer to these steels as LCLV (low carbon - low vanadium alloy), LCHV (low carbon - high vanadium alloy) and HCHV (high carbon - high vanadium alloy). The high vanadium alloys have twice the concentration of vanadium of the low vanadium one and the high carbon alloy has twice the concentration of carbon compared to the low carbon ones. The atomic ratio of vanadium to carbon is close to 1 in the LCLV and HCHV steels and close to 2 in the LCHV alloy. The manganese concentration is the same in all alloys and the concentration of the other elements

is as low as possible. The choice of these steel compositions aims to elucidate and disentangle the effects of vanadium and carbon on the phase-transformation and the precipitation kinetics.

Table 5.1. Chemical composition of the investigated steels in wt.% and at.% with balance Fe.

Steel		C	Mn	V	Si	P	Cr	Al
LCLV	wt.%	0.071	1.84	0.29	0.010	0.0010	0.010	0.004
	at.%	0.330	1.86	0.32	0.026	0.0018	0.011	0.008
LCHV	wt.%	0.075	1.83	0.57	0.014	0.0010	0.006	0.006
	at.%	0.350	1.85	0.62	0.028	0.0018	0.011	0.012
HCHV	wt.%	0.140	1.83	0.57	0.013	0.0010	0.007	0.008
	at.%	0.620	1.85	0.62	0.026	0.0018	0.007	0.002

The steel alloys were provided as 3 mm thick hot-rolled plates. I-shaped specimens were machined from the center of the plates and are 1 mm thick. The specimen dimensions are chosen so that they fit in a furnace [24] employed for applying the heat-treatments to the specimens during the in-situ ND and SANS measurements. This furnace uses radiation heating from molybdenum-lanthanum wires and helium gas for cooling. K-type thermocouples are used for temperature control of the specimens.
The thermal cycles followed during the in-situ and simultaneous ND and SANS measurements are shown in Fig. 5.1. The steels are heated up to T_D = 1050 °C (for LCLV specimens) or 1100 °C (for LCHV and HCHV specimens) with a rate of 5 °C/s and held at this temperature for 15 min. These temperatures are ~50 °C higher than the precipitate dissolution temperatures of each steel according to ThermoCalc [25] calculations (see Table 5.5). At these temperatures the steels are fully austenitic and all elements are in solid solution. The specimens are afterwards cooled to 650 °C or 700 °C with a cooling rate of about 15 °C/s. The austenite-to-ferrite phase transformation and precipitation are followed during a 10-hour isothermal annealing treatment at these temperatures. Finally, the samples are cooled to room temperature.

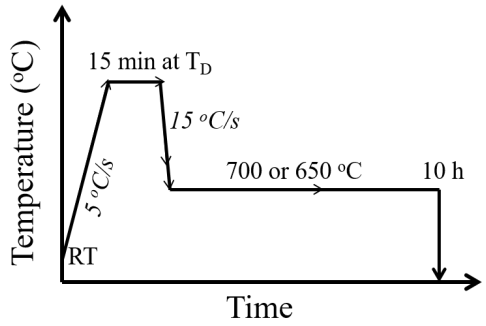

Fig. 5.1. Thermal cycles applied during the in-situ simultaneous ND and SANS measurements.

The in-situ and simultaneous ND and SANS measurements are performed at the Larmor Instrument [26] at the ISIS Neutron and Muon Source, STFC Rutherford Appleton Laboratory, UK [27]. The experimental set up is schematically shown in Fig. 5.2. The furnace operates between the pole shoes of a 3473-70 GMW magnet, which is used to generate a vertical magnetic field of 1.5 T (strong enough to magnetically saturate the specimens) perpendicular to the neutron beam. The furnace is rotating around its vertical axis in order to minimize possible texture effects induced by the materials history, i.e., from the hot-rolling process.
All contributions to the signal that do not come from the sample are subtracted from the data. These contributions are determined through additional ND and SANS measurements performed with an empty furnace (without sample but including all other parts, e.g. heat-shields, etc.) at room temperature while rotating it. The SANS data is normalized to absolute

units using the scattering from a reference polymer sample which is a solid blend of hydrogenous and perdeuterated polystyrene. The ND as well as the SANS raw data reduction is performed using the Mantid framework [28].
The size of the incident neutron beam is 8x8 mm^2 and the wavelength range for the SANS measurements is 0.42-1.33 nm. The SANS detector is a 600×600 mm^2 ^{3}He tube array with an 8×8 mm^2 pixel size, located at 4.3 m from the sample. The scintillator ND detector [29] consists of 128 pixels and is placed on one side of the sample at a distance of 1.15 m from the sample. The ND detector measures d-spacing values from 0.07-0.3 nm over a diffraction angle range from 49.5 to 76.5º, which corresponds to a wavelength range of 0.11-0.58 nm. Further information on the sample environment and the equipment is given in Ref. [24].
The event-mode data acquisition of the Larmor instrument records both ND and SANS scattering events. Using this mode, each neutron event that is detected has its own time stamp. This allows the re-binning of the data over preferred time slices to be determined after the measurements. Long-time slices provide better statistics and short-time slices a higher temporal resolution of the measured phenomena. Due to the fact that the first hour is more critical for the phase transformation kinetics, 1-min consecutive time slices are chosen during the first hour of annealing and, 5-min time slices every 30 min of measurement time for annealing times longer than 1 hour for the ND data ordering. For SANS, 5-min consecutive time slices are chosen during the first hour of annealing and 30-min consecutive time slices for annealing times longer than 1 hour.

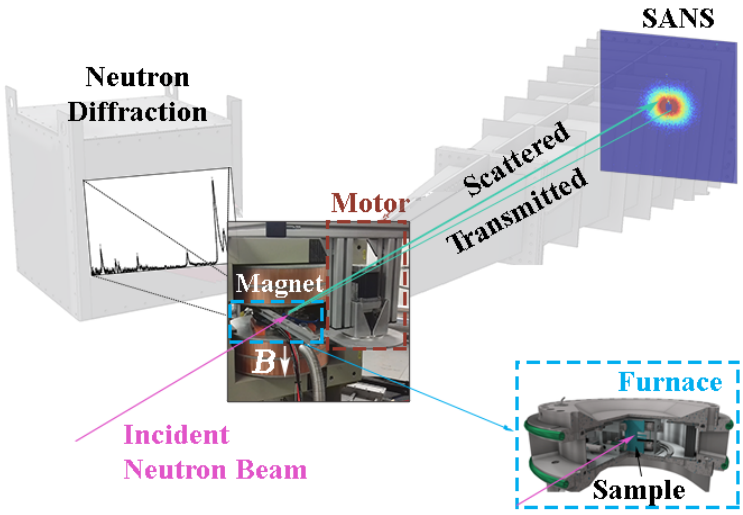

Fig. 5.2. Experimental set up of the in-situ simultaneous ND and SANS.

TEM is used to support the SANS data analysis as it provides complementary information on the precipitate size and shape. The specimens for TEM are heat-treated in a DIL-805 A/D dilatometer using inductive heating under a pressure of 10^{-2} mbar and cooling by helium gas. They have rectangular shapes with dimensions 14×10×1 mm^3. The same thermal cycles as the ones shown in Fig. 5.1 are applied for all TEM steel samples, with the temperature controlled by an S-type thermocouple spot-welded in the center of the specimen. Samples of all steels have undergone another heat-treatment consisting of heating them up to the soaking temperature, T_D, and then directly quenching them to room temperature. These samples are used to determine the Prior Austenite Grain Size (PAGS).
A JEOL 2010 Transmission Electron Microscope with an accelerating voltage of 200 kV is used for the TEM investigations. Thin foils were prepared for the TEM analysis. 3 mm diameter discs were first extracted from the annealed samples and then ground to 80 μm thickness using

a Gatan disc grinder. Electrochemical polishing was performed in a solution of 5% perchloric acid (HClO4) and 95% acetic acid at 15 °C and a voltage of 25 V with Struers Tunepol 3.
As mentioned above, we have found that the magnetic field applied during the in-situ SANS and ND measurements affects the austenite-to-ferrite phase-transformation kinetics. This effect is prominent when comparing the phase-transformation kinetics observed by dilatometry and neutron diffraction. This effect is further investigated by in-situ magnetization measurements during isothermal annealing treatments, using a 7307 vibrating sample magnetometer calibrated with a National Institute of Standards and Technology (NIST) nickel specimen. The samples have a rectangular parallelepiped shape of 2×2×1 mm^3 (mass 54.8 mg) and are machined from the center of heat-treated dilatometry specimens. A custom made furnace, that can heat the samples up to ~900 °C, is used to apply the required heat-treatments and is placed between the poles of the magnet. The magnetization curves are obtained during a similar thermal cycle under a magnetic field of 1.6 T.

5.3. Phase transformation kinetics
5.3.1. Neutron Diffraction data analysis

Neutron diffraction patterns obtained during the thermal cycle allow for a quantitative analysis of the phase-transformation kinetics during the isothermal annealing stage of the thermal treatment.
During cooling from the soaking temperature to the isothermal annealing temperature, thus before the isothermal holding, the ND patterns do not show any indication of phase transformation. Our quantitative analysis of the phase transformation during the isothermal holding focuses on the time evolution of the ND peak positions and intensities. The peak positions allow the identification of the existent phases while the relative peak intensities (area under the diffraction peaks) are used to determine the fraction of each phase at a specific moment of the annealing (duration of time slice). An example of the time evolution of the diffraction peaks of α-Fe (ferrite) and γ-Fe (austenite) during the first hour of isothermal annealing of the HCHV steel at 650 °C is presented in Fig. 5.3. During annealing, austenite is transforming to ferrite since the peak area of the austenitic peaks is decreasing while the area below the ferrite peaks is increasing. All plots that illustrate the time evolution of the ferrite (α-Fe) and austenite (γ-Fe) diffraction peaks in the LCLV, LCHV and HCHV steels annealed at 650 and 700 °C are provided in Appendix C (Fig. C2).

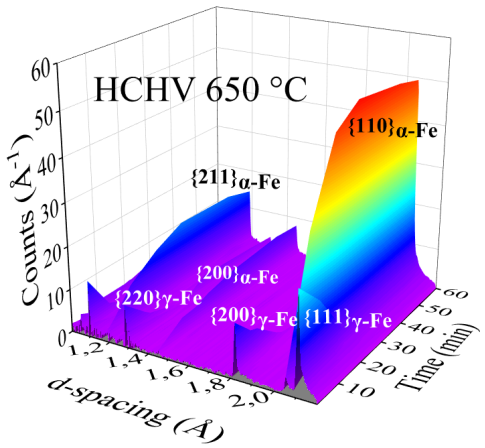

Fig. 5.3. Time evolution of the diffraction peaks of α-Fe and γ-Fe during the first hour of isothermal annealing of the HCHV steel at 650 °C. The most intense peaks are marked.

In order to obtain the peak areas and positions, we fit the ND peaks using a back-to-back exponential function, which it is the most appropriate function for the analysis of time-of-flight diffraction data [30], and accounts for the non-symmetric peak shape arising from pulse shape of ISIS' second target station. The function is calibrated using Si and NaCaAlF standards. In

total five ferritic and three austenitic peaks are fitted. Other peaks, such as the austenitic peaks of {311} and {222} families, are excluded from the calculations because their intensities are very low and comparable to the background. Fig. 5.4 shows, as an example, the resulting peak fitting of the diffraction peaks of the LCLV sample during the first minute of annealing at 650 °C, after subtraction of the background. The red line is the fitting result and the experimental points are shown in black.

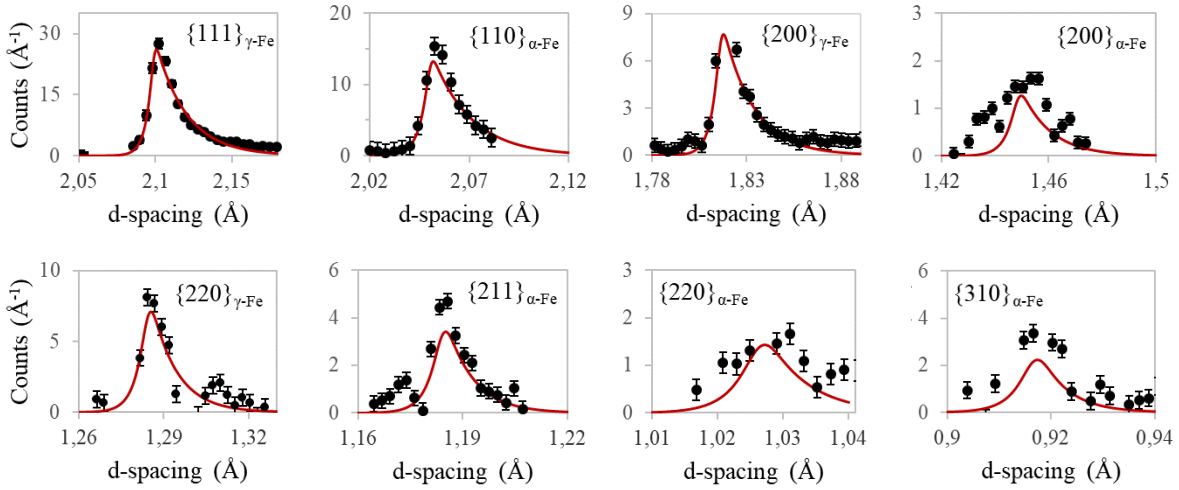

Fig. 5.4. Peak fitting of the diffraction peaks, yielding both their position and intensity, of the LCLV steel during the 1st minute of annealing at 650 °C.

Fitting this model yields the peak area and position (d-spacing where the peak intensity is maximum) of the eight peaks of interest for each pattern (each time-slice). By applying this fitting during the entire annealing time, the evolution of the peak area of all peaks is obtained. The area of each ferritic peak is afterwards normalised to the maximum area of this particular peak (obtained for each ferrite peak after phase transformation completion). The peak area of each austenitic peak is also normalised to its maximum (obtained in the beginning of the isothermal annealing). Fig. 5.5 shows the time evolution of the normalized peak intensities for 5 peaks in the LCLV steel annealed at 650 °C. The data is rather noisy due to counting statistics. Nevertheless, the trend of the peak area evolution with time is the same in all steels, which brings us to the conclusion that the specific texture in the samples does not affect the derived transformed fraction.

For the final calculation of the phase fraction of ferrite formed during each individual time-slice, the weighted average of the area fraction evolution of the normalised ferrite and 1-(normalised austenite) (Fig. 5.5) peak areas is calculated.

The lattice parameters of austenite and ferrite at 650 and 700 °C are obtained from the positions of the diffraction peaks corresponding to each phase. The lattice parameter of each phase at a certain temperature is the average value of the lattice parameters calculated from the positions of the measured peaks of this phase, averaged also over the annealing period that this phase is present. The resulting austenite lattice parameter is $a_{\gamma\text{-Fe}} = 0.364 \pm 0.006$ nm and the ferrite lattice parameter is $a_{\alpha\text{-Fe}} = 0.290 \pm 0.001$ nm. The effect of temperature on the lattice parameter of each phase is not detected since the 2 temperatures are very close.

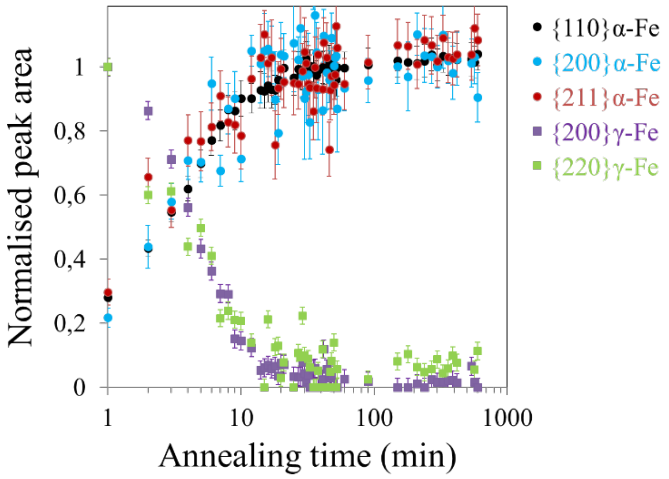

Fig. 5.5. Time evolution of the normalized peak intensity area for 3 ferritic and 5 austenitic peaks for the LCLV steel annealed at 650 °C.

5.3.2. Neutron Diffraction results and discussion

The phase transformation kinetics derived from the neutron diffraction data analysis of the LCLV, LCHV and HCHV steels at the two annealing temperatures of 650 °C and 700 °C is presented in Figs. 5.6a and b. The graphs in Figs. 5.6c and d depict enlarged parts of the plots of Fig. 5.6a and b, respectively, showing the phase-transformation kinetics during the first hour of annealing. Austenite-to-ferrite phase transformation takes place in all steels at both temperatures since the isothermal annealing temperature is lower than the A_3 temperature of these steels (Table 5.3). In all cases, the phase transformation is completed during the 10 h annealing treatment.

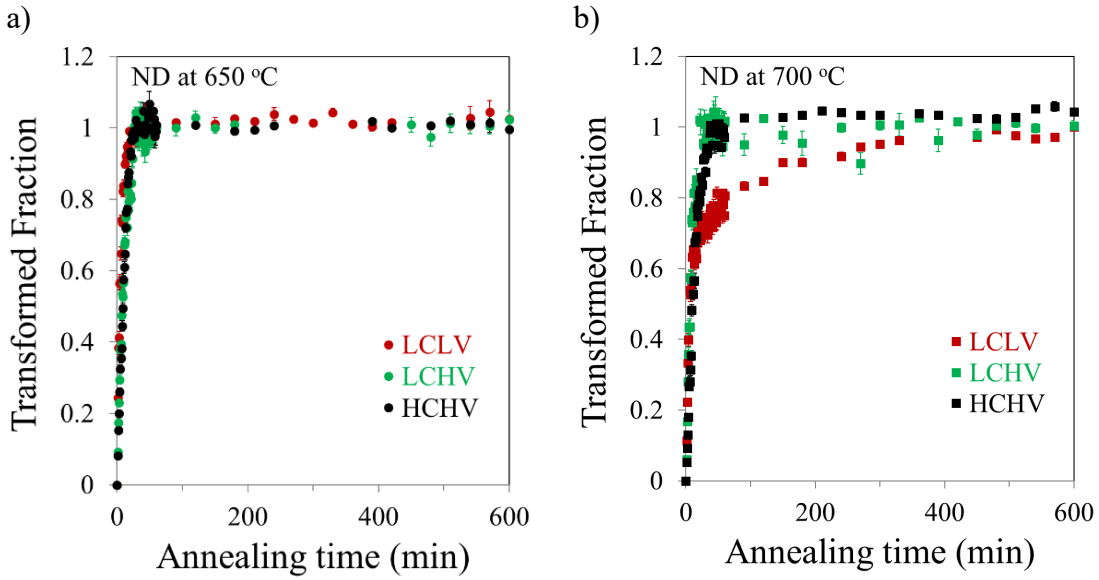

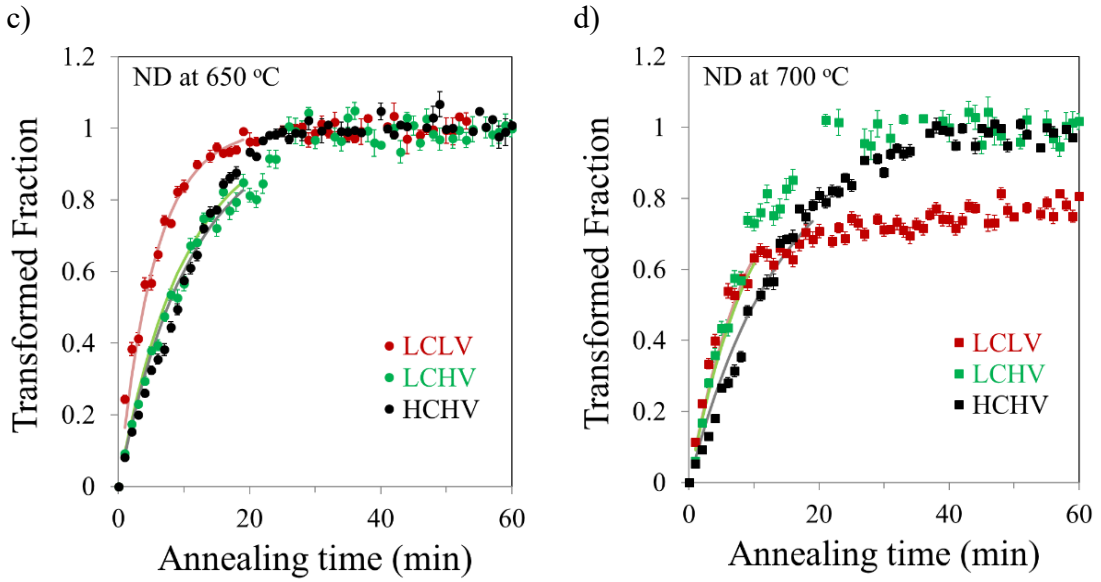

Fig. 5.6. Time evolution of the transformed austenite fraction in the LCLV, LCHV and HCHV steels at a) 650 °C and b) 700 °C. The graphs in Figs. c and d are enlarged parts of the plots of Fig. a and b, respectively, showing the phase transformation kinetics during the first hour of annealing. The solid lines in each curve are the fits of the phase transformation kinetics during the first minutes of annealing with Eq. (5.1).

According to the Kolmogorov-Johnson-Mehl-Avrami (KJMA) equation [31], the transformed phase fraction f as a function of annealing time t is given by:

$$f(t) = 1 - \exp\left(-A \cdot t^{n}\right), \tag{5.1}$$

with A the rate constant, which contains information on the nucleation and growth characteristics, and n the Avrami exponent. Cahn et al. [32] report that for site-saturated phase transformations on grain surfaces n =1 and Eq. (5.1) can be written as:

$$f(t) = 1 - \exp\left(-A \cdot t\right), \tag{5.2}$$

where $A = 2 \cdot B \cdot v$, with B the grain surface-to-volume ratio (in m^{-1}) and v a constant growth rate. According to Chen et al. [18], the increase in the ferrite fraction, f_α, can be calculated from the relation:

$$\mathrm{d}f_a = \frac{\upsilon_{\alpha\gamma}}{d_\gamma}\mathrm{d}t \;\Rightarrow\; \upsilon_{\alpha\gamma} = \frac{\mathrm{d}f_a}{\mathrm{d}t} d_\gamma, \tag{5.3}$$

where $\upsilon_{\alpha\gamma}$ is the overall austenite/ferrite interface velocity and d_γ is half the prior austenite grain size.

In order to quantify and understand the phase-transformation kinetics of the three alloys during annealing at 650 °C and 700 °C, the phase transformation curves plotted in Figs. 5.6c and d are fitted to Eq. (5.2). The fits are performed on the data of the first 10 or 20 min of the isothermal annealing, depending on the steel composition and annealing temperature, because this is the period during which more than half of the austenite is transformed to ferrite (see Figs. 5.6c and

d). The quality of the fits is highlighted by the agreement between the (fitted) solid lines and the experimental data points shown in Figs. 5.6c and d. For these fits, we use n =1, a value which is consistent with the data and indicates that all samples undergo a site-saturated phase transformation on grain surfaces with a constant growth rate [32]. This fitting procedure thus leads to the determination of the A value for each sample. The interface velocity $\upsilon_{\alpha\gamma}$ which reflects the speed of the austenite-to-ferrite phase transformation is calculated from Eq. (5.3) as the product of the A value with the half of the prior austenite grain size, d_γ. d_γ is experimentally measured from the dilatometry treated samples heated up to the soaking temperature and directly quenched to room temperature. The results are summarized in Table 5.2.

Table 5.2. The parameter, A, of the phase transformation curves, half the PAGS, d_γ, and the obtained austenite/ferrite interface velocity, $\upsilon_{\alpha\gamma}$, for the three steels at two annealing temperatures, obtained by the fits of the in-situ ND patterns.

	Annealing T (°C)	***A*** **(min^{-1})**	**PAGS (µm)**	$\boldsymbol{d_\gamma}$ **(µm)**	$\boldsymbol{\upsilon_{\alpha\gamma}}$ **(µm/s)**
LCLV	650	0.114 ± 0.013	63 ± 3	31.5 ± 1.5	0.060 ± 0.007
	700	0.101 ± 0.012	63 ± 3	31.5 ± 1.5	0.053 ± 0.007
LCHV	650	0.096 ± 0.002	66 ± 2	33 ± 1	0.053 ± 0.002
	700	0.096 ± 0.011	66 ± 2	33 ± 1	0.053 ± 0.006
HCHV	650	0.090 ± 0.008	62 ± 2	31 ± 1	0.047 ± 0.005
	700	0.070 ± 0.002	62 ± 2	31 ± 1	0.036 ± 0.001

In an attempt to understand the phase-transformation kinetics in the three steels at 650 °C and 700 °C, in the following we consider resolving the combined effects of vanadium and carbon as well as the effect of the precipitates on the velocity of the austenite/ferrite interface, $\upsilon_{\alpha\gamma}$. $\upsilon_{\alpha\gamma}$ is described by the equation [33]:

$$\upsilon_{\alpha\gamma} = M \cdot \Delta G_{\text{net}} \ , \tag{5.4}$$

where ΔG_{net} is the total driving force for the phase transformation and M is the intrinsic mobility of the interface without taking into account the solute drag effect. The interface mobility is expressed as [34]:

$$M = M_{\text{o}} \cdot \exp\left(-\frac{Q_{\text{o}}}{\text{R}T}\right), \tag{5.5}$$

where M_{o} is a pre-exponential factor, Q_{o} is the activation energy for the transfer of atoms across the interface and R is the gas constant (8.31 J mol^{-1} K^{-1}).
The total driving force for the phase transformation, ΔG_{net}, is the chemical driving force for phase transformation in the beginning of annealing reduced by the dissipation of Gibbs energy caused a) by the diffusion of the solute atoms, i.e. vanadium, carbon and manganese, being dragged along with the migrating interface: $\Delta G_{\text{diss}}{}^{\text{V}}$, $\Delta G_{\text{diss}}{}^{\text{C}}$ and $\Delta G_{\text{diss}}{}^{\text{Mn}}$, respectively, and b) by the Zener pinning force, P_{z}, caused by the precipitates. The net difference in Gibbs free energy available to drive the γ/α interface against the interface friction is:

$$\Delta G_{\text{net}} = \Delta G_{\text{chem}} - \Delta G_{\text{diss}}^{\text{V}} - \Delta G_{\text{diss}}^{\text{C}} - \Delta G_{\text{diss}}^{\text{Mn}} - P_{\text{z}} \, . \tag{5.6}$$

ΔG_{chem} is obtained for each steel at a certain temperature using the ThermoCalc software. Furthermore, the precipitate Zener pinning force can be calculated from [35]:

$$P_{\text{z}} = \frac{3 \cdot f_{\text{V}} \cdot \gamma_{\text{p}}}{d_{\text{p}}} \ , \tag{5.7}$$

where f_{V} is the volume fraction of precipitates, d_{p} is the diameter of the precipitates and γ_{p} is the interface energy between the precipitates and their matrix (taken as 0.5 J/m^2 here [36]). Combining Eqs. (5.4) and (5.6) leads to:

$$\upsilon_{\alpha\gamma} = M \cdot \left(\Delta G_{\text{chem}} - \Delta G_{\text{diss}}^{\text{V}} - \Delta G_{\text{diss}}^{\text{C}} - \Delta G_{\text{diss}}^{\text{Mn}} - P_{\text{z}} \right) \ . \tag{5.8}$$

According to the Hillert–Sundman dissipation model, the Gibbs energy dissipation or the solute drag force is [37], [38]:

$$\Delta G_{\text{diss}} = -\frac{V_{\text{M}}}{\dot{S}} \int_{-\delta}^{\delta} J \cdot \frac{\text{d}\mu}{\text{d}s} \, \text{d}s \, . \tag{5.9}$$

In Eq. (5.9), $\dot{S}$ is the growth rate (being equal to υαγ in our case), V_{M} is the molar volume, μ is the chemical potential of a solute in the α/γ interphase boundary region given by:

$$\mu = \text{R} \cdot T \cdot \left(\ln x + \sum_j \varepsilon_j x \right) + E + \Delta E \cdot \left(1 + \frac{s}{\delta} \right) \ , \tag{5.10}$$

and J is the diffusion flux of a solute through the interface:

$$J = \frac{D^{\text{b}} \cdot x}{\text{R} \cdot T} \cdot \frac{\partial \mu}{\partial s} \, . \tag{5.11}$$

In Eqs. (5.9), (5.10) and (5.11), x is the solute concentration, δ is half the thickness of the boundary, s is a coordinate taking values in the range [-δ,δ], E is the interaction potential of the solute to the α/γ interface, ΔE is half the difference in the free energy of solute between ferrite and austenite, ε_{j} is the Wagner's parameter reflecting the interaction of the solute with the other j solutes, and D^{b} is the diffusion coefficient of a solute inside the interphase boundary (taken constant inside the boundary).
Using Eqs. (5.10) and (5.11), Eq. (5.9) can be finally written as:

$$\Delta G_{\text{diss}} = -\frac{V_{\text{M}}}{\upsilon_{\alpha\gamma}} \cdot \frac{D^{\text{b}} \cdot x}{\text{R} \cdot T} \cdot \frac{\Delta E^2}{\delta} \cdot 2 = C \frac{x}{\upsilon_{\alpha\gamma}} \ , \tag{5.12}$$

where $C = -2 \cdot \frac{V_{\text{M}} \cdot D^{\text{b}} \cdot \Delta E^2}{\text{R} \cdot T \cdot \delta}$, and its value is different for each element, in our case, vanadium, C^{V}, carbon, C^{C}, or manganese, C^{Mn}, since D^{b} and ΔE are different for the three elements.
Based on the above, Eq. (5.8) can be rewritten as:

$$\upsilon_{\alpha\gamma} = M \cdot \left(\Delta G_{\text{chem}} - C^{\text{V}} \cdot \frac{x^{\text{V}}}{\upsilon_{\alpha\gamma}} - C^{\text{C}} \cdot \frac{x^{C}}{\upsilon_{\alpha\gamma}} - C^{\text{Mn}} \cdot \frac{x^{\text{Mn}}}{\upsilon_{\alpha\gamma}} - \frac{3 \cdot f_{\text{V}} \cdot \gamma_{\text{p}}}{d_{\text{p}}} \right) \quad . \tag{5.13}$$

The Gibbs energy dissipation as a result of the manganese spike in front of the γ/α interface is neglected in these calculations, since the work of Chen et al. [39] shows that this contribution is minor when the interface velocity is of the order of 10^{-7} m/s. The latter study refers to the isothermal bainitic ferrite formation at 550 °C and we assume similar trends at 650 °C and 700 °C, however, this should be further investigated in the future. The Gibbs energy dissipation due to the vanadium spike is also neglected here, according to Ref. [15], [40]. The precipitate volume fraction and size that are necessary for the Zener pinning force calculation are obtained experimentally from the quantitative SANS data analysis described later in this paper. Possible energy dissipation due to the presence of curved boundaries that cause pressure increase is considered to be negligibly small as in Ref. [41].

We use Eq. (5.13) to analyze the behavior of the LCLV, LCHV, and HCHV steels at each annealing temperature, 650 °C and 700 °C. By solving the set of the equations, we obtain the C^{V}, C^{C} and C^{Mn} values and eventually calculate the $\Delta G_{\text{diss}}{}^{\text{V}}$, $\Delta G_{\text{diss}}{}^{\text{C}}$ and $\Delta G_{\text{diss}}{}^{\text{Mn}}$. The results show that the Gibbs energy dissipation due to carbon segregation at α/γ interfaces, $\Delta G_{\text{diss}}{}^{\text{C}}$, is close to zero and can therefore be neglected. $\Delta G_{\text{diss}}{}^{\text{C}}$ is considered to be zero in other studies as well, as for example in Ref. [41]. However, despite the negligible $\Delta G_{\text{diss}}{}^{\text{C}}$, carbon may have an indirect effect on the total Gibbs energy dissipation through its participation in the precipitation.

The derived $\Delta G_{\text{diss}}{}^{\text{V}}$, $\Delta G_{\text{diss}}{}^{\text{Mn}}$ and P_{z} and the resulting ΔG_{net} for the LCLV, LCHV and HCHV steels at 650 °C and 700 °C annealing temperatures are summarized in Table 5.3. The errors in the $\Delta G_{\text{diss}}{}^{\text{V}}$ and $\Delta G_{\text{diss}}{}^{\text{Mn}}$ are based on the uncertainties (~5 %) introduced by the calculation of the interface velocities.

The intrinsic mobility of the interface is calculated from the fit of the experimental data using Eq. (5.13) and it is for each annealing temperature: M_{650} = 1.5 x 10^{-10} m mol J^{-1} s^{-1} at 650 °C and M_{700} = 2.9 x 10^{-10} m mol J^{-1} s^{-1} at 700 °C.

The activation energy for the transfer of atoms across the interface, Q_{o}, can also be obtained using Eq. (5.8) and it is found to amount to 90 kJ/mol. Ideally, in-situ measurements during the austenite-to-ferrite phase transformation in pure iron should be performed in order to determine it. A value of 140 kJ/mol for Q_{o} is often mentioned in the literature [42], reported by Krielaart and van der Zwaag [34]. Hillert [37] reported a similar value, Q_{o} = 144 kJ/mol, but this was experimentally obtained during recrystallization in pure Fe, not during austenite-to-ferrite phase transformation. Our Q_{o} = 90 kJ/mol differs substantially from the literature values. The precipitation that takes place simultaneously to phase transformation as well as the magnetic field that is applied during the measurements significantly affect the mobility, the interface velocity and the energy dissipation, eventually resulting in a different Q_{o} value.

The time evolution of the transformed austenite fraction or, in other words, the ferrite fraction evolution during annealing of the LCLV, LCHV and HCHV steels is determined as described in Section 5.3.1. Fig. 5.6a shows the results for the annealing temperature of 650 °C and Fig. 5.6b for 700 °C. Austenite-to-ferrite phase transformation is observed in all steels at both temperatures and it is completed during the 10 h annealing treatment in all cases. This is in agreement with ThermoCalc calculations which also show that phase transformation takes place in all steels, at both temperatures and that the equilibrium ferrite fraction is larger than 98 % in all cases. The phase-transformation kinetics vary depending on the steel composition, i.e. the concentration of vanadium and carbon in each alloy, as well as on the annealing temperature. The kinetics is reflected in the calculated velocities $\upsilon_{\alpha\gamma}$ listed in Table 5.2.

Table 5.3. List of parameters calculated for the alloys of interest. The A_3 temperature and the ΔG_{chem} are calculated by ThermoCalc. The ΔG_{diss}^{V}, the ΔG_{diss}^{Mn}, the P_z and the ΔG_{net} are obtained by solving the set of equations as explained in text.

Steel	Annealing T (°C)	A_3 (°C)	ΔG_{chem} (J/mol)	ΔG_{diss}^{V} (J/mol)	ΔG_{diss}^{Mn} (J/mol)	P_z (J/mol)	ΔG_{net} (J/mol)
LCLV	650	830	435	53 ± 10	7 ± 21	3	372 ± 23
	700	830	241	20 ± 10	34 ± 13	2	185 ± 16
LCHV	650	853	457	117 ± 25	8 ± 24	4	328 ± 35
	700	853	262	40 ± 11	34 ± 12	3	185 ± 16
HCHV	650	834	435	131 ± 25	9 ± 27	3	292 ± 37
	700	834	239	58 ± 14	50 ± 18	4	127 ± 23

The derived phase-transformation kinetics curves show that the first hour of annealing, and more specifically the first 20 min, are the most critical for the transformation. In all steels after 20 min more than 80 % of austenite has already been transformed at 650 °C, while at 700 °C this fraction is more than 60 %. For all alloys, the kinetics is significantly faster at 650 °C than at 700 °C, which we attribute to the larger driving force for phase transformation at the lower temperature. However, we note that this difference is very small for the LCHV sample.

The comparison of the kinetics observed for the different samples gives insight into the effect of the different concentrations of vanadium and carbon on the rate of phase transformation. At 650 °C, the fastest phase-transformation kinetics is measured for the LCLV steel. The kinetics for the LCHV steel are slower and the HCHV steel has the slowest phase-transformation velocity. After 30 min of annealing the phase transformation has been completed in all steels. At 700 °C, during the first 10 min of annealing, the phase transformation in the LCLV and LCHV steels occurs with the same rate and with a lower rate in the HCHV steel. However, at longer times the transformation in the LCLV steel is not faster than in the other two steels. After 40 min of annealing at 700 °C the phase transformation has been completed in the LCHV and HCHV steels but not in the LCLV alloy in which 10 h are necessary to complete the phase transformation.

Additions of vanadium and carbon to the steel composition cause the retardation of the phase transformation. In each steel, the effect of the element concentrations on the kinetics of phase transformation is explained through the Gibbs energy dissipation as described above. The different element additions determine the dissipation of the Gibbs energy due to each element, ΔG_{diss}, affecting the total driving force for the phase transformation, ΔG_{net}, which together with the mobility control the ferrite growth velocity. The precipitate pinning force has a small effect on the velocity comparing to the effect of energy dissipation.

At both temperatures, 650 °C and 700 °C, ΔG_{net} is the largest for the alloy with the lowest vanadium and carbon concentration, i.e., for the LCLV. Adding vanadium to the steel causes a systematic decrease in ΔG_{net} (comparison between LCLV and LCHV) and the same trend is observed with the addition of carbon (comparison between LCHV and HCHV), despite the high uncertainty in the calculations (reflected in the errors). ΔG_{diss} due to vanadium is increasing either by adding vanadium or carbon to the steel, or by lowering the annealing temperature, while the dissipation due to manganese is not affected by these factors.

For each individual alloy annealed at 700 °C, the energy dissipation due to vanadium is smaller than at 650 °C, while the opposite trend is observed for the manganese dissipation, leading to the conclusion that the temperature effect on the Gibbs energy dissipation can vary between the different elements causing the dissipation. According to Eq. (5.12), the annealing

temperature affects the energy dissipation directly, but also through its effect on ΔE and the diffusion coefficient of each solute. The magnetic field applied during the measurements also affects the Gibbs energy dissipation as will be explained in Section 5.3.3.

5.3.3. Effect of the external magnetic field on the phase transformation kinetics

A delay in the onset and time evolution of austenite-to-ferrite phase transformation is observed in the results obtained from the ND experiments compared to the ones obtained from the dilatometry heat-treatments applied for the TEM sample preparation. An example is shown in Fig. 5.7, in which we compare the time evolution of the transformed austenite fraction measured by ND and dilatometry for the LCLV steel at 650 °C. These samples have been submitted to the same heat treatment and the only difference is that a magnetic field of ~1.5 T is applied during the ND measurements. In the following we discuss the effect of the external magnetic field on the austenite-to-ferrite phase-transformation kinetics by comparing (zero field) dilatometry with in-situ magnetometry under a magnetic field of 1.6 T.

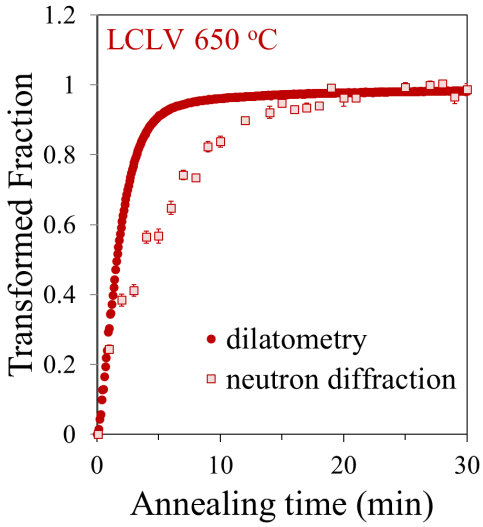

Fig. 5.7. Transformed austenite fraction measured by ND and dilatometry for the LCLV steel at 650 ºC.

As the furnace used for the magnetometer measurements is not able to reach temperatures higher than 900 °C, we applied a slightly different heat-treatment for this set of samples used for dilatometry and magnetometry. For these measurements the samples are first heat treated in the dilatometer at 1050 °C for 10 min and then quenched to room temperature in order to dissolve the precipitates that are initially present at room temperature (Fig. 5.8a). Afterwards, a heat treatment is applied including holding at 900 °C for 10 min to austenitize the sample, followed by an isothermal holding at 650 °C for 55 min. The phase-transformation kinetics at 650 °C is therefore measured by both techniques individually for each alloy. In order to obtain the phase-transformation kinetics by magnetometry, the magnetization evolution of the specimen is translated to volume fraction evolution of the ferromagnetic phase, i.e. the ferrite (austenite is paramagnetic). This is done by normalizing the magnetization at each moment of annealing to the maximum magnetization reached after 50 min when the austenite-to-ferrite phase transformation is complete. The time evolution of the magnetization during annealing of the LCLV at 650 °C is provided in Appendix C (Fig. C3).
The time evolution of the ferrite phase fraction for the LCLV steel obtained during annealing at 650 °C from magnetometry under a magnetic field of 1.6 T is plotted in Fig. 5.8b, together with the corresponding fraction obtained from the zero field dilatometry measurements. The comparison of the two curves highlights the delay in the phase-transformation kinetics induced

by the magnetic field. This delay cannot be explained by the Zeeman energy effect because, according to Ref. [43], when a small magnetic field is applied, the critical temperatures for phase transformation do not significantly change. In addition, these small changes in the critical temperatures due to the magnetic field, would slightly increase the driving force for phase transformation accelerating in this way the phase-transformation kinetics. This is contradictory to our observations. Possible explanations for the observed retardation of the phase-transformation kinetics by the magnetic field might be related to a modification of the carbon diffusivity below and above the Curie temperature due to magnetostriction [44], as well as modification of the grain boundary energy. The magnetization of ferrite above and below the Curie temperature, as well as the magnetization of austenite are critical factors for ferrite nucleation when a magnetic field is applied. In addition, research is required on the effect of the magnetic field on the phase-transformation kinetics in different steels heat-treated at different temperatures. The magnetic-field effect may be dependent on the steel composition and the annealing temperature. For example, we observe a delay in the phase-transformation kinetics in the LCLV steel annealed at 700 °C after 10 min of annealing (Fig. 5.6b), which may be due to the magnetic field. It is important to mention here that the magnetic field may influence the mobility, M, and the dissipation energy due to different elements which finally affect the $v_{\alpha\gamma}$, thus it would be interesting if future research could quantify these effects. To conclude, more extensive work is required in order to explain the effect of the magnetic field on the phase-transformation kinetics. Such a study, however is beyond the scope of this paper.

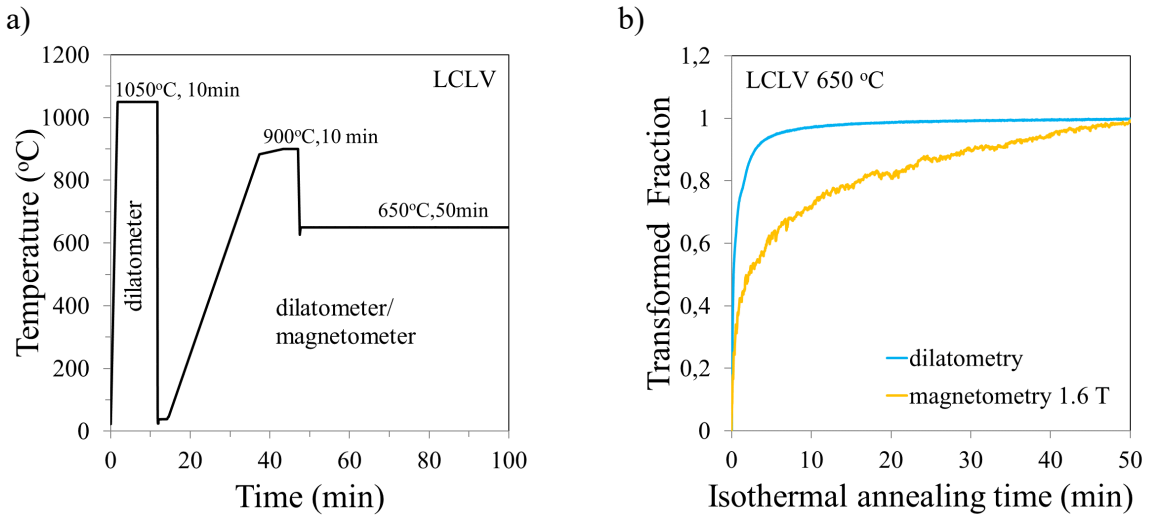

Fig. 5.8. a) Heat treatment applied to the LCLV steel. b) Comparison of phase transformation kinetics of the LCLV steel obtained during annealing at 650 °C by dilatometry (at zero magnetic field) and magnetometry (under a magnetic field of 1.6 T).

5.4. Precipitation kinetics

5.4.1. SANS data analysis

The time evolution of the SANS intensity during annealing reveals the precipitation kinetics in the studied steels. It is a 2D pattern from which the macroscopic differential scattering cross-section, $(d\Sigma/d\Omega)(\mathbf{Q})$, can be obtained after background correction and neutron flux calibration [45]. $(d\Sigma/d\Omega)(\mathbf{Q})$ is a function of the scattering vector, $\mathbf{Q}$, and has two components, the nuclear, $(d\Sigma/d\Omega)_{NUC}(Q)$, and the magnetic, $(d\Sigma/d\Omega)_{MAG}(Q)$, cross sections. These two components originate from the strong nuclear interaction of the neutrons with the nuclei and from the dipole-dipole interaction of the neutron magnetic moments with the unpaired electrons of the

atoms respectively [46]. Due to the specific selection rules of the magnetic scattering, it is possible to unambiguously separate the magnetic contribution from the nuclear contribution to the cross-section, by applying a magnetic field, high enough to saturate the magnetization of the specimen, along a direction contained in the SANS detector plane. In this case, the macroscopic differential scattering cross-section equals to [46]:

$$\left(\frac{d\Sigma}{d\Omega}\right)(\mathbf{Q}) = \left(\frac{d\Sigma}{d\Omega}\right)_{NUC}(Q) + \left(\frac{d\Sigma}{d\Omega}\right)_{MAG}(Q)\cdot\sin^2\varphi \ , \tag{5.14}$$

where φ is the angle between the magnetic field direction and **Q**. In this study we average $(d\Sigma/d\Omega)(\mathbf{Q})$ azimuthally over sectors of 30° around the transmitted neutron beam, oriented parallel and perpendicular to the magnetic field, respectively. In this way, we obtain $(d\Sigma/d\Omega)_{NUC}(Q)$ and $(d\Sigma/d\Omega)_{NUC}(Q) + (d\Sigma/d\Omega)_{MAG}(Q)$, respectively, and from the difference between these two values we calculate $(d\Sigma/d\Omega)_{MAG}(Q)$.
The determination of $(d\Sigma/d\Omega)_{NUC}(Q)$ requires an accurate background subtraction. Since the SANS measurements are performed on samples being heat-treated inside the furnace, the background signal consists of the scattering signal from the furnace and from the steel matrix. The latter is determined from measurements on a reference steel without precipitates, at soaking temperature. Therefore, after background subtraction, $(d\Sigma/d\Omega)_{NUC}(Q)$ contains only the scattering from the precipitates.
Examples of the SANS nuclear differential scattering cross sections obtained at different annealing times of the LCLV steel at 650 °C are shown in Fig. 5.9a. The corresponding magnetic scattering cross sections are shown in Fig. 5.9b. The SANS cross sections increase with time, as expected for precipitation. More SANS results obtained during annealing of the LCLV, LCHV and HCHV steels at 650 and 700 °C can be found in Appendix C (Figs. C4-6).

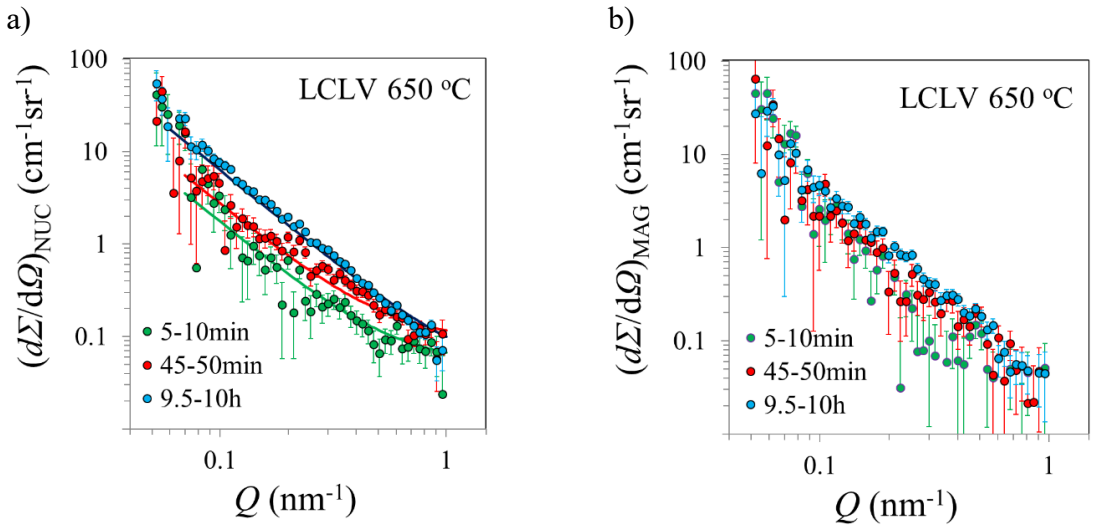

Fig. 5.9. Time evolution of the SANS scattering cross section, corrected for background and dislocation scattering, of the LCLV steel annealed at 650 °C. a) nuclear scattering; b) magnetic scattering. The solid lines in a) are fits with Eq. (5.15).

$(d\Sigma/d\Omega)_{NUC}(Q)$ is analyzed to obtain quantitative information on the precipitation kinetics, which, for a dilute system of precipitates within a homogeneous matrix, is given by [45]:

$$\left(\frac{d\Sigma}{d\Omega}\right)_{NUC}(Q) = \Delta\rho^2_{NUC} \cdot \int D_N(r) \cdot V^2(r) \cdot P^2(Q,r)\,dr, \tag{5.15}$$

where r and V are the precipitate radius and volume, respectively, $D_N(r)$ is the precipitate size distribution, $\Delta\rho^2_{NUC}$ is the difference in nuclear scattering length density between the matrix and the precipitates (nuclear contrast), and $P(Q,r)$ is the orientation-averaged form factor reflecting the precipitate shape. For ellipsoidal precipitates, the form factor is [47]:

$$P(Q,r) = 3\frac{\sin(Qr) - (Qr)\cos(Qr)}{(Qr)^3}, \tag{5.16}$$

where $r = \left(R_{eq}^2 \sin^2\psi + R_p^2 \cos^2\psi\right)^{1/2}$. (5.17)

ψ is the angle between the axis of the ellipsoid and the **Q**, R_{eq} is the equatorial radius (radius perpendicular to the rotational axis of the ellipsoid) and R_p is the polar radius (radius along the rotational axis of the ellipsoid). In this study, the precipitate is modelled as an oblate ellipsoidal for all steels, based on TEM analysis (see Fig. 5.10). Fitting trials of the SANS data to model the precipitate shape as spherical were initially performed, but it was found that the spherical model is not able to describe the precipitate shape for all alloys and annealing temperatures. Examples of the precipitate ellipsoidal shape are illustrated in the TEM micrographs of Figs. 5.10a and b, which correspond to LCLV steel samples annealed at 650 °C and 700 °C, respectively. More TEM micrographs can be found in Appendix C (Fig. C7). Note here that TEM is used for a qualitative investigation of the precipitate shape in order to contribute to the SANS analysis, and not to obtain quantitative information on the precipitate shape and size. The reason behind this is in the differences in the phase-transformation and precipitation kinetics between the steels heat-treated in the dilatometer without a magnetic field and in the furnace under the effect of an external magnetic field. This is explained in detail later in the text.

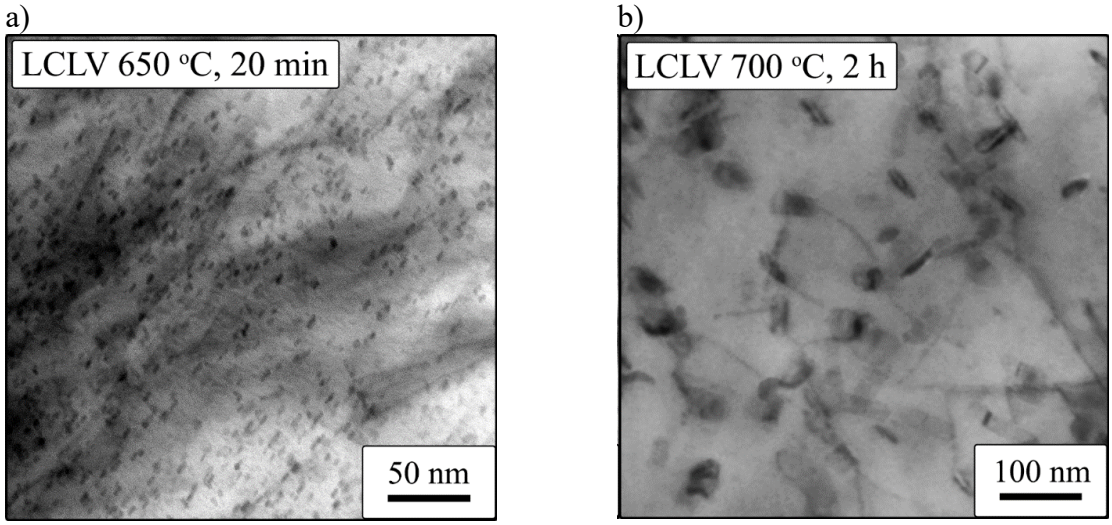

Fig. 5.10. TEM bright field images obtained from thin foils showing the ellipsoidal shape of the precipitates. The micrographs correspond to samples from the LCLV steel annealed at a) 650 °C for 20 min and b) at 700 °C for 2 h.

Finally, in Eq. (5.15), the term $\Delta\rho^2_{NUC}$ is the nuclear contrast between the precipitates and the matrix. This contrast is composition dependent and can be calculated according to [14]. Therefore, $\Delta\rho^2_{NUC}$ is different for the three steels, since the precipitate chemical composition varies with the steel composition and the temperature [14]. In the following we assume that all precipitates in the same steel annealed at the same temperature have the same composition.
In order to obtain quantitative information on the precipitation kinetics from the SANS data, we fit the $(d\Sigma/d\Omega)_{NUC}(Q)$ curves to the model of Eq. (5.15) using the SasView software [48]. The $(d\Sigma/d\Omega)_{MAG}(Q)$ component can also be used for quantifying the precipitation kinetics providing the same results as the $(d\Sigma/d\Omega)_{NUC}(Q)$. The corresponding magnetic contrast between the precipitates and the matrix, $\Delta\rho_{MAG}$, is also composition dependent and can be calculated as explained in Ref. [14] and in Chapter 4 of this thesis (Eqs. 4.6 and 4.7). In the following analysis, we use the $(d\Sigma/d\Omega)_{NUC}(Q)$ curves and fit them to the model of Eq. (5.15). For this purpose we assume an oblate ellipsoidal precipitate shape, according to Eqs. (5.16) and (5.17), with R_{eq} and R_p of the precipitates following a log-normal distribution. The fitting parameters of the model are the precipitate-size distribution (i.e., R_{eq}, R_p and their log-normal distribution) and the precipitate volume fraction, f_V, for each SANS curve that corresponds to a specific time-slice of annealing. The precipitate number density, N_p, is eventually calculated from the f_V, R_{eq} and R_p values, taking into account the volume of the oblate ellipsoidal:

$$N_p = \frac{f_V}{\frac{4}{3}\cdot\pi\cdot R_{eq}^2\cdot R_p} \tag{5.18}$$

It is important to note that the $(d\Sigma/d\Omega)_{NUC}(Q)$ curves measured during cooling from the austenization temperature to the isothermal temperature indicate that no precipitation is taking place before the isothermal annealing temperature is reached. Indeed, the SANS curves captured during cooling (1 min time-slices) and those at the soaking temperature overlap.
In a dual phase system and for small precipitate volume fractions, the precipitate volume fraction is expressed as [46]:

$$f_V \cong \frac{Q_{o,NUC}}{2\pi^2\Delta\rho^2_{NUC}}, \tag{5.19}$$

where the invariant $Q_{o,NUC}$ is the area under the Kratky plot curve, $Q^2(d\Sigma/d\Omega)_{NUC}(Q)$ vs Q plot, given by:

$$Q_{o,NUC} = \int_0^\infty Q^2\left(\frac{d\Sigma}{d\Omega}\right)_{NUC}(Q)\,dQ = 2\pi^2\Delta\rho^2_{NUC}f_V \quad . \tag{5.20}$$

From Eq. (5.19), it is clear that the precipitate's chemical composition and consequently $\Delta\rho^2_{NUC}$, determine the resulting precipitate volume fraction values. The determination of the precipitate's chemical composition, size and volume fraction is thus challenging and strongly depends on the concentration gradients around the precipitate.
For precipitates with a vanadium-rich core and an iron-rich shell as considered in Ref. [14] and as shown in Fig. 5.11, representation I, the precipitate size depends on the size of the iron concentration in the outer part of the precipitate. For short annealing times, the size of the iron-rich shell is large and the size of the vanadium rich core is small, giving a small overall precipitate contrast when interacting with the neutrons. According to Eq. (5.19), this results in

large precipitate volume fraction values. Since the concentration of iron in the precipitates is found to decrease with annealing time [14], the effective size of the iron shell decreases, giving rise to a continuous increase of $\Delta\rho^2_{NUC}$ during annealing. This change in the contrast, however, would according to Eq. (5.19) lead to an unrealistic decrease of the precipitate volume fraction with time, even though in reality the vanadium-rich core is increasing in size. This evolution of the precipitate volume fraction is plotted in Fig. 5.12, curve I. The missing points in Fig. 5.12 are due to an interruption of the neutron beam. In this case, the precipitate profile can, for a certain moment of annealing, be mimicked as shown in Fig. 5.11 for the precipitate representation I.

For a quantitative analysis of the precipitate volume fraction evolution, one may consider an effective precipitate core with a homogenous composition that remains constant during annealing. The composition of the core can be for example, either the equilibrium composition as calculated by ThermoCalc, or the stoichiometric composition of the pure vanadium carbide (VC). The corresponding precipitate profiles in each case are depicted in Fig. 5.11, cases II and III, respectively. The effective precipitate size is described by the effective precipitate volume, V_{eff}, and in the case of ellipsoidal precipitates, by the two effective ellipsoidal radii, $R_{eq,eff}$ and $R_{p,eff}$. In this way, when considering this effective precipitate size, i.e. the size of the precipitate core, an effective precipitate volume fraction, $f_{V,eff}$, can be obtained, which is related to f_V from Eq. (5.19):

$$f_{V,eff} = \frac{\Delta\rho^2_{NUC}}{\Delta\rho^2_{NUC,eff}} \cdot f_V \quad . \tag{5.21}$$

In Eq. (5.21), $\Delta\rho^2_{NUC}$ is the contrast of the $(Fe_xMn_zV_{1-x})C_y$ precipitates according to [14], and f_V is the corresponding volume fraction. The $f_{V,eff}$ is the effective precipitate volume fraction corresponding to the $\Delta\rho^2_{NUC,eff}$ used, for either the precipitates of representation II or III.

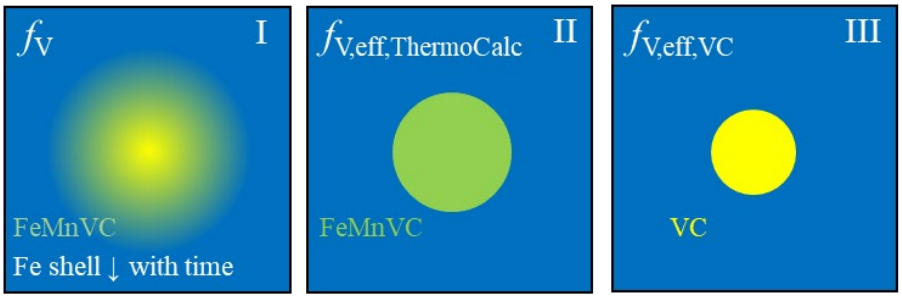

Fig. 5.11. Precipitate effective size and volume fraction at a certain moment of annealing. Precipitate representation I with volume fraction f_V and composition according to Ref. [14], precipitate representation II with effective volume fraction $f_{V,eff,ThermoCalc}$ and equilibrium composition from ThermoCalc, and precipitate representation III with effective volume fraction $f_{V,eff,VC}$ and composition of the stoichiometric vanadium carbide.

The fitting of Eq. (5.15) can be performed using either the nuclear contrast values, $\Delta\rho^2_{NUC,eff}$, for precipitates with the equilibrium composition that ThermoCalc predicts (representation II, Fig. 5.11) or the stoichiometric VC composition (representation III, Fig. 5.11). The values of $\Delta\rho^2_{NUC,eff}$ used for all three steels are listed in Table 5.4.

The precipitate volume fraction resulting from the fit of the time evolution of the SANS intensity in the LCLV steel during annealing at 650 °C is shown as an example in Fig. 5.12 for the precipitate representations I, II and III. The precipitation kinetics of the precipitates of

representations II and III show the same trend. The corresponding curves for the LCLV steel annealed at 700 °C and for the LCHV and HCHV steels annealed at both 650 °C and 700 °C are presented in Appendix C (Fig. C8).

Table 5.4. The nuclear contrast values, $\Delta\rho^2_{NUC,eff}$, used to calculate the "effective" volume fraction of the precipitates with composition that ThermoCalc predicts (precipitate representation II, Fig. 5.11) and with the stoichiometric VC composition (precipitate representation III, Fig. 5.11) in all three steels.

Steel	Annealing T (°C)	$\Delta\rho^2_{NUC,eff}$ x10^{-7} nm^{-4} case II	Precipitate composition by ThermoCalc	$\Delta\rho^2_{NUC,eff}$ x10^{-7} nm^{-4} case III	VC
LCLV	650	1.42	$(Fe_{0.156}V_{0.84}Mn_{0.006})C_{0.872}$	1.88	VC
	700	1.50	$(Fe_{0.133}V_{0.86}Mn_{0.004})C_{0.869}$	1.85	VC
LCHV	650	1.99	$(Fe_{0.049}V_{0.95}Mn_{0.001})C_{0.839}$	1.88	VC
	700	1.94	$(Fe_{0.050}V_{0.95}Mn_{0.001})C_{0.843}$	1.85	VC
HCHV	650	1.49	$(Fe_{0.140}V_{0.86}Mn_{0.005})C_{0.871}$	1.88	VC
	700	1.51	$(Fe_{0.130}V_{0.87}Mn_{0.004})C_{0.869}$	1.85	VC

In the following discussions, we refer to the precipitates of representation II, i.e. we present the precipitation kinetics of the effective volume fraction $f_{V,eff,ThermoCalc}$, and the corresponding radii and volume.

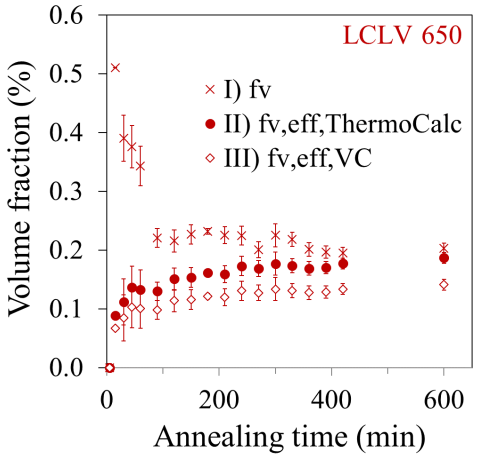

Fig. 5.12. Time evolution of the precipitate volume fraction in the LCLV alloy during annealing at 650 °C, calculated in different ways as described in the text. I, II and III sets correspond to the I, II and III precipitate representations of Fig. 5.11.

5.4.2. SANS results and discussion

The precipitation kinetics in the LCLV, LCHV and HCHV steels during isothermal annealing at either 650 °C or 700 °C as obtained from the fitting of the $(d\Sigma/d\Omega)_{NUC}(Q)$ is shown in Figs. 5.13a-i, where we depict the time evolution of the precipitate effective volume fraction (for precipitates with equilibrium composition from ThermoCalc), number density and size. The error bars in all plots originate from the fits of the SANS data and are thus related to the counting statistics. Therefore, the larger error bars at short annealing times, i.e. at the beginning of the isothermal holding, are due to the short measuring times and the consequently lower counting statistics.

Precipitation takes place in all three steels at both annealing temperatures. The effective precipitate volume fraction increases during annealing in all cases, as shown in Figs 5.13a-c, but the equilibrium volume fraction as calculated from ThermoCalc and presented in Table 5.5 is not reached in any of the steels. This means that after 10 h of annealing there is still supersaturation of vanadium in solid solution in the ferrite matrix. In Appendix C, we provide graphs (Fig. C9) showing the time evolution of the fraction of vanadium in solid solution and in the precipitates during annealing in all steels. At each annealing temperature, the final precipitate volume fraction after 10 h of annealing in the HCHV steel is approximately twice the corresponding volume fraction in the LCLV and LCHV alloys. The precipitate volume fraction in all steels is larger at 700 than at 650 °C during the entire annealing period of 10 h.
Comparable behavior is observed for the effective precipitate size. Figs. 5.13d-f and 5.13g-i show the increase in the precipitate size with annealing time and manifest the presence of larger precipitates at 700 °C in all steels. The precipitate shape is modelled as oblate ellipsoidal as explained above. The ratio R_{eq}/R_p is smaller at 650 °C than at 700 °C for all steels. The average R_{eq}/R_p ratio during annealing is 2.9, 3.0 and 2.9 for the LCLV, LCHV and HCHV steels at 650 °C, respectively, and 18.3, 12.3 and 5.4, for the LCLV, LCHV and HCHV steels at 700 °C, respectively.
According to the Zener model [49], [50], the time evolution of the precipitate radius at the early stages of growth is given by:

$$R(t) \propto \sqrt{D_V (t - t_s)} \ , \tag{5.22}$$

where t is the time of annealing, t_s is the time when nucleation occurs and D_V is the diffusion coefficient of vanadium in the ferrite matrix. During this stage, the diffusion fields of the neighboring precipitates do not overlap and coarsening does not take place. Since the diffusion coefficient of vanadium is larger at higher temperatures, for all steels the precipitates formed at 700 °C are larger than those formed at 650 °C.
The precipitate number density evolution in all alloys is shown in Figs. 5.13g-i. The number density is higher during the first minutes of annealing and gradually decreases after ~100 min. This implies that precipitate coarsening is taking place since the precipitate volume fraction is continuously rising during this period. The HCHV steel exhibits a larger volume fraction and number density of precipitates after 10 h of annealing compared to the LCLV and LCHV steels due to its higher vanadium and carbon concentrations.
In all steels, more precipitates are formed at 650 °C than at 700 °C. The driving force for nucleation of vanadium carbides in ferrite is calculated by ThermoCalc and is given for the three alloys and the two isothermal holding temperatures in Table 5.5. The nucleation rate of the precipitates, $\dot{N}$, depends on the driving force for precipitation [51]:

$$\dot{N} \propto \exp\left(-\frac{\Delta G^* + Q_D}{k_B T} \right) . \tag{5.23}$$

In Eq. (5.23), T is the temperature, k_B the Boltzmann constant and Q_D the activation energy for the vanadium diffusion. ΔG^* is the activation energy for the nucleation of the precipitates described by [51]:

$$\Delta G^* = \frac{\Psi}{\left(\Delta G_V - g_s \right)^2} \ , \tag{5.24}$$

where ΔG_V is the chemical driving force for the precipitate nucleation, g_s is the strain energy due to nucleation, and Ψ is a parameter containing details on the energies of the interfaces involved in nucleation and the shape of the nucleus [52].
Due to the larger driving force for precipitation when the isothermal annealing is performed at a lower temperature (Eq. (5.23)), a larger density of precipitates is observed at 650 °C. The presence of larger and fewer precipitates at 700 °C than at 650 °C in all steels is confirmed by TEM investigations (e.g. Figs. 5.10a and b referring to the LCLV steel).

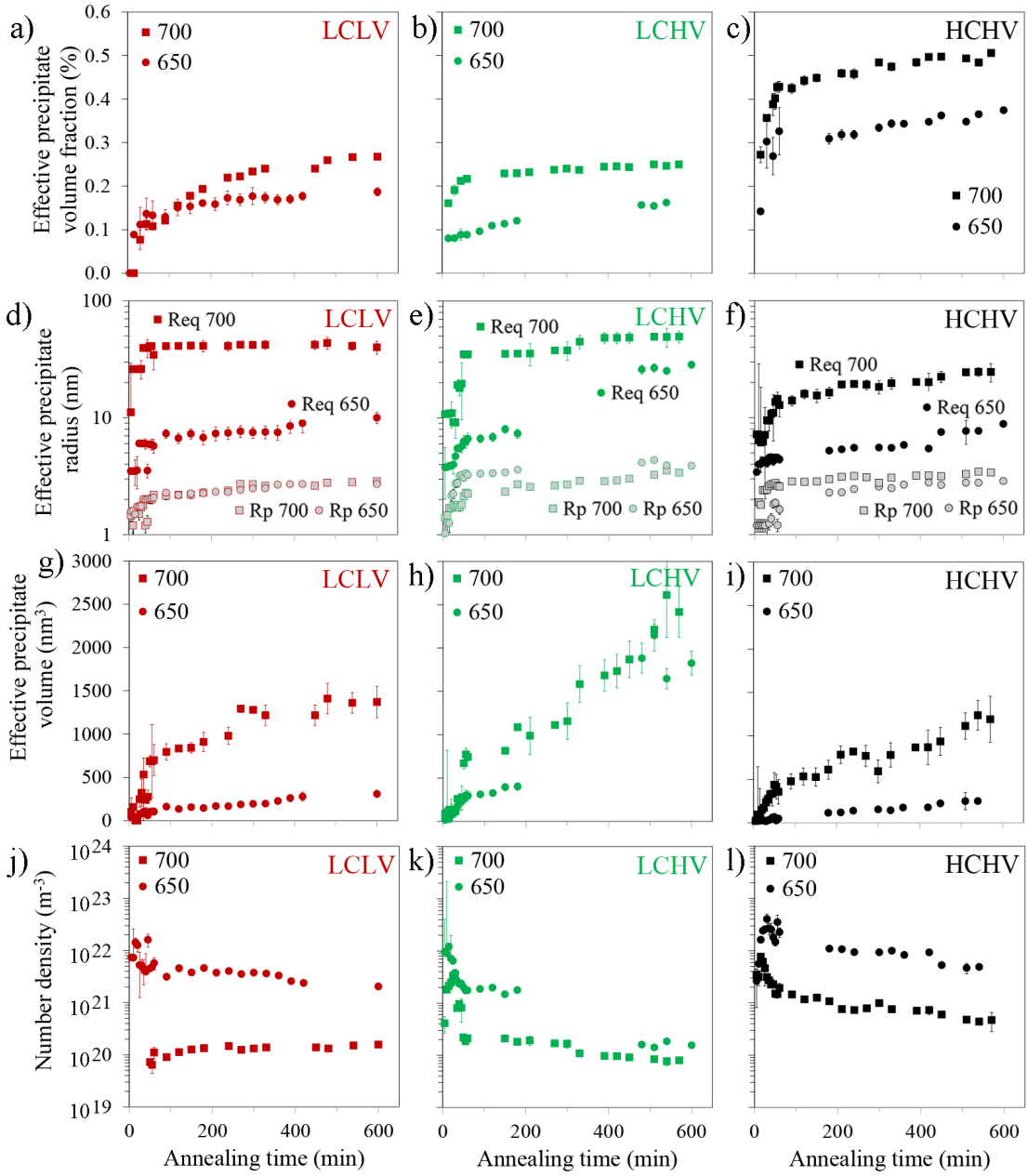

Fig. 5.13. Time evolution of the effective a-c) volume fraction, d-f) polar and equatorial mean radii, g-i) volume and j-l) number density of the precipitates in all steels during annealing at 650 and 700 °C.

Table 5.5. Precipitate dissolution temperature, T_D, driving force for precipitation in ferrite, $\Delta G_{V,p}$, equilibrium precipitate volume fraction, $f_{V,equil}$, for the alloys of interest calculated by ThermoCalc, and measured volume fraction after 10 h of annealing, $f_{V,eff}$ - 10h.

Steel	T_D (°C)	Annealing T (°C)	$\Delta G_{V,p}$ (kJ/mol)	$f_{V,equil}$ (%)	$f_{V,eff}$ - 10h (%)
LCLV	990	650	24.3	0.56	0.19
	990	700	21.0	0.52	0.27
LCHV	1060	650	26.9	0.64	0.16
	1060	700	23.7	0.63	0.25
HCHV	1069	650	28.8	1.08	0.37
	1069	700	25.8	1.06	0.47

5.5. Interaction between the phase transformation and precipitation kinetics

In-situ simultaneous ND and SANS experiments have been performed in steels with different concentrations of vanadium and carbon. The coupling of the SANS to ND results allows studying the relation between the precipitation kinetics and phase-transformation kinetics during annealing at 650 or 700 °C. The time evolution of the size, number density and volume fraction of the precipitates in the LCLV, LCHV and HCHV steels is presented in Fig. 5.14, together with the evolution of the transformed austenite fraction in each steel at each annealing temperature.

As illustrated in Fig. 5.14, in all steels the precipitation takes place during and after the phase transformation and the precipitation kinetics follow the phase-transformation kinetics. This indicates that the austenite-to-ferrite phase transformation initiates the vanadium carbide precipitation. The precipitate number density at 650 °C is larger than at 700 °C, not only due to the larger driving force for precipitation at the lower temperature as explained above, but also due to faster phase-transformation kinetics at 650 °C. We also measure a higher precipitate growth rate and larger precipitates at 700 °C than at 650 °C (Fig. 5.13j-l) because of the faster diffusion of vanadium at the higher temperature. The slower phase-transformation kinetics at 700 °C may also lead to higher aspect ratios between the precipitate ellipsoidal radii, R_{eq}/R_p, because vanadium diffusion along the austenite/ferrite interface is faster than perpendicular to the interface. This may lead to faster precipitate growth along the interface compared to growth perpendicular to the interface.

The promoted precipitation during the phase transformation is attributed to the solubility decrease of the vanadium and carbon when austenite transforms to ferrite, increasing the driving force for precipitation [5]. Since austenite-to-ferrite phase transformation takes place in all alloys at both temperatures, precipitates are detected in all cases.

The precipitate number density, size and volume fraction increase during austenite-to-ferrite phase transformation. This is an indication that the precipitation takes place at the migrating austenite/ferrite interface during the phase transformation, i.e. interphase precipitation. During phase transformation, the precipitate nucleation and growth are dominant over coarsening. When phase transformation is complete, the precipitate growth and coarsening are dominant since the precipitate number density does not increase while the precipitate size and volume fraction increase with time (Fig. 5.14). In all steels apart from the LCLV annealed at 700 °C, precipitate coarsening is observed since the number density decreases after having reached a maximum (Figs. 5.14a, c-f). The precipitation kinetics in the LCLV steel at 700 °C do not reach the coarsening stage (number density continuously increasing – Fig. 5.14b). This is attributed to the slow phase transformation kinetics in this steel at longer annealing times (Fig. 5.6d).

It is important to note that, even though the phase transformation is complete after 10 h of annealing of all three steels at both temperatures, the precipitation phenomenon is not complete. f_V has not reached a plateau but is continuously increasing (Figs. 5.13a-c). According to ThermoCalc calculations (Table 5.5, column 5), the precipitate volume fraction, f_V, has not reached the equilibrium value after 10 h of annealing.

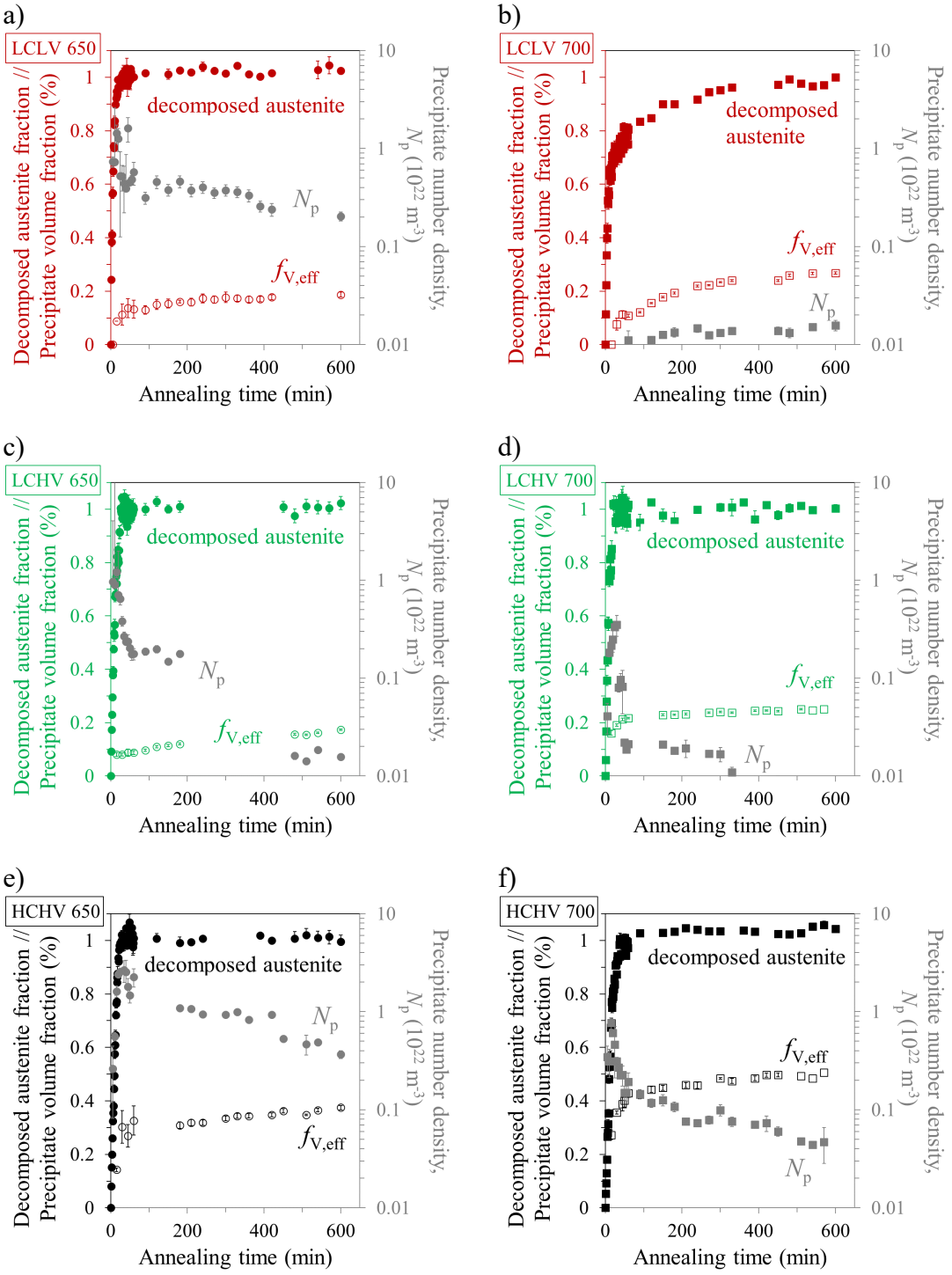

Fig. 5.14. Austenite-to-ferrite phase transformation kinetics and precipitation kinetics during the 10 h isothermal annealing of the LCLV, LCHV and HCHV steels at 650 and 700 °C. The time evolution of the transformed austenite fraction, the precipitate volume fraction and number density are plotted.

In a previous study the precipitation kinetics in the LCLV and in the HCHV steels at 650 °C was measured by ex-situ SANS [16], in samples heat treated in a dilatometer before the SANS measurements. Differences are observed between the precipitation kinetics obtained by in-situ and ex-situ SANS in the same steels with the same heat-treatments. Since the applied magnetic field during the in-situ SANS measurements retards the austenite-to-ferrite phase-transformation kinetics, and the phase-transformation kinetics drive the precipitation kinetics, the different precipitation kinetics obtained by in-situ SANS are attributed to the effect of the magnetic field. The retardation of phase transformation, i.e., the slower movement of the austenite/ferrite interface, results in a lower precipitate nucleation rate which leads to lower precipitate number densities and smaller precipitate volume fractions. These differences are presented in Figs. 5.15a and b for the LCLV alloy annealed at 650 °C as an example. Note here that the precipitation kinetics analysis for the ex-situ SANS measurements is performed considering VC precipitates (representation III, Fig. 5.11).

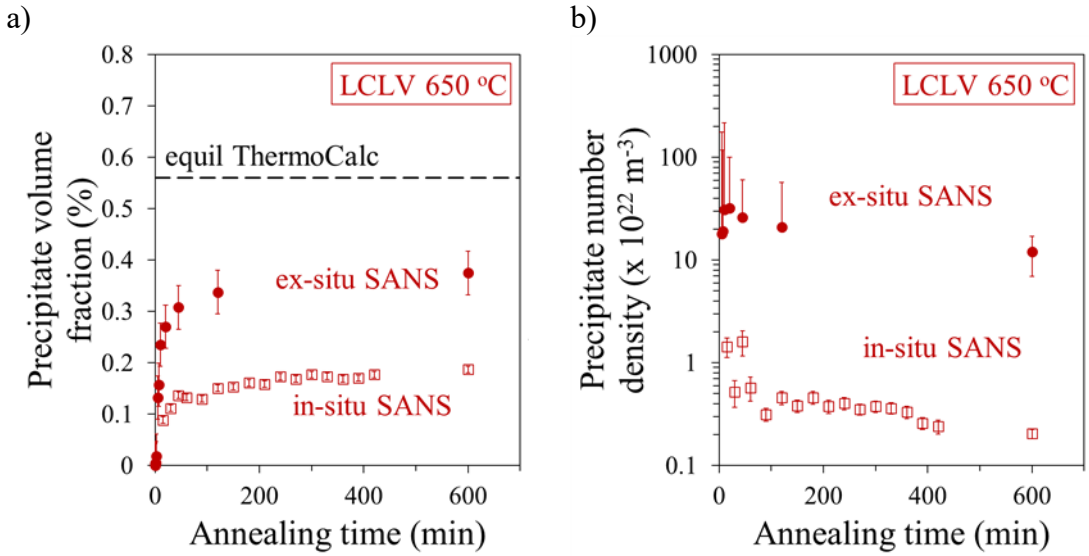

Fig. 5.15. Time evolution of the precipitate a) volume fraction and b) number density in the LCLV steel annealed at 650 °C, obtained by ex-situ SANS in dilatometry heat-treated specimens and by in-situ SANS during the applied thermal cycle and under an external magnetic field of 1.5 T.

Finally, regarding the precipitate size, larger precipitates are observed during the in-situ SANS measurements [16]. Slower phase-transformation kinetics leads to a higher accumulation of vanadium in the austenite/ferrite interface, thus, vanadium has time to diffuse into the precipitates and accelerate their growth. Since, as explained above, the accumulated vanadium atoms diffuse faster along the interface than perpendicular to it, higher aspect ratios between the precipitate ellipsoidal radii, R_{eq}/R_p, are promoted due to the slower phase-transformation kinetics when an external magnetic field is applied.

Since we observe that the precipitation kinetics are affected by an external magnetic field due to its effect on the phase transformation kinetics, the TEM analysis in the dilatometry heat-treated samples (without magnetic field) is used to obtain qualitative information on the precipitates shape, i.e. the precipitate shape can be modelled as ellipsoid. Quantitative information such as the aspect ratio between the precipitate ellipsoidal radii and the exact precipitate size are obtained from the fit of the SANS data.

Moreover, in a recent study [14], we measured the precipitates chemical composition evolution during annealing at 650 °C and 700 °C in the same LCLV, LCHV and HCHV alloys. We have

observed faster increase in the vanadium metal fraction in the precipitates when increasing the alloying elements content, either the vanadium or the carbon concentration. Correlating this finding to the phase transformation and to the precipitation kinetics, the austenite-to-ferrite phase transformation is more sluggish when adding vanadium or carbon to the steel nominal composition, allowing more time for the vanadium to diffuse to the precipitates, increasing their vanadium concentration.

So far, the effect of the austenite-to-ferrite phase-transformation kinetics on the precipitation kinetics is discussed. The effect of the precipitation on the phase transformation should also be addressed. The precipitation may affect the phase transformation in three ways [42]. The first is through the pinning force, P_z, that they induce which contributes to the reduction of the α/γ interface velocity as described in Eqs. (5.6) and (5.7). The second effect originates from the fact that a fraction of vanadium is consumed in the precipitates, reducing the vanadium concentration in solid solution and weakening the solute drag effect due to vanadium, eventually promoting a higher phase transformation velocity. Adding vanadium to the steel nominal composition (comparison between LCLV and LCHV alloys), results in a higher vanadium concentration that is in solid solution (Fig. C9 in Appendix C – see vanadium in solid solution the first minutes of annealing). Consequently, the energy dissipation due to the solute drag of vanadium is higher in the LCHV than in the LCLV steel (Table 5.3), retarding the phase-transformation kinetics in the LCHV steel, compared to the LCLV steel. The third effect is related to the role of carbon. When interphase precipitation takes place, there is carbon consumption at the interphase boundary due to the precipitate formation. Therefore, there is no long-range diffusion of carbon, which otherwise would diffuse in the residual austenite, retarding the phase transformation kinetics.

5.6. Summary and conclusions

In-situ and simultaneous ND and SANS measurements in steels with different vanadium and carbon concentrations provide a unique insight into the interaction between the austenite-to-ferrite phase transformation and the precipitation kinetics during isothermal annealing at 650 and 700 °C. The conclusions of the in-situ studies are the following:

- Austenite-to-ferrite phase transformation is observed in all steels during annealing at 650 °C and 700 °C, and the transformation kinetics depends on the temperature and on the alloy composition. Faster kinetics at 650 °C than at 700 °C is measured in all alloys due to the larger driving force for phase transformation at lower temperatures.
- Additions of vanadium and carbon to the steel composition cause the retardation of the onset of phase transformation. At both temperatures, the net driving force for phase transformation is the largest for the low-carbon low-vanadium alloy, while adding vanadium or carbon to the steel causes a decrease in the net driving force, as a result of an increase in the energy dissipation due to vanadium solute drag.
- In all steels, the austenite-to-ferrite phase transformation initiates the vanadium carbide precipitation. This is attributed to the decrease of the solubility of vanadium and carbon when austenite transforms to ferrite, increasing the driving force for precipitation.
- The precipitate number density, size and volume fraction increase during the phase transformation in all steels, indicating that the precipitation takes place at the migrating austenite/ferrite interface during the phase transformation. After the completion of the phase transformation, the precipitates grow and coarsen. Larger and fewer (~1-2 orders of magnitude) precipitates are measured at 700 °C than at 650 °C in all steels, and a larger density of precipitates in the steel with the higher concentration of vanadium and carbon. The precipitate number density at 650 °C is higher than at 700 °C due to the larger driving force for precipitation and to the faster phase-transformation kinetics at the lower temperature. The

larger precipitate growth rate and the larger precipitate size is measured at 700 °C compared to 650 °C is attributed to the faster diffusion of vanadium at the higher temperature.
- Ellipsoidal precipitates are detected in all conditions, indicating faster precipitate growth along the austenite/ferrite interface than perpendicular to it because of the faster vanadium diffusion along the interface. The slower phase transformation kinetics at 700 °C enable more time for the vanadium diffusion along the austenite/ferrite interface and lead to higher aspect ratios between the precipitate ellipsoidal radii. The polar radius, R_p, of the precipitates evolves in the range of 1-4 nm in all conditions, while the radius in the equatorial plane, R_{eq}, can reach maximum values from 10 to 50 nm, depending on the alloy and the annealing temperature.
- An interesting outcome is the delay in the onset and time evolution of the phase transformation due to the external magnetic field applied during the in-situ measurements, which consequently affects the precipitation kinetics, i.e. fewer and larger precipitates are formed. This once more confirms the coupling between the phase transformation and the precipitation kinetics.
Overall, our in-situ investigations provide quantitative information on the interaction of the austenite-to-ferrite phase-transformation kinetics with the vanadium-carbide precipitation kinetics. The outcome of this study can open new horizons in acquiring valuable quantitative data during the processing of steels with different compositions. The quantitative results can contribute to modelling and eventually predicting the precipitation and phase-transformation kinetics in steels which can lead to the optimization of steel design for automotive applications with reduced energy consumption.

Acknowledgements

This work was financially supported by the Materials Innovation Institute M2i (www.m2i.nl), project S41.5.14548, in the framework of the M2i Partnership Program, and the Technology Foundation TTW (www.stw.nl), which is part of the Netherlands Organization for Scientific Research (www.nwo.nl). The authors would like to acknowledge the use of the Larmor beamline at ISIS (experiment number RB1869024 [53]) and the Nederlandse Organisatie voor Wetenschappelijk Onderzoek Groot grant no. LARMOR 721.012.102. The help of the support staff from ISIS during the neutron experiments is greatly acknowledged and very much appreciated. The authors are grateful to Tata Steel in Europe for providing the materials as hot-rolled plates. Finally, the authors thank Vitaliy Bliznuk for his assistance on TEM investigations in Ghent University.

References

[1] K. Seto, Y. Funakawa, and S. Kaneko, “Hot rolled high strength steels for suspension and chassis parts "NANOHITEN and ‘BHT® steel,’” JFE Tech. Rep., vol. 10, no. 10, pp. 19–25, 2007.
[2] A. Rijkenberg, A. Blowey, P. Bellina, and C. Wooffindin, “Advanced High Stretch-Flange Formability Steels for Chassis & Suspension Applications,” Conf. Steels Cars Truck., vol. 2014, no. 4, pp. 426–433, 2014.
[3] Y. Funakawa, T. Shiozaki, K. Tomita, T. Yamamoto, and E. Maeda, “Development of high strength hot-rolled sheet steel consisting of ferrite and nanometer-sized carbides,” ISIJ Int., vol. 44, no. 11, pp. 1945–1951, 2004, doi: 10.2355/isijinternational.44.1945.
[4] T. N. Baker, “Microalloyed steels,” Ironmak. Steelmak., vol. 43, no. 4, pp. 264–307, 2016, doi: 10.1179/1743281215Y.0000000063.
[5] T. N. Baker, “Processes, microstructure and properties of vanadium microalloyed steels,” Mater. Sci. Technol., vol. 25, no. 9, pp. 1083–1107, 2009, doi: 10.1179/174328409X453253.

[6] S. Z. and B. H. Rune Lagneborg, Tadeusz Siwecki, “Role of vanadium in microalloyed steels,” Stal’, no. 12, pp. 58–59, 2001.
[7] P. Gong, X. G. Liu, A. Rijkenberg, and W. M. Rainforth, “The effect of molybdenum on interphase precipitation and microstructures in microalloyed steels containing titanium and vanadium,” Acta Mater., vol. 161, pp. 374–387, 2018, doi: 10.1016/j.actamat.2018.09.008.
[8] G. Miyamoto, R. Hori, B. Poorganji, and T. Furuhara, “Interphase precipitation of VC and resultant hardening in V-added medium carbon steels,” ISIJ Int., vol. 51, no. 10, pp. 1733–1739, 2011, doi: 10.2355/isijinternational.51.1733.
[9] Y. J. Zhang et al., “Effects of transformation temperature on VC interphase precipitation and resultant hardness in low-carbon steels,” Acta Mater., vol. 84, pp. 375–384, 2015, doi: 10.1016/j.actamat.2014.10.049.
[10] Y. Q. Wang et al., “Investigating nano-precipitation in a V-containing HSLA steel using small angle neutron scattering,” Acta Mater., vol. 145, pp. 84–96, 2018, doi: 10.1016/j.actamat.2017.11.032.
[11] Y. Oba et al., “Quantitative analysis of precipitate in vanadium-microalloyed medium carbon steels using small-angle X-ray and neutron scattering methods,” ISIJ Int., vol. 51, no. 11, pp. 1852–1858, 2011, doi: 10.2355/isijinternational.51.1852.
[12] S. Shanmugam, M. Tanniru, R. D. K. Misra, D. Panda, and S. Jansto, “Microalloyed V-Nb-Ti and V steels Part 2 - Precipitation behaviour during processing of structural beams,” Mater. Sci. Technol., vol. 21, no. 2, pp. 165–177, 2005, doi: 10.1179/174328405X18656.
[13] Thierry Epicier; Daniel Acevedo-Reyes; MichelPerez, “Crystallographic structure of vanadium carbide precipitates in a model Fe-C-V steel,” Int. J. Prod. Res., vol. 23, no. september, pp. 1–36, 2010.
[14] C. Ioannidou et al., “Evolution of the precipitate composition during annealing of vanadium micro-alloyed steels by in-situ SANS,” Acta Mater., vol. 201, pp. 217–230, 2020, doi: 10.1016/j.actamat.2020.09.083.
[15] M. Nöhrer, S. Zamberger, S. Primig, and H. Leitner, “Atom probe study of vanadium interphase precipitates and randomly distributed vanadium precipitates in ferrite,” Micron, vol. 54–55, pp. 57–64, 2013, doi: 10.1016/j.micron.2013.08.008.
[16] C. Ioannidou et al., “Interaction of precipitation with austenite-to-ferrite phase transformation in vanadium micro-alloyed steels,” Acta Mater., vol. 181, pp. 10–24, 2019, doi: 10.1016/j.actamat.2019.09.046.
[17] C. Ioannidou, Z. Arechabaleta, A. Rijkenberg, R. M. Dalgliesh, A. A. van Well, and S. E. Offerman, “Vc-precipitation kinetics studied by small-angle neutron scattering in nano-steels,” Mater. Sci. Forum, vol. 941 MSF, pp. 236–244, 2018, doi: 10.4028/www.scientific.net/MSF.941.236.
[18] M. Y. Chen, M. Gouné, M. Verdier, Y. Bréchet, and J. R. Yang, “Interphase precipitation in vanadium-alloyed steels: Strengthening contribution and morphological variability with austenite to ferrite transformation,” Acta Mater., vol. 64, pp. 78–92, 2014, doi: 10.1016/j.actamat.2013.11.025.
[19] Y. J. Zhang, G. Miyamoto, K. Shinbo, and T. Furuhara, “Effects of α/γ orientation relationship on VC interphase precipitation in low-carbon steels,” Scr. Mater., vol. 69, no. 1, pp. 17–20, 2013, doi: 10.1016/j.scriptamat.2013.03.020.
[20] G. Miyamoto, R. Hori, B. Poorganji, and T. Furuhara, “Crystallographic analysis of proeutectoid ferrite/austenite interface and interphase precipitation of vanadium carbide in medium-carbon steel,” Metall. Mater. Trans. A Phys. Metall. Mater. Sci., vol. 44, no. 8, pp. 3436–3443, 2013, doi: 10.1007/s11661-013-1702-2.
[21] Y. J. Zhang, G. Miyamoto, K. Shinbo, and T. Furuhara, “Quantitative measurements of phase equilibria at migrating α/γ interface and dispersion of VC interphase precipitates:

Evaluation of driving force for interphase precipitation," Acta Mater., vol. 128, pp. 166–175, 2017, doi: 10.1016/j.actamat.2017.02.020.
[22] X. Zhang et al., "Microstructure, precipitate and property evolution in cold-rolled Ti-V high strength low alloy steel," Mater. Des., vol. 192, 2020, doi: 10.1016/j.matdes.2020.108720.
[23] S. Dhara, R. K. W. Marceau, K. Wood, T. Dorin, I. B. Timokhina, and P. D. Hodgson, "Precipitation and clustering in a Ti-Mo steel investigated using atom probe tomography and small-angle neutron scattering," Mater. Sci. Eng. A, vol. 718, no. November 2017, pp. 74–86, 2018, doi: 10.1016/j.msea.2018.01.070.
[24] A. Navarro-López et al., "Furnace for in situ and simultaneous studies of nano-precipitates and phase transformations in steels by SANS and neutron diffraction," Rev. Sci. Instrum., vol. 91, no. 12, 2020, doi: 10.1063/5.0022507.
[25] Andersson J.O., Helander T., Höglund L., Shi P.F., and Sundman B., (2002). Thermo-Calc and DICTRA, Computational tools for materials science. Calphad, 26, 273-312., [Online]. Available: Andersson J.O., Helander T., Höglund L., Shi P.F., and Sundman B., (2002). Thermo-Calc and DICTRA, Computational tools for materials science. Calphad, 26, 273-312.
[26] https://www.isis.stfc.ac.uk/Pages/Larmor.aspx.
[27] https://www.isis.stfc.ac.uk/Pages/home.aspx.
[28] O. Arnold et al., "Mantid - Data analysis and visualization package for neutron scattering and μ SR experiments," Nucl. Instruments Methods Phys. Res. Sect. A Accel. Spectrometers, Detect. Assoc. Equip., vol. 764, pp. 156–166, 2014, doi: 10.1016/j.nima.2014.07.029.
[29] L. Van Eijck et al., "Design and performance of a novel neutron powder diffractometer: PEARL at TU Delft," J. Appl. Crystallogr., vol. 49, no. 5, pp. 1398–1401, 2016, doi: 10.1107/S160057671601089X.
[30] N. Yano, T. Yamada, T. Hosoya, T. Ohhara, I. Tanaka, and K. Kusaka, "Application of profile fitting method to neutron time-of-flight protein single crystal diffraction data collected at the iBIX," Sci. Rep., vol. 6, no. August, pp. 4–12, 2016, doi: 10.1038/srep36628.
[31] M. Avrami, "Kinetics of phase change. I: General theory," J. Chem. Phys., vol. 7, no. 12, pp. 1103–1112, 1939, doi: 10.1063/1.1750380.
[32] J. W. Cahn, "The kinetics of grain boundary nucleated reactions," Acta Metall., vol. 4, no. 5, pp. 449–459, 1956, doi: 10.1016/0001-6160(56)90041-4.
[33] E. G. Dere, "Microstructure Control of Fire-Resistant, Low-Alloy Steel, An In-situ 3D X-Ray Diffraction and Small-Angle X-Ray Scattering Study, Phd Thesis TUDelft 2013."
[34] G. P. Krielaart and S. Van Der Zwaag, "Kinetics of γ→γ phase transformation in Fe-Mn alloys containing low manganese," Mater. Sci. Technol., vol. 14, no. 1, pp. 10–18, 1998, doi: 10.1179/mst.1998.14.1.10.
[35] V. Shah, M. Krugla, S. E. Offerman, J. Sietsma, and D. N. Hahlon, "Effect of silicon, manganese and heating rate on the ferrite recrystallization kinetics," ISIJ Int., vol. 60, no. 6, pp. 1312–1323, 2020, doi: 10.2355/isijinternational.ISIJINT-2019-475.
[36] Q. Yong, X. Sun, Z. Li, Z. Wang, and K. Zhang, "Physical Metallurgical Principles of Titanium Microalloyed Steel---Dissolution and Precipitation of Titanium-Bearing Secondary Phases," in Titanium Microalloyed Steel: Fundamentals, Technology, and Products, X. Mao, Ed. Singapore: Springer Singapore, 2019, pp. 71–139.
[37] M. Hillert, "Diffusion and interface control of reactions in alloys," Metall. Trans. A, vol. 6, no. 1, pp. 5–19, 1975, doi: 10.1007/BF02673664.
[38] H. Guo and M. Enomoto, "Effects of substitutional solute accumulation at α/γ boundaries on the growth of ferrite in low carbon steels," Metall. Mater. Trans. A Phys. Metall. Mater. Sci., vol. 38, no. 6, pp. 1152–1161, 2007, doi: 10.1007/s11661-007-9139-0.
[39] H. Chen, K. Zhu, L. Zhao, and S. Van Der Zwaag, "Analysis of transformation stasis during the isothermal bainitic ferrite formation in Fe-C-Mn and Fe-C-Mn-Si alloys," Acta Mater., vol. 61, no. 14, pp. 5458–5468, 2013, doi: 10.1016/j.actamat.2013.05.034.

[40] S. Clark, V. Janik, Y. Lan, and S. Sridhar, “Interphase precipitation - An interfacial segregation model,” ISIJ Int., vol. 57, no. 3, pp. 524–532, 2017, doi: 10.2355/isijinternational.ISIJINT-2016-544.
[41] R. Okamoto and J. Agren, “A model for interphase precipitation based on finite interface solute drag theory,” vol. 58, pp. 4791–4803, 2010, doi: 10.1016/j.actamat.2010.05.016.
[42] H. Dong et al., “Unraveling the effects of Nb interface segregation on ferrite transformation kinetics in low carbon steels,” Acta Mater., p. 117081, 2021, doi: 10.1016/j.actamat.2021.117081.
[43] M. Enomoto, H. Guo, Y. Tazuke, Y. R. Abe, and M. Shimotomai, “Influence of magnetic field on the kinetics of proeutectoid ferrite transformation in iron alloys,” Metall. Mater. Trans. A Phys. Metall. Mater. Sci., vol. 32, no. 3, pp. 445–453, 2001, doi: 10.1007/s11661-001-0061-6.
[44] H. Fujii, “Effects of magnetic-field on elemental process for microstructural development of iron-based polycrystalline materials, PhD thesis, Tohoku University, 2009.”
[45] T. Narayanan, “Synchrotron Small-Angle X-Ray Scattering Studies of Colloidal Suspensions,” in Applications of Synchrotron Light to Scattering and Diffraction in Materials and Life Sciences, M. Gomez, A. Nogales, M. C. Garcia-Gutierrez, and T. A. Ezquerra, Eds. Berlin, Heidelberg: Springer Berlin Heidelberg, 2009, pp. 133–156.
[46] A. Wiedenmann, “CHAPTER 10 - Small Angle Neutron Scattering Investigations of Magnetic Nanostructures,” in Neutron Scattering from Magnetic Materials, T. Chatterji, Ed. Amsterdam: Elsevier Science, 2006, pp. 473–520.
[47] L. A. Feigin, D. I. Svergun, and G. W. Taylor, “Determination of the Integral Parameters of Particles,” in Structure Analysis by Small-Angle X-Ray and Neutron Scattering, G. W. Taylor, Ed. Boston, MA: Springer US, 1987, pp. 59–105.
[48] SasView, SasView for small angle scattering analysis. http://www.sasview. org/index.html, 2017. (Accessed 4 January 2017).
[49] S. G. E. Te Velthuis, N. H. Van Dijk, M. T. Rekveldt, J. Sietsma, and S. Van Der Zwaag, “A three-dimensional model for the development of the microstructure in steel during slow cooling,” Mater. Sci. Eng. A, vol. 277, no. 1–2, pp. 218–228, 2000, doi: 10.1016/s0921-5093(99)00531-6.
[50] C. E. I. C. Ohlund, J. Weidow, M. Thuvander, and S. E. Offerman, “Effect of ti on evolution of microstructure and hardness of martensitic Fe-C-mn steel during tempering,” ISIJ Int., vol. 54, no. 12, pp. 2890–2899, 2014, doi: 10.2355/isijinternational.54.2890.
[51] H. Sharma, J. Sietsma, and S. E. Offerman, “Preferential nucleation during polymorphic transformations,” Sci. Rep., vol. 6, no. August, pp. 1–7, 2016, doi: 10.1038/srep30860.
[52] S. E. Offerman et al., “Reply to the discussion by Aaronson et al. to ‘Grain nucleation and growth during phase transformations’ by S.E. Offerman et al., Science, 298, 1003 (November 1, 2002),” Scr. Mater., vol. 51, no. 9, pp. 937–941, 2004, doi: 10.1016/j.scriptamat.2004.06.031.
[53] S. E. Offerman, E. van der Wal, A.A. van Well, C. Ioannidou, A. Navarro-López, R.M. Dalgliesh, “In-situ and simultaneous SANS and ND to study the precipitation and phase transformation kinetics in V-containing Nano-steels, STFC ISIS Neutron and Muon Source (2019).” https://doi.org/10.5286/ISIS.E.100757775.

Appendix A

Supplementary material to Chapter 2

A1. Precipitation kinetics at 900 °C and at 750 °C

The graphs in Figs. A1a and b show the nuclear and magnetic scattering cross sections, $(d\Sigma/d\Omega)(Q)$, of the LCLV and HCHV steels, respectively, that have followed an isothermal annealing treatment at 900 °C and 750 °C for 10 hours. These SANS components are compared to the nuclear and magnetic scattering intensity of the specimen of each steel that is directly quenched from the soaking temperature to room temperature. The directly quenched specimen is fully martensitic and does not contain any precipitates. In Figs. A1a and b, it is shown that there is no increase in the nuclear intensity curve after annealing for 10 hours at 900 °C or at 750 °C with respect to the nuclear intensity of the directly quenched specimen. The same behaviour is observed for the magnetic scattering components in both steels, from which we conclude that no precipitates are detected at 900 °C and at 750 °C after 10 hours of annealing. All these curves follow a Q^{-4} behaviour (Porod's Law), indicating that scattering originates from objects like grain boundaries and interfaces [1],[2],[3]. No deviations from the Q^{-4} behaviour are observed, confirming that precipitates are not detected in any of these conditions. The absence of precipitates at 900 °C and at 750 °C in both steels is closely related to (near) absence of the austenite-to-ferrite phase transformation, based on dilatometry and SEM. Since austenite-to-ferrite phase transformation does not take place at 900 °C in both steels and at 750 °C in HCHV steel, and due to the high solubility of the vanadium carbide precipitates in austenite, precipitates are not formed in these conditions. Precipitates are also not detected in the LCLV steel at 750 °C after 10 hours of isothermal holding, although a small fraction of austenite is transformed to ferrite in this steel. Nucleation of precipitates might have started in this condition, however, the precipitates size and volume fraction are expected to be extremely small and therefore not detectable by the SANS technique.

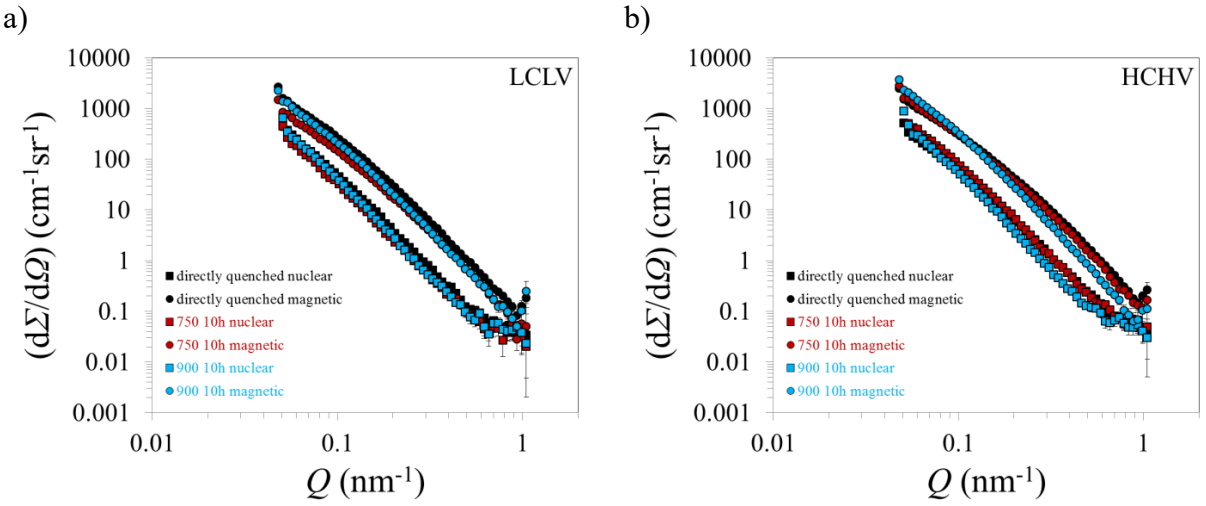

Fig. A1. Nuclear and magnetic differential scattering cross sections as a function of Q of a) LCLV and b) HCHV steels after annealing at 900 °C or at 750 °C for 10h and quenched to room temperature. They are compared to the scattering of the specimen directly quenched from soaking to room temperature.

References

[1]. S. M. He, N. H. van Dijk, M. Paladugu, H. Schut, J. Kohlbrecher, F. D. Tichelaar, and S. van der Zwaag, In situ determination of aging precipitation in deformed Fe-Cu and Fe-Cu-B-N alloys by time-resolved small-angle neutron scattering, Phys. Rev. B 82 (2010) 174111 1-14.
[2]. T. Narayanan, Synchrotron Small-Angle X-Ray Scattering, in R. Borsali, R. Pecora (Eds.), Soft-Matter Characterization, Springer (2008) 899-948.
[3]. G. G. Long, L.E. Levine, Ultra-small-angle X-ray scattering from dislocation structures, Acta Crystallographica (2005) Section A61, 557-567.

Appendix B

Supplementary material to Chapter 4

B1. Small-Angle Neutron Scattering measurements

The experimental configuration of the Small-Angle Neutron Scattering (SANS) measurements is shown in Fig. B1. The furnace components, the detector plane and the magnetic field direction are illustrated.

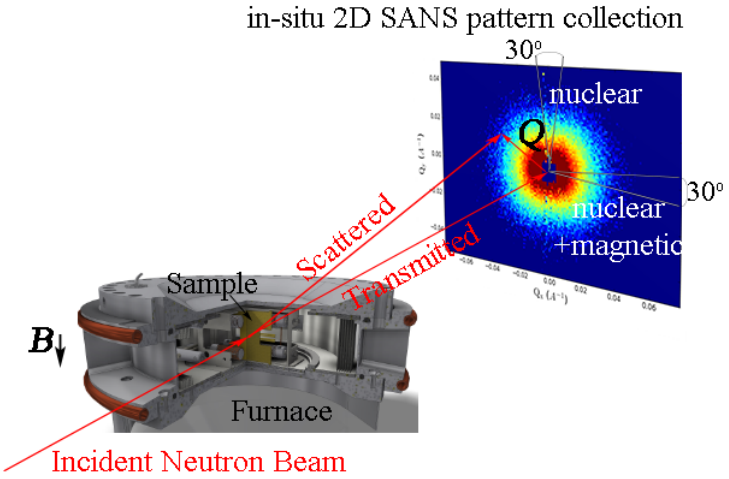

Fig. B1. Experimental configuration of the SANS measurements

B1.1. Nuclear and magnetic SANS components

The differential scattering cross sections of the LCLV, LCHV and HCHV steels obtained by in-situ SANS during annealing at 650 °C and at 700 °C are shown in the graphs of Figs. B2a-l. These curves are obtained after the background subtraction, therefore consist only of the precipitation scattering contribution. The subtracted background signal consists of the furnace scattering contribution and the scattering from a steel without precipitates (obtained from the scattering of the samples at soaking temperature). The SANS intensity during cooling (obtained by using 1 min time-slice) was compared to the SANS signal at high temperature and the curves are overlapping, indicating no precipitation before the isothermal annealing temperature is reached.

Four representative time slices are chosen and the SANS intensity time evolution during isothermal holding is shown. The nuclear scattering curves of the LCLV, LCHV and HCHV steels at 650 °C are plotted in Figs. B2a, c and e, respectively, and their corresponding magnetic components in Figs. B2b, d and f. Likewise, the nuclear scattering curves of the LCLV, LCHV and HCHV steels at 700 °C are shown in Figs. B2g, i and k, while their magnetic components in Figs. B2h, j and l.

For all steels, both nuclear and magnetic intensities are increasing with time due to precipitation, and the amount of intensity increase depends on the volume fraction of the precipitates formed. In all steels, the intensity increases more rapidly during the first hour of annealing indicating faster kinetics in the beginning of annealing. The intensity curves belonging to shorter annealing times have larger error bars because of the shorter time slices. The errors are smaller when longer time slices are chosen.

a)

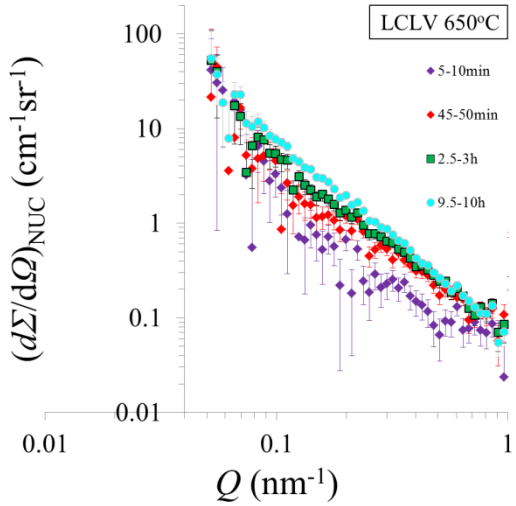
LCLV 650ºC
5-10min
45-50min
2.5-3h
9.5-10h
$(d\Sigma/d\Omega)_{NUC}$ (cm^{-1}sr^{-1})
Q (nm^{-1})

b)

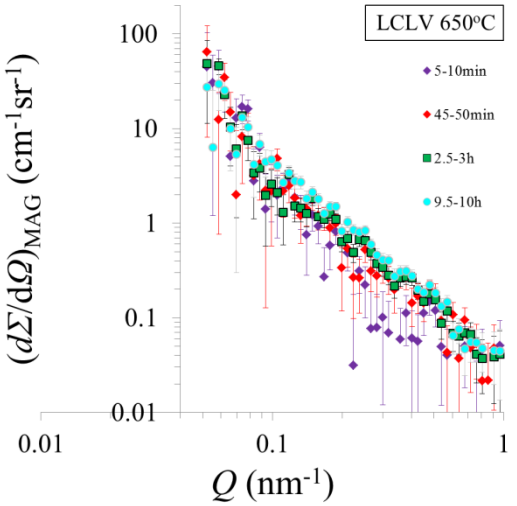
LCLV 650ºC
5-10min
45-50min
2.5-3h
9.5-10h
$(d\Sigma/d\Omega)_{MAG}$ (cm^{-1}sr^{-1})
Q (nm^{-1})

c)

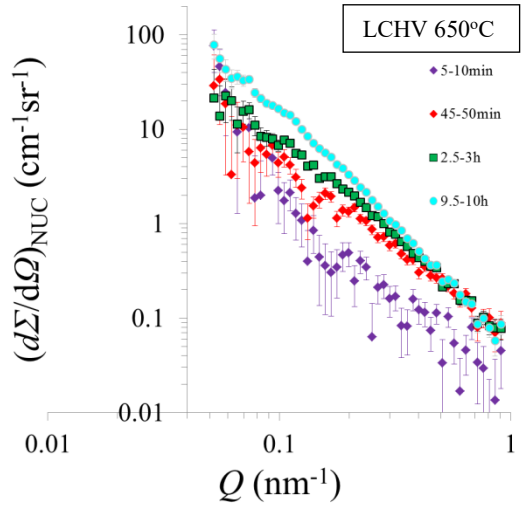
LCHV 650ºC
5-10min
45-50min
2.5-3h
9.5-10h
$(d\Sigma/d\Omega)_{NUC}$ (cm^{-1}sr^{-1})
Q (nm^{-1})

d)

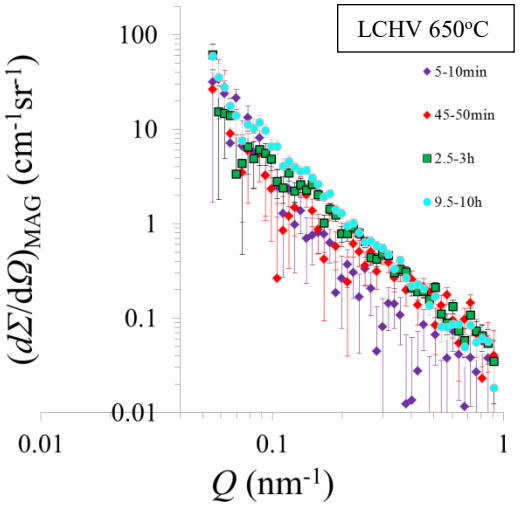
LCHV 650ºC
5-10min
45-50min
2.5-3h
9.5-10h
$(d\Sigma/d\Omega)_{MAG}$ (cm^{-1}sr^{-1})
Q (nm^{-1})

e)

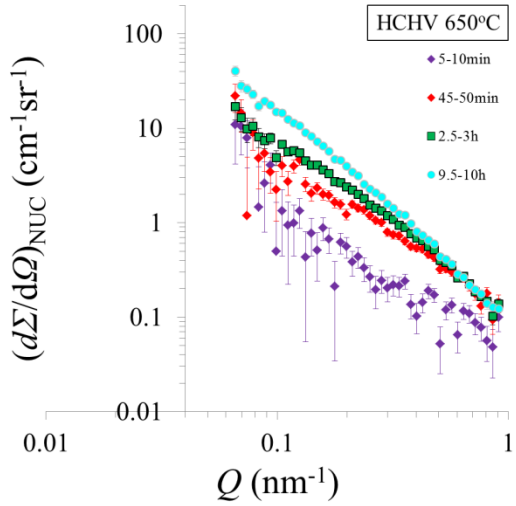
HCHV 650ºC
5-10min
45-50min
2.5-3h
9.5-10h
$(d\Sigma/d\Omega)_{NUC}$ (cm^{-1}sr^{-1})
Q (nm^{-1})

f)

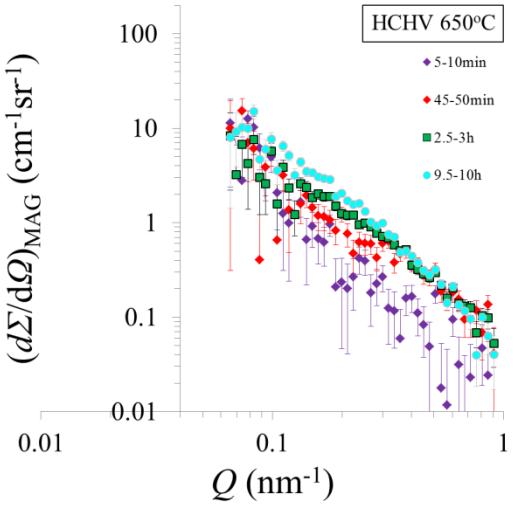
HCHV 650ºC
5-10min
45-50min
2.5-3h
9.5-10h
$(d\Sigma/d\Omega)_{MAG}$ (cm^{-1}sr^{-1})
Q (nm^{-1})

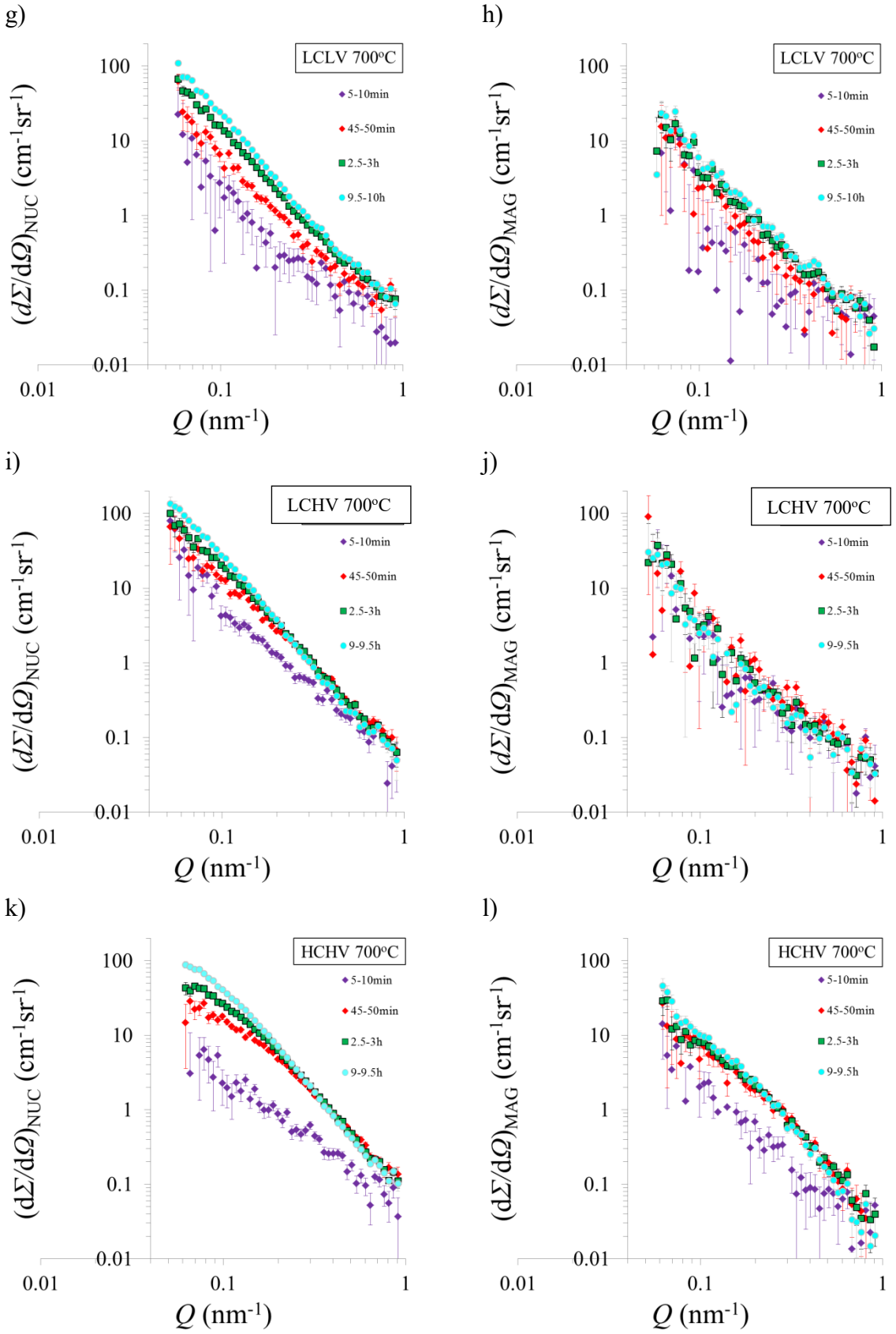

Fig. B2. Nuclear differential scattering cross sections during annealing of the: LCLV steel at a) 650 and g) 700 °C, LCHV steel at c) 650 and i) 700 °C and HCHV steel at e) 650 and k) 700 °C. The corresponding magnetic differential scattering cross sections are plotted in b), h), d), j), f) and l), respectively. The scattering curves of selected times are shown.

B1.2. *Q*-independency of the experimental $(d\Sigma/d\Omega)_{NUC}/(d\Sigma/d\Omega)_{MAG}$ ratio

As explained in Chapter 4, the in-situ SANS measurements allow for an optimum background subtraction and therefore for an accurate precipitate signal collection. If the magnetic saturation is reached, the precipitates have the same nuclear and magnetic size. As a result, the $(d\Sigma/d\Omega)_{NUC}/(d\Sigma/d\Omega)_{MAG}$ ratio is related only to the composition of the precipitates and is free from any other contributions, i.e. the experimental $(d\Sigma/d\Omega)_{NUC}/(d\Sigma/d\Omega)_{MAG}$ ratio is equal to $\Delta\rho^2_{NUC}/\Delta\rho^2_{MAG}$ and it should not be Q dependent in each individual time slice.
In other words, the inconsiderable Q dependency of the $(d\Sigma/d\Omega)_{NUC}/(d\Sigma/d\Omega)_{MAG}$ ratio is critical for the precipitate chemical composition analysis. It is the required condition so that the equation

$$\frac{\left(\frac{d\Sigma}{d\Omega}\right)_{NUC}(Q)}{\left(\frac{d\Sigma}{d\Omega}\right)_{MAG}(Q)} = \frac{(\Delta\rho_{NUC})^2}{(\Delta\rho_{MAG})^2} \qquad \text{(Eq. 4.4, Chapter 4)}$$

is valid. Only if this criterion is met, the ratio is determined only by the chemical composition of the precipitates.
The plots in Figs. B3a-h are examples of the Q independency of the $(d\Sigma/d\Omega)_{NUC}/(d\Sigma/d\Omega)_{MAG}$ ratio (through same Q dependency of the nuclear and the magnetic components) in LCLV, LCHV and HCHV steels annealed at 650 °C and 700 °C for some selected time slices. Figs. B3a-d belong to LCLV, B3e-h to LCHV and B3i-l to HCHV specimens.
Deviations from the same Q dependency of the nuclear and the magnetic components in the low-Q area are attributed to the large scatter in the values during that time slice because of the counting statistics. The contribution of these points to the calculations is minimized by the use of the weighted average for the $(d\Sigma/d\Omega)_{NUC}/(d\Sigma/d\Omega)_{MAG}$ ratio over Q for each time slice.

a)

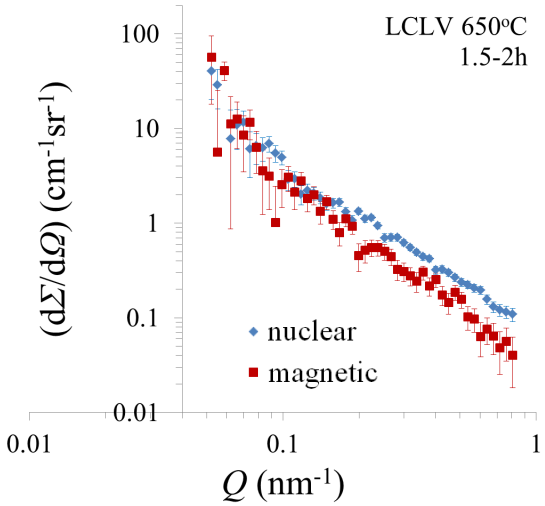
LCLV 650ºC
1.5-2h
nuclear
magnetic
(dΣ/dΩ) (cm⁻¹sr⁻¹)
Q (nm⁻¹)
100
10
1
0.1
0.01
0.01
0.1
1

b)

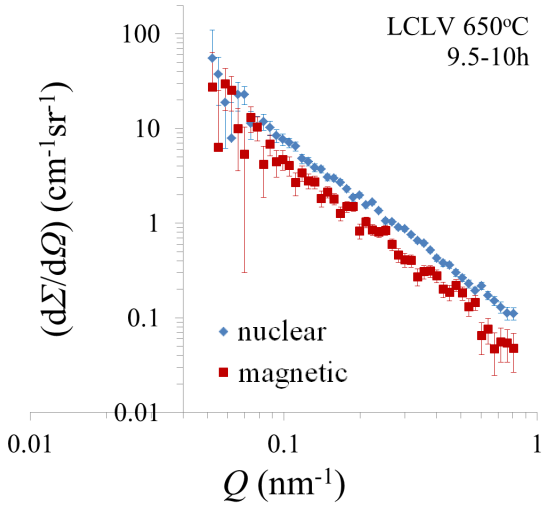
LCLV 650ºC
9.5-10h
nuclear
magnetic
(dΣ/dΩ) (cm⁻¹sr⁻¹)
Q (nm⁻¹)
100
10
1
0.1
0.01
0.01
0.1
1

c)

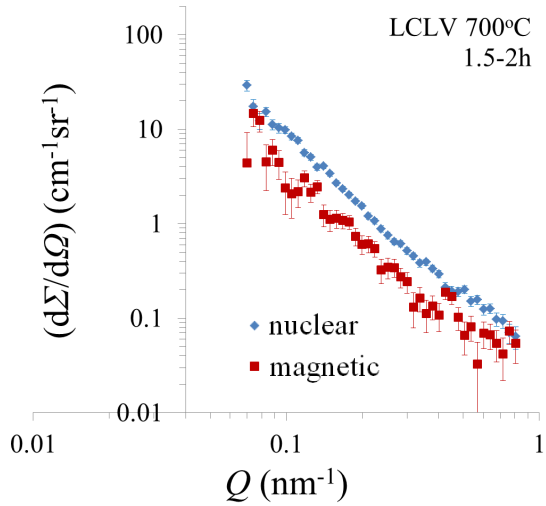
LCLV 700ºC
1.5-2h
nuclear
magnetic
(dΣ/dΩ) (cm⁻¹sr⁻¹)
Q (nm⁻¹)
100
10
1
0.1
0.01
0.01
0.1
1

d)

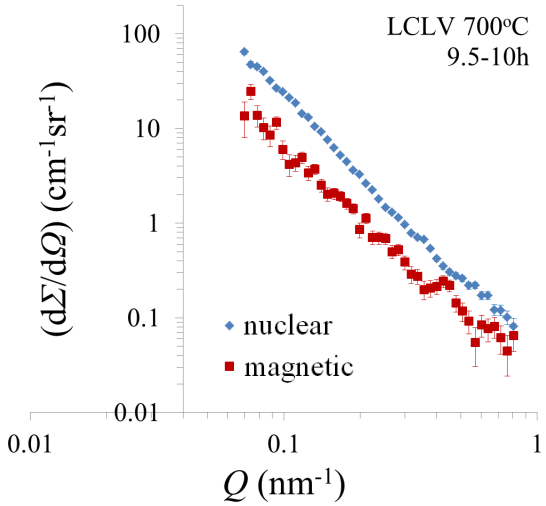
LCLV 700ºC
9.5-10h
nuclear
magnetic
(dΣ/dΩ) (cm⁻¹sr⁻¹)
Q (nm⁻¹)
100
10
1
0.1
0.01
0.01
0.1
1

e)

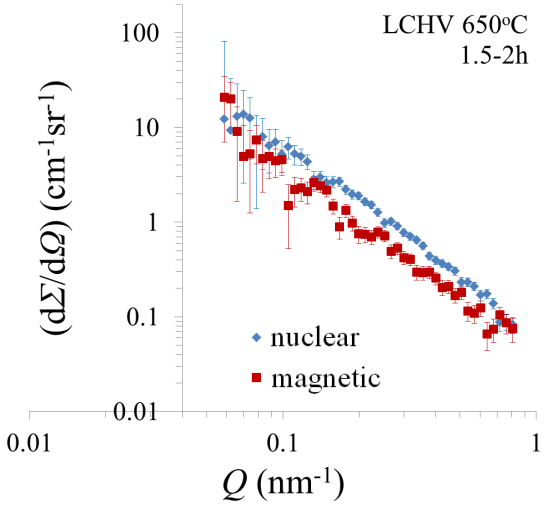
LCHV 650ºC
1.5-2h
nuclear
magnetic
(dΣ/dΩ) (cm⁻¹sr⁻¹)
Q (nm⁻¹)
100
10
1
0.1
0.01
0.01
0.1
1

f)

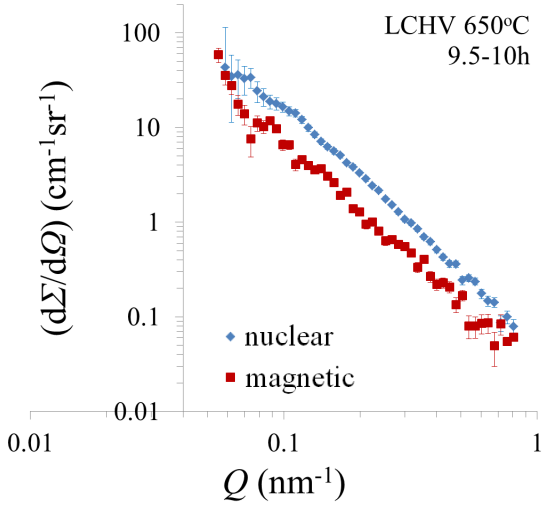
LCHV 650ºC
9.5-10h
nuclear
magnetic
(dΣ/dΩ) (cm⁻¹sr⁻¹)
Q (nm⁻¹)
100
10
1
0.1
0.01
0.01
0.1
1

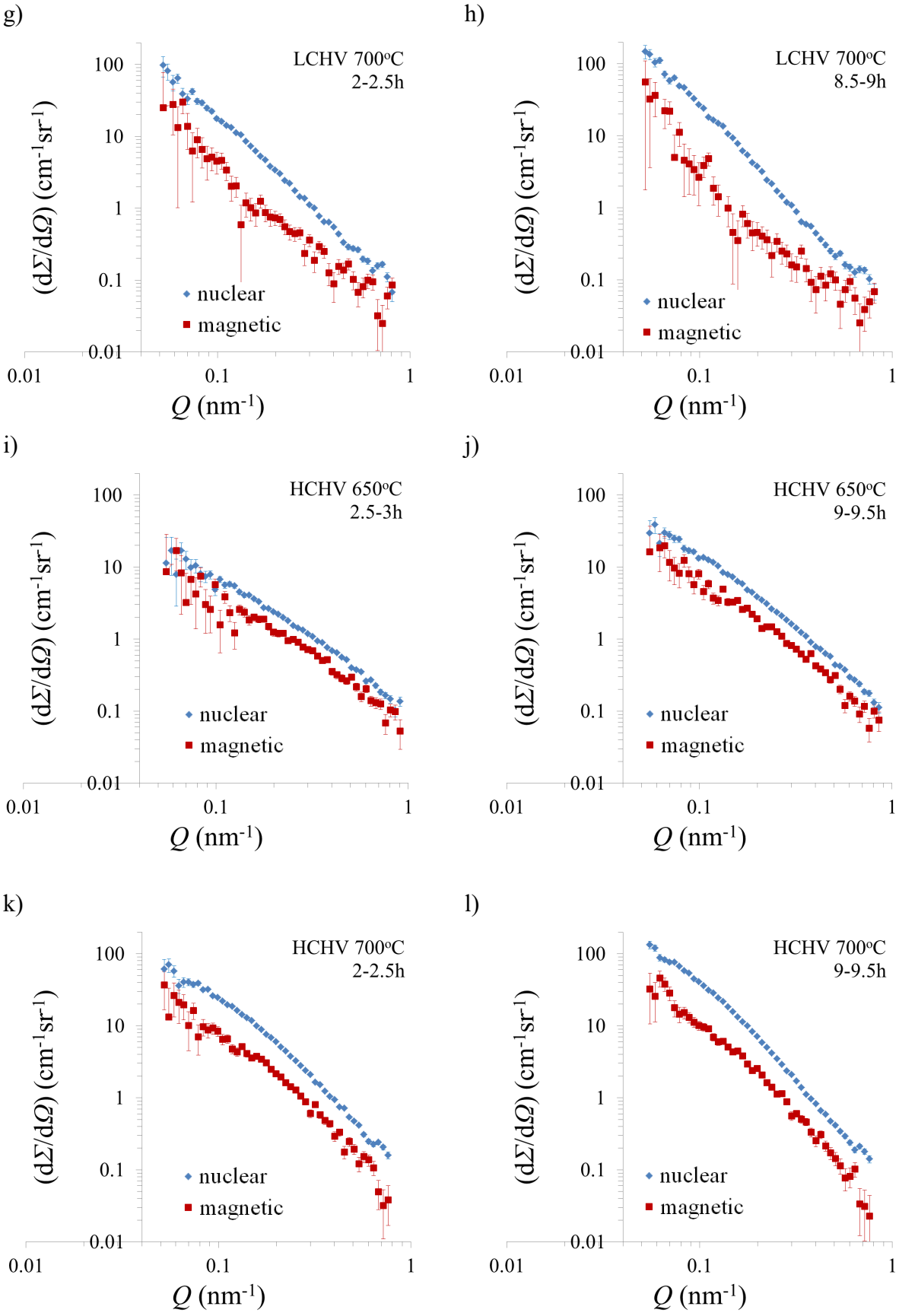

Fig. B3. Representative curves of nuclear and magnetic differential scattering cross sections vs Q of the a-d) LCLV, e-h) LCHV and i-l) HCHV specimens annealed at 650 °C and 700 °C.

B2. Atom Probe Tomography measurements

B2.1. 3D APT maps of V and C atoms

Fig. B4 shows representative 3D vanadium and carbon atom maps in the same tip belonging to a LCLV steel sample annealed at 650 °C for 10 h. The vanadium and carbon rich regions correspond to vanadium carbides.

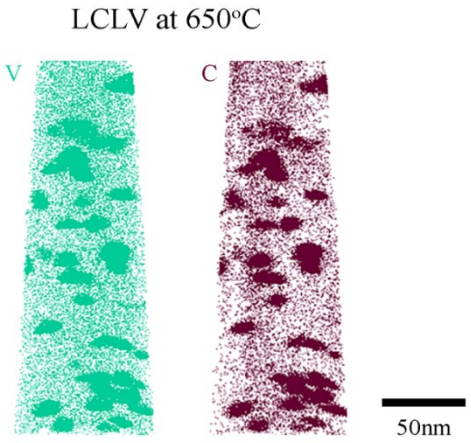

Fig. B4. From left to right: 3D APT maps of V atoms and C atoms in a tip belonging to a LCLV steel sample annealed at 650 °C for 10 h.

B2.2. APT Proximity Diagrams

Proximity Diagrams (proxigrams) based on iso-concentration surfaces (iso-surfaces) of 2 at%V are used to provide the precipitates' chemical composition profile. The 1D composition profiles of two precipitates in each steel annealed at 650 °C for 10 h are presented in Figs. B5-7 as a proof of the presence of precipitates with different substoichiometric ratios.

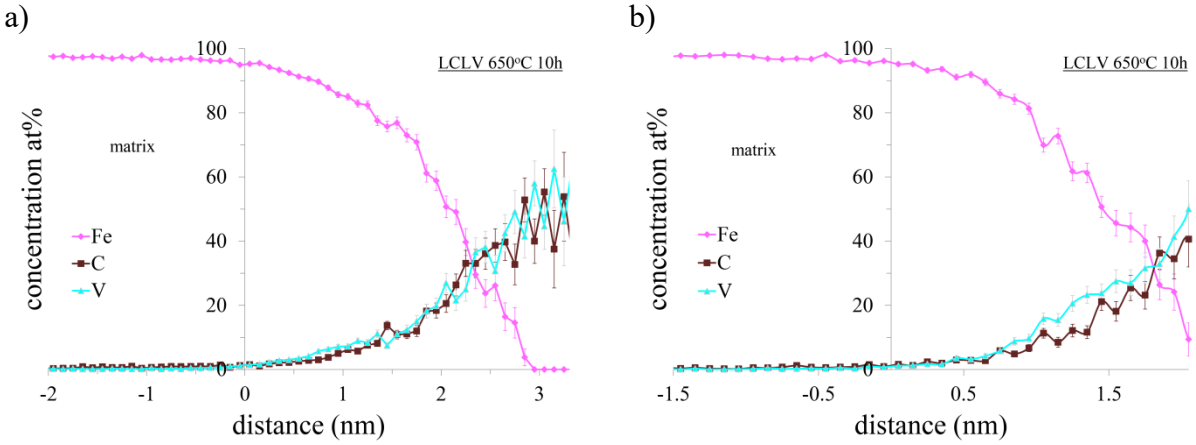

Fig. B5. Representative proximity diagrams of two precipitates differing in stoichiometry in the LCLV steel annealed at 650 °C for 10 h. In a), the carbon-to-metal ratio is closer to the stoichiometric ratio than in b).

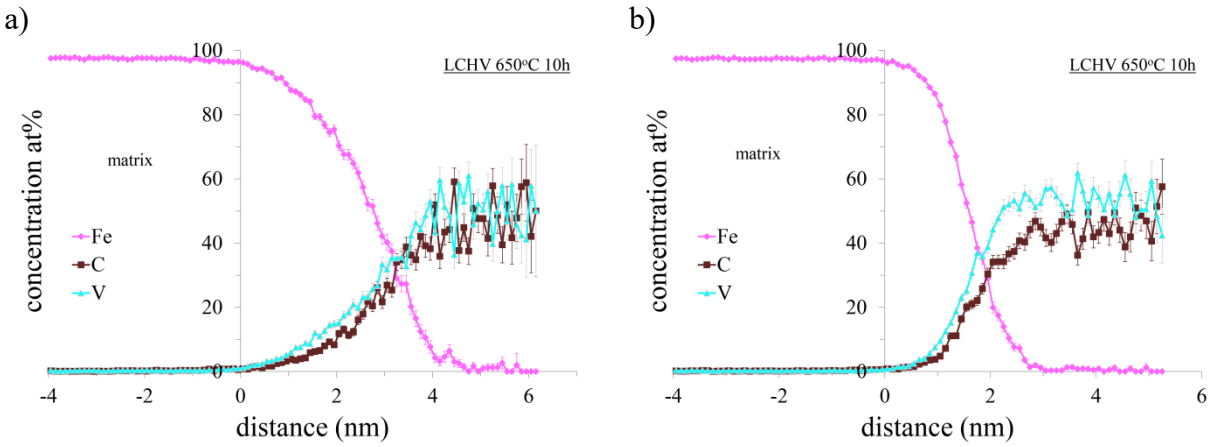

Fig. B6. Representative proximity diagrams of two precipitates differing in stoichiometry in the LCHV steel annealed at 650°C for 10 h. In a), the carbon-to-metal ratio is closer to the stoichiometric ratio than in b).

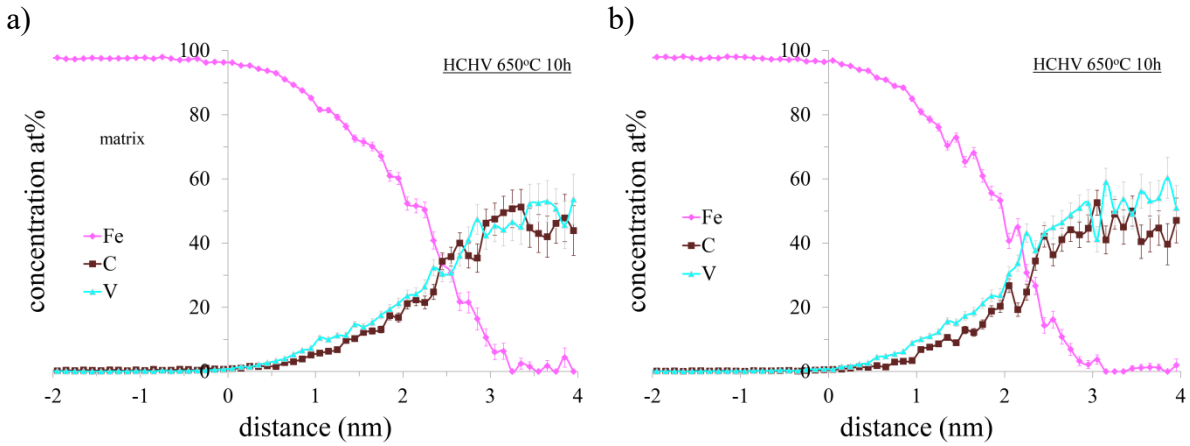

Fig. B7. Representative proximity diagrams of two precipitates differing in stoichiometry in the HCHV steel annealed at 650°C for 10 h. In a), the carbon-to-metal ratio is closer to the stoichiometric ratio than in b).

Appendix C

Supplementary material to Chapter 5

C1. Phase transformation kinetics by neutron diffraction

The first step in the neutron diffraction data analysis is subtracting the background signal (empty furnace measurement) from the overall signal (consisting of background + specimen signal). In this way, the signal originating only from the sample is isolated. Fig. C1 shows the diffraction patterns of the empty furnace and the steel specimen after the background subtraction, during the 10th min of isothermal holding of the LCLV steel at 650 °C. The diffraction pattern obtained from the empty furnace is recorded at room temperature. This pattern is considered to be the background signal and is subtracted from the diffraction signals obtained from the steel specimen.

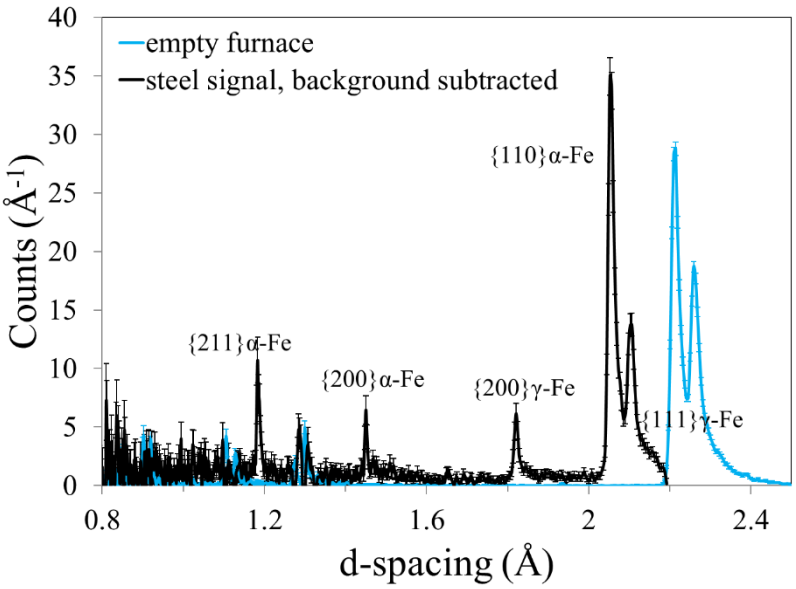

Fig. C1. Diffraction patterns of the empty furnace and the steel specimen after background subtraction, obtained during the 10th min of isothermal holding of the LCLV steel at 650 °C.

The time evolution of the ferrite and austenite diffraction peaks in the LCLV, LCHV and HCHV steels during the first hour of isothermal annealing at 650 °C and at 700 °C is presented in Fig. C2. During annealing, austenite is transforming to ferrite therefore the peak area of the austenitic peaks is decreasing while the area below the ferritic peaks is increasing.

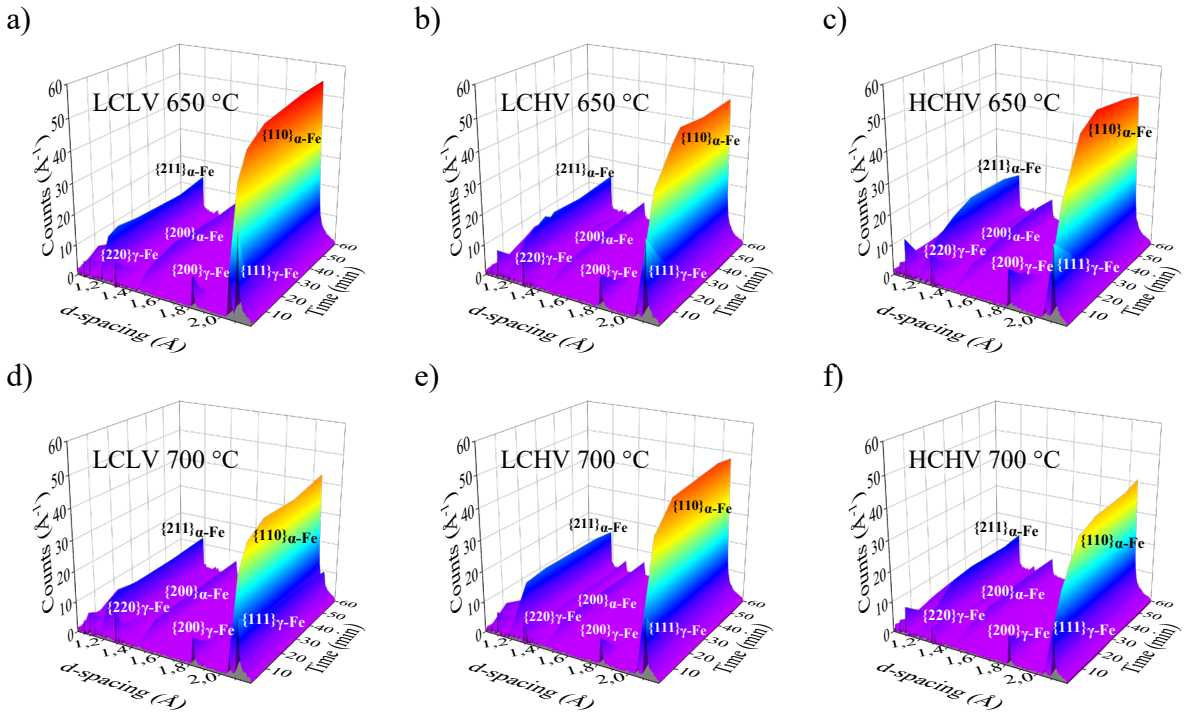

Fig. C2. Time evolution of the diffraction peaks of α-Fe and γ-Fe during the first hour of the isothermal annealing of the a) LCLV, b) LCHV and c) HCHV steels at 650 °C, and of the d) LCLV, e) LCHV and f) HCHV steel at 700 °C. The most intense peaks are marked.

In Chapter 5, we explain the delay in the onset and time evolution of austenite to ferrite phase transformation in the results obtained from the neutron diffraction experiments compared to the ones obtained from the dilatometry heat-treatments. We discuss the effect of the external magnetic field on the austenite-to-ferrite phase-transformation kinetics by comparing (zero field) dilatometry with in-situ magnetometry under a magnetic field of 1.6 T. The time evolution of the magnetization during annealing of the LCLV steel at 650 °C is presented in Fig. C3 below.

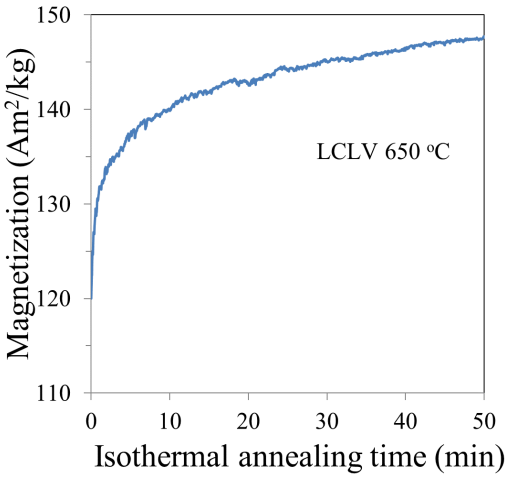

Fig. C3. Time evolution of the magnetization during annealing of the LCLV steel at 650 °C.

C2. Precipitation kinetics by Small-angle Neutron Scattering

The plots in Figs. C4-C6 include the SANS nuclear and the magnetic differential scattering cross sections of the LCLV, LCHV and HCHV steels obtained at different annealing times at 650 °C and 700 °C.

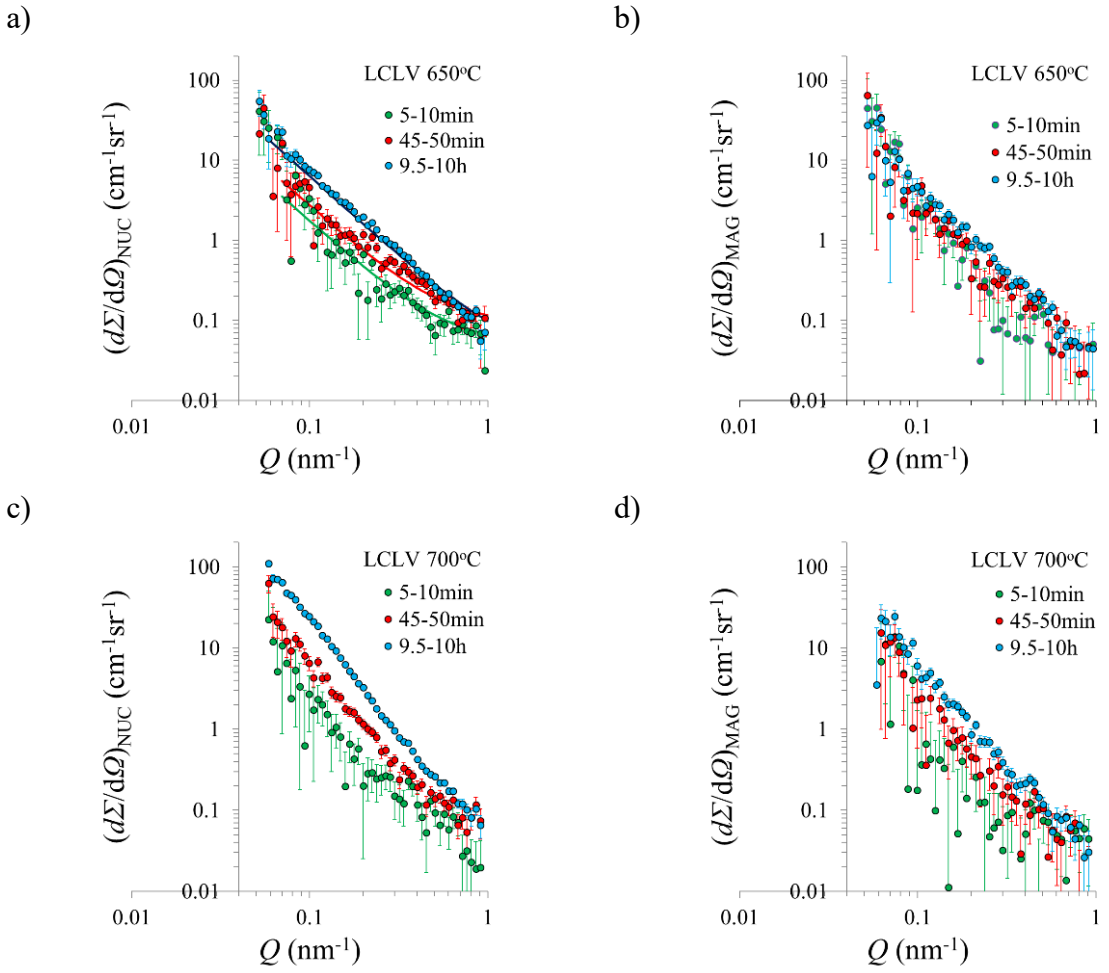

Fig. C4. Time evolution of the a) nuclear and b) magnetic SANS scattering cross section of the LCLV steel annealed at 650 °C for various annealing times. In c) and d) the time evolution of the c) nuclear and d) magnetic SANS scattering cross section of the LCLV steel annealed at 700 °C.

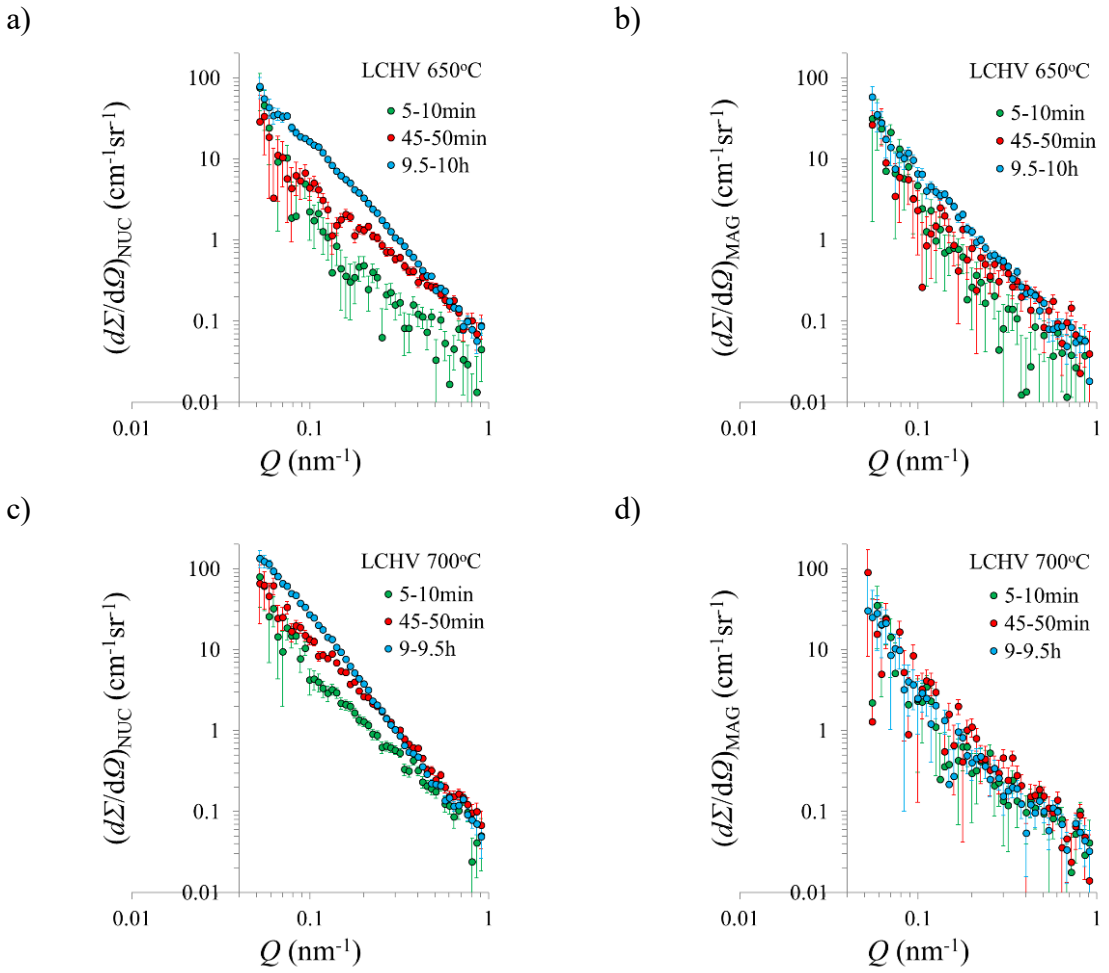

Fig. C5. Time evolution of the a) nuclear and b) magnetic SANS scattering cross section of the LCHV steel annealed at 650 °C for various annealing times. In c) and d) the time evolution of the c) nuclear and d) magnetic SANS scattering cross section of the LCHV steel annealed at 700 °C.

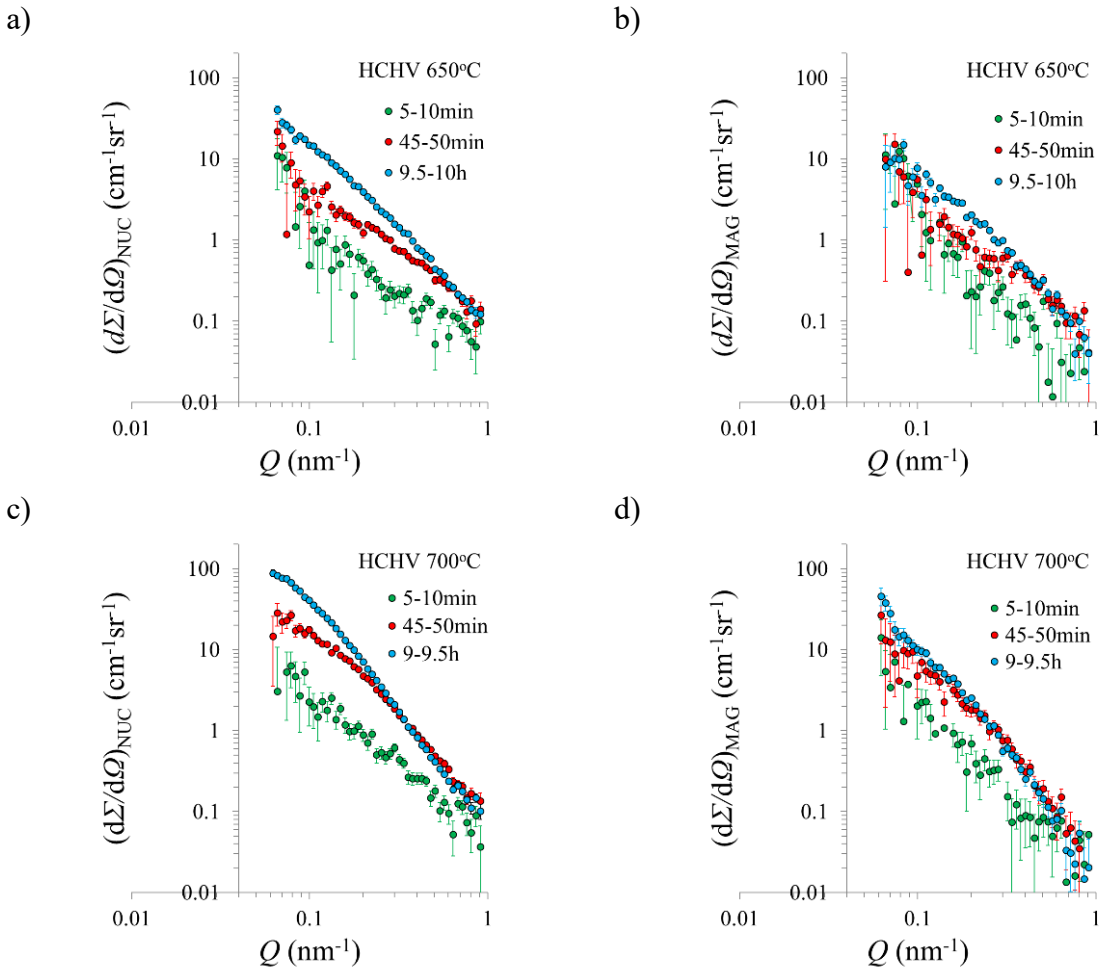

Fig. C6. Time evolution of the a) nuclear and b) magnetic SANS scattering cross section of the HCHV steel annealed at 650 °C for various annealing times. In c) and d) the time evolution of the c) nuclear and d) magnetic SANS scattering cross section of the HCHV steel annealed at 700 °C.

C3. Transmission electron microscopy

TEM is used to investigate the shape of precipitates and this information is used as input for SANS data analysis. Examples of TEM micrographs corresponding to LCLV, LCHV and HCHV steels annealed at 650 °C or 700 °C for different isothermal holding times are shown in Figs. C7a-d. Based on the TEM analysis, the precipitate shape is modelled as oblate ellipsoidal. The details of the SANS data analysis using an ellipsoidal model are explained in the manuscript. Note here that TEM is used for a qualitative investigation of the precipitate shape in order to contribute to the SANS analysis, and not to obtain quantitative information on the precipitate shape and size. The reason behind this is the differences in the phase transformation and precipitation kinetics between the steels heat-treated in the dilatometer without a magnetic field and in the furnace under the effect of an external magnetic field.

a) LCLV at 650 °C for 20 min

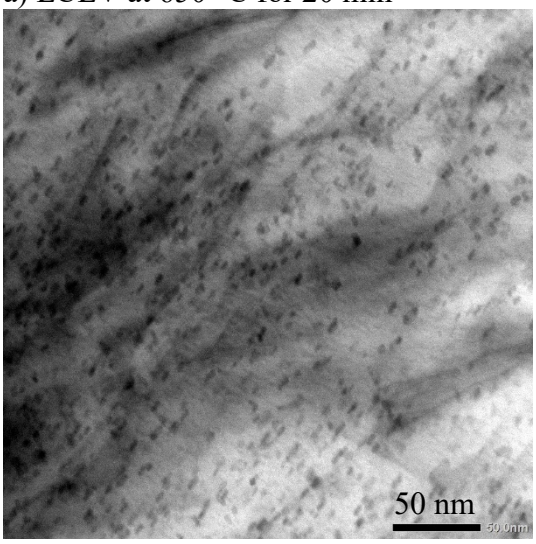

b) LCLV at 700 °C for 2 h

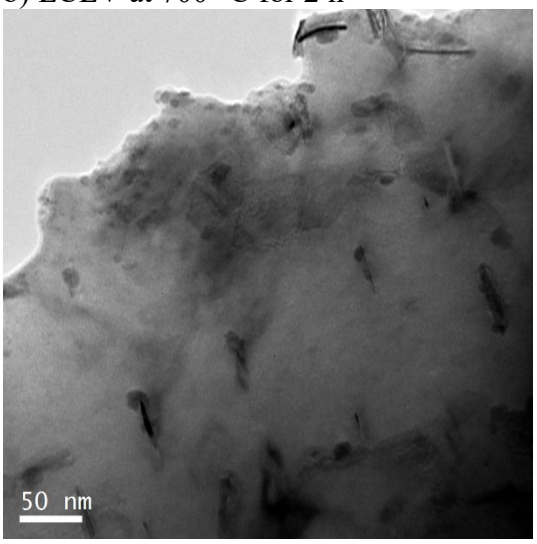

c) LCHV at 700 °C for 2 h

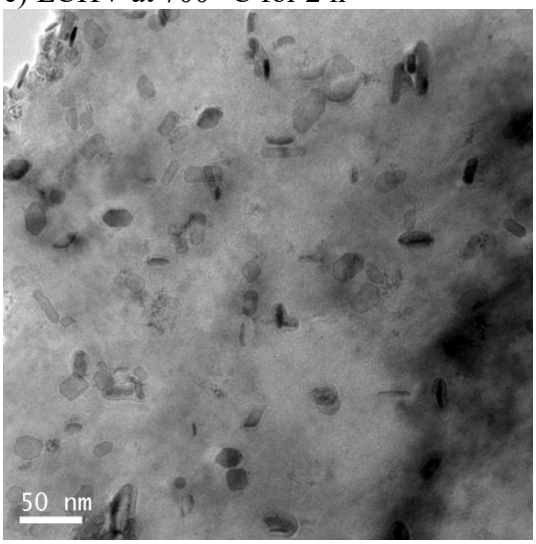

d) HCHV at 650 °C for 20 min

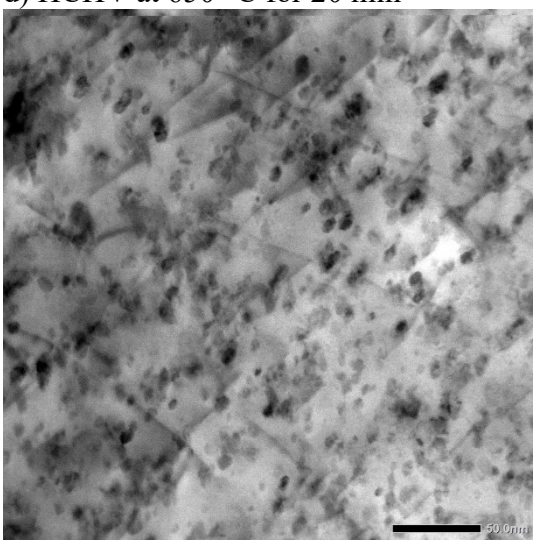

Fig. C7. TEM bright field images of the LCLV, LCHV and HCHV steels heat treated at 650 or 700 °C for different annealing times.

C4. Effective precipitate volume fraction

The time evolution of the precipitate volume fraction in the LCLV, LCHV and HCHV steels at 650 °C and 700 °C is shown in Figs. C8a-f. The calculations on the volume fraction and the effective volume fraction of the precipitates are described in Chapter 5. The I, II and III point sets correspond to the I, II and III precipitate representations of Fig. 5.11 in Chapter 5.

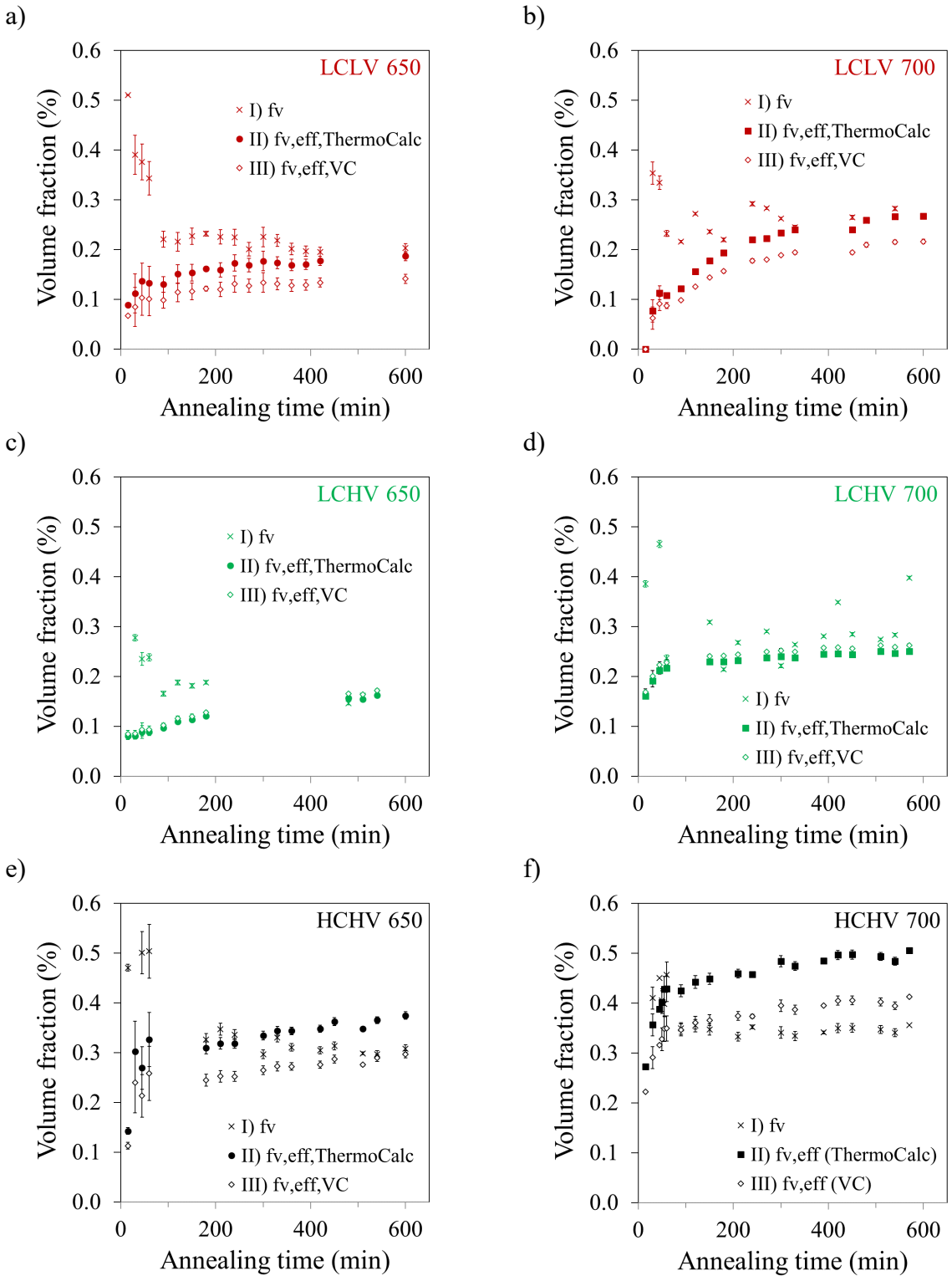

Fig. C8. Time evolution of the precipitate volume fraction in the a) LCLV, c) LCHV and e) HCHV steels at 650 °C, and in the b) LCLV, d) LCHV and f) HCHV steel at 700 °C, calculated in different ways as described in Chapter 5. The I, II and III curves correspond to the I, II and III precipitate representations of Fig. 5.11, Chapter 5.

C5. Fraction of vanadium in solid solution and in the precipitates

The time evolution of the fraction of vanadium in solid solution and in the precipitates in all steels at 650 °C and 700 °C is shown in Figs. C9a-f. The calculations are for precipitate representation II. The comparison to phase transformation kinetics is also presented.

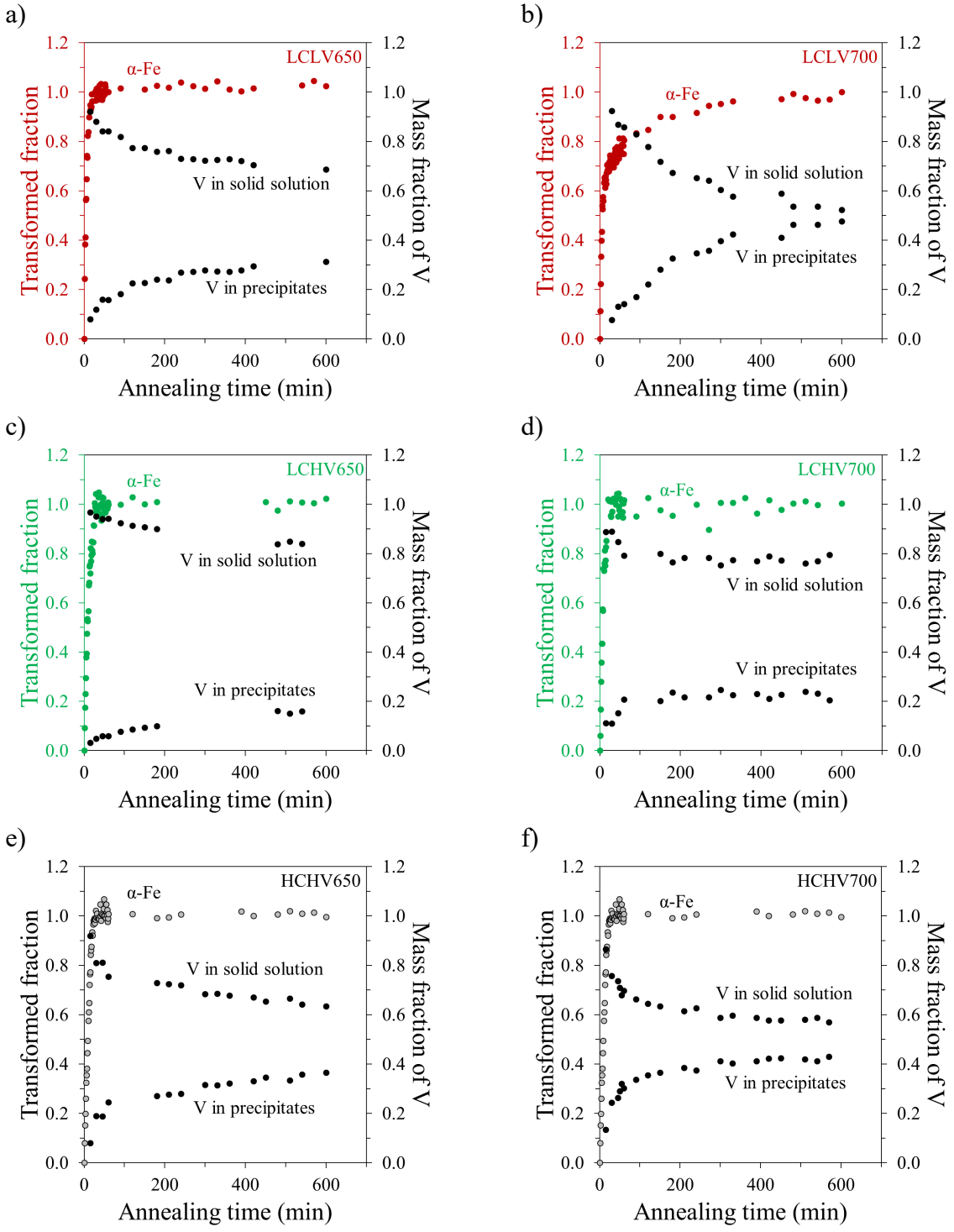

Fig. C9. Time evolution of the fraction of vanadium in solid solution and in the precipitates in the a) LCLV, c) LCHV and e) HCHV steels at 650 °C, and in the b) LCLV, d) LCHV and f) HCHV steel at 700 °C. The comparison to phase transformation kinetics is also presented.

Acknowledgements

Doing my PhD in TUDelft was a magnificent experience. I learned a lot, faced many challenges but also enjoyed it. I could not have managed to complete this chapter of my life and conduct this research work without the support of the people referred below.
Firstly, I would like to sincerely thank my daily supervisors, prof. S. Erik Offerman and prof. Ad A. van Well for the continuous support, discussions and collaboration during my PhD. I feel lucky to be accompanied by their motivation, guidance, encouragement, understanding and knowledge. They gave me the opportunity to be involved in the Nano-steel project, to join their teams, to work in a professional environment and to collaborate with experts while they were always showing respect to my questions and opinion. I could not have better mentors and I really appreciate that.
Besides my daily supervisors, I would like to thank prof. Catherine Pappas and prof. Jilt Sietsma for their insightful comments during our meetings that were always a food for thought for me. I learnt a lot from them and I am very thankful to have had discussions with them.
In addition, I wish to express gratitude to Tata Steel Europe and NWO for providing financial support to this work through their contribution to M2i. Special thanks to Arjan Rijkenberg from Tata steel Europe for the fruitful discussions, the material and his contribution to the progress of the project. I would also like to acknowledge the contribution of Peter Smaal Foundation and express my sincere thank you for the 3-month financial support. My special thanks to Robert Dalgliesh and his colleagues from STFC ISIS laboratory for their assistance on the neutron measurements and data analysis. I wish to acknowledge the contribution of the engineer Ernst van der Wal on the furnace design and our excellent collaboration. I also would like to thank the technicians of 3mE for their assistance, training sessions and help in the labs of 3mE, TUDelft. Many thanks to Xukai and prof. Bart Kooi from Groningen University for the good collaboration and the TEM measurements and to Sebastian Koelling for the APT measurements.
My special thanks to my colleague and friend Alfonso Navarro López for the great collaboration in the Nano-steel project. I thank him for the discussions, for his support for PhD but also life issues, and for all the fun we had in that one year of our collaboration and during the 4 years of my PhD. I also thank our fellow colleague Zaloa Arechabaleta for the one year of working together and for the discussions.
It is very important for me to thank my friends and colleagues from TUDelft. Many cordial thanks to Sudhee and Wei with whom we started our PhDs together and were sharing our thoughts and experiences during all these years. Vangeli, Artemi, Konstantina, Konstantine, Mohsen, Behnam, Viviam, Javi, Marilia, Tim, Carola, thanks for the moments that we spent together. I would also like to thank Prisca and Saskia, the secretaries of our group who were always there willing to help, and all the colleagues from the MSE department for the discussions.
My sincere thanks belong to my friends outside Delft. Katerina, Kiki and Christo, thank you so much for all the years of support whatever the distance between us. I am looking forward to share more experiences with you.
Special and cordial thanks belong to my partner Alexis for his understanding, for his support, for encouraging me to start the PhD, for being a great listener, advisor, motivator and inspirator, for teaching me to be patient and never give up, and above all, for being present in all the important moments. It is my honor and pleasure to have him in my life.
Last but of major importance is the very big thank you that I would like to say to my family. I would like to thank my brother Thodoris-Nikos for being my hug and my constant during my whole life. Thanks to my beloved parents, my mother, Evangelia, and my father, Dimosthenis, who are always encouraging me to become a better person and are always by my side. I

appreciate everything that they have done for me. Thanks also to my uncles, grandparents and all my family for their support.
Thanks to all people that motivated me to finish this work and also to those that made my life a bit difficult but taught me a lesson and helped me to improve.

Σας ευχαριστώ όλους πάρα πολύ, ήταν μία μοναδική εμπειρία, τα λέμε στο Ντέλφτ!

Delft, March 2022
Chrysoula Ioannidou

About the author

Chrysoula Ioannidou

2020 - present	Postdoctoral researcher in metal Additive Manufacturing, KTH University, Sweden.
2016 - 2022	PhD candidate in Materials Science and Engineering, Delft University of Technology, the Netherlands. Research project: Resource efficient nano-steels through in-situ and simultaneous studies of the precipitation and phase transformation kinetics by Small-Angle Neutron Scattering and Neutron Diffraction.
2013 - 2015	MSc in Nanosciences and Nanotechnologies, Aristotle University of Thessaloniki, Greece. Specialization: Nanomaterials and Nanomechanics.
2008 - 2013	Electrical and Computer Engineering Diploma (BSc and MSc), Aristotle University of Thessaloniki, Greece. Specialization: Electrical energy.

List of publications

- C. Ioannidou, Z. Arechabaleta, A. Rijkenberg, R. M. Dalgliesh, A. A. van Well, S. E. Offerman, "VC-Precipitation Kinetics Studied by Small-Angle Neutron Scattering in Nano-Steels", Materials Science Forum 941 (2018) 236–244.

- C. Ioannidou, Z. Arechabaleta, A. Navarro-López, A. Rijkenberg, R. M. Dalgliesh, S. Kölling, V. Bliznuk, C. Pappas, J. Sietsma, A. A. van Well, S. E. Offerman, "Interaction of precipitation with austenite-to-ferrite phase transformation in vanadium micro-alloyed steels', Acta Materialia 181 (2019) 10–24.

- A. Navarro-López, C. Ioannidou, E. M. van der Wal, Z. Arechabaleta, R. van den Oever, M. N. Verleg, R. M. Dalgliesh, J. Sykora, F. A. Akeroyd, N. Geerlofs, J. Sietsma, C. Pappas, A. A. van Well, S. E. Offerman, "Furnace for In-situ and Simultaneous Studies of Nano-Precipitates and Phase Transformations in Steels by SANS and Neutron Diffraction", Review of Scientific Instruments 91 (2020), 123903.

- C. Ioannidou, A. Navarro-López, A. Rijkenberg,R. M. Dalgliesh, S. Koelling, C. Pappas, J. Sietsma, A. A. van Well, S. E. Offerman, "Evolution of the precipitate composition during annealing of vanadium micro-alloyed steels by in-situ SANS", Acta Materialia 201 (2020) 217–230.

- X. Zhang, C. loannidou, G. H. ten Brink, A. Navarro-López, J. Wormann, J. Campaniello, R. M. Dalgliesh, A. A. van Well, S. E. Offerman, W. Kranendonk, B. J. Kooi, "Microstructure, precipitate and property evolution in cold-rolled Ti-V high strength low alloy steel", Materials and Design 192 (2020) 108720.

- C. Ioannidou, A. Navarro-López, R. M. Dalgliesh, A. Rijkenberg, X. Zhang, B. Kooi, N. Geerlofs, C. Pappas, J. Sietsma, A. A. van Well, S. E. Offerman, "Phase-transformation and precipitation kinetics in vanadium micro-alloyed steels by in-situ, simultaneous neutron diffraction and SANS", Acta Materialia 220 (2021) 117317.